Dipl.-Ing. Christian Winkler, BSc

Modeling charge-transport relevant quantities of organic and hybrid nanomaterials

DOCTORAL THESIS

to achieve the university degree of

Doktor der technischen Wissenschaften

submitted to

Graz University of Technology

Supervisor

Ao.Univ.-Prof. Dipl.-Ing. Dr. Egbert Zojer

Institute of Solid State Physics

Graz, December 2020

Affidavit

I declare that I have authored this thesis independently, that I have not used other than the declared sources/resources, and that I have explicitly indicated all material which has been quoted either literally or by content from the sources used. The text document uploaded to TUGRAZonline is identical to the present doctoral thesis.

Date

Signature

Danksagung

Würde man Lebenszeit in Kapitel unterteilen so wäre eine Dissertation sicherlich ein eigenes Kapitel. Nicht nur weil man einige Jahre für die Durchfürhrung einer solchen Arbeit benötigt, sondern insbesondere auch weil man stets etwas Neues lernt während dieser Zeit. Dieses Neue bezieht sich dabei aber nicht nur auf Fachwissen sondern auf so viel mehr, dass eine Aufzählung diesen Rahmen hier sprengen würde. Somit bleibt mir nun am Ende dieses Kapitels all jenen Danke zu sagen die mich während dieser Zeit unterstützt haben und von denen ich etwas Erlernen konnte.

Beginnen möchte ich mit meinem Betreuer Egbert Zojer, für seine exzellente Betreuung und sein großes Engagement. Besonders Herausstreichen möchte ich, dass er einen stets ermuntert neugierig zu sein und seinen Interessen zu folgen. Sei dies wissenschaftlich mal ein wenig aus dem Projekt auszubrechen oder einfach mal Weiterbildungen zu besuchen die einem Dinge über die Wissenschaft hinaus näher bringen. So konnte ich wirklich sehr viel während meiner Dissertation dazu lernen und in meinen Fähigkeiten wachsen. Bedanken möchte ich mich auch bei Oliver Hofmann für seine hilfreichen und kritischen Fragen die meine wissenschaftliche Arbeit stets verbessert haben. Außerdem möchte ich mich für die Zeit in Warwick bedanken wo ich dank der Einladung von Oliver und Reinhard Maurer meine Arbeit vorstellen konnte und bei so mancher Diskussion wieder viel dazulernen konnte. Für die Unterstützung bei meiner Exkursion in die Welt der Röntgenstrukturanalyse möchte ich mich bei Roland Resel bedanken.

Nun aber weiter zu einem großen Dankeschön, dass ich an meine Kollegen richten möchte. Danke, ohne euch wäre diese Zeit sicher viel mühsamer und weniger unterhaltsam gewesen. Dieses Dankeschön gilt natürlich allen derzeitigen und auch ehemaligen Mitgliedern des Advanced Materials Modeling Teams, geht aber auch an die Bewohner des k-Raums. Ein besonderes Dankeschön geht an Elisabeth Stern, für ihre stets positive Art und die zahlreichen lustigen Gespräche.

Für die finanzielle Unterstützung möchte ich mich beim Österreichischen Wissenschaftsfonds (FWF) im Rahmen des Projektes P28051-N36 bedanken. Weiters gilt mein Dank der TU Graz, welche mich im Rahmen des Lead Projektes “Porous Materials at Work”

(LP-03) unterstützt hat. Generell möchte ich mich bei allen Mitlgiedern des Lead Projektes bedanken, die gemeinsamen Meetings waren immer spannend und unterhaltsam. Ein Danke geht auch an das Support Team des Vienna Scientific Cluster VSC3.

Ein sehr großes Dankeschön geht außerdem an meine Familie, die mich stets in jedweder Art und Weise und uneingeschränkt unterstützt hat. Danke!

Theresa, meine Partnerin, schafft es stets meine Gedanken mal von der Arbeit loszueisen und hilft mir wieder einen frischen Kopf zu bekommen. Dafür und für noch so viel mehr möchte ich mich bei ihr bedanken.

Abstract

Computational modeling has emerged as a valuable tool for understanding the structural and electronic properties of organic and hybrid nanomaterials. Especially charge transport is of great interest, as the ability to efficiently transport charges is a beneficial property for many applications. Thus, in the field of organic semiconductors, numerous models for describing and predicting charge transport in these materials have been developed. Despite the large efforts that have been made, no single model which can describe charge transport for the entire range of organic semiconductors, comprising different geometric and electronic structures, has been identified. However, closely inspecting the various transport models one can identify certain quantities that can be modeled employing dispersion corrected density functional theory and used for getting a qualitative understanding of charge transport in a material. Such quantities are the electronic couplings between neighboring molecules within the crystalline structure of the material or the effective masses of the respective charge carriers.

This thesis is concerned with obtaining a reliable description of these quantities for crystalline organic semiconductors, porous metal-organic frameworks, and layered covalent organic frameworks. Especially the influence of the structural arrangement of neighboring molecular moieties within these materials on the respective electronic couplings and effective masses is investigated. Furthermore, the correlation between the electronic couplings of a certain molecular arrangement and the energetic stability of this arrangement is investigated.

First, based on the example of a prototypical organic semiconductor, different approaches for obtaining the electronic couplings and effective masses are evaluated. It is shown, how fitting a suitably complex tight-binding model function to the electronic bands obtained from density functional theory calculations yields a reliable description of the intermolecular electronic couplings. Furthermore, based on this model, one not only gets all the electronic couplings of interest but can also decompose the electronic band structure into the individual contributions stemming from these couplings.

Based on quinacridone one can construct a model system and investigate the electronic couplings between neighboring molecules and this arrangement's energetic stability simultaneously. The physical origin of the correlation between energetic stability and electronic coupling is investigated for the periodic structure by decomposing the interaction energy between the molecules into physically well-defined contributions. For layered covalent organic frameworks, the interaction energy between consecutive layers is decomposed into individual contributions, similar to the quinacridone model system. This allows investigating how individual interactions determine the energetic stability of specific layer arrangements.

Another part of the present work is concerned with transferring knowledge on charge transport in organic semiconductors to the newly emerging field of electrically conductive metal-organic frameworks. Several metal-organic frameworks exist where charge transport pathways similar to organic semiconductor crystals are found. For Zn_2(TTFTB), a representative example of these materials, the electronic couplings between neighboring molecular moieties comprising the transport pathway are investigated as a function of the arrangement of these moieties. Additionally, the influence of defects on the charge transport relevant quantities (electronic couplings and effective masses) is discussed.

Kurzfassung

Computerunterstützte Modellierung hat sich als wertvolles Werkzeug erwiesen um die strukturellen und elektronischen Eigenschaften organischer und hybrider Nanomaterialien zu verstehen. Insbesondere der Transport von elektrischen Ladungen ist von großem Interesse, da die Fähigkeit, Ladungen effizient zu transportieren, für viele potentielle Anwendungen eine vorteilhafte Eigenschaft darstellt. Auf dem Gebiet der organischen Halbleiter wurden daher zahlreiche Modelle zur Beschreibung und Vorhersage des Ladungstransports entwickelt. Trotz der großen Anstrengungen wurde kein einheitliches Modell identifiziert, das den Ladungstransport für die gesamte Palette organischer Halbleiter mit unterschiedlichen geometrischen und elektronischen Strukturen beschreiben kann. Bei genauer Betrachtung der verschiedenen Transportmodelle können jedoch bestimmte Größen identifiziert werden, die mithilfe der Dichtefunktionaltheorie modelliert und zum qualitativen Verständnis des Ladungstransports in einem Material herangezogen werden können. Solche Größen sind die elektronischen Kopplungen zwischen benachbarten Molekülen innerhalb der Kristallstruktur des Materials sowie die effektiven Massen der jeweiligen Ladungsträger.

Die vorliegende Dissertation befasst sich mit der Beschreibung dieser Größen für kristalline organische Halbleiter, poröse metallorganische Gerüstverbindungen und kovalente organische Netzwerke. Insbesondere wird der Einfluss der strukturellen Anordnung benachbarter Moleküleinheiten innerhalb dieser Materialien auf die jeweiligen elektronischen Kopplungen und effektiven Massen untersucht. Weiterhin wird die Korrelation zwischen den elektronischen Kopplungen einer bestimmten molekularen Anordnung und der energetischen Stabilität dieser Anordnung untersucht.

Zunächst werden am Beispiel eines prototypischen organischen Halbleiters verschiedene Ansätze zur Ermittlung der elektronischen Kopplungen und effektiven Massen verglichen. Es wird gezeigt, wie die Anpassung einer geeignet komplexen *tight-binding* Modellfunktion an die elektronischen Bänder, welche mithilfe der Dichtefunktionaltheorie berechnet wurden, eine zuverlässige Beschreibung der intermolekularen elektronischen Kopplungen

liefert. Darüber hinaus erhält man basierend auf diesem Modell alle inkludierten elektronischen Kopplungen, und außerdem kann die elektronische Bandstruktur in die Beiträge der einzelnen Kopplungen zerlegt werden.

Weiters, kann man basierend auf Chinacridon ein Modellsystem konstruieren um die elektronischen Kopplungen zwischen benachbarten Molekülen und die energetische Stabilität dieser Anordnung simultan zu untersuchen. Der physikalische Ursprung der Korrelation zwischen energetischer Stabilität und elektronischer Kopplung wird für die periodischen Systeme untersucht, indem die Wechselwirkungsenergie zwischen den Molekülen in physikalisch genau definierte Beiträge zerlegt wird. Bei geschichteten kovalenten organischen Netzwerken wird die Wechselwirkungsenergie zwischen aufeinanderfolgenden Lagen ähnlich wie beim Chinacridon-Modellsystem in einzelne Beiträge zerlegt. Dies ermöglicht es zu untersuchen, wie einzelne Wechselwirkungen die energetische Stabilität bestimmter Anordnungen der Lagen des Materials bestimmen.

Ein weiterer Teil der vorliegenden Arbeit befasst sich damit Wissen über den Ladungstransport in organischen Halbleitern auf das neu aufkommende Gebiet der elektrisch leitenden metallorganischen Gerüstverbindungen zu übertragen. Es gibt mehrere metallorganische Gerüsteverbindungen, in denen elektrische Ladungen entlang ähnlicher Pfade wie in organischen Halbleiterkristallen transportiert werden. Für Zn_2(TTFTB), ein repräsentatives Beispiel dieser Materialien, werden die elektronischen Kopplungen zwischen benachbarten molekularen Einheiten, als Funktion der Anordnung dieser Einheiten untersucht. Zusätzlich wird der Einfluss von Defekten auf die ladungstransportrelevanten Größen diskutiert.

Structure of the Thesis

The following work will be a *cumulative* PhD Thesis, consisting of peer-reviewed scientific articles which I authored during my PhD studies. According to the structure suggested by the Doctoral School of Physics it consists of a general introduction putting the work into context, followed by the set of original publications including the respective supporting information.

During my time as a PhD student I prepared 5 scientific publications as the leading author. The first paper (see 2D Materials **2018**, 5, 035019 - i.e. Ref. [1]) is based on ideas that where developed during the course of my Master Thesis. Therefore, it is not included here. At the present stage three manuscripts are enclosed as original publications. The fourth one is included as a draft which is about to be submitted. The introductory part of this thesis is meant to introduce the scientific questions which have been tackled in the individual Publications together with the relevant methods that were used.

Prior to each publication the contributions of each (co-)author are listed.

List of Publications

Publication I

Analyzing the Electronic Coupling in Molecular Crystals - The Instructive Case of α-Quinacridone[2]

Christian Winkler, Florian Mayer, and Egbert Zojer

Advanced Theory and Simulations, **2019**, 2, 1800204

Publication II

Understanding the Correlation between Electronic Coupling and Energetic Stability of Molecular Crystal Polymorphs: The Instructive Case of Quinacridone[3]

Christian Winkler, Andreas Jeindl, Florian Mayer, Oliver T. Hofmann, Ralf Tonner, and Egbert Zojer

Chemistry of Materials, **2019**, 31, 7054-7069

Publication III

Strategies for Controlling Through-Space Charge Transport in Metal-Organic Frameworks via Structural Modifications[4]

Christian Winkler and Egbert Zojer

Nanomaterials, **2020**, 10, 2372 (selected as *Editor's choice*)

Publication IV

Determining the role of electrostatic and dispersion interactions for the stacking motif of covalent organic frameworks

Christian Winkler and Egbert Zojer

in preparation

Contents

1. Introduction

Solid materials consist of closely packed entities (atoms or molecules), which strongly interact. The nature of these entities, their arrangement, and the corresponding interactions define the mechanical, electrical, optical, magnetic, and thermal properties of a solid. In this work I focus on the electrical properties of crystalline solids with special interest in charge transport. Efficient charge transport is one of the essential properties for numerous applications. Therefore, from an application oriented as well as from a fundamental perspective it is important to understand charge transport in a solid (material) and how it might be engineered. The general term materials is, of course, very broad and one needs to specify which kind of materials are studied. So within this thesis I focus on organic and hybrid materials which exhibit a great versatility in engineering their actual structures and thus, their properties (electrical, optical, magnetic, thermal). Three specific material types are studied in this context: crystalline organic semiconductors (OSCs), metal-organic frameworks (MOFs), and covalent organic frameworks (COFs).

These materials seem quite different at first glance. Nevertheless, I will present how one can get a qualitative understanding of charge transport within these materials based on a small set of parameters. This will allow me to consider some of the findings which have been obtained for the already quite mature field of OSCs and transfer them to the emerging class of electrically conductive COFs and MOFs.

All major content of this PhD thesis has been published (or is under review) in scientific journals. Therefore, this content is presented in the form of the corresponding publications. Nevertheless, in the very first chapter of the thesis I introduce the scientific questions that have been addressed within these works. Importantly, I outline how the various questions are connected to one another and how they help to improve our understanding of the interplay between the atomistic structure of the materials and their charge transport properties while also identifying useful methodologies for doing so. At the end of this thesis all major findings are wrapped up in a final chapter, Section 6, where the individual findings are connected across the different materials.

Before we dive right into the contents I briefly present the structure of this introductory chapter of the thesis. Let me start by introducing crystalline organic semiconductors in Section 1.1. There I also review the huge number of transport models that have been developed for this kind of materials. I will show that despite this large number of models and their differences certain common parameters can be identified, which allow a qualitative description of charge transport. Further considering the available literature on OSCs one can find that the majority of these materials usually exhibits packing arrangements with rather poor transport properties. To identify potential mechanisms behind this correlation an instructive example of an OSC has been considered. This OSC is based on the small H-bonded organic pigment quinacridone and is introduced in Section 1.1.4. Two aspects have been addressed considering this example: (i) *Which parameters can be used to get a qualitative description of charge transport within such a material?* (***Publication I***) (ii) *Does the size of intermolecular electronic couplings influence the energetic stability of relative molecular arrangements?* (***Publication II***)

As a next step, metal-organic frameworks are introduced in Section 1.2, with a special focus on electrically conductive systems. There, the structures of these systems are considered, as well as the charge transport mechanisms relevant in such systems. One of these mechanisms, the so called *through-space* charge transport, shows great similarity to mechanisms present in crystalline OSCs. Therefore, the knowledge gained by studying charge transport in OSCs is used for understanding charge transport in these MOFs. Again, special attention is paid to structure to property relationships (***Publication III***).

The last class of systems which is considered in this work are covalent organic frameworks. These systems are introduced in Section 1.3 with special focus put on two-dimensional (2D) COFs. Comparing these layered materials to the OSCs presented in Section 1.1 one can identify several similarities in their interlayer (intermolecular) interactions. As the electronic bands along the stacking direction of layered COFs largely rely on the overlap of the π-systems of neighboring layers it is of great importance to identify the preferred layer arrangement. Equally important is to identify the individual interactions that are active and how they determine the stacking arrangement. These issues are tackled and presented in ***Publication IV***.

All the publications included in this thesis rely on dispersion corrected density functional theory (DFT). Therefore, in Section 1.4 a short overview of the basic concepts of DFT is provided. Additionally, tight binding models used for obtaining transfer integrals by fitting these models to the DFT data are discussed. Already within ***Publication II*** the interaction energy of two molecules in the unit cell has been decomposed into physically

meaningful contributions. At this stage the decomposition was done by a collaborator. For studying the COFs in ***Publication IV*** I developed a custom decomposition scheme, which is largely based on one of the very few available schemes for periodic systems. This newly derived scheme together with its parent is presented in Section 1.4.3.

1.1. Organic Semiconductors and Charge Transport

Organic semiconductors are materials based on π-conjugated molecules or polymers. These materials can exist as ordered crystalline solids or as amorphous (thin) films. Our considerations focus on the former, ordered, highly crystalline systems. In general, one can note that the usage of OSCs as active elements in (opto-)electronic and photonic devices is increasing.[5–15] This increase has certainly to do with the numerous advantegous properties of these materials comprising the tunability of their electrical and optical properties,[16] mechanical flexibility,[17] and the possibility to build biocompatible electronics.[18–20] For all these applications charge transport is an essential property. However, it turns out that the description of charge transport within these materials is far from straightforward. In the following, we are going to elaborate on the microscopic transport mechanisms that can be active in OSCs. The following sections will be largely based on three reviews: The first one by Coropceanu et al.[21] is already a bit older but still covers all the essential basics. The second, more recent, one by Oberhofer et al.[22] presents a deeper level of theory while also including recent advancements. The third review, by Fratini and colleagues is a major foundation for the following considerations on transient localization theory.[23]

Let us start with the general definition of the electrical conductivity $\boldsymbol{\sigma}$ of any material. This conductivity is determined by the density of mobile charge carriers ρ_c and their mobility $\boldsymbol{\mu}$ - as shown in equation 1.1. Here the conductivity $\boldsymbol{\sigma}$ and the mobility $\boldsymbol{\mu}$ are tensors of rank 2. The charge of the carriers is denoted by q.

$$\boldsymbol{\sigma} = q\rho_c\boldsymbol{\mu} \tag{1.1}$$

The charge carrier density ρ_c of a material can be seperated into intrinisic and extrinsic contributions. The intrinsic contributions arise from the thermally excited states of the electronic bands while the extrinsic contributions emerge from defects to the structure of the material.[22] Such defects can be missing molecules, interstitial molecules, or interfaces with other (different) materials.[22] A detailed and complete assessment of the charge transport properties of an OSC or related materials would have to consider both, the

density of mobile charge carriers and the charge carrier mobility. However, focussing on the latter, one can already get a decent understanding of charge transport within a material. Therefore, we are going to focus our considerations on the description of $\boldsymbol{\mu}$. This is insofar a viable strategy, as including extrinsic contributions to the carrier density can be rather challenging within computational models. One reason making the description of ρ_c challenging is that it typically depends on operation conditions.

In the following, we consider the charge carrier mobility and the parameters determining this mobility. Independent of the underlying transport mechanism, the mobility can be defined as the velocity response of a charge carrier to an external electric field.[22] The corresponding expression is given in equation 1.2. Please note that in general the electric field as well as the resulting velocity are three-dimensional (3D) vectors. Therefore, the mobility, $\boldsymbol{\mu}$, and consequently the conductivity, $\boldsymbol{\sigma}$, are rank 2 (3 x 3) tensors.

$$\mu_{ij} = \frac{\langle v \rangle_i}{E_j} \tag{1.2}$$

Furthermore, one has to be aware that also other definitions of the charge carrier mobility exist - linearizing $\langle v \rangle$ with respect to the field or linking charge carrier mobilities to the classical kinetic theory via the Einstein-Smulochowski[24,25] equation. The corresponding expression is shown in equation 1.3, where the diffusion coefficient D_{ij} is typically field dependent. This expression relates the carrier mobility to the diffusion coefficient of a material and the thermal energy $k_B T$. Important to note is that the equality of the introduced definitions of the charge carrier mobility is not guaranteed for all regimes of charge transport.[22] Therefore, which mobility definition is employed has to be treated with caution and this choice might have to be adapted depending on the experimental technique that serves as the reference.[22]

$$\mu_{ij} = \frac{D_{ij}\, q}{k_B T} \tag{1.3}$$

The determination of this charge carrier mobility then indeed depends on the transport mechanism dominating in the material of interest. In general, one can distinguish two limiting cases, fully coherent band transport and incoherent hopping transport.

In the limit of hopping transport and considering crystalline materials, charge carriers are localized on lattice sites and can perform activated hops between these sites. For band transport, charge carriers are fully delocalized in electronic bands. The carriers can move

through the crystal with an effective mass. This effective mass depends on the inverse of the curvature of the energy dispersion relation at the band extremum. In the following, we are going to briefly review these two limiting regimes and we are also going to comment on intermediate cases. Such intermediate cases mean that electron-phonon coupling plays an essential role with respect to the transport properties (charge carrier mobility) of a material. The purpose of this review is not to give the reader a complete overview of all the details of each transport regime and the various theories or methodological approaches that have been developed for each of them. Rather, this review shall highlight the basic concepts of the transport regimes and which parameters are the essential ones determining the charge carrier mobility. Importantly, we are going to show that electronic couplings between neighboring molecules are essential quantities for understanding charge transport within OSCs. As the magnitude of such electronic couplings is intimately related to the relative arrangement of the involved molecules[21] this quantity will allow us to investigate the interplay between structure and charge transport properties. For more detailed and thorough reviews the reader is refered to References [21–23, 26].

1.1.1. Hopping Transport

Hopping transport is a process describing charge transport in crystalline (or also disordered) materials where charge carriers are localized at specific sites. Charge transport then occurs through activated discrete jumps (hops) of the charges between the sites. In a molecular crystal, such sites can be either single molecules, smaller parts of a molecule, or a collection of molecules. This depends on the degree of localization present in the material. In general, three mechanisms can lead to the localization of charge carriers in a crystalline material.[22] Within small polaron theory the interaction of the charge carrier with the medium can cause a localization. This interaction means that the charge causes a local (nuclear) distortion, which leads to a stabilization of the localized charge.[22] Another recent theory by Troisi and co-workers[23,27–29] describes that the localization is caused by thermal fluctuations of the coupling between sites (molecules). These fluctuations arise from the thermal motions of the molecules, which induce changes of the couplings between the involved molecules. Transient localization theory builds upon this coupling and has proven highly succesfull for describing the charge transport properties of high-mobility organic semiconductors.[27] This theory will be described in Section 1.1.3. Finally, static disorder can also induce a localization of charge carriers within the system.

Regardless of the underlying mechanism causing the localization of charge carriers, within hopping models charge transfer is described through discrete jumps between lattice sites and expressed in terms of transfer rates. A famous and still widely used approach is

the Marcus charge transfer rate.[30,31] In the semi-classical limit (treating the molecular vibrations as classical oscillators) the corresponding expression for the transfer rate k_{ab} can be expressed as shown in equation 1.4.

$$k_{ab} = \frac{2\pi}{\hbar} \frac{t_{ab}^2}{\sqrt{4\pi\lambda k_B T}} e^{-\frac{\lambda}{4k_B T}} \tag{1.4}$$

Here t_{ab} is the electronic coupling (transfer integral) between polaronic sites a and b $t_{ab} = \langle \Psi_a | \hat{H} | \Psi_b \rangle$, and λ is the reorganization energy.

Deriving an expression for the charge transfer rate based on polaronic rate theory yields an analagous expression see Ref [22]. In particular, when considering the non-adiabatic limit one finds that the derived transfer rate (equation 1.5) is analogous to the Marcus rate:

$$k_{ab} = \frac{2\pi}{\hbar} \frac{1}{\sqrt{4\pi\lambda k_B T}} t_{ab}^2 e^{-\frac{\Delta G^\ddagger}{k_B T}} \Gamma_n. \tag{1.5}$$

In this non-adiabatic limit the electronic coupling is much smaller than the reorganization energy. As a consequence, $\lambda + \Delta G^0 >> t_{ab}$, which then results in the above expression for the charge transfer rate. Here ΔG^0 is the difference in free energy between the initial polaronic state a and the final polaronic state b and $\Delta G^\ddagger$ is the activation energy of the transfer process. Furthermore, Γ_n is the nuclear tunneling factor, which corrects for quantum effects of the nuclear degress of freedom that can lead to an enhanced transfer rate. This correction factor is often set to 1 as the enhancements of the transition rates are mostly relevant at rather low temperatures.[22]

Based on the rates in equations 1.4 and 1.5 we find that they are proportional to the square of the electronic coupling between sites a and b. Furthermore, the charge carrier mobility is proportional to the rate k_{ab} and thus to t_{ab}^2 as indicated in equation 1.6.

$$\mu_{ab} \propto k_{ab} \propto t_{ab}^2 \tag{1.6}$$

This proportionality between the square of the electronic coupling and the charge carrier mobility is especially helpful for obtaining a qualitative description of the interplay between structural arrangements in OSCs and charge transport. It has been shown that depending on the relative displacement of consecutive molecules, the electronic coupling between these entities can vary by orders of magnitude.[21,32–36] Assuming hopping transport, as described above, this orders of magnitude change of the intermolecular

electronic coupling would then translate into comparable changes of the carrier mobility. Thus, already from determining molecular arrangements in the crystal and calculating the intermolecular electronic couplings one gets a first understanding of charge transport within the material.

In addition to the intermolecular electronic coupling t_{ab} being an essential quantity for describing charge transport in OSCs also the intermolecular spacing r can be important. To show this, let us consider a charge carrier moving along a simple 1D array of molecules with an intermolecular spacing r. For such a system one can write the diffusion coefficient as $D = r^2\, k_{ab}$ and link this with equation 1.3 to the charge carrier mobility. This means that the charge carrier mobility is not onyl proportional to the square of the electronic coupling but also to the square of the intermolecular spacing $\mu \propto (r \cdot t_{ab})^2$, i.e. the mean-free displacement of the charge carrier. Therefore, for making qualitative statements about hopping transport within a material, one has to consider the respective intermolecular electronic couplings, as well as the corresponding lattice spacings. Considering only the electronic coupling can be quite misleading as one can see from the data discussed in ***Publication I*** (Chapter 2).

1.1.2. Band Transport

The other limiting case for charge transport is fully coherent band transport. Within this regime charges are assumed to be delocalized in periodic bands. The basis of this transport theory is the solution of the electronic problem for an unperturbed periodic lattice. There the charge carriers form Bloch waves which have a certain momentum $\boldsymbol{k}$ and energy $\epsilon_\alpha(\boldsymbol{k})$ and can travel through the material as wavepackages.[37]

Furthermore, upon negelecting scattering processes, all transport properties of a material are determined by its electronic band structure, i.e. the energy dispersion relation $\epsilon_\alpha(\mathbf{k})$. As an example for such an electronic band structure we consider a polymorph of quinacridone, for which the electronic bands have been calculated in ***Publication II*** (Ref [2]). They are shown in Figure 1.1.

When applying an electric field (see equation 1.2 for the corresponding mobility definition) charge carriers experience an acceleration and their velocity changes simply by a Newtonian equation of motion.[22,37] Now, one very important aspect to consider is that in realistic systems there are various effects present which act contrary to the acceleration of the particles. These effects are scattering events on defects or lattice vibrations (phonons). The resulting interplay between the acceleration caused by the electric field and the deceleration caused by scattering events leads to a steady-state condition. Consequently,

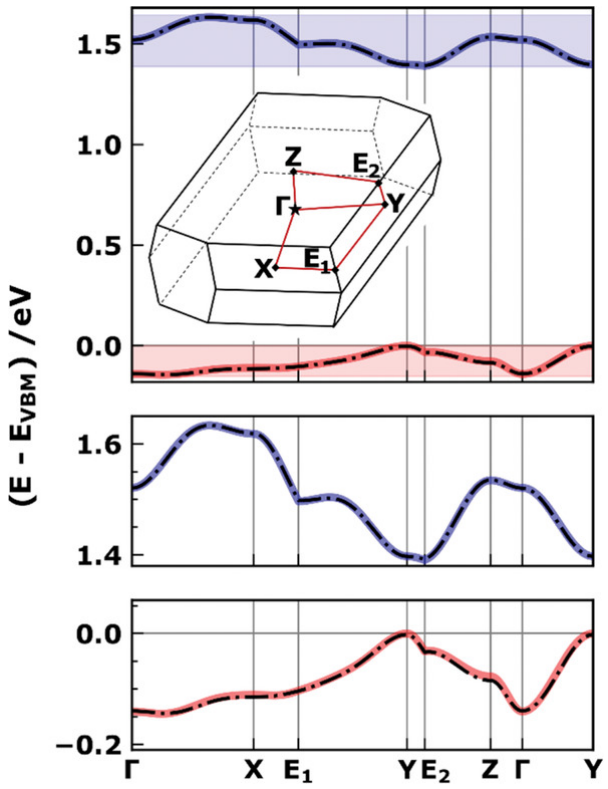

Figure 1.1.: Calculated electronic band structure of the α-polymorph of quinacridone (solid lines). The energies are aligned relative to the top of the valence band and the first Brillouin zone is shown as an inset. The lower panel includes a zoom into the regions of the valence and the conduction band. A tight-binding model has been fitted to the bands as discussed in Section 1.4.2 and is shown by the black dash dotted line. Reprinted with permission from Ref [2].

charge transport in this regime can be modelled by the Boltzmann transport equation.[22,37] By introducing the so called relaxation-time approximation one obtains a time constant τ describing the average time between scattering events.[37] As a result one gets the mobility expression shown in equation 1.7.

$$\mu_{ij} = \frac{q}{m^*_{ij}} \tau_{ij} \tag{1.7}$$

Here q denotes the charge, τ_{ij} is the mean relaxation time between collisions (scattering events) and m^*_{ij} is the effective mass. Both, τ_{ij} and m^*_{ij} are rank-2 (3 x 3) tensors, with i and j being indices that denote the reciprocal space vectors. Based on expression 1.8 for semiconductors one can calculate the effective mass directly from the electronic band structure as the inverse of the curvature of the electronic band at the respective extremum. For holes, this means that one has to consider the valence band maximum,

while for electrons the conduction band minimum is the relevant one. As long as one does not have an analytical expression for the electronic band structure, this means that the components of the effective mass tensor have to be calculated numerically along the reciprocal space directions.

$$\left(\frac{1}{m^*}\right)_{ij} = \frac{1}{\hbar^2}\frac{\partial\epsilon_\alpha(\boldsymbol{k})}{\partial k_i \partial k_j} \tag{1.8}$$

However, when one is interested in only a single spatial direction, or the material is completely isotropic, the effective mass can be estimated in simpler ways. The first one relies on the energy dispersion relation derived from a nearly free-electron model.[37] In this approximation the dispersion relation $\epsilon_\alpha(\boldsymbol{k})$ exhibits a parabolic dependence on the reciprocal space vector $\boldsymbol{k}$. The corresponding expression is shown in equation 1.9. Consequently, this means that we can obtain the effective mass simply by fitting a parabola to the energy eigenvalues close to the band extremum.[†] It is apparent that for the considered 1D system $|\boldsymbol{k}| = k$.

$$\epsilon_\alpha(\boldsymbol{k}) = \epsilon_0 + \frac{\hbar^2 |\boldsymbol{k}|^2}{2m^*} \tag{1.9}$$

Another approach would rely on fitting elaborate tight-binding model functions to the energy eigenvalues of each band α. Such tight-binding models are discussed in detail in section 1.4.2. At this point we will only briefly introduce a simple model for 1D systems with only nearest-neighbor couplings t_{ab} between equivalent sites a and b being relevant. The following expression is then obtained for the energy of the electronic states as a function of wavevector $\boldsymbol{k}$:[‡]

$$\epsilon_\alpha(k) = \epsilon_{0,\alpha} - 2t_{ab,\alpha}\, cos(kr) \tag{1.10}$$

This expression can be fitted to the calculated band structure of band α. During this fit $\epsilon_{0,\alpha}$ and $t_{ab,\alpha}$ serve as fit parameters. As a result we obtain an analytical expression for the energy dispersion relation and can calculate the effective mass by taking the second derivative of this system with respect to k:

[†]In principle, this ansatz using a parabolic form of the energy dispersion relation works for any $\boldsymbol{k}$-point. Here, however, we are mainly interested in the effective mass at the band extrema.

[‡]Writing the cosine in equation 1.10 as a Taylor series and truncating it after the second term one obtains equation 1.9 describing the free electron model.

$$m^* = \left(2t_{ab,\alpha}\, r^2\, cos(kr)\right)^{-1} \tag{1.11}$$

Evaluating the expression for the effective mass given in equation 1.11 at a specific k-point, $k_{extremum}$, and entering the corresponding term into the expression for the charge carrier mobility in equation 1.7 one finds that the mobility μ is proportional to the electronic coupling $t_{ab,\alpha}$ and the square of the lattice spacing r:

$$\mu \propto t_{ab}\, r^2 \tag{1.12}$$

This means that again the electronic coupling between neighboring sites is an essential quantity for the description of μ.

As a result of fitting the expression in equation 1.10 to the electronic band, we also obtained the intermolecular electronic coupling between neighboring sites a and b within the 1D crystalline system. This approach of determining elaborate tight-binding model functions and fitting them to the calculated electronic band structures is not restricted to 1D systems. In Section 1.4.2 we are going to discuss such tight-binding approaches for 3D crystals with up to two different sites per unit cell.

1.1.3. Transient Localization Theory

Quite a large number of OSCs neither exhibit situations where the charge carrier is fully localized at one site nor are these carriers fully delocalized in an electronic band. As a result, charge transport within these materials is covered by neither hopping nor band transport. This is a consequence of several microscopic interactions exhibiting characteristic energies that are of comparable magnitude. These interactions are the intermolecular electronic couplings t_{ab} (roughly 10 to 100 meV), the zero point energies of intramolecular (100 to 200 meV) and intermolecular vibrational modes (around 10 meV), and the polaron energy (50 to 200 meV).[23] The latter denotes the energy that is gained when the geometric structure of individual molecules is relaxed when these molecules accomodate charge. Additionally, at room temperature (300 K), also the thermal energy k_BT=25 meV has a comparable magnitude. This similarity of the energy scales of all these interactions comprises a major difficulty for the theoretical description of this intermediate regime. There is no clear starting point from where to apply perturbation theory. Therefore, an alternative approach is needed and has been developed over the last

years. In the following, we provide an overview of the basics of this so called transient localization theory based on Ref [23].

At the core of this approach is the observation that the intermolecular electronic couplings (later also referred to as transfer integrals) are strongly affected by temperature induced movements of the molecules. A reason for the emergence of these termal movements (fluctuations) are the relatively weak van der Waals interactions present in typical OSCs. Therefore, such movements at room temperature typically have amplitudes of around 0.1 Å.[38] It is well known that the intermolecular transfer integrals are sensitive to molecular displacements.[21,32–36] Especially important is that the amplitudes of temperature induced variations of the transfer integrals are comparable to the average value of the transfer integrals - see the example of temperature induced variations in rubrene[39] and see Ref [40] for data on additional high-mobility molecular semiconductors. A major consequence of this dynamic disorder is that the density of states (DOS) gets broadened and a localization of the instantaneous eigenstates is induced.[27] Importantly, this quantum mechanical effect is especially strong at the band edges which is insofar relevant as the free charge carriers typically reside there.[28] However, it has been described that as the localization fluctuates in time, localization in the traditional sense cannot be considered.[27] Rather, it has been proposed that dynamic disorder causes a transient localization over a length L_τ and for a certain fluctuation time τ.[23,41,42] The resulting expression for the charge carrier mobility, for such a situation becomes:[23,27]

$$\mu = \frac{e}{k_B T} \frac{L_\tau^2}{2\tau} \tag{1.13}$$

Here, τ is given by the inverse of the typical intermolecular oscillation frequency as $\tau \sim \omega_0^{-1}$. Inspecting equation 1.13 we find that this expression for the mobility shows no explicit dependence on the intermolecular transfer integrals. Any potential influence stemming from the magnitude of the transfer integrals can only enter via the transient localization lenght L_τ.

In a recent publication by Troisi and co-workers, Ref [27], it has been observed that this transient localization theory works very well for high-mobility organic semiconductors. The basis of the theoretical considerations in that research work is a two-dimensional tight-binding model. Here, the authors argue that for high-mobility organic semiconductors one can always identify a two-dimensional (high-mobility) plane within which charge transport is likely to occur. This plane is identified as the one parallel to the π-stacking interaction.
Based on this model, they suggest that the absolute value of the transfer integral has only

a minor influence on the charge carrier mobility. Importantly, they find that achieving situations where the transfer integrals between all neighboring molecules (sites) are of (almost) equal magnitude and where the product of these transfer integrals shows a positive sign maximize the transient localization length. Consequently also the charge carrier mobility is maximized for such situations. This finding is in sharp contrast to the findings for band transport ($\mu \propto t$) and hopping transport ($\mu \propto t^2$). There, the absolute value of the transfer integral directly influences the charge carrier mobility, i.e. a larger transfer integral leads to an increased mobility. What indeed has a significant influence on μ within transient localization theory is the ratio of the variations of the transfer integral and its absolute value $\Delta t/t$. The smaller this ratio the larger the charge carrier mobility (see Ref [27]).

In contrast, for a one-dimensional system it has been shown in Ref [23] that optimizing the absolute value of the transfer integral could lead to increased charge carrier mobilities. In the range of typical parameters for rubrene, the authors identified a power-law dependence of the transient localization length L_τ^2, on the transfer integral t. Consequently, also the charge carrier mobility μ shows the same dependence. An exhaustive discussion of how varying the intermolecular $\pi - \pi$ stacking distance, long axis shifts, reducing the coupling to intermolecular motions, and increasing the intermolecular influences the dependence of L_τ^2 on t can be found in the original work - Ref [23]. Here, we briefly summarize the major findings of these investigations. It has been observed that decreasing the $\pi - \pi$ stacking distance of neighboring molecules will actually result in a decrease of the mobility. Regarding shifts of neighboring molecules along their long molecular axis it was derived that increasing the transfer integral will increase the charge carrier mobility. These quite different dependencies are determined by system specific parameters and thus prevent the derivation of a general rule for how the charge carrier mobility depends on the transfer integral. As a result, for each system of interest which could be described by a one-dimensional system analogous to Ref [23] seperate calculations are needed.

Remarks on the Engineering of Charge Carrier Transport

For the two limiting regimes, hopping and band transport, it is known and has been demonstrated that the charge carrier mobility is proportional to the square of the transfer integral ($\mu \propto t$ for band transport and $\mu \propto t^2$ for hopping transport). This means that in cases where these transport models can be applied, increasing the value of the transfer integral comprises a viable strategy for improving transport properties. For intermediate cases, however, the absolute magnitude of the transfer integral alone might not be a sufficient tuning handle. Within systems falling into that category one should rather

consider achieving an isotropic situation, meaning that the transfer integrals to all nearest neighbors have similar magnitudes.[27] However, depending on the dimensionality of the transport mechanism as well as the structure of the considered system, a correlation between larger transfer integrals and enhanced charge carrier mobilities should still be likely. Therefore, we are going to base the following considerations regarding charge transport on the intermolecular transfer integrals within crystalline systems. In the spirit of transient localization theory also the anisotropy of the transfer integrals is studied in addition to the absolute values of these quantities. In ***Publication I*** several approaches for evaluating the intermolecular transfer integrals and their respective anisotropy in OSCs are tested. Further, in ***Publication II***, we employ the findings of ***Publication I*** and investigate whether intrinsic driving forces exist that push molecular arrangements towards situations with small intermolecular transfer integrals. All these investigations are done on an instructive test system, which we introduce in the following short subsection.

1.1.4. Quinacridone - An Instructive Model System

While reviewing the available approaches for describing charge transport in OSCs, in the previous section transfer integrals between neighboring molecules were identified as essential parameters. Improving the absolute value of these transfer integrals (for band and hopping transport mainly) as well as lowering their anisotropy have been identified as viable optimization strategies. Still, we need to find ways to determine these transfer integrals in a reliable manner based on the electronic structure of the crystalline systems. To address this issue we chose an instructive model system for organic semiconductor crstals. This model system comprises the 3 known polymorphs of quinacridone (α, β, and γ).[43] Quinacridone is a small H-bonded organic pigment which has already been succesfully used in organic field effect transistors.[20,44] This system was chosen as a test system for several reasons: (i) most typical interaction motifs for organic semiconductors (π-stacking, H-bonding, and van der Waals interactions) are present in this system, (ii) considering the three spatial directions, the dominant interaction along each of these directions is fundamentally different, (iii) α-quinacridone contains only 1 molecule per unit cell, which makes it quite easy to handle from a computational and methodological point of view (see Section 1.4.2), and (iv) the structure of α-quinacridone reveals various directions with similar intermolecular distances and arrangements, which is interesting with respect to anisotropy. As an example, the structure of the α-polymorph can be found in Figure 1.2.

Additional aspects rendering α-quinacridone a particularly relevant test system lie in its rather complex electronic band structure. Several effects cause this complexity of

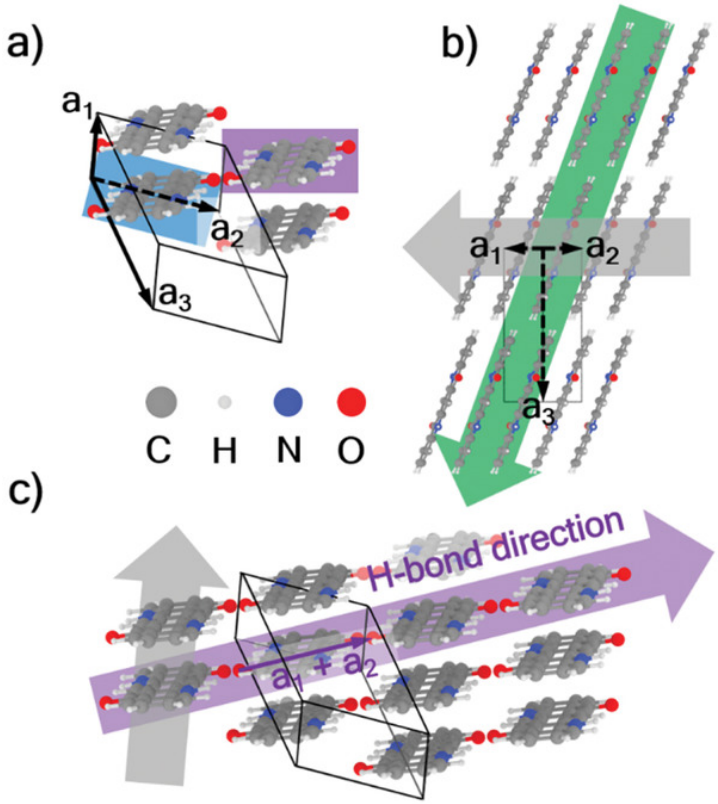

Figure 1.2.: Crystal structure of the α-polymorph of quinacridone. a) Shows the unit cell of the system with periodic replica of the original quinacrione molecule (blue rectangle) in directions $\boldsymbol{a}_1$, $\boldsymbol{a}_2$, and $\boldsymbol{a}_1 + \boldsymbol{a}_1$. b) Side view of the crystal structure where the π-stacking direction is marked with a grey arrow and the van der Waals stacking direction with a green arrow. c) Perspective view to indicate the π-stacking and H-bonding direction (purple arrow). Reprinted with permission from Ref [2].

the electronic bands. These are discussed in detail in ***Publication I*** (Section 2). At this point, we only mention one example: along certain directions we observe that the electronic bands comprise contributions from couplings between nearest as well as next-nearest neighbor molecules. Furthermore, based on α-quinacridone we constructed an orthorhombic model crystal, which was used in ***Publication II*** for investigating the interplay between the magnitude of the transfer integrals and the energetic stability of the corresponding molecular arrangements.

From the results presented in ***Publication II*** it will become apparent that driving forces exist, which stabilize molecular arrangements with low transfer integrals. As a consequence, in order to improve the charge transport properties of such systems one has to come up with strategies to enforce molecular arrangements with large transfer integrals. At this point metal-organic frameworks and covalent-organic frameworks become

interesting. These materials typically offer a level of control over the stacking arrangement that is hard to achieve in OSCs. Therefore, in the following sections we provide a short introduction into these two materials classes.

1.2. Metal-Organic Frameworks

Reticular chemistry focuses on linking discrete chemical entities by strong bonds in order to make extended, open framework structures like metal-organic frameworks (MOFs) and covalent organic frameworks (COFs).[45] As indicated in Figure 1.3 in the case of MOFs organic molecules (ligands) and polynuclear metal clusters (nodes or secondary building units) are linked together by coordination bonds to form porous frameworks with versatile structures.[45–52] The versatility of these structures emerges from the combination of the synthetic control available when making organic molecules and the large geometric and compositional variations achievable when designing the metal clusters. Importantly, the resulting structures can have quite different properties with respect to porosity, surface area, host-guest chemistry and their response to external stimuli (electric, magentic, mechanical, or thermal).[51] This, together with the good control over the achievable structures renders MOFs interesting for various applications and has triggered an ever growing interest in these materials. To give the reader a glimps on the different structures of MOFs, we provide the structures of MOF-5,[53] HKUST-1,[54] and MOF-74[55] as typical examples in Figure 1.4.

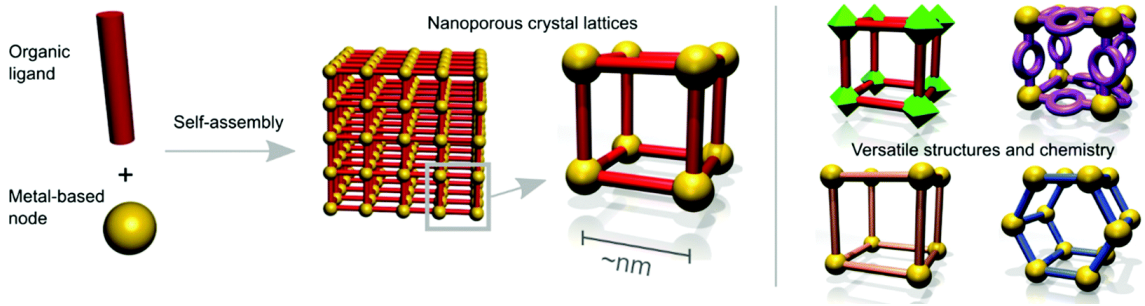

Figure 1.3.: Schematic representation of MOFs indicating the structural variability of these systems. The left panel shows how metal nodes and organic ligands are combined to form the (nano-) porous crystal lattice. The right panel schematically shows that a variety of structures can be achieved by combining different nodes and linkers. Adapted from Ref [51] with permission of the Royal Society of Chemistry.

Traditionally, mainly owing to their exceptionally high-surface areas, MOFs have been investigated for applications like gas storage,[56–58] catalysis,[59–61] and gas seperation.[62,63]

Only recently, MOFs which are electrically conductive started to gain considerable attention.[51,64–66] Such systems can open up an avenue towards additional applications like electrocatalysis,[67–71] chemiresistive sensing,[72–77] and energy storage.[78–80] Therefore, interest in designing electrically conductive MOFs as well as in understanding the underlying transport mechanisms has increased recently. In fact, several transport mechanisms that are active in MOFs have been identified.[51,64–66] Therefore, we briefly review these transport mechanisms with a focus on so-called *through-space* charge transport which is the mechanism relevant in ***Publication III***. Importantly, for this transport mechanism certain similarities to charge transport in OSCs can be identified, as will become apparent below and in ***Publication III***. Thus, inspired by these similarities, one aim of ***Publication III*** was to trigger the transfer of knowledge from the established and well advanced field of charge transport in OSCs to MOFs.

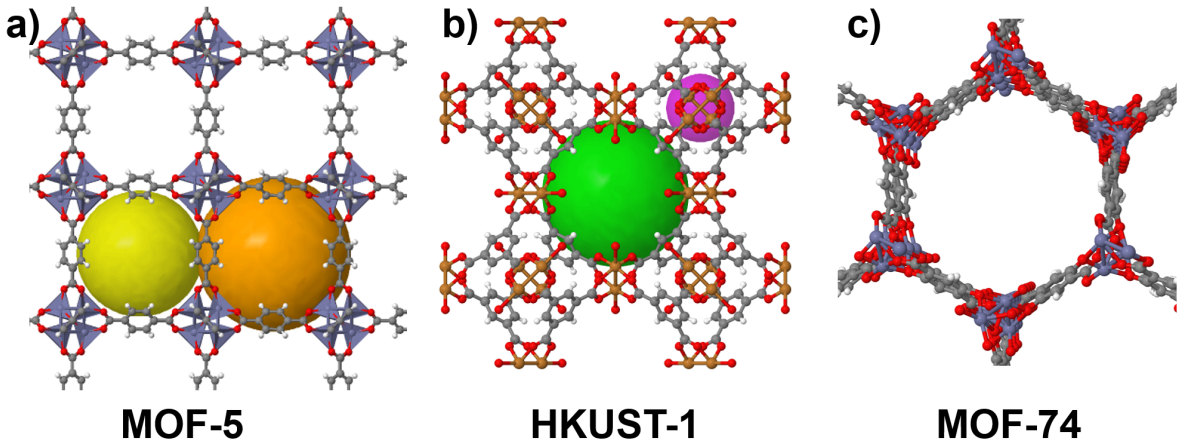

Figure 1.4.: Typical structures of MOFs with different topologies. Panel a) shows the structure of MOF-5, which is formed from Zn_4O nodes connected by 1,4-benzodicarboxylate linkers. Taken from `www.chemtube3d.com/mof-mof5/` b) HKUST-1, which is formed from copper nodes and 1,3,5-benzenetricarboxylic acid based linkers. Taken from `www.chemtube3d.com/mof-hkust-1-2/` c) MOF-74, formed from divalent cations Zn^{2+} and 2,5-dihydroxybenzenedicarboxylic acid based linkers. Structure taken from Ref [55] and rendered with Ovito.[81] The spheres in panels a) and b) denote the pore size for gas storage.

1.2.1. Charge Transport Mechanisms in Metal-Organic Frameworks

Before talking about charge transport in MOFs let us note that the electronic and optical properties of a solid are determined, in a first approximation, by its electronic band structure. Considering MOFs we find that these systems typically show rather flat bands.[51] This can be nailed down to the weak hybridization between states localized on the organic

linkers and states localized on the inorganic nodes.[64*] Furthermore, the π-systems of neighboring organic linkers show only little overlap due to the relatively large spatial seperation of the linkers. This property is common for many structural types of MOFs, as it is a consequence of the inherent porosity of these materials. Especially isotropic structures are affected by this large spatial seperation between linkers (see the example of MOF-5 in Figure 1.4). Still, due to the chemical and structural tunability of MOFs strategies and approaches for overcoming these limitations have been developed.[51,64–66] Versatile electrically conducting MOFs, exhibiting different transport mechanisms, have been synthesized and characterized.[64] Below we provide an overview of the transport mechanisms and current strategies that are put forward with the goal of achieving higher electrical conductivities in MOFs.

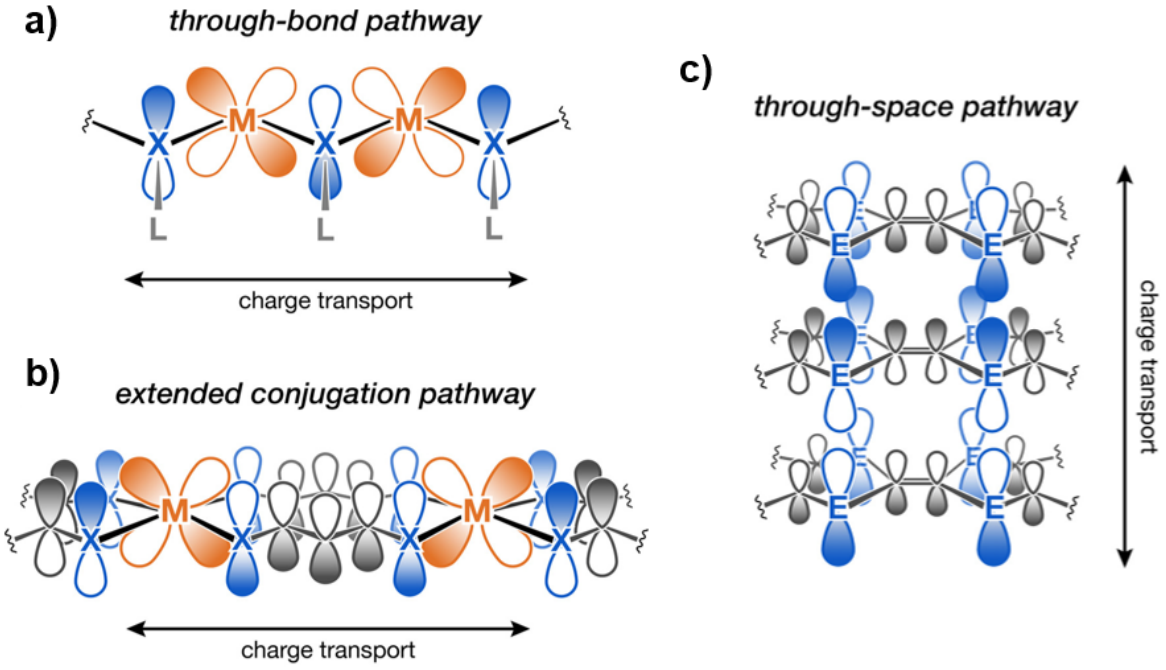

Figure 1.5.: Schematic of potential transport pathways in MOFs represented by the involved orbitals. a) Through-bond pathway where orbitals from the metal and the functional group of the ligand (L) are involved. b) Extended conjugation pathway, which also involves the ligand core. c) Through-space pathway, which involves π-stacking of organic moieties (E=S for tetrathiafulvalene a common component in MOFs with through-space pathways). In panels a) and b) M denotes a transition metal. Adapted with permission from Ref [64]. Copyright 2020 American Chemical Society

*As a large number of MOFs relies on carboxylate linkers, ionic bonds tend to be formed between these linkers and the metals. This leads to large energy gaps and confined electronic states.[64]

Through-Bond Pathways

Within the through-bond mechanism, charge transport is promoted by continous pathways created by coordination and covalent bonds between the metal nodes and the functional groups of the ligands (see Figure 1.5a). Such pathways emerge when the energy levels of the metal and the ligands are well matched and the orbital overlap of these entities is large.[64]

One difficulty when trying to achieve through bond pathways arises from the typically used carboxylate linkers. The largely ionic bond that is formed between the metal and the ligand comprises little orbital overlap. Consequently the resulting electronic bands are narrow.[64] This means that the states of the metal and the ligands are localized and, as a result, these systems exhibit poor conductivity. One successful strategy for improving the transport properties of such MOFs is to use ligands where the atoms forming the bond with the metals are either sulfur or nitrogen instead of oxygen. This approach has proven quite successful when applied to MOF-74 analogs.[64,82–84]

For the above described through-bond approach only the metal nodes and the functional group of the ligand constitute the charge carrier pathway. However, when considering ligands with functional groups that are conjugated with its organic core, one can construct frameworks exhibiting extended conjugation between the nodes and the ligands (Figure 1.5b). Also for this so-called *extended conjugation* approach a large orbital overlap between the functional groups and the metals is essential. Various two-dimensional, 2D, MOFs have been constructed relying on this principle.[64,65,73,85–90] For these systems conjugation within the plane is achieved via interactions of the ligands π-orbitals and the metal d-orbitals. This π-d conjugation results in the charge carriers being delocalized within the plane, ultimately leading to improved conductivities.[64] The individual layers of these 2D MOFs then stack on top of each other, forming the bulk structure of the material. As a result, the π-systems of consecutive layers overlap significantly and, thus, can create additional charge carrier pathways. This means that when talking about charge carrier transport in layered systems with extended π-systems through-space charge transport (see below) is important as well.

Guest-Promoted Transport

The inherent porosity of MOFs offers the possibility to occupy the pores with electroactive molecules, so-called guests. As a result, guest-guest or guest-host (framework) interactions can create charge transport pathways. Although this strategy might lead to increased

charge transport properties of the framework,[91,92] one has to keep in mind that occupying the pores with guest molecules leads to a lowering or even a loss of porosity. Thus, one of the key properties of these framework materials is removed, which prevents the use of this approach for applications that would rely on the porosity of MOFs.[51,64] Although this reduction of porosity upon introducing guest molecules to the framework is generally true, one can still obtain host-guest systems with large surface areas when choosing a framework with high porosity and different pore sizes.[92–96] Upon a clever design of such frameworks the probability of the guests occupying only pores of a certain size and shape can be increased. Thus, a certain surface area remains.

Through-Space Pathways

Considering organic semiconductors and the relevant charge transport mechanisms outlined in Section 1.1 it has been found that the intermolecular electronic coupling (or transfer integral) is an essential quantitiy determining the charge carrier mobility. This transfer integral depends strongly on the π-orbital overlap of the involved molecules. Within MOFs the involved molecules are the organic linkers, or, respectively, parts of these molecules. Like for OSCs improving the overlap of the π-systems of neighboring molecules should yield improved charge transport properties. Therefore, the so-called through-space approach focuses on intermolecular interactions, i.e improving the overlap of π-orbitals of neighboring linkers (see Figure 1.5c).

A key aspect of this through-space approach is to exploit the tendency of planar conjugated organic molecules to form structures that exhibit π-π-stacking.[64] As a result, the (frontier) orbitals of these molecules exhibit sizeable overlaps, which in turn leads to large band widths and transfer integrals. In the introductory part on OSCs (Section 1.1) we briefly discussed that these materials typically exhibit rather small charge carrier mobilities which are far from their inorganic counterparts[23,97] and also far from their own optimum. In ***Publication II*** this behavior is traced back to the Pauli exchange repulsion enforcing molecular arrangements with low intermolecular electronic couplings (transfer integrals). An interesting aspect of MOFs is that they offer a fine control over the stacking arrangement of the linkers which is difficult to achieve in OSCs. This higher level of control over the structure (stacking arrangement) can be traced to the inorganic nodes and the organic linkers within MOFs being linked via strong bonds.[45,50] Therefore, combining linkers and nodes with known geometry and coordination environments can be exploited as a strategy for designing MOFs with specific structures.[45,50,51] The better control over the stacking arrangement renders MOFs interesting for designing electrically conductive systems. Enforcing a certain arrangement of the organic linkers π-systems

can be used to engineer the charge transport properties of the MOF. It is still essential to understand how charge transport properties and structural arrangement play together. We can rephrase this issue into two questions: *How do the π-systems have to be arranged to yield favorable charge transport properties? Furthermore, how sensible are the charge transport properties to structural changes?* Below we elaborate a bit more in detail on these questions based on MOFs which have been shown to exhibit considerabe through-space charge transport. A detailed computational investigation addressing the questions raised above is presented in ***Publication III***.

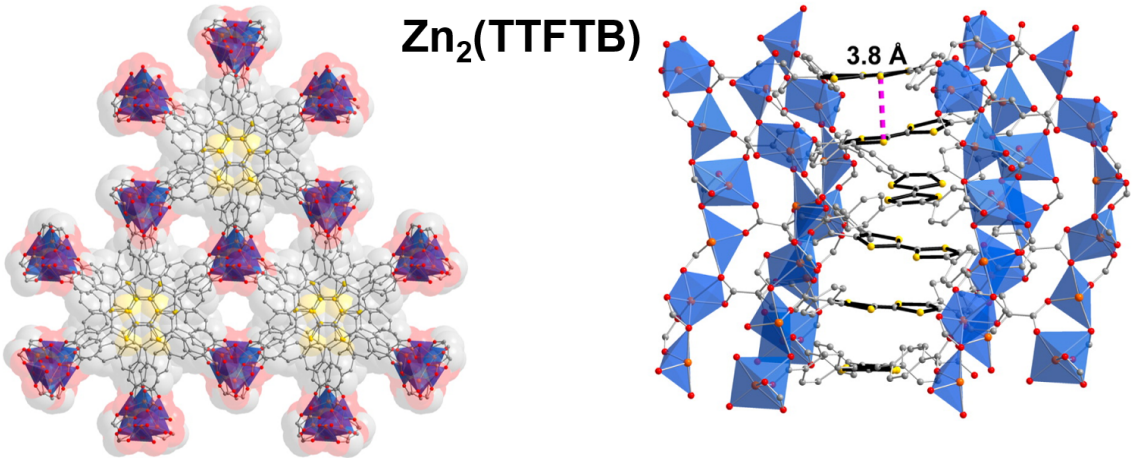

Figure 1.6.: Structure of the electrically conducting Zn_2(TTFTB) MOF. The left panel shows a view of the structure along the crystallographic c-axis. Pores and individual TTF stacks can be seen from this view. The right panel shows a side view of the helical TTF stack. Orange, yellow, red, and gray spheres represent Zn, S, O, and C atoms, respectively. H atoms and water molecules were omitted for clarity. Adapted with permission from Ref [98]. Copyright 2012 American Chemical Society

Quite a number of frameworks based on the organosulfur compound tetrathiafulvalene (TTF) have been realized bearing the through-space approach in mind.[98–102] Indeed, these systems were shown to exhibit π-stacking pathways together with sizeable electrical conductivities. Importantly, in most of these systems one-dimensional charge carrier transport pathways are formed. Actually, the presence of one-dimensional transport pathways is not so surprising when bearing standard topologies of MOFs in mind (see Figure 1.3). Typically, spatially well seperated stacks of organic linkers are found in these systems. Consequently, only linker molecules that are within the same stack can potentially exhibit significant π-orbital overlap, when the stacking distances are close enough. Distances of 4 Å or less are typically needed for molecules to exhibit such significant π-orbital overlap. When this condition is fulfilled, a one-dimensional charge transport pathway is obtained. In Figure 1.6 one can see Zn_2(TTFTB) as a typical

example for a TTF-based MOF exhibiting one-dimensional through-space transport pathways. In this system the stacking distance of consecutive linkers is around 3.5 Å. This system is at the core of ***Publication III***, where various structural changes are introduced and their influence on charge transport is investigated. Additional systems with one-dimensional stacks of π-conjugated molecules have been constructed based on MOF-74 and containing anthracene-based building blocks.[103] However, due to the large stacking distance of consecutive anthracene moieties (around 5.7 Å) transport will likely not occur through the π-stacking pathway created by these moieties but will rather occur through hopping between the metal-oxo chains between the nodes, as postulated in the original work.[103] That the stacking distance is of utter importance for charge transport is well known from OSCs and can be traced back to the exponential dependence of the orbital overlap on this distance. However, not only the stacking distance, but rather any changes in the molecular arrangement can have a significant impact on the electronic structure and, consequently, on the charge transport properties.

Essential for the actual charge transport properties within MOFs containing through-space pathways is how the transfer integral depends on the actual stacking arrangement of the linker molecules, especially their respective molecular orbitals. It is well known from OSCs that already small relative displacements or rotations of neighboring molecules can lead to significant changes of the respective transfer integrals.[32–35] In the context of layered MOFs it has also been predicted that the proximity of the layers[104] as well as their relative lateral arrangement[90,105,106] influences the electronic band structure. Consequently, also the transfer integrals are affected by such structural changes. Therefore, this interplay between structural arrangement and transfer integral is investigated in a systematic manner in ***Publication III*** (Chapter 4) for the example of Zn_2(TTFTB).

Remembering the extended conjugation approach we should note that 2D MOFs which exhibit an extended conjugation within the 2D plane are π-stacked to form the bulk. This means that for such systems in addition to charge transport in the plane also transport perpendicular to this plane might be of relevance. Therefore, it is of even greater importance to gain an in-depth understanding of through-space charge transport and its interplay with the MOF structure. Furthermore, talking about layered systems with extended π-systems covalent organic frameworks are quite similar to such 2D MOFs. Also for these systems the arrangement of consecutive layers is of great importance for the resulting properties. This will be outlined in the following Section on COFs (section 1.3).

A further aspect that I would like to bring up in the context of charge transport within MOFs is the role of defects. Several properties of MOFs have already been shown to

depend on defects, respectively the density of defects present in the material. These properties comprise the electronic structure (energy gaps), redox conductivity, and the (photo-)catalytic activity amongst others.[107–111] Charge transport, i.e. relevant quantities like transfer integrals, mobilities, and conductivities, however, have rarely been studied as a function of defect densities. Only for layered MOFs the influence of defects has been considered in a few computational studies.[90,105] The authors identified a drastic dependence of the electronic structure of the investigated systems on the presence of defects. Importantly, they found that the observation that a certain layered MOF was predicted to be metallic and observed to be semiconducting might lie in the presence of defects in the real system.[105] Apart from these studies we are not aware of detailed and systematic investigations of the interplay between defects/defect density and (through-space) charge transport within MOFs. Therefore, in ***Publication III*** we also study the role of defects (missing linkers, offset molecules, and other structural distortions) for the electronic band structure, transfer integrals, and effective masses. This contribution is meant to highlight the importance of defects for charge transport in MOFs and is expected to trigger further investigations.

1.3. Covalent Organic Frameworks

Covalent Organic Frameworks (COFs) are materials that consist of organic building blocks which are linked by covalent bonds.[112–119] Similar to MOFs, also COFs form highly crystalline porous framework structures. The resulting structures can be categorized into 2D and 3D COFs. In 2D COFs the organic building blocks are linked by covalent bonds within a plane, forming highly regular 2D layers and these layers then stack along the direction perpendicular to the plane, forming the bulk. These stacks are held together mostly by van der Waals interactions and the π-systems of consecutive COF layers show significant orbital overlap.

COFs, and especially 2D COFs, have been succesfully used for a variety of applications including gas storage,[119–121] gas seperation,[122–125] catalysis,[126–128] energy storage[129–131] and optoelectronics.[132–138] Essential for, in principle, all of these applications are the electronic structure and the pore shape of these systems. Both are determined by the topology together with the exact packing motif of the individual COF layers.[139] Common topologies together with the actual structures of two exemplary COFs are shown in Figure 1.7. Importantly, the electronic structure of 2D COFs can be significantly altered by only small displacements between consecutive layers. As mentioned already several times, this can be rationalized by studies performed on OSCs, where the electronic

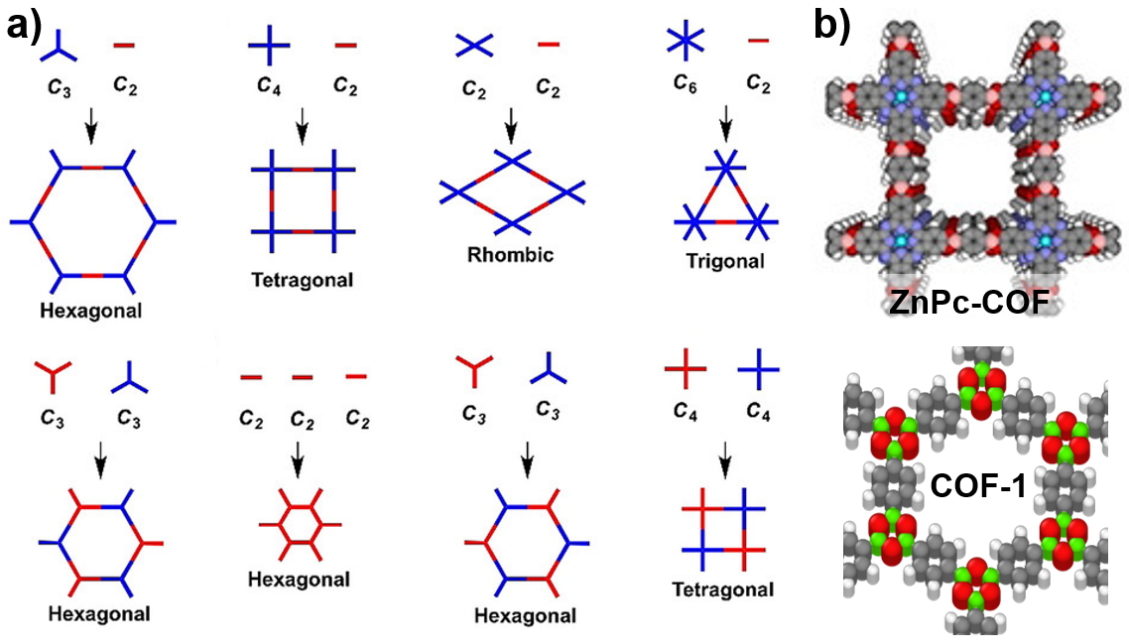

Figure 1.7.: Topologies and typical structures of COFs. a) Topologies depending on the symmetries of the organic building blocks. b) Schematic representation of the structure of typical π-stacked COFs. The examples shown here are ZnPc-COF and COF-1. Panel a) and ZnPc-COF in panel b) are adapted with permission from Ref [117]. Copyright 2019 Wiley-VCH Verlag GmbH & Co. KGaA, Weinheim

structure of molecular dimers, cluster, and solids has been investigated as a function of relative intermolecular displacements.[21,32–36] Please note that regarding this interplay of the electronic structure and relative displacements of consecutive moieties (molecules in OSCs, organic linkers in MOFs, and layers of 2D COFs) there is no fundamental difference between the systems considered in this thesis which belong exactly to these classes of materials. What is different though is the control over the stacking arrangement, which can be achieved and the number of degrees of freedom which are accesible to the indivudal moieties. In MOFs as well as in COFs some of these degrees of freedom are blocked or at least hindered by the framework structure. For 2D COFs and MOFs the intralayer arrangement is determined by the covalent bonds that are formed within the individual layers. Concerning the interlayer arrangement, however, several interactions of comparable strength are important. Therefore, it is essential to understand how these interactions relate to the interlayer arrangement and potentially even enforce a certain arrangement. As varying layer arrangements directly influence the electronic structure of COFs[104] a detailed understanding of the interplay between interlayer interactions and arrangements is highly important.

Knowing how the interlayer arrangement influences the electronic structure and how the individual interlayer interactions determine this layer arrangement, one can start to think about ways to tune these interactions and enforce certain layer arrangements, i.e. create COF structures with improved/desired properties. Nevertheless, the starting point is to actually gather that understanding of the individual interactions (van der Waals, electrostatic, exchange repulsion) as a function of the layer arrangement. In ***Publication IV*** we aim at gaining this understanding based on exemplary test systems, namely COF-1 and COF-5. The interaction energy between consecutive layers together with the vdW, electrostatic and repulsion interactions are studied as a function of interlayer displacements parallel to the plane of the layers and perpendicular to it. In order to get the individual contributions to the interaction energy acting between the layers we had to decompose this interaction energy into physically relevant terms. Thus, in Section 1.4.3 we introduce an energy decomposition scheme for periodic systems. To date such decomposition schemes are common for clusters but are rarely available for periodic systems. Therefore, inspired by the decomposition scheme from Ref [140] already employed in ***Publication II***, a similar method has been implemented to work with FHI-aims.[141] Details on this scheme and the actual implementation and validation data can be found in Section 1.4.3 and in the Appendix.[†]

1.4. Methodological Considerations

Understanding the electronic structure of a material can be considered as an essential foundation for understanding the material itself and occuring phenomena. As a consequence, for realistic systems one has to deal with a the many-electron problem. One very succesful and widely used method for describing the electronic structure of materials is density functional theory, DFT. Therefore, in the present section, we will to introduce the fundamental aspects of DFT (Section 1.4.1). The bulk of the following considerations are based on an excellent book by Richard M. Martin.[142] Building upon the results from DFT we introduce methods to derive quantities like transfer integrals (Section 1.4.2) and individual contributions to interaction energies (Section 1.4.3).

[†]Several reasons lead to the idea of implementing our "own" energy decomposition scheme: (i) having access to the very details of the scheme; (ii) making an energy decomposition scheme for periodic systems available in one of our standard simulation codes.

1.4.1. Density Functional Theory

The starting point for the determination of the electronic structure of a material is the time-independent Schrödinger equation.

$$\hat{H}\Psi(\boldsymbol{r}_i, \boldsymbol{R}_I) = E\Psi(\boldsymbol{r}_i, \boldsymbol{R}_I) \tag{1.14}$$

Here $\Psi(\boldsymbol{r}_i, \boldsymbol{R}_I)$ is the many-electron wavefunction depending on the spatial coordinates of the electrons $\boldsymbol{r}_i$ and the nuclei $\boldsymbol{R}_I$. Lowercase subscripts denote the indizes of the electrons while uppercase subscripts denote those of the nuclei. The Hamiltonian $\hat{H}$ for such a system of electrons and nuclei with charge Z_I and mass M_I reads as follows.

$$\begin{aligned}\hat{H} = \frac{\hbar^2}{2m_e}\sum_i \nabla_i^2 - \sum_i\sum_I \frac{Z_I e^2}{|\boldsymbol{r}_i - \boldsymbol{R}_I|} + \frac{1}{2}\sum_i\sum_{j\neq i}\frac{e^2}{|\boldsymbol{r}_i - \boldsymbol{r}_j|} \\ - \sum_I \frac{\hbar^2}{2M_I}\nabla_I^2 + \frac{1}{2}\sum_I\sum_{J\neq I}\frac{Z_I Z_J e^2}{|\boldsymbol{R}_I - \boldsymbol{R}_J|}\end{aligned} \tag{1.15}$$

The first three terms denote the kinetic energy of the electrons, the attractive electron-nuclei interactions, and the repulsive electron-electron interactions. The last two terms deal with the nuclei and denote the kinetic energy of the nuclei and the repulsive nuclei-nuclei interactions. Considering that the nuclei are much heavier than the electrons one can employ the Born-Oppenheimer approximation.[143] This means that the electrons are considered in a field generated by the nuclei, which are assumed as being fixed in space. As a result, the kinetic energy of the nuclei is not contained in the electronic Schrödinger equation and the interaction between the nuclei becomes a constant E_{II}. The resulting electronic Hamiltonian can then be written as

$$\hat{H} = \hat{T} + \hat{V}_{ext} + \hat{V}_{int} + E_{II}. \tag{1.16}$$

Here, the following operators are included: $\hat{T}$ denotes the kinetic energy of the electrons, $\hat{V}_{ext}$ denotes the potential created by the nuclei, and $\hat{V}_{int}$ denotes the electron-electron interaction.

Despite this simplification of the problem, we are still left with an expression that depends on the coordinates of all electrons present in the system. This is the point where the theorems of Hohenberg and Kohn become essential,[144] as they significantly reduce the complexity of the problem. The basic statement of these theorems is that any property of

a system of many interacting particles is determined by the ground state electron density $n_0(\boldsymbol{r})$ of that system. This ground state electron density is a scalar function of position, i.e. it only depends on position $\boldsymbol{r}$. Furthermore, a functional $E_{HK}[n]$ for the energy in terms of the density $n(\boldsymbol{r})$ can be defined, see equation 1.17.

$$E_{HK}[n] = T[n] + E_{int}[n] + \int d^3r \; V_{ext}(\boldsymbol{r})n(\boldsymbol{r}) + E_{II} \tag{1.17}$$

The first two terms of this expression for the interacting electron system are summarized in the Hohenberg-Kohn functional $F_{HK}[n]$ as:[142]

$$F_{HK}[n] = T[n] + E_{int}[n]. \tag{1.18}$$

For any external potential $V_{ext}(\boldsymbol{r})$ the exact ground-state energy of the system is the global minimum of the universal functional $E_{HK}[n]$. Further, the density $n(\boldsymbol{r})$ which minimizes the functional is the exact ground state density $n_0(\boldsymbol{r})$. Importantly, this functional $E_{HK}[n]$ alone is sufficient for determining the exact ground state density and energy. What remains unknown, however, is the form of the exact energy functional. The main difficulty is the description of the kinetic energy as a function of the electron density. This problem was addressed by Kohn and Sham (KS).[145] They suggested to replace the original many-body (many-electron) problem of interacting particles by an auxiliary problem of independent non-interacting particles, where the ground state densities of these two systems are identical. Now, the problem is treated by N (with N being the number of electrons in the system) independent-particle equations and all difficulties associated with the problem of interacting, correlated electrons are incorporated into the so-called exchange-correlation functional $E_{xc}[n]$.

In the following we introduce such an auxiliary system through single electron KS-orbitals ϕ_i. The density of this system can then be obtained as

$$n(\boldsymbol{r}) = \sum_i \left|\phi_i(\boldsymbol{r})\right|^2 . \tag{1.19}$$

Within the Kohn-Sham approach the energy functional (equation 1.17) is then rewritten as

$$E_{KS}[n] = T_S[n] + \int d\boldsymbol{r} V_{ext}(\boldsymbol{r})n(\boldsymbol{r}) + E_{Hartree}[n] + E_{II} + E_{xc}[n]. \tag{1.20}$$

The kinetic energy T_S of the independent particle system can be expressed as

$$T_S = \frac{1}{2}\sum_i \left\langle \phi_i \left| \bigtriangledown^2 \right| \phi_i \right\rangle = \frac{1}{2}\sum_i \int d\boldsymbol{r} \left| \bigtriangledown \phi_i(\boldsymbol{r}) \right|^2, \tag{1.21}$$

and the classical Coulomb interaction energy of the electron density with itself can be expressed as

$$E_{Hartree}[n] = \frac{1}{2}\int\int d\boldsymbol{r} d\boldsymbol{r}' \frac{n(\boldsymbol{r})n(\boldsymbol{r}')}{|\boldsymbol{r}-\boldsymbol{r}'|} \tag{1.22}$$

Here atomic units ($\hbar = m_e = e = 4\pi/\epsilon_0 = 1$) have been employed. The exchange-correlation energy $E_{xc}[n]$ is then defined by the equality of $E_{HK}[n]$ and $E_{KS}[n]$ as:

$$E_{xc}[n] = F_{HK}[n] - (T_S[n] + E_{Hartree}[n]) = T[n] - T_S[n] + E_{int}[n] - E_{Hartree}[n]. \tag{1.23}$$

As a next step, the Kohn-Sham auxiliary system is solved for the ground state. This is achieved by minimizing the energy functional of equation 1.20 with respect to the density. This procedure finally yields the Kohn-Sham (KS) equations:

$$(-\frac{1}{2}\bigtriangledown^2 + V_{KS}(\boldsymbol{r}))\phi_i(\boldsymbol{r}) = \epsilon_i \phi_i(\boldsymbol{r}) \tag{1.24}$$

with the Kohn-Sham potential $V_{KS}(\boldsymbol{r})$ as

$$V_{KS}(\boldsymbol{r}) = V_{ext}(\boldsymbol{r}) + V_{Hartree}(\boldsymbol{r}) + V_{xc}(\boldsymbol{r}). \tag{1.25}$$

These Kohn-Sham equations 1.24 are Schrödinger like independent particle equations with solutions represented by Kohn-Sham orbitals ϕ_i with energies ϵ_i. These equations must be solved under the condition that the potential and the density are consistent. In practice, one starts with an initial guess for the density and the corresponding potential is determined following equation 1.25.[‡] Then, as a first step of an iterative process, the KS-equations (1.24) are solved for the initial potential. Based on this solution, the KS-orbitals in particular, a new density is evaluated according to equation 1.19. The obtained

[‡]The Hartree potential $V_{Hartree}$ and the exchange correlation potential V_{xc} denote the partial derivative of the respective energies with respect to the density $n(\boldsymbol{r})$

new (updated) density then again enters in the first step of the iterative process, i.e. the calculation of the KS-potential following equation 1.25. Again, solving the KS-equations and evaluating the corresponding density are the subsequent steps. This procedure is repeated (iterated) until a certain convergence criterion or a set of convergence criteria is met. Thus, the KS-equations are solved in a self-consistent manner, where the iterative procedure is referred to as the self-consistency cycle.

Functionals for Exchange and Correlation

One part of the KS-equations is still unknown at this point, namely the exchange and correlation functional $E_{xc}[n]$. So far, no approximations have been applied (apart from Born-Oppenheimer) and knowing the correct exchange-correlation functional would result in the exact solution of the problem. However, to date, the exact form of this functional remains unknown and approximations have to be made in order to find solutions to the KS-equations. Nevertheless, many approximations proved quite succesful, resulting in DFT being the most widely used method for electronic structure calculations. In the following we introduce the basic approximations that can be made to the exchange correlation functional.

The simplest approximation is the Local-Density-Approximation (LDA), which is based on the assumption that several solids, metals in particular, are close to the limit of the homogeneous electron gas. The corresponding expression for the energy functional reads as

$$E_{xc}[n] = \int d\boldsymbol{r} \epsilon_{xc}^{hom}(n(\boldsymbol{r}))n(\boldsymbol{r}). \tag{1.26}$$

Here ϵ_{xc}^{hom} is the exchange-correlation energy density equivalent to the one in a homogeneous electron gas. This functional only depends on the electron density and yields the correct solution for a uniform (homogeneous) electron gas. However, numerous materials differ quite a bit from the homogeneous electron gas. Especially the materials considered in this work, OSCs, MOFs, and COFs cannot be modelled well by the simple LDA approach. A more accurate approximation can be achieved by including a generalized gradient of the electron density into the considerations. This results in the so called Generalized-Gradient-Approximation (GGA).[146] The energy functional now takes the following form

$$E_{xc}[n] = \int d\boldsymbol{r} \epsilon_{xc}(n(\boldsymbol{r}), |\bigtriangledown n(\boldsymbol{r})|) n(\boldsymbol{r}). \tag{1.27}$$

The most widely used form of these GGA functionals is the famous Perdew-Burke-Ernzerhof (PBE) functional.[146] This functional is used in this thesis, unless otherwise stated. Although this PBE functional is known to achieve quite accurate results for various physical observables, it also has well-known deficiencies.[147] An example is the self-interaction error, which denotes a spurious interaction of an electron with itself.[147,148] This self-interaction error raises the energy of localized states, and favors delocalization.[147,149–152] Hybrid approaches, which incorporate a fraction α of exact Hartree-Fock (HF) exchange, and a fraction $1 - \alpha$ of the GGA exchange partially correct for the self-interaction error.[147,153] A widely used functional following these considerations is the hybrid functional PBE0.[154] There, 25% of exact Hartree-Fock exchange is mixed to PBE:

$$E_{xc}^{PBE0} = 0.25\ E_x^{HF} + 0.75\ E_x^{PBE} + E_c^{PBE}. \tag{1.28}$$

A different family of hybrid functionals are the so-called range-seperated hybrid functionals. These functionals are based on the idea that screening depends on the distance. This means that the functional is divided into short-range (little screening) and long-range (larger screening) parts by introducing a certain seperation length η. The HSE functional[155] is a member of this family of range-seperated hybrid functionals and is a widely used choice for solids. For this functional the long-range HF part is ignored and only short range HF is included, as shown in equation 1.29.[142]

$$E_{xc} = E_{xc}^{PBE} + 0.25(E_x^{HF,SR}(\eta) - E_x^{PBE,SR}(\eta)). \tag{1.29}$$

This expression reduces to the standard PBE expression when $\eta \to \infty$ or to the PBE0 hybrid when $\eta \to 0$. In this Thesis HSE06[155,156] has been used, where the range-separation length η is chosen as $0.11/a_0$, here a_0 denotes the Bohr radius. We mostly employed this functional to check whether the inclusion of HF-exchange changes the dispersion of the electronic bands, which are quantities at the core of ***Publications I*** ,***II***, and ***III***. In the Supporing Information of these works one can find that the band gap shows the expected change when comparing semi-local PBE to HSE06. However, the dispersion of the electronic bands only shows minor changes in all instances.

van der Waals Forces

One aspect that cannot be described by standard functionals are long range van der Waals interactions. These interactions are, however, essential in weakly bonded materials. They arise from fluctuations of the multipoles of an entitiy (atom or molecule) that induce multipoles on one another. These interactions are of non-local and attractive nature. For large distances R between entities, vdW interactions are typically determined by a $1/R^6$ term. These long-range interactions are essential for understanding systems like OSCs, COFs, and MOFs correctly. Various ways how to incorporate vdW interactions exist, while most implementations rely on treating vdW interactions outside the self-consistency cycle. In the following, we will briefly discuss an approach introduced by Tkatchenko and Scheffler, vdW^{TS}.[157] While solely this correction scheme is discussed below, several reviews shall be referenced that thoroughly discuss vdW interactions within DFT.[158–162]

vdW^{TS} is a pairwise additive correction to the energy. Within this correction scheme, the vdW interaction energy of two entities A and B is considered seperately from the rest of the system. Many body effects are ignored by this scheme. The corresponding vdW energy E_{vdW} is calculated by the following expression:

$$E_{vdW} = -\frac{1}{2}\sum_{AB}\frac{C_{6AB}}{R_{AB}^6} f(R_{AB}). \tag{1.30}$$

Here R_{AB} is the interatomic distance, C_{6AB} are the so-called van der Waals coefficients and $f(R_{AB})$ is a damping function, which is designed to avoid singularities of the energy at short distances. R_{AB} and C_{6AB} are obtained from the ground state electron density via Hirshfeld partitioning. The vdW^{TS} approach has been applied in all Publications presented in this thesis.

DFT in Practice

There are certain parameters which have to be specified prior to any DFT calculation. Essential parameters comprise a first guess of the atomic coordinates and the lattice vectors (for periodic systems). Furthermore, the functional, the basis set as well as the vdW correction scheme ought to be initialized.

For the DFT calculations included in this Thesis mainly two different programs have been used: the Vienna Ab Initio Simulation Package, VASP,[163] and the Fritz-Haber Institute ab-initio molecular simulation package, FHI-Aims.[141] The main differences

between these codes are the representation of the basis and the treatment of core and valence electrons. In VASP, the basis functions are plane waves and the interactions between valence electrons and core is described by the projected-augemented plane wave method (PAW). In FHI-Aims the basis consists of numerical atom-centered orbitals and a full-potential ansatz is applied. The localized nature of the FHI-Aims basis functions will become important for the energy decomposition scheme, see Section 1.4.3. In principle, these codes give equal results, provided that convergence settings are chosen tight enough. This has been demonstrated in a recent publication.[164] The specific settings employed in our work can be found in the Methods Section of the respective Publication and in the corresponding Supporting Information.

1.4.2. Tight-Binding Models

No matter which of the charge transport models described in Section 1.1 is considered, the transfer integral is an essential parameter. One approach for obtaining transfer integrals for periodic systems is to fit elaborate tight-binding (TB) model functions to an electronic band structure, which has been calculated with DFT. Therefore, the present section introduces the tight-binding approach and highlights certain aspects that ought to be considered when setting up model functions and fitting them to the DFT data. Of course, one could also employ an inverted approach and calculate transfer integrals using one of the numerous cluster-based approaches and then enter these transfer integrals into a suitable tight-binding model for getting the electronic band structure. In most instances such an approach might be a viable method, while it fails for systems where, for example, superexchange like effects are important (***Publication I***). In our works, tight binding models have been fitted to electronic band structures obtained by DFT in ***Publications I*** and ***II***, while in ***Publication III*** simple TB models used for rationalizing the results.

General Introduction

This section supplements and extends the theory discussed briefly in Ref [165] for the initial development and implementation of the TB-models. The tight-binding model is an approach to describe/calculate the electronic band structure of a solid by a linear combination of wave functions that are localized at individual lattice sites (atoms or molecules). This approach is well suited for systems where neighboring entities are electronically only weakly coupled, which is the case for all systems considered here. The following considerations focus on the description of the electronic bands by considering

the frontier orbitals of the molecular entities at the individual lattice sites. In principle, the number of orbitals that are considered for each lattice site is not limited.

The starting point for the considerations in this chapter is the time-independent Schrödinger equation:

$$\hat{H}\Psi_{n,\boldsymbol{k}}(\boldsymbol{r}) = \epsilon_n(\boldsymbol{k})\Psi_{n,\boldsymbol{k}}(\boldsymbol{r}) \tag{1.31}$$

Here $\Psi_{n,\boldsymbol{k}}(\boldsymbol{r})$ denote the single particle states in the crystal, n labels the band index and $\boldsymbol{k}$ denotes the wavevector. A viable ansatz for $\Psi_{n,\boldsymbol{k}}(\boldsymbol{r})$, which are eigenfunctions of the crystal Hamiltonian, is a linear superposition of wavefunctions $\psi_{cell,n}(\boldsymbol{r})$ centered at each unit cell:

$$\Psi_{n,\boldsymbol{k}}(\boldsymbol{r}) = \frac{1}{\sqrt{N}} \sum_m e^{i\boldsymbol{k}\boldsymbol{T}_m} \psi_{cell,n}(\boldsymbol{r} - \boldsymbol{T}_m). \tag{1.32}$$

Here $\boldsymbol{T}_m$ denotes a translation vector which is given by a linear combination of the real space lattice vectors $\boldsymbol{a}_i$ with integer values h, k, l as: $\boldsymbol{T}_m = h\boldsymbol{a}_1 + k\boldsymbol{a}_2 + l\boldsymbol{a}_3$. Furthermore, N denotes the number of states in the crystal.

The wavefunctions $\psi_{cell,n}(\boldsymbol{r})$ themselves can then be expressed as a linear superposition of basis functions (molecular orbitals) $\phi^{MO}_{\alpha,I}$ corresponding to state n and centered at the individual sites (molecules) $\boldsymbol{r}_I$ in the primitive unit cell. Here the index α denotes the molecular orbital and index I denotes the molecule in the primitive unit cell. In this thesis we focus on systems with only one molecular orbital per site, represented by a single wavefunction. So, for the valence band it is assumed that only the highest occupied state at each site is relevant, while for the conduction band the lowest unoccupied state at each site is the relevant one. Note that also for situations with more orbitals per site one could derive tight-binding expressions. Furthermore, it is assumed that all molecular orbitals are of the same type, as a consequence one can index the molecular orbital of site A with a single index as $\phi_{\alpha,A}(\boldsymbol{r} - \boldsymbol{r}_A) \equiv \phi^{MO}_A(\boldsymbol{r} - \boldsymbol{r}_A)$. Based on these orbitals and using a linar ansatz one obtains the wavefunction $\psi_{cell,n}$ describing the primitive unit cell of a crystal as

$$\psi_{cell,n}(\boldsymbol{r}) = \sum_I c^n_I \ \phi^{MO}_I(\boldsymbol{r} - \boldsymbol{r}_I). \tag{1.33}$$

Here I sums over the molecules in the basis, where $\boldsymbol{r}_I$ is the position of the molecule in the primitive unit cell. Entering the wavefunction for the primitive unit cell to equation 1.32 we end up with an expression that obeys Bloch's theorem and comprises an eigenfunction $\Psi_{n,\boldsymbol{k}}(\boldsymbol{r})$ of the Hamiltionian:

$$\begin{aligned}\Psi_{n,\boldsymbol{k}}(\boldsymbol{r}) &= \frac{1}{\sqrt{N}} \sum_m e^{i\boldsymbol{k}\boldsymbol{T}_m}\ \psi_{cell,n}(\boldsymbol{r}-\boldsymbol{T}_m) \\ &= \frac{1}{\sqrt{N}} \sum_m e^{i\boldsymbol{k}\boldsymbol{T}_m} \left(\sum_I c_I^n\ \phi_I^{MO}(\boldsymbol{r}-\boldsymbol{r}_I-\boldsymbol{T}_m) \right).\end{aligned} \tag{1.34}$$

Now we use the wavefunction $\Psi_{n,\boldsymbol{k}}(\boldsymbol{r})$ to evaluate the Schrödinger equation. In order to solve the Schrödinger equation one has to obtain the coefficients c_I^n defining the linear combination of the basis functions ϕ_I^{MO}. In order to obtain these coefficients we multiply the Schrödinger equation 1.31 with a certain molecular orbital which is localized at site A, $\phi_A^{MO}(\boldsymbol{r}-\boldsymbol{r}_A)$, from the left. Evaluating the resulting expression under the assumption that only nearest-neighbors have non-negligible contributions, i.e. summation indizes m and I only include nearest neighbors, and that neighboring orbitals show zero overlap we end up with the expression shown in equation 1.36. We add a small value δ to the expression which shall indicate and account for deviations from the above mentioned assumptions. In the following, this δ is assumed to be 0, i.e. the assumptions are well satisfied by the considered systems.

$$\left\langle \phi_A^{MO} \right| \hat{H} \left| \Psi_{n,\boldsymbol{k}} \right\rangle = \epsilon_n(\boldsymbol{k}) \left\langle \phi_A^{MO} | \Psi_{n,\boldsymbol{k}} \right\rangle \tag{1.35}$$

$$c_A^n \left\langle \phi_A^{MO} \right| \hat{H} \left| \phi_A^{MO} \right\rangle + \sum_{m\ \epsilon\ n.n.} \sum_I c_I^n \left\langle \phi_A^{MO} \right| \hat{H} \left| \phi_I^{MO} \right\rangle e^{i\boldsymbol{k}\boldsymbol{T}_m} = \epsilon_n(\boldsymbol{k}) c_A^n \left\langle \phi_A^{MO} | \phi_A^{MO} \right\rangle + \delta \tag{1.36}$$

In order to be able to determine all coefficients, each orbital $\phi_I^{MO}(\boldsymbol{r}-\boldsymbol{r}_I)$ has to be considered. Meaning that this orbital has to be multiplied from the left to the Schrödinger equation 1.31, which yields expressions analogous to equation 1.36. The resulting set of equations then has to be solved in order to obtain the energy dispersion relation $\epsilon_n(\boldsymbol{k})$. Now, in the employed fitting approach the on-site terms $\left\langle \phi_A^{MO} \right| \hat{H} \left| \phi_A^{MO} \right\rangle$ and the transfer integrals $\left\langle \phi_A^{MO} \right| \hat{H} \left| \phi_I^{MO} \right\rangle$ are not evaluated explicitly, but rather are fitted to reproduce the electronic band calculated with dispersion corrected density functional theory.

In the next part, we evaluate expressions for situations with one or two inequivalent sites (molecules) per unit cell. For each wavefunction included in our ansatz we obtain an expression analagous to equation 1.36 with a specific coefficient c_A^n.

One Site per Unit Cell

Starting from expression 1.36 we ignore the small deviations denoted as δ and assume that wavefunctions located in different unit cells have vanishing overlap. Additionally, we include the onsite term $\left\langle \phi_n^{MO} \right| \hat{H} \left| \phi_n^{MO} \right\rangle$ in the sum over the nearest neighbors. This means that the term with $\boldsymbol{T}_m = 0$ is included in the range of index m for $m = 0$. As we have only one site at position $\boldsymbol{r}_A$ within the unit cell and we only consider a single molecular orbital $\phi_A^{MO}(\boldsymbol{r} - \boldsymbol{r}_A)$ for each site we end up with an expression, that reads as

$$\sum_m \left\langle \phi_A^{MO}(\boldsymbol{r} - \boldsymbol{r}_A) \right| \hat{H} \left| \phi_A^{MO}(\boldsymbol{r} - \boldsymbol{r}_A - \boldsymbol{T}_m) \right\rangle e^{i\boldsymbol{k}\boldsymbol{T}_m} = \epsilon_n(\boldsymbol{k}). \tag{1.37}$$

The transfer integral can now be written as

$$t_m = \left\langle \phi_A^{MO}(\boldsymbol{r} - \boldsymbol{r}_A) \right| \hat{H} \left| \phi_A^{MO}(\boldsymbol{r} - \boldsymbol{r}_A - \boldsymbol{T}_m) \right\rangle \tag{1.38}$$

Using the above expression one can simplify equation 1.37 to the following form:

$$\epsilon_n(\boldsymbol{k}) = \sum_m t_m e^{i\boldsymbol{k}\boldsymbol{T}_m} \tag{1.39}$$

This model for the energy dispersion relation $\epsilon_n(\boldsymbol{k})$ is then fitted to the electronic band structure. Important to note is that for one site per unit cell and one orbital per site, the transfer integrals are uniquely determined. This is a consequence of the model function representing a Fourier series of the energy dispersion relation where the transfer integrals are the Fourier coefficients.[2]

Two Sites per Unit Cell

The second case that is included in the present considerations is a system of two inequivalent sites A and B per unit cell with one molecular orbital $\phi_N^{MO}(\boldsymbol{r}-\boldsymbol{r}_N),\ N\epsilon\{A,B\}$ per site. Similar to the previous case and as outlined in the general introduction on tight-binding, one has to multiply the Schrödinger equation with orbitals $\phi_A^{MO}(\boldsymbol{r}-\boldsymbol{r}_A)$ and $\phi_B^{MO}(\boldsymbol{r}-\boldsymbol{r}_B)$ from the left, to obtain the system of equations which determines the coefficients of the linear combination of the basis functions. This set of two equations reads in matrix notation as follows

$$\begin{pmatrix} \sum_m t_m^{AA} e^{i\boldsymbol{k}\boldsymbol{T}_m} & \sum_m t_m^{AB} e^{i\boldsymbol{k}\boldsymbol{T}_m} \\ \sum_m t_m^{BA} e^{i\boldsymbol{k}\boldsymbol{T}_m} & \sum_m t_m^{BB} e^{i\boldsymbol{k}\boldsymbol{T}_m} \end{pmatrix} \begin{pmatrix} c_A \\ c_B \end{pmatrix} = \epsilon(\boldsymbol{k}) \begin{pmatrix} c_A \\ c_B \end{pmatrix}, \tag{1.40}$$

or in a simplified notation as

$$\begin{pmatrix} H_{AA}(\boldsymbol{k}) & H_{AB}(\boldsymbol{k}) \\ H_{BA}(\boldsymbol{k}) & H_{BB}(\boldsymbol{k}) \end{pmatrix} \begin{pmatrix} c_A \\ c_B \end{pmatrix} = \epsilon(\boldsymbol{k}) \begin{pmatrix} c_A \\ c_B \end{pmatrix}. \tag{1.41}$$

The transfer integrals t_m^{XY} are represented by the following expression, where the sub- and superscripts X and Y denote the orbitals at sites A and B:

$$t_m^{XY} = \left\langle \phi_X^{MO}(\boldsymbol{r}-\boldsymbol{r}_X) \right| \hat{H} \left| \phi_Y^{MO}(\boldsymbol{r}-\boldsymbol{r}_Y-\boldsymbol{T}_m) \right\rangle \tag{1.42}$$

Solving the eigenvalue problem results in two eigenvalues which represent the $\boldsymbol{k}$-dependent model functions for systems with two sites per unit cell. Consequently two electronic bands are described by equation 1.43

$$\epsilon_{1,2}(\boldsymbol{k}) = \frac{H_{AA}(\boldsymbol{k}) + H_{BB}(\boldsymbol{k})}{2} \pm \sqrt{\frac{(H_{AA}(\boldsymbol{k}) - H_{BB}(\boldsymbol{k}))^2}{4} + H_{AB}(\boldsymbol{k}) H_{BA}(\boldsymbol{k})} \tag{1.43}$$

This expression comprises the function that is fitted to the electronic band structure obtained from the DFT calculations. How to perform such a fit by using the code developed in our group (mainly by Florian Mayer and myself), is presented in the Appendix B in the form of a short tutorial which I designed for the remote onboarding of new Bachelor and Master students. Within the fit function the transfer integrals are

the fit parameters which are adapted to reproduce the DFT calculated electronic bands with minimal deviation.

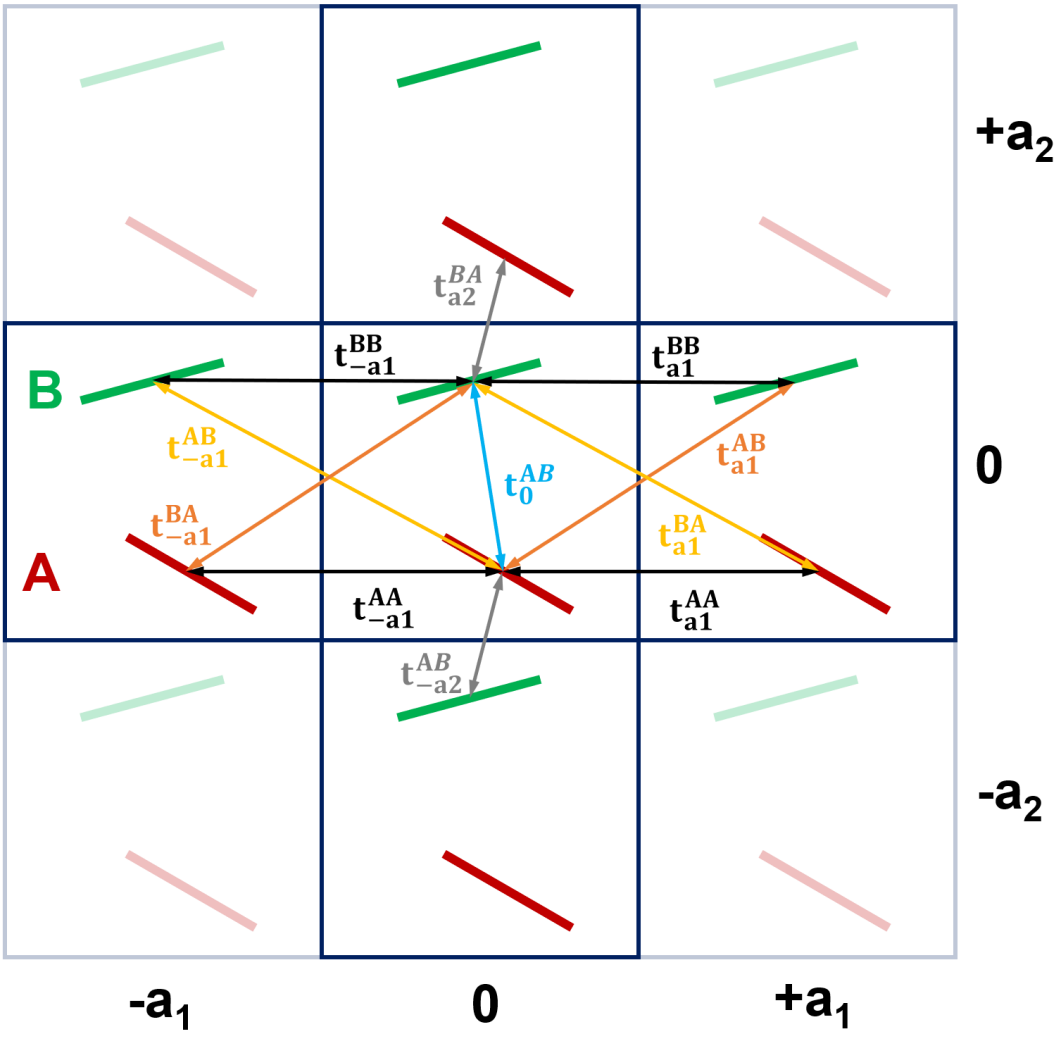

Figure 1.8.: Sketch for a two-dimensional tight-binding model.

In order to illustrate the construction of a tight-binding model function for a two-dimensional system with two inequivalent sites A and B per unit cell we consider the example shown in Figure 1.8. All transfer integrals that are considered to be non-negligible are indicated. The rest of the transfer integrals is assumed to be 0. For setting up the model function we start by looking at the terms comprising sites of the same type $H_{AA}(\boldsymbol{k})$ and $H_{BB}(\boldsymbol{k})$. In the model, these sites only have non-zero couplings along direction $\boldsymbol{a}_1$. The first term of the resulting equation 1.44 denotes the on-site energy of site A, this means that the phase factor equals 1. The transfer integral between site A in the original unit cell to A sites in neighboring unit cells along directions $\pm\boldsymbol{a}_1$ are denoted as $t^{AA}_{\boldsymbol{a}1}$ and

$t^{AA}_{-\boldsymbol{a}1}$. A completely analogous expression can be obtained for transfer integrals between sites of type B.

$$H_{AA}(\boldsymbol{k}) = \epsilon_0^{AA} + t^{AA}_{\boldsymbol{a}1} e^{i\boldsymbol{k}\boldsymbol{a}_1} + t^{AA}_{-\boldsymbol{a}1} e^{-i\boldsymbol{k}\boldsymbol{a}_1} \tag{1.44}$$

The couplings between different sites A and B can also be derived in a similar fashion and read as follows

$$H_{AB}(\boldsymbol{k}) = t_0^{AB} + t^{AB}_{\boldsymbol{a}1} e^{i\boldsymbol{k}\boldsymbol{a}_1} + t^{AB}_{-\boldsymbol{a}1} e^{-i\boldsymbol{k}\boldsymbol{a}_1} + t^{AB}_{-\boldsymbol{a}2} e^{-i\boldsymbol{k}\boldsymbol{a}_2}. \tag{1.45}$$

and

$$H_{BA}(\boldsymbol{k}) = t_0^{BA} + t^{BA}_{\boldsymbol{a}1} e^{i\boldsymbol{k}\boldsymbol{a}_1} + t^{BA}_{-\boldsymbol{a}1} e^{-i\boldsymbol{k}\boldsymbol{a}_1} + t^{BA}_{\boldsymbol{a}2} e^{i\boldsymbol{k}\boldsymbol{a}_2} \tag{1.46}$$

Now, one could simply go ahead and evaluate the eigenvalues based on equation 1.43. However, inspecting the model system in Figure 1.8 one observes that several transfer integrals have to be equal due to symmetry reasons. Again we start by inspecting terms belonging to equivalent sites. There we find that $t^{AA}_{\boldsymbol{a}1} = t^{AA}_{-\boldsymbol{a}1}$ and similarly $t^{BB}_{\boldsymbol{a}1} = t^{BB}_{-\boldsymbol{a}1}$. Using these expressions for simplifying equation 1.44 yields the more simple expression

$$H_{AA}(\boldsymbol{k}) = \epsilon_0^{AA} + 2t^{AA}_{\boldsymbol{a}1} cos(\boldsymbol{k}\boldsymbol{a}_1) \tag{1.47}$$

with a reduced number of parameters. Again the expression for BB is analogous. Now we go ahead and consider the symmetry equivalent couplings for terms dealing with different sites: $t_0^{AB} = t_0^{BA}$, $t^{AB}_{-\boldsymbol{a}1} = t^{BA}_{\boldsymbol{a}1}$, $t^{AB}_{\boldsymbol{a}1} = t^{BA}_{-\boldsymbol{a}1}$, $t^{AB}_{-\boldsymbol{a}2} = t^{BA}_{\boldsymbol{a}2}$. For the individual terms $H_{AB}(\boldsymbol{k})$ and $H_{BA}(\boldsymbol{k})$ these symmetries have no immediate consequences as the equivalent transfer integrals appear either in equation 1.45 or in equation 1.46. However, inspecting equation 1.43 we find that the product of these terms enters the expression for the eigenvalues. For this product the symmetries lead to a significant reduction of parameters (transfer integrals), as shown in equation 1.48.

$$\begin{aligned} H_{AB}(\boldsymbol{k}) \cdot H_{BA}(\boldsymbol{k}) =& (t_0^{AB})^2 + (t^{AB}_{\boldsymbol{a}1})^2 + (t^{AB}_{-\boldsymbol{a}1})^2 + (t^{AB}_{-\boldsymbol{a}2})^2 + \\ & 2t_0^{AB}(t^{AB}_{\boldsymbol{a}1} + t^{AB}_{-\boldsymbol{a}1}) cos(\boldsymbol{k}\boldsymbol{a}_1) + 2t^{AB}_{\boldsymbol{a}1} t^{AB}_{-\boldsymbol{a}1} cos(2\boldsymbol{k}\boldsymbol{a}_1) + \\ & 2t^{AB}_{-\boldsymbol{a}2}[t^{AB}_{-\boldsymbol{a}1} cos(\boldsymbol{k}(\boldsymbol{a}_1 - \boldsymbol{a}_2)) + t_0^{AB} cos(\boldsymbol{k}\boldsymbol{a}_2) + \\ & t^{AB}_{\boldsymbol{a}1} cos(\boldsymbol{k}(\boldsymbol{a}_1 + \boldsymbol{a}_2))] \end{aligned} \tag{1.48}$$

A reduced number of parameters is desirable from a numerical point of view, as it can significantly increase the numerical stability of the fit. However, depending on the actual form of the expressions for the eigenvalues multiple solutions can exist for the individual transfer integrals. Let us illustrate this problem by considering a one-dimensional system, i.e. setting $t^{AB}_{-\boldsymbol{a}2} = t^{BA}_{\boldsymbol{a}2} = 0$. Furthermore, we assume that the transfer integral $t^{AB}_{-\boldsymbol{a}1}$ is equal to zero. These simplifications of the model yield the following expression for the term dealing with different sites A,B:

$$H_{AB}(\boldsymbol{k}) \cdot H_{BA}(\boldsymbol{k}) = (t_0^{AB})^2 + (t^{AB}_{\boldsymbol{a}1})^2 + 2t_0^{AB} t^{AB}_{\boldsymbol{a}1} cos(\boldsymbol{k}\boldsymbol{a}_1). \tag{1.49}$$

Inspecting this expression we find that terms with two distinct phase factors, 0 and $\boldsymbol{k}\boldsymbol{a}_1$, exist. Now, when fitting the eigenvalue expression to the DFT data, what can be determined are terms with different phases (phase factors). So for the inequivalent sites considered in our example this means that one obtains two (fit-) coefficients c_1 and c_2 as:

$$\begin{aligned} c_1 &= (t_0^{AB})^2 + (t^{AB}_{\boldsymbol{a}1})^2 \\ c_2 &= 2t_0^{AB} t^{AB}_{\boldsymbol{a}1} \end{aligned} \tag{1.50}$$

When one wants to calculate the individual transfer integrals, one has to deal with this nonlinear system of equations. For this very basic example, one would end up with 4 solutions for the transfer integrals.

$$\begin{aligned} t_0^{AB} &= \pm\sqrt{\frac{1}{2}\left(c_1 \pm \sqrt{c_1^2 - c_2^2}\right)} \\ t^{AB}_{\boldsymbol{a}1} &= \frac{c_2}{2t_0^{AB}} \end{aligned} \tag{1.51}$$

Although one might be able to retrieve the correct solution by employing some prior knowledge on the size of the two distinct couplings for this simple model system, for more complex systems (more transfer integrals and, thus, nonlinear equations of higher order) finding the values for the distinct transfer integrals might be hardly possible. Therefore, the main conclusion is that for systems with two inequivalent sites per molecule, in general, the indidvidual transfer integrals between these sites, i.e. the values of t^{AB}, cannot be determined seperately. Only the inclusion of prior knowledge (cluster based results or trends of the transfer integrals as in ***Publication II***) offers the possibility to obtain physically meaningful values for the individual transfer integrals. However, each

case has to be considered seperately, as depending on the actual structure, the systems inherent symmetries need to be determined and the corresponding model function has to be constructed. Unfortunatley, even when considering all symmetries and incorporating them in a model function, several transfer integrals might not be uniquely defined. An additional example where only a combination of transfer integrals can be determined is obtained when considering the quinacridone model system studied in ***Publication II***. The corresponding analysis can be found in the Supporting Information of that publication (see Chapter 2).

Performing an analogous analysis for the terms containing transfer integrals between equivalent sites t^{AA} and t^{BB} in the eigenvalue expression (equation 1.43) one finds that they can suffer similar limitations. Thus, for each model system with two inequivalent sites a thorough analysis of the tight-binding model function is essential. Only based on such an analysis one can decide whether the correct values of the individual transfer integrals can be retained and a physical interpretation makes sense. Otherwise, the transfer integrals shall only be considered as mere fit parameters. Still, the obtained analytical epxression for the energy dispersion relation could be used to derive quantities like the effective mass tensor.

Let us briefly comment on a different approach to obtain tight-binding model functions for a material with specific molecular arrangements. One can set up the model like outlined above, but instead of getting the transfer integrals by fitting the model to the DFT data one can extract the corresponding molecular dimers and calculate the transfer integrals for these systems. Often such an approach will result in an already quite accurate description of the materials' electronic band structure. This renders such approaches interesting for screening databases of known structures for materials with beneficial charge transport properties.[166,167] However, contributions to the electronic bands stemming from interactions that go beyond simple molecular dimers are not included in this approach, as discussed in ***Publication I***.

1.4.3. Energy Decomposition

Considering OSCs it has been shown in the past that the intermolecular transfer integrals, which are essential parameters for charge transport, depend on the arrangement of the molecules. Small displacements of neighboring molecules can lead to changes by orders of magnitude.[32–35] For layered MOFs and COFs similar dependencies can be assumed. Therefore, it is of great importance to understand the interplay of the individual interactions that determine the relative arrangement of the molecules in the solid.

In ***Publication II*** we investigated this interplay based on a model system inspired by the α-polymorph of quinacridone. To obtain physically meaningful contributions to the interaction energy between consecutive molecules one has to apply an energy decomposition scheme. Unfortunately, it turns out that while for clusters numerous energy decomposition schemes exist, they are rarely available for periodic systems. Nevertheless, Ralf Tonner and co-workers recently developed an energy decomposition scheme for periodic systems named pEDA, which stands for periodic energy decomposition analysis.[140,168] This pEDA scheme is based on the energy decomposition analysis (EDA) method for clusters/molecules.[169–171] To address the topics in ***Publication II*** we teamed up with Ralf Tonner, who applied the pEDA scheme to the quinacridone model crystals. Therefore, we briefly introduce the basics of this decomposition scheme. Importantly, the pEDA scheme triggered the idea to implement a similar approach to the all-electron based DFT code FHI-AIMS. During the course of my PhD work I adapted the pEDA scheme for FHI-AIMS, implemented, and benchmarked a first stage of this "new" scheme. That first stage allows us to get the electrostatic contributions to the interaction energy. We applied this scheme in ***Publication IV*** in order to understand the driving forces determining the packing arrangement of 2D layered COFs. In principle, the applicability of this decomposition scheme is not restricted to OSCs and COFs. One can go ahead and apply it to decompose the interlayer interactions in 2D MOFs or vdW heterostructures for example.

In the following, we introduce the pEDA scheme following References [140, 168, 172] and based on these explanations we introduce the decomposition scheme for FHI-Aims.

periodic Energy Decomposition Analysis (pEDA) Scheme

The periodic EDA scheme developed by Raupach and Tonner is based on the molecular EDA scheme.[169–171] In essence, in their work, the EDA scheme has been extended to periodic boundary conditions. The working principle of the molecular EDA is shown by the schematic description in Figure 1.9. The first step of this scheme is to consider that the overall bond dissociation energy ΔE_{bond} for a system consisting of fragments (molecules) A and B is composed as the sum of the preparation energy ΔE_{prep} and the total interaction energy ΔE_{int} (sometimes also referred to as intrinsic bond energy). The preparation energy consists of contributions from structural deformations of the fragments to obtain the geometry in the bonded system and electronic excitations.[140] Therefore, this energy term can be calculated by the energies of the isolated fragments in their relaxed ground state (E_A^{GS}, E_B^{GS}) and the distorted states E_A, E_B, including

geometric distortions and possibly electronic excitation, which the fragments exhibit in the combined system as[140]

$$\Delta E_{prep} = (E_A^{GS} + E_B^{GS}) - (E_A + E_B). \tag{1.52}$$

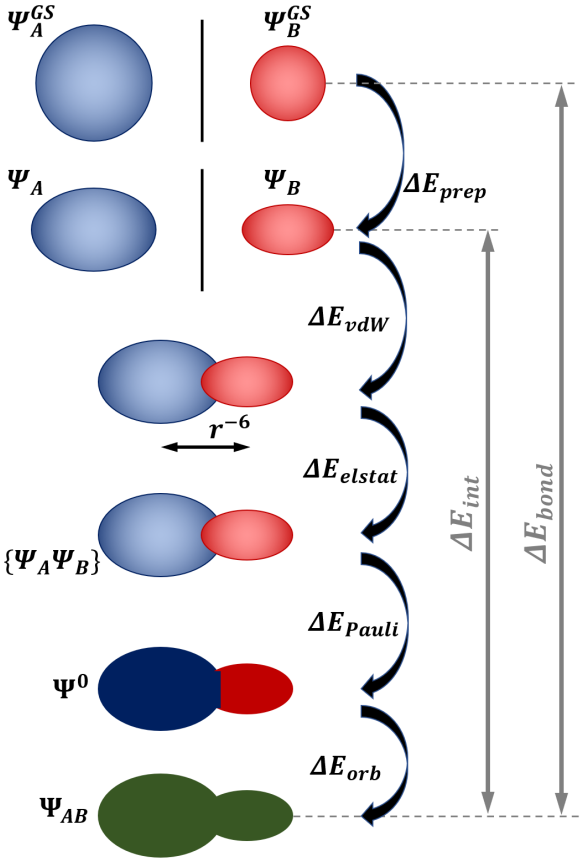

Figure 1.9.: Schematic description of the steps in a energy decomposition analysis of a chemical bond between fragments A and B forming the combined entity AB. The indidvidual energy contributions to the overal bond formation energy ΔE_{bond} are denoted by the black arrows. The wavefunctions of the individual fragments are shown as blue (A) and red ellipses (B). Black lines between the two fragments denote that the isolated fragments are considered. This scheme is based on Ref. [140].

The interaction energy ΔE_{int} results from the difference of the energy of the combined system E_{AB} and the individual fragments E_A and E_B in the distorted states they exhibit in the combined system. This is indicated in Figure 1.9. The basic idea of the EDA scheme is to partition this total interaction energy ΔE_{int} into physically well defined contributions,

$$\Delta E_{int} = E_{AB} - E_A - E_B = \Delta E_{elstat} + \Delta E_{Pauli} + \Delta E_{orb} + \Delta E_{vdW}. \tag{1.53}$$

The energy contribution corresponding to the vdW interactions ΔE_{vdW} can be easily obtained by the difference of the vdW energies of system AB and the fragments as

$$\Delta E_{vdW} = E_{vdW}^{AB} - E_{vdW}^{A} - E_{vdW}^{B}. \tag{1.54}$$

These vdW energy terms are usually available from standard DFT calculations, especially when employing a posteriori vdW corrections. Subtracting this vdW term ΔE_{vdW} from the total interaction energy results in the electronic part of the interaction energy $\Delta E_{int,elec}$ which can then be further decomposed. The next step is to consider the fragments to be infinitely far apart, still exhibiting the same geometric distortions as in the combined system. To get the quasiclassical electrostatic energy between the charge densities n_A and n_B of these isolated fragments one simply has to bring the fragments, i.e. their charge densities, to the positions of the combined system. The resulting system is denoted as $\{A, B\}$. The energy difference associated to this step equals the electrostatic contribution to the electronic interaction energy as shown in equation 1.55.

$$\Delta E_{elstat} = E_{elstat}^{\{A,B\}} - E_{elstat}^{A} - E_{elstat}^{B} \tag{1.55}$$

This electrostatic energy ΔE_{elstat} corresponds to the energy change upon bringing the distorted fragments into the positions they exhibit in the combined system without optimizing the wavefunctions. The wavefunction of this combined system $\{A, B\}$ does not obey the Pauli exclusion principle, which is accounted for in the next step. Therefore, the wavefunction corresponding to system $\{A, B\}$ is antisymmetrized and normalized, which leads to an intermediate wavefunction Ψ^0 with the corresponding energy E^0. The associated energy difference (equation 1.57) is denoted as Pauli exchange repulsion ΔE_{Pauli}. In the last step, the molecular orbitals of the intermediate wavefunction are allowed to relax and the final (fully relaxed) wavefunction Ψ^{AB} for the combined system AB is obtained. The difference between the energy corresponding to the intermediate state Ψ^0 and the final state Ψ^{AB} denotes the orbital rehybridization ΔE_{orb}, see equation 1.56.

$$\Delta E_{orb} = E_{AB} - E^0 \tag{1.56}$$

$$\Delta E_{Pauli} = E^0 - (E_A + E_B + \Delta E_{elstat}) \tag{1.57}$$

More details on this decomposition scheme as well as on the implementation for periodic systems, the actual pEDA, can be found in References [140, 168, 172]. In principle, one has to take care of each $\boldsymbol{k}$-point seperately when constructing the intermediate wave functions and performing the orthogonalization steps. Other than that, the scheme is analogous to the molecular case. This pEDA scheme has been succesfully applied in ***Publication II*** and triggered the idea to implement a very similar scheme for the all-electron DFT code FHI-aims. In the following section we describe how the adapted decomposition scheme works and also show how it performs for the systems considered in ***Publication II***. This scheme will then be used in ***Publication IV*** to get the individual energy contributions for the interaction between consecutive layers of 2D COFs.

Energy Decomposition Scheme for FHI-AIMS

The following considerations deal with fundamental and technical aspects concerning the implementation of an energy decomposition scheme in FHI-aims. This scheme is largely based on the (p)EDA scheme presented in the previous section. An essential first step for the decomposition of the interaction energy is the calculation of the combined system AB and the fragments A and B. From these calculations we already get the energies E_{AB}, E_A, E_B as well as the individual van der Waals terms E^{AB}_{vdW}, E^{A}_{vdW}, E^{B}_{vdW}. Based on these energies and using equations 1.53, 1.54 one can already evaluate the total interaction energy ΔE_{int} together with the corresponding vdW contribution ΔE_{vdW}. Furthermore, also the electrostatic energies of the individual fragments E^{A}_{elstat} and E^{B}_{elstat} can be extracted from the output of the corresponding calculations. What is missing for calculating the electrostatic contribution to the interaction energy is the electrostatic energy of the combined system $\{A, B\}$. In the following, the construction of this combined system based on the calculations of the individual fragments A and B is outlined.

Importantly, from the DFT calculations one also gets the eigenvectors of the individual systems together with the corresponding occupation numbers as well as the Hamiltonian and overlap matrices. The eigenvectors of the isolated fragments A and B are needed for calculating the electrostatic contribution to the interaction energy. In the following we describe how these eigenvectors can be used to construct the electron density of the combined system $\{A, B\}$ which is used to calculate the corresponding electrostatic energy $E^{\{A,B\}}_{elstat}$. In the following, we are solely considering the case of crystalline systems, i.e. periodic boundary conditions have to be employed. Therefore, the KS-equations depend

on the wavevector $\boldsymbol{k}$ with different solutions $\Psi_{l,\boldsymbol{k}}(\boldsymbol{r})$ at each $\boldsymbol{k}$-point in the first Brillouin zone. Let us start by considering the representation of the wavefunction for a state with index l in terms of the real space basis functions $\phi_j^{at}(\boldsymbol{r})$:

$$\Psi_{l,\boldsymbol{k}}(\boldsymbol{r}) = \sum_m \sum_j c_{lj}(\boldsymbol{k}) \cdot e^{i\boldsymbol{k}\boldsymbol{T}_m} \cdot \phi_j^{at}(\boldsymbol{r} - \boldsymbol{T}_m). \tag{1.58}$$

Here j sums over all basis functions for all atoms in the primitive unit cell. Note that basis functions belonging to a certain atom are centered at the respective position $\boldsymbol{R}_{at}$ of that atom. Furthermore, m is the summation index for the translation vector which is given by a linear combination of the real space lattice vectors $\boldsymbol{a}_i$ with integer values a, b, c as: $\boldsymbol{T}_m = a\boldsymbol{a}_1 + b\boldsymbol{a}_2 + c\boldsymbol{a}_3$. This definition also leads to $\boldsymbol{k}$-point dependent eigenvectors given by the coefficients $c_{lj}(\boldsymbol{k})$ and to $\boldsymbol{k}$-dependent elements in the hamiltonian and the overlap matrices. With this basis at hand one can go ahead and construct the charge density based on the eigenvectors and the basis functions:

$$n(\boldsymbol{r}) = \sum_l \sum_{\boldsymbol{k}} f_{l,\boldsymbol{k}} \left|\Psi_{l,\boldsymbol{k}}(\boldsymbol{r})\right|^2 \tag{1.59}$$

Here $f_{l,\boldsymbol{k}}$ denotes the weighted occupation number of a state with index l. The construction of the electron density corresponding to a defined set of eigenvectors can be handled by the *restart* functionality of FHI-aims. Employing this functionality the eigenvectors are read in for each $\boldsymbol{k}$-point, the corresponding wavefunction and charge density are constructed, and a new calculation of the total energy according to the Harris functional is invoked (see Ref [141] and Appendix A for details).

Now, the eigenvectors/wavefunctions for the combined system $\{A, B\}$ can be constructed based on the eigenvectors of the isolated fragments. In the following, the eigenvectors for each $\boldsymbol{k}$-point are represented by the corresponding coefficient matrices $\mathbb{C}_A(\boldsymbol{k})$, $\mathbb{C}_B(\boldsymbol{k})$, and $\mathbb{C}_{\{A,B\}}(\boldsymbol{k})$. As an example we write the coefficient matrix corresponding to fragment A in more explicit terms below, where Nb denotes the number of basis functions included for fragment A and Nst dentoes the number of states for this fragment.

$$\mathbb{C}_A(\boldsymbol{k}) = \begin{bmatrix} c_{1,1}^A(\boldsymbol{k}) & c_{1,2}^A(\boldsymbol{k}) & \dots & c_{1,Nb}^A(\boldsymbol{k}) \\ c_{2,1}^A(\boldsymbol{k}) & c_{2,2}^A(\boldsymbol{k}) & \dots & c_{2,Nb}^A(\boldsymbol{k}) \\ \vdots & \vdots & \ddots & \vdots \\ c_{Nst,1}^A(\boldsymbol{k}) & c_{Nst,2}^A(\boldsymbol{k}) & \dots & c_{Nst,Nb}^A(\boldsymbol{k}) \end{bmatrix} \tag{1.60}$$

Based on coefficient matrices $\mathbb{C}_A(\boldsymbol{k})$ and $\mathbb{C}_B(\boldsymbol{k})$ the coefficient matrix corresponding to system $\{A, B\}$ is constructed as

$$\mathbb{C}_{\{A,B\}}(\boldsymbol{k}) = \begin{bmatrix} \mathbb{C}_{A,occ}(\boldsymbol{k}) & 0 \\ 0 & \mathbb{C}_{B,occ}(\boldsymbol{k}) \\ \mathbb{C}_{A,virt}(\boldsymbol{k}) & 0 \\ 0 & \mathbb{C}_{B,virt}(\boldsymbol{k}) \end{bmatrix}. \tag{1.61}$$

The occupation vector corresponding to system $\{A, B\}$ is constructed as

$$f_{\{A,B\}}(\boldsymbol{k}) = \big[f_{A,occ}(\boldsymbol{k}), \quad f_{B,occ}(\boldsymbol{k}), \quad f_{A,virt}(\boldsymbol{k}), \quad f_{B,virt}(\boldsymbol{k})\big] \tag{1.62}$$

Here, $f_{A,occ}(\boldsymbol{k})$, for example, contains all occupied states belonging to fragment A, while $f_{A,virt}(\boldsymbol{k})$ contains all unoccupied states for A. Based on the coefficient matrix and the occupation vector shown in expressions 1.61 and 1.62 one can evaluate the quasiclassical electrostatic contribution, $E_{elstat}^{\{A,B\}}$, arising from the interaction of the charge densities of the isolated fragments assembled in the combined system. This energy can be obtained by starting an FHI-Aims calculation from the coefficient matrices $\mathbb{C}_{\{A,B\}}(\boldsymbol{k})$ and the corresponding occupation vectors $f_{\{A,B\}}(\boldsymbol{k})$. The electrostatic energy $E_{elstat}^{\{A,B\}}$ corresponding to this system can then be readily taken from the output of the calculation. Employing this energy together with the electrostatic energies of the individual fragments E_{elstat}^{A} and E_{elstat}^{B} one can calculate the electrostatic part of the interaction energy as $\Delta E_{elstat} = E_{elstat}^{\{A,B\}} - E_{elstat}^{A} - E_{elstat}^{B}$. The explicit form of this energy in terms of the electron densities of the individual fragments is shown in expression 1.63. For more details on the evaluation of these energies see the Appendix A.

$$\begin{aligned} \Delta E_{elstat} = \sum_{\nu \epsilon A} \sum_{\mu \epsilon B} \frac{Z_\mu Z_\nu}{|\vec{R}_\mu - \vec{R}_\nu|} - \sum_{\nu \epsilon A} \int \frac{Z_\nu n_B(\vec{r}_i)}{|\vec{R}_\nu - \vec{r}_i|} d\vec{r}_i - \sum_{\nu \epsilon B} \int \frac{Z_\nu n_A(\vec{r}_i)}{|\vec{R}_\nu - \vec{r}_i|} d\vec{r}_i \\ +2 \int \int \frac{n_A(\vec{r}_i) n_B(\vec{r}_j)}{|\vec{r}_i - \vec{r}_j|} d\vec{r}_i d\vec{r}_j \end{aligned} \tag{1.63}$$

At the present stage we are mainly interested in contributions to the interaction energy that stem from vdW and electrostatic interactions. Therefore, we can write the interaction energy ΔE_{int} as

$$\begin{aligned}\Delta E_{int} &= \Delta E_{elstat} + (\Delta E_{Pauli} + \Delta E_{orb}) + \Delta E_{vdW} \\ &= \Delta E_{elstat} + \Delta E_{Pauli,orb} + \Delta E_{vdW}.\end{aligned} \tag{1.64}$$

As ΔE_{Pauli} and ΔE_{orb} are not considered seperately in our approach, we combine them in a single term $\Delta E_{Pauli,orb}$. This term is then obtained by subtracting vdW and electrostatic contributions from the overall interaction energy. Several interesting scientific questions like the layer arrangement of COFs discussed in ***Publication IV*** can already be addressed by decomposing the interaction energy into these contributions. For getting the terms comprising the Pauli exchange repulsion and the orbital rehybridization explicitly, several problems associated with the all-electron nature of the basis functions and the determination of the total energy arise. These problems are discussed in the Appendix A. A validation of the electrostatic term evaluated with the implemented scheme is also presented in Appendix A.1.

2. Different methods for obtaining the electronic coupling in molecular crystals

2.1. Author contributions

E. Zojer and C. Winkler conceived the idea that some of the currently applied methods for getting intermolecular electronic couplings could be misleading in some instances. Therefore we decided to compare these methods based on a prototypical crystalline organic semiconductor. C. Winkler carried out all the DFT calculations and primary analysis of the data. The data were interpreted by C. Winkler and E. Zojer. F. Mayer and C. Winkler developed the code which is employed for fitting tight-binding models to the DFT data. C. Winkler wrote the first version of the manuscript and prepared all figures. The project was supervised by E. Zojer. C. Winkler and E. Zojer revised the manuscript in several iterations.

The following paper is published in Advanced Theory and Simulations and inserted here as original publication together with the Supporting Information. Reprinted with permission from "Winkler C., Mayer F., and Zojer E., Analyzing the Electronic Coupling in Molecular Crystals - The Instructive Case of α-Quinacridone, Advanced Theory and Simulations, 2019, 2, 1800204".

2.2. Main paper

ADVANCED THEORY AND SIMULATIONS

www.advtheorysimul.com

Analyzing the Electronic Coupling in Molecular Crystals—The Instructive Case of α-Quinacridone

*Christian Winkler, Florian Mayer, and Egbert Zojer**

In the present article, an evaluation of different approaches for estimating the electronic coupling and charge-transport parameters in organic semiconductors is provided. As a testbed for that comparison, the α-polymorph of quinacridone is chosen. This system is particularly well suited for the purpose, as α-quinacridone intermolecular interactions in distinct crystallographic directions are dominated by the three mechanisms most relevant in organic semiconductors: π-stacking, H-bonding, and van der Waals stacking. Density-functional theory-based simulations yield a comparably complex band structure, which provides the means for demonstrating shortcomings of commonly applied approaches. These include the estimation of transport properties based on bandwidths and the calculation of electronic transfer integrals considering molecular dimers. As a particularly promising alternative, the fitting of suitably complex tight-binding models to the DFT-calculated bands in the entire Brillouin zone is proposed. These fits bear the advantage of directly producing intermolecular coupling constants for all relevant neighboring molecules as input parameters for hopping and dynamic disorder models. They also yield an analytic expression for the electronic bands. These allow the extraction of parameters relevant for band-transport models (like group velocities and effective masses) in the entire Brillouin zone.

1. Introduction

Organic semiconductors have attracted increasing attention over the past years because of numerous advantageous properties, including the tunability of electrical and optical properties,[1] mechanical flexibility,[2] and the possibility to build biocompatible electronics out of small hydrogen-bonded pigments.[3–5] For all these applications, the charge transport properties of the employed materials are highly relevant. Their description is, however, far from straightforward, as one is dealing with systems in which the electronic coupling between neighboring molecules is typically on the same order as the electron–phonon coupling.[6]

Therefore, various models have been developed (or adapted from related fields) to describe the carrier mobilities of organic semiconductors, μ.[6–9] The approaches comprise band-transport models explicitly considering electron–phonon coupling (and the associated band narrowing) via the Holstein–Peierls Hamiltonian,[10–12] dynamic disorder–based models,[13–18] and purely hopping-based approaches building on Marcus theory.[6–8,19] The popularity of these models has varied over time and their suitability for a given system typically depends on the types of considered molecules, their arrangements, the temperature range of interest, and the degree of disorder present.[6–9] Still, an essential ingredient for all these transport models is the electronic coupling between neighboring molecules. Especially for hopping and dynamic disorder models, it can be expressed through transfer integrals, t, while for band-transport parameters like the effective masses, m^*, are most relevant.[6–9,18]

A seemingly straightforward and often applied approach for determining that coupling, at least for crystalline materials, is to calculate the electronic band structure of the system. This is usually done applying state-of-the-art density functional theory (DFT) methods. In principle, this band structure then contains all information on transfer integrals and effective masses, including the full crystal environment for each molecule. Nevertheless, it turns out that extracting the parameters quantifying the intermolecular electronic coupling from band structures can be difficult, misleading, and dependent on the methods and approximations used.

Thus, as a first step, we recapitulate commonly used methods for extracting transport relevant quantities from electronic band structures of crystalline materials. One of the simplest ways is to consider the widths of the electronic bands in high-symmetry directions. When employing a one dimensional nearest-neighbor tight-binding model, one obtains the following relation between the energy of the electronic states, E, and the wavevector, k:[20]

$$E(k) = \varepsilon - 2t \cdot \cos(k \cdot a) \tag{1}$$

Here ε is the on-site energy, t the transfer integral between neighboring units, and a is the real space distance between the lattice

C. Winkler, F. Mayer, Prof. E. Zojer
Institute of Solid State Physics
NAWI Graz
Graz University of Technology
Petersgasse 16, 8010 Graz, Austria
E-mail: egbert.zojer@tugraz.at

The ORCID identification number(s) for the author(s) of this article can be found under https://doi.org/10.1002/adts.201800204

DOI: 10.1002/adts.201800204

sites. Notably, Equation (1) also holds for orthogonal 3D unit cells in the unit cell directions, as long as only nearest neighbors are considered. For such a band shape, the transfer integral, t, is obtained as a quarter of the bandwidth, BW. Comparing transfer integrals or, equivalently, BWs obtained for different directions, one can then try to rationalize the anisotropy of charge transport within the material.[21–23]

A more elaborate approach to obtain transfer integrals is to fit DFT-evaluated bands along high-symmetry directions by a 3D nearest-neighbor tight-binding expression considering the actual symmetry of the crystal. In this way, one gets direct access to the transfer integrals as fit parameters.[24] A limitation of this strategy is that only information on the calculated directions is considered in the fit, which becomes problematic for low-symmetry systems, where a more homogeneous sampling of the Brillouin zone is necessary. Even when the latter is done, the question remains, how many and which of the neighboring molecules need to be taken into account for setting up the "ideal" tight-binding Hamiltonian. In particular, it needs to be determined under which circumstances one needs to go beyond nearest neighbors and what consequences this will have.

Finally, when band-transport mechanisms dominate, another option for determining preferential transport directions is to identify the band extrema and then to calculate the effective mass tensors at these k-points by numerical differentiation of the ab initio data. This then allows an analysis of the effective mass m^* as a function of direction.[21–23,25,26]

All above-described approaches build on band structure calculations. As an alternative approach that is particularly widespread in the field of organic semiconductors, transfer integrals are routinely extracted from calculations of molecular dimers[26–31] employing the "energy splitting in dimer" (ESD) method or related, more advanced approaches.[6,7,32] These approaches are often computationally less demanding than band structure calculations and are particularly useful when dealing with non-crystalline materials. Moreover, simulations on dimers are also insightful when trying to understand the impact of shifting or rotating neighboring molecules relative to each other.[30,33–35] The obtained transfer integrals can then be employed for calculating hopping rates and also charge-carrier mobilities.[36–40] For obtaining these mobilities, the transfer integrals are often combined with Monte Carlo–based approaches.[37–41] Dimer-derived transfer integrals have also been used to construct tight-binding model functions, which can then be employed for calculating band structures and effective masses.[42,43] The molecules surrounding the dimers in the actual crystalline environment are typically not considered in such approaches. Therefore, they bear the risk of missing relevant physical effects resulting from more complex intermolecular coupling effects beyond mere pair interactions.[44]

In the following, we will critically assess the above-mentioned methods for extracting the electronic coupling in organic semiconductors, including implications for charge-carrier transport properties. This will be done for the instructive case of the α-polymorph of quinacridone. To overcome the encountered limitations of the above approaches, we will present a strategy based on comparably complex tight-binding fits, which we find well suited for obtaining the electronic coupling parameters needed in hopping as well as band-transport models.

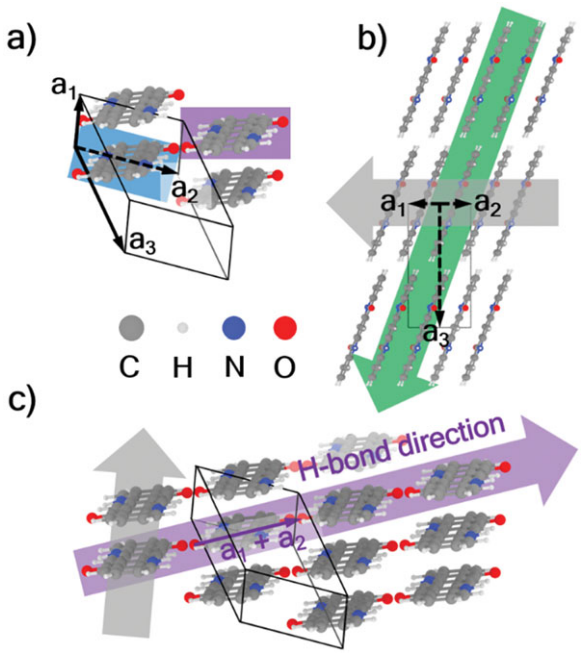

Figure 1. Crystal structure of the quinacridone α-polymorph. a) View of the unit cell with the molecule in the original cell marked by a blue rectangle and the closest H-bonding partner in $\mathbf{a_1}+\mathbf{a_2}$ direction marked by a purple rectangle. b) Side view of the crystal structure along $\mathbf{a_1}+\mathbf{a_2}$. c) View to indicate the H-bonding and stacking directions. The most important directions for assessing the anisotropic charge-transport parameters are indicated by colored arrows: gray for π-stacking, purple for H-bonding, and green for vdW stacking.

2. Studied Model System

The choice of α-quinacridone as test system is motivated by the observation that in this material the intermolecular interactions are fundamentally different in all three spatial directions. Notably, they comprise the most relevant interaction motifs typically found in organic semiconductors: (seemingly ideal) π-stacking, H-bonding, and van der Waals stacking. Moreover, applying the approaches mentioned in the introduction section is comparably straightforward for α-quinacridone, as it contains only one molecule per unit cell. This results in comparably simple expressions for the tight-binding models and avoids band-crossings involving the frontier bands.

Different views of the crystal structure of the quinacridone α-polymorph[45] are shown in **Figure 1**, where $\mathbf{a}_1$, $\mathbf{a}_2$, and $\mathbf{a}_3$ denote the unit cell vectors in real space. The directions of the different interactions are indicated by colored arrows: the green arrow indicates the direction of van der Waals stacking ($\mathbf{a}_1+\mathbf{a}_2+\mathbf{a}_3$), the purple arrow the direction of hydrogen bonding ($\mathbf{a}_1+\mathbf{a}_2$), and the gray arrow the direction of π-stacking ($\mathbf{a}_1$).

There are several additional aspects that make α-quinacridone ideally suited for the present study (as will become apparent from the discussion below): i) Along certain spatial directions, one observes noncosine-shaped bands implying that in those directions a nearest-neighbor tight-binding description cannot be sufficient. (ii) In other directions, diagonal couplings become relevant. These massively modify the calculated band structures. (iii)

Moreover, for certain directions, the interactions with the surrounding molecules in the crystalline environment turn out to be particularly relevant resulting in improper results obtained from dimer models.

3. Analyzing the Electronic Band Structure

The valence- (VB) and conduction bands (CB) of α-quinacridone calculated using dispersion-corrected density-functional theory at the Perdew–Burke–Enzerhof (PBE)[46,47] level are shown in **Figure 2**.

The widths of these bands (defined as the energetic difference between the highest and lowest energy states for a specific ***k***-path within the first Brillouin zone, BZ) are compiled in **Figure 3**b. The high-symmetry directions in reciprocal space are neither parallel to the real-space lattice vectors $\mathbf{a}_1$, $\mathbf{a}_2$, $\mathbf{a}_3$ (representing the periodic arrangement of the molecules) nor to the directions of H-bonding, π-stacking, and vdW stacking. They are also not parallel to the short (**S**) or long (**L**) molecular axes, or perpendicular to the molecular plane (**P**). Therefore, we also calculated the bandwidths along paths between the Γ-point and the Brillouin-zone boundary parallel to $\mathbf{a}_1$, $\mathbf{a}_2$, $\mathbf{a}_3$, **S**, **L**, and **P**, as indicated in Figure 3a. Note that the aforementioned vectors in the following discussions will also be used as labels for the corresponding **k**-paths.

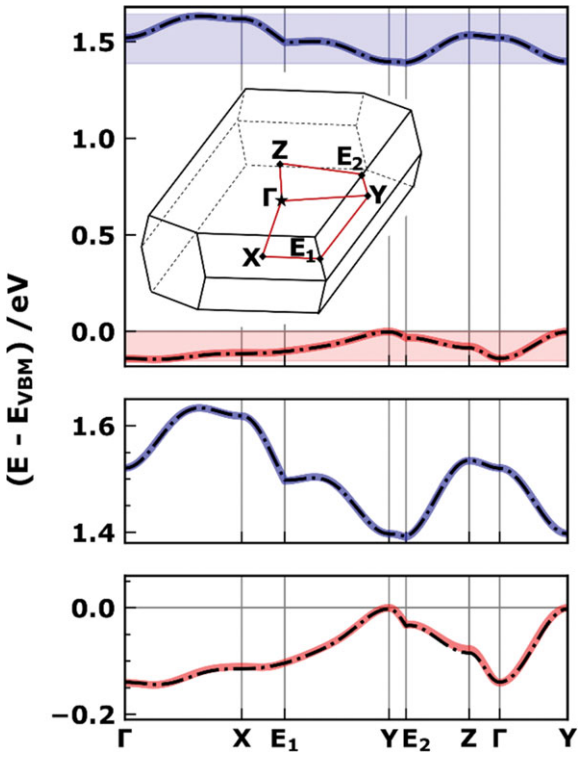

Figure 2. DFT-calculated electronic band structure of α-quinacridone along a set of high-symmetry paths (solid thick lines). The first BZ including the chosen *k*-path is shown as an inset in the topmost panel. The energies are given relative to the maximum of the valence band, E_{VBM}. The results of the TB fit discussed in Section 4 are shown as dash–dotted black lines (essentially coinciding with the DFT calculated bands). A zoom into the regions of conduction and valence band is shown in the two lower panels.

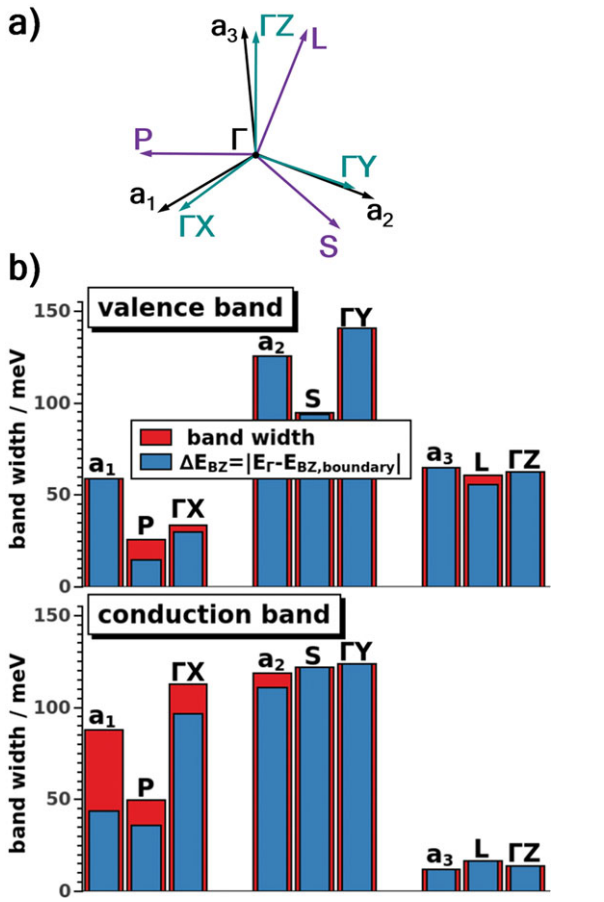

Figure 3. a) Unit vectors starting at the Γ point and pointing in the directions of the unit cell axes in real space ($\mathbf{a}_1$, $\mathbf{a}_2$, and $\mathbf{a}_3$), the unit cell axes in reciprocal space (**ΓX**, **ΓY**, and **ΓZ**), the π-stacking direction (**P**) and the directions of short (**S**) and long (**L**) molecular axes. b) Bandwidth and ΔE_{BZ} along the chosen paths in reciprocal space for valence and conduction band. Data sets which describe similar paths are grouped, for example, $\mathbf{a}_2$, **S**, and **ΓY**.

Observing a large bandwidth, BW, along a certain path suggests that the electronic coupling in that direction is large. Thus, the comparison of the bandwidths in Figure 3 allows first conclusions concerning the anisotropy of the electronic coupling. Within the simple 1D tight-binding model mentioned in the introduction, this also yields a first estimate of the anisotropy of the associated transfer integrals, $t = \mathrm{BW}/4$: For the valence band, the BW is largest along a path parallel to the **ΓY** direction, similarly large parallel to $\mathbf{a}_2$, and only somewhat smaller along the short molecular axis (**S**). It is intermediate along paths in the π-stacking direction ($\mathbf{a}_1$) and along the long molecular axis (**L**), and smallest for paths perpendicular to the molecular plane (**P**). For the conduction band, the main differences are that the bandwidths in all directions close to the long molecular axis ($\mathbf{a}_3$, **L**, and **ΓZ**) become particularly small, while they increase somewhat for paths pointing in the π-stacking and in the **P** directions. For the latter two, they, however, still remain well below 100 meV.

At first glance, this appears somewhat surprising considering the seemingly ideal π-stacking in α-quinacridone, which one might assume to maximize the corresponding electronic couplings. The reason for the strongly reduced coupling in the π-stacking direction lies in the details of the arrangement of the molecules: The **P** and $\mathbf{a}_1$ directions are not parallel, resulting in a slip of neighboring molecules along their long and short molecular axes. As a consequence of the symmetry of the involved orbitals, this results in a sharply reduced electronic coupling, as discussed in detail, for the examples of tetracene, anthradithiophene, and sexithienyl in refs. 6,30,33.

A closer inspection of the band structure displayed in Figure 2 reveals that along several paths, the bands clearly deviate from the (according to Equation (1)) expected half-wave cosine shape with extrema at Γ and the BZ boundary. To more systematically identify such cases, we define a second parameter related to the widths of the band, namely the (absolute value of the) energetic difference between the state at the Γ point and the state at the BZ boundary along a specific direction, ΔE_{BZ}.

The values of ΔE_{BZ} are also contained in Figure 3. Major deviations between ΔE_{BZ} and BW indicate paths along which the simple relation of t equaling a quarter of the bandwidth no longer holds. Small deviations can also originate from the fact that apart from **ΓX**, **ΓY**, and **ΓZ**, the ***k***-paths for which the bandwidths are displayed in Figure 3 are not parallel to reciprocal lattice vectors. The largest difference between ΔE_{BZ} and the BW is found for the conduction band along the $\mathbf{a}_1$ path. Other paths which are potentially not described correctly by the simple tight-binding expression from Equation (1) are **P** and **L** for the valence- and $\mathbf{a}_2$, **P**, and **ΓX** for the conduction band. Notably, analyzing bandwidths allows us to identify these problematic directions, but does not provide us with tools for improving the analysis.

4. Tight-Binding Fits versus Dimer Models

Therefore, we have gone beyond the simple model from Equation (1), applying a more general tight-binding ansatz of the following form:[20]

$$E(\mathbf{k}) = \varepsilon + \sum_j \mathrm{t}_j \cdot \mathrm{e}^{\pm i\mathbf{k}\cdot\mathbf{R}_j} \tag{2}$$

Here ε denotes the on-site energy, t_j is the transfer integral for neighboring molecules along direction j and $\mathbf{R}_j$ is the vector connecting the central molecule with the respective neighbor. Due to the inversion symmetry of α-quinacridone, the two neighbors at $\mathbf{R}_j$ and $-\mathbf{R}_j$ are equivalent. Therefore, the associated transfer integrals are also the same and one obtains two terms $t_j \cdot e^{i\mathbf{k}\cdot\mathbf{R}_j}$ and $t_j \cdot e^{-i\mathbf{k}\cdot\mathbf{R}_j}$ for each index j, resulting in $2t_j \cos(\mathbf{k}\cdot\mathbf{R}_j)$. When fitting the tight-binding model to the DFT band structure, the fit parameters are ε and t_j, while $\mathbf{R}_j$ is determined by the crystal structure. As there is only one molecule per unit cell, the possible values of $\mathbf{R}_j$ in α-quinacridone are sums of integer multiples of the unit cell vectors $\mathbf{a}_1$, $\mathbf{a}_2$, and $\mathbf{a}_3$. In the following, these will also be used for naming the different transfer integrals and when referring to bands for the corresponding **k**-paths.

For developing the tight-binding model, we start by considering a subset of nearest neighbor molecules and gradually include more neighbors until the root mean square error between the tight-binding model and the DFT bands falls below 5 meV. In this context, it needs to be stressed that the fitting must not be done along the high-symmetry directions alone, as then one only obtains good agreement in these directions, while there are large errors in other parts of the Brillouin zone. Therefore, we homogeneously sampled the entire BZ employing a tight *k*-grid (for details see Section 8). This yields a highly accurate description of the bands not only on that grid, but also along the high-symmetry directions. This is shown in Figure 2 (black line). In passing, we mention that increasing the number of neighbor molecules included in the fit does not change the transfer integrals for the previously considered neighbors. This can be seen in **Table 1**, when comparing the t_j for the "simplified" and the "full" model. It is a consequence of the model function representing a Fourier decomposition of the energy dispersion relation, with the transfer integrals serving as Fourier coefficients. Notably, these coefficients are independent of each other (for details see Supporting Information).

An appealing aspect of the tight-binding fit is that it yields an analytical expression for the band structure. From that expression, group velocities and effective masses can also be calculated analytically at any point in reciprocal space from derivatives of the band structure with respect to k (see below). Additionally, the fit immediately yields the electronic couplings (transfer integrals) between all relevant neighbors considering the full 3D crystal environment.

For organic semiconductors, the transfer integrals are more commonly determined employing the ESD[6] method, where they are calculated as half of the energetic splitting between dimer orbitals viewed as bonding and antibonding linear combinations of the frontier orbitals of isolated molecules. In passing we note that more sophisticated approaches like the fragment orbital (FO) methods need to be employed whenever the molecules are symmetry inequivalent, as the ESD approach would not properly account for differences in site energies arising from the molecules polarizing each other differently.[32] This is, however, no major concern here, as the dimers derived from the α-polymorph of quinacridone show inversion symmetry.[32]

A disadvantage of the ESD approach is that it treats the molecular dimer as an isolated entity neglecting the role of most of the neighboring molecules in the crystalline environment. To assess the impact of this approximation, we first compare the transfer integrals from the tight-binding fit with the ones obtained via the ESD method (see Table 1). Overall, there is a rather good agreement between the two approaches for both bands (VB and CB) and most of the considered directions (also considering certain methodological differences in the DFT calculations on dimers and periodic structures – see Section 8). Excellent agreement is found, especially for the $\mathbf{a}_2+\mathbf{a}_3$ direction, for both bands and for $\mathbf{a}_1$ and $\mathbf{a}_1+\mathbf{a}_2$ for the valence band. Conversely, for the CB, we find a large deviation of 12 meV for the latter direction. To rationalize this discrepancy, one has to remember that the $\mathbf{a}_1+\mathbf{a}_2$ direction is the one of the intermolecular H-bonds (see Figure 1). Notably, one of the properties of quinacridone is that the four H-bonds each molecule undergoes in a crystalline environment (two involving the amine and two involving the ketone groups)

Table 1. Parameters for the tight-binding fit of the frontier bands of the quinacridone α-polymorph considering only the molecules with the smallest distance from the central molecule ("simplified") and for an increased number of transfer integrals included in the fit ("full"). The reason why $t_{\mathbf{a}1+\mathbf{a}2}$ is considered in the "simplified" model is that this direction corresponds to the H-bonding direction with particularly short intermolecular distances. Likewise, the distance between (symmetry inequivalent) atoms is shorter in the $\mathbf{a}_2+\mathbf{a}_3$ direction than in the $\mathbf{a}_3$ direction, which is the reason why we have included $t_{\mathbf{a}2+\mathbf{a}3}$ and not $t_{\mathbf{a}3}$ (see Figure 6). The root mean square error (RMSE) in the last line is calculated as $\mathrm{RMSE} = \sqrt{\frac{\sum_{i=1}^{N} |\hat{E}_{i,\mathrm{DFT}} - E_{i,\mathrm{TB}}|^2}{N}}$, with $E_{i,\mathrm{TB}}$ and $E_{i,\mathrm{DFT}}$ referring to the energies of the individual states calculated by the tight-binding, respectively, by the DFT approach. Note that differences smaller than 1 meV are within the convergence errors of our calculations.

	VB_{full} [meV]	$VB_{simplified}$ [meV]	Dimer [meV]	CB_{full} [meV]	$CB_{simplified}$ [meV]	Dimer [meV]
ε	852.7	852.7		2462.1	2462.1	
t_{a1}	4.8	4.8	4.4	−18.4	−18.4	−17.0
t_{a2}	−9.7	−9.7	−6.0	38.3	38.3	44.0
t_{a3}	0.4	—	0.3	−0.5	—	−0.3
t_{a1+a2}	−9.9	−9.9	−10.5	−5.1	−5.1	−17.0
t_{a3-a1}	0.0	—		0.0		
t_{a2+a3}	−12.2	−12.2	−14.2	−1.3	−1.3	−1.6
$t_{a2+a3-a1}$	−5.2	—	2.9	−1.0		−1.5
$t_{2\cdot a1+a2}$	−0.1	—		−0.4	—	
$t_{2\cdot a1-a3}$	0.0	—		0.1	—	
$t_{2\cdot a1}$	2.0	—		−13.2	—	
$t_{a1+a2+a3}$	3.3	—		−0.9	—	
$t_{a2\cdot a1}$	−0.6	—		1.3	—	
$t_{2\cdot a2}$	0.5	—		0.0	—	
$t_{3\cdot a1}$	1.5	—		−0.4	—	
RMSE	3.2	13.7		1.9	26.7	

change the nature of the molecule, driving it toward a more conjugated structure with the H atoms "shared" between neighboring N and O atoms.[5] The reason why the impact of this effect is much stronger for the CB than for the VB is not fully understood. It is most likely related to the different shapes of the involved dimer orbitals (for further details see Supporting Information). Deviations in the $\mathbf{a}_2$ direction are attributed to the same effect, as the $\mathbf{a}_2$ direction is only somewhat inclined relative to $\mathbf{a}_1+\mathbf{a}_2$.

Another possible reason for deviations between dimer simulations and full band structure calculations in the $\mathbf{a}_1+\mathbf{a}_2$ direction becomes apparent when decomposing the conduction band into its individual TB components. The outcome is shown in **Figure 4**, where, quite unexpectedly, the main contribution to the band dispersion in the $\mathbf{a}_1+\mathbf{a}_2$ direction does not stem from t_{a1+a2} but rather from t_{a2}. To understand that, one has to realize that the $\mathbf{a}_2$ vector has a sizable component in the $\mathbf{a}_1+\mathbf{a}_2$ direction. Consequently, the scalar product $\mathbf{k}\cdot\mathbf{R}_j$ from Equation (2) is significant also, when $\mathbf{R}_j = \mathbf{a}_2$ and $\mathbf{k}$ is parallel to $\mathbf{a}_1+\mathbf{a}_2$. Therefore, for the conduction band, where t_{a2} is much larger than t_{a1+a2} (which is also true when considering the LUMO/LUMO+1 splitting of the respective dimers) the band structure in the H-bonding direction is dominated by the diagonal electronic coupling via t_{a2}. Another interesting aspect is that for the conduction band, t_{a2} and t_{a1+a2} have different signs. Consequently, their superposition reduces the band dispersion in the $\mathbf{a}_1+\mathbf{a}_2$ direction (see Figure 4). Therefore, while the combination of the two couplings provides additional transport pathways for incoherent hopping, for band transport it increases the effective mass and, therefore, is detrimental for charge transport.

The previous analysis of the conduction band in $\mathbf{a}_1+\mathbf{a}_2$ direction was triggered by differences between TB and dimer results. Alternatively, it can also happen that the two methods give the same transfer integrals between neighboring molecules and still the description of the material is incomplete when only interactions between dimers are considered. This is, for example, the case for the conduction band along the $\mathbf{a}_1$ path (i.e., in π-stacking direction). There, TB and dimer values for t_{a1} agree nicely, but already the large deviation between BW and ΔE_{BZ} (Figure 3) suggests that the shape of the band strongly deviates from a single cosine. This implies that more than one intermolecular electronic coupling is important, an assessment which is confirmed by a decomposition into tight-binding components (see **Figure 5**). Considering only the t_{a1} component yields the expected cosine-shaped band with a far too large energetic difference between the states at the Γ-point and the BZ boundary. Moreover, it completely misses the aspect that in the DFT calculations the band maximum in the π-stacking direction is approximately half-way between Γ and the BZ boundary. The latter suggests that a second component with a twice as high frequency must be added to the t_{a1} component to reasonably reproduce the band shape. This can be realized considering also the coupling to the next nearest neighbor at $2\cdot\mathbf{a}_1$, where indeed a sizable value for $t_{2\cdot a1}$ is found for the conduction band (see Table 1). This raises the question concerning the physical origin of that next-nearest neighbor coupling. Direct coupling can be ruled out, as we calculate a vanishingly small transfer integral for a dimer consisting of the original molecule and the next nearest neighbor molecule alone (also when including the basis functions associated with the molecule in between). Therefore, we attribute the comparably large value

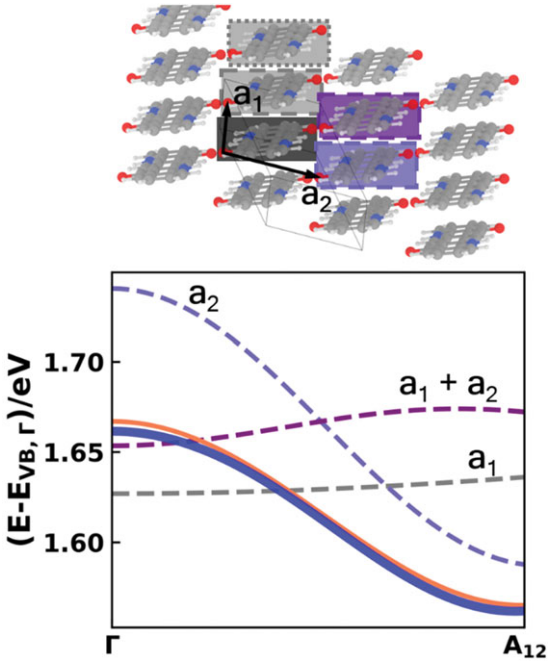

Figure 4. Conduction band and main tight-binding components along a path parallel to the H-bonding direction ($\mathbf{a}_1$+$\mathbf{a}_2$). A_{12} denotes the Brillouin-zone boundary in that direction. The DFT data are shown as a thick blue solid line. All other lines show contributions evaluated from the TB model. The individual contributions are shown in purple for t_{a1+a2}, slate blue for t_{a2}, and gray for t_{a1}. The sum of these contributions is shown by the orange solid line, which is already almost perfectly on top of the DFT data. The top panel shows the crystal structure with the relevant molecules highlighted using the same color code as for the band components. The area around the central molecule is highlighted in dark gray.

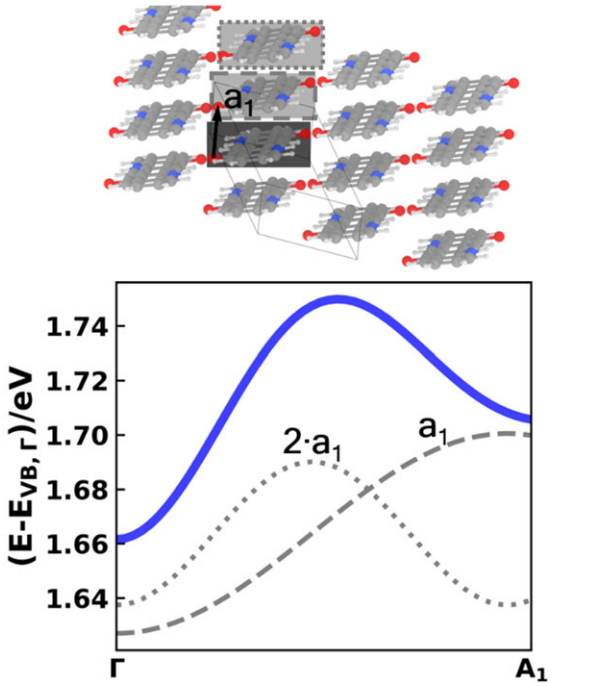

Figure 5. Conduction band and main tight-binding components along a path parallel to the π-stacking direction $\mathbf{a}_1$. A_1 denotes the Brillouin-zone boundary in that direction. The DFT data are shown as blue solid line. All other lines show contributions evaluated from the TB model: dashed gray line for t_{a1} and dotted gray line for t_{2a1}. The top panel shows the crystal structure with the relevant molecules highlighted using an equivalent color code.

of $t_{2\cdot a1}$ to a coupling between next-nearest neighbors mediated by the molecule in between.[44,48–50] Notably, such effects will only be captured when analyzing the full band structure of the system in question.

The last direction we examine in detail is $\mathbf{a}_3$. Here TB and dimer transfer integrals agree and also ΔE_{BZ} and BW are the same. Thus, one might expect that for this direction the simple model considering only t_{a3} should provide reliable results. An inspection of Table 1, however, shows that t_{a3} is negligibly small, implying a vanishing bandwidth along a path parallel to $\mathbf{a}_3$ (see dotted line in **Figure 6**). This is, however, not the case when calculating the full band structure (solid red line in Figure 6).

The explanation for this seeming contradiction is again the appearance of diagonal couplings. The situation is particularly complex here, as several neighboring molecules are at distances only slightly larger than $\mathbf{a}_3$ (namely the molecules at $\mathbf{a}_2$+$\mathbf{a}_3$, $\mathbf{a}_2$+$\mathbf{a}_3$-$\mathbf{a}_1$, and $\mathbf{a}_2$+$\mathbf{a}_3$+$\mathbf{a}_1$; see top panel in Figure 6). In fact, when considering the distances between nearby atoms rather than the distances between molecular centers, for some of these neighbors one might even expect electronic couplings larger than t_{a3}. This is indeed the case (see Table 1), and consequently, the diagonal coupling contributions t_{a2+a3}, $t_{a2+a3-a1}$, and $t_{a2+a3+a1}$ dominate the band dispersion in the $\mathbf{a}_3$ direction (see Figure 6). At this stage, one might argue that transport in $\mathbf{a}_3$ direction is only of minor relevance, considering the small associated bandwidth (6 meV). This assessment, however, misses the fact that large intermolecular distances increase hopping mobilities, as will be discussed in the next section.

5. Implications for Hopping Transport

Even for "benign" bands, one must keep in mind that for transport the distance between neighboring molecular sites in a specific direction plays an equally important role as the transfer integrals. For the case of hopping transport, this follows from the diffusion coefficient (for a 1D system) being proportional to $(t_{R_j} \cdot |\boldsymbol{R}_j|)^2$.[6,9,38] The latter quantity in the following will be referred to as diffusion parameter, d_{R_j}. Like in the tight-binding ansatz in Equation (2), for a material with only one molecule in the unit cell, the intermolecular center to center distances, $\mathbf{R}_j$, can be expressed as linear combinations of the lattice vectors. In this way, they directly reflect the periodicity of the crystal as they are the distances between all lattice sites. The expression for the diffusion parameter implies that to maximize hopping rates, one needs to maximize transfer integrals especially in directions of large inter-site distances.

Our test system, α-quinacridone, is triclinic[45] with unit cell vectors of significantly different lengths (a combination often observed for semiconductor crystals). Therefore, considering intermolecular distances is crucial for assessing transport anisotropies. Consequently, in **Table 2**, we summarize the

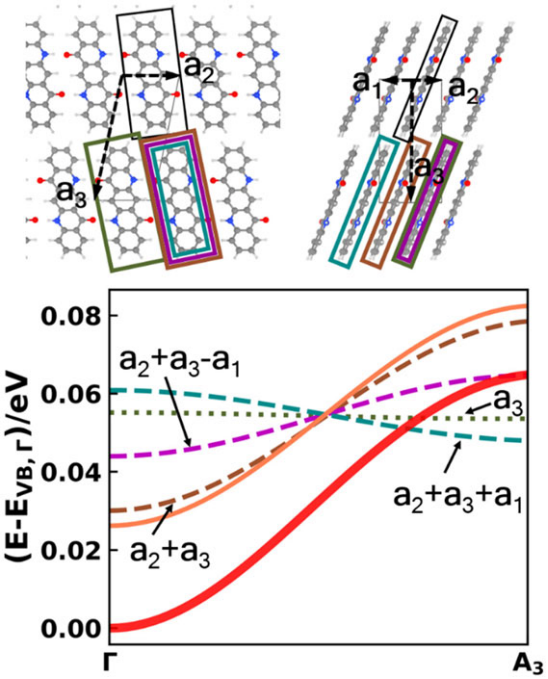

Figure 6. Valence band in $\mathbf{a}_3$ direction. The DFT data are displayed in red. The green dotted line shows the contribution from t_{a3}, the sienna colored line that from t_{a2+a3}, and the violet and cyan lines those from $t_{a2+a3-a1}$ and $t_{a2+a3+a1}$. The sum of the latter three contributions is shown by an orange line. The top panel shows the crystal structure with the relevant molecules highlighted using an equivalent color code.

Table 2. Comparison of diffusion parameters $d_{Rj} = (t_{Rj} \cdot |\mathrm{R}_j|)^2$ and transfer integrals for electrons and holes, obtained by fitting a TB model to the electronic band structure.

Directions		Holes		Electrons	
$\mathbf{R}_j$	$\lvert\mathbf{R}_j\rvert$ [Å]	d_{Rj} 10^{-3}·[eV·Å]^2	t_{Rj} [meV]	d_{Rj} 10^{-3}·[eV·Å]^2	t_{Rj} [meV]
a_1	3.80	0.3	4.8	4.9	−18.4
a_2	6.61	4.1	−9.7	64.1	38.3
a_3	14.49	0.0	0.4	0.1	−0.5
a_1+a_2	6.90	4.7	−9.9	1.2	−5.1
a_2+a_3	14.77	32.5	−12.2	0.4	−1.3

corresponding diffusion parameters for the directions of dominant transfer integrals. This finally allows us to judge the anisotropy of charge transport in α-quinacridone when a hopping mechanism dominates.

Analyzing the diffusion parameters for holes, one observes an anisotropy that is much more pronounced than for the transfer integrals. This is in part related to the fact that the diffusion parameters are proportional to ${t_{Rj}}^2$. The main reason is, however, that the square of the intermolecular distance also enters into the expression of d_{Rj}. This, for a given transfer integral, improves charge transport in directions in which nearest neighbor distances are particularly large. As a consequence, the diffusion rates to neighboring molecules in the $\mathbf{a}_2+\mathbf{a}_3$ direction are nearly an order of magnitude larger than in any other direction. Conversely, for the π-stacking direction ($\mathbf{a}_1$), characterized by the smallest intermolecular distance, the diffusion parameter becomes particularly small.

For the same reason, electron transport in the π-stacking direction becomes inefficient, in this case despite the comparably large transfer integral t_{a1}. In contrast to the situation for hole transport, the dominant diffusion parameter for electrons is found close to the H-bonding direction along $\mathbf{a}_2$. Here, the reason for the large value of d_{a2} is the rather high associated transfer integral. This means that in α-quinacridone transport is not only highly anisotropic but even the preferred transport directions for electrons and holes are different.

6. Effective Mass and Band Transport

When considering band instead of hopping transport (e.g., at low temperatures), a further complication arises from the observation that the band extrema do not occur at the Γ-point but rather at Y (for the valence band) and at E_2 (for the conduction band; see Figure 2). Thus, an analysis of the bands in the high-symmetry directions as in Section 3 provides only limited insight into the actual transport properties of α-quinacridone. Considering that the tight-binding fit provides an analytical expression for the entire band structure, it is however straightforward to directly calculate effective mass tensors, $\mathbf{m}^*$, at any point in reciprocal space. In the following, we will focus on the "diagonal terms" of $\mathbf{m}^*$. These are obtained from the inverse of the second derivative of the energy with respect to $\mathbf{k}$ in a specific direction $\vec{d}$ according to Equation (3).

$$\left(m^*_{\vec{d}}\right)^{-1} = \vec{d}^{\,T} \cdot \left[\frac{\partial^2 E(\boldsymbol{k})}{\partial k_i \partial k_j}\right]_{i,j\ \epsilon[x,y,z]} \cdot \vec{d} \tag{3}$$

The diagonal terms of $\mathbf{m}^*$ link carrier flow in a specific direction with the electric field acting in the same direction. They are the most relevant components of $\mathbf{m}^*$, considering common device architectures. The values obtained at the extrema of the frontier bands projected onto a sphere are shown in **Figure 7**a,b.

At the valence band maximum (Y), we find the smallest effective mass in $\mathbf{a}_2+\mathbf{a}_3$ direction, which is perfectly in line with the observations made for the transfer integrals and the diffusion parameters (see Table 2). Interestingly, around the $\mathbf{a}_2+\mathbf{a}_3$ direction, there is quite a large region showing comparable values of m^*. This suggests that hole transport in α-quinacridone is reasonably efficient, provided that it occurs in directions close to parallel to the long molecular axes. The highest effective masses are found close to the $\mathbf{a}_1$ direction implying particularly poor hole transport in the π-stacking direction consistent with the relatively small value of t_{a1} (Table 1) and the comparably even smaller one for $(t_{a1} \cdot |\boldsymbol{a}_1|)^2$ (Table 2). For the sake of comparison, we also calculated $\mathbf{m}^*$ at the Γ point. Interestingly, the $\mathbf{a}_2+\mathbf{a}_3$ direction is still the one associated with the lowest absolute value of the effective mass (see Figure 7c,d). As the Γ point is not a band extremum, the sign of m^* in that direction is, however, positive rather than negative (see Figure 7e,f). Moreover, m^* diverges where the sign of m^* changes (i.e., for directions in which the deep blue and deep red regions in Figure 7e,f meet). Both aspects suggest that the effective mass at the Γ point and, therefore, also all other quantities

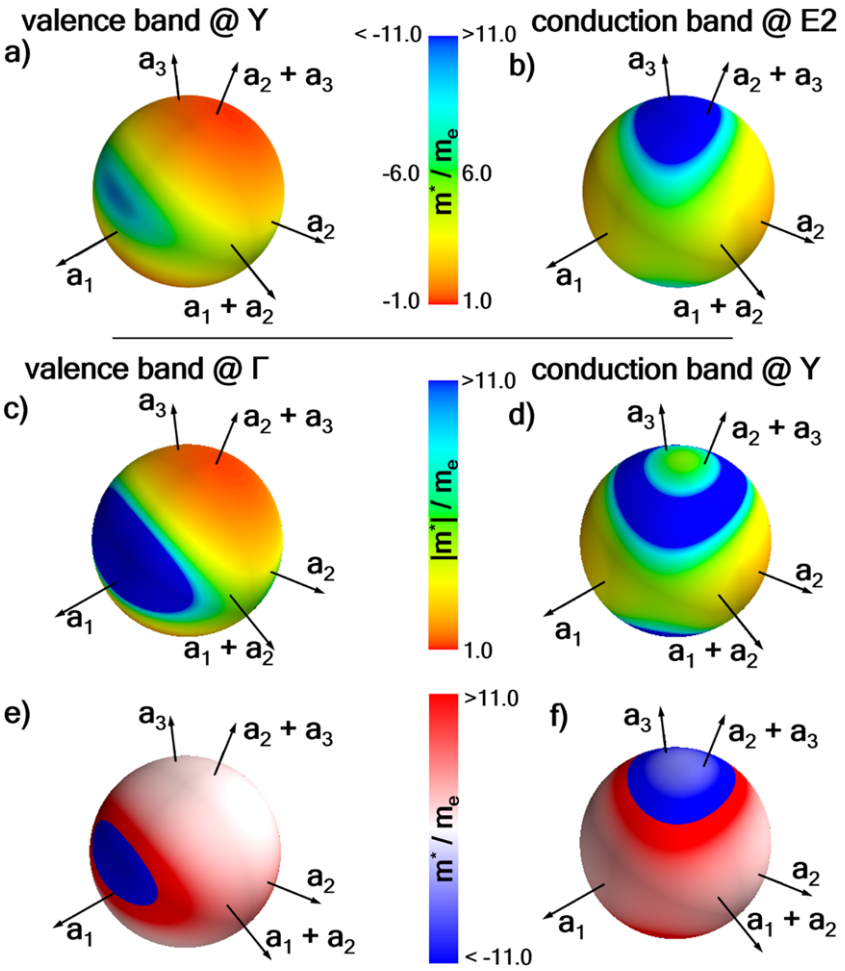

Figure 7. Effective mass m^* of VB and CB evaluated at the respective band extrema (top panels). Additionally, for the VB, m^* is also evaluated at the Γ point (central and bottom left panels) and for the CB at a k-point that is within kT from the minimum (i.e., at Y, central and bottom right panels). The two central panels contain absolute values of m^*, while in the other panels the sign of the effective electron mass is considered (note that a negative effective electron mass means a positive effective hole mass).

derived from paths originating at the Γ point contain quite misleading information regarding band transport in α-quinacridone.

For the conduction band with its minimum at E_2, we find particularly large effective masses for directions close to $\mathbf{a}_3$ and $\mathbf{a}_2+\mathbf{a}_3$, in sharp contrast to the situation for the valence band. The smallest effective mass for the CB is found in direction $\mathbf{a}_2$, consistent with the particularly large transfer integral in that direction. This suggests that electron transport is most efficient in directions close to the short molecular axis and the H-bonding direction ($\mathbf{a}_1+\mathbf{a}_2$). Thus, also for band transport, the preferred transport directions for α-quinacridone are fundamentally different for electrons and holes.

As the bands in organic semiconductors are comparably flat, the question arises whether the effective mass tensor changes significantly for other thermally accessible states. For the conduction band, we tested that for the Y point, which is only 5 meV above the E_2 point. There, the absolute value of m^* becomes intermediate around directions $\mathbf{a}_3$ and $\mathbf{a}_2+\mathbf{a}_3$. At the same time, the sign of m^* changes in that region (not surprisingly, as the Y point is not a minimum of the conduction band). This suggests that merely considering a single effective mass for electrons and holes for each direction is not necessarily sufficient for modeling band transport in organic semiconductors. In such cases, for obtaining a semi-classical description of charge transport properties within the band picture, it becomes inevitable to consider the full band structure. From the tight-binding fits, this quantity is readily available as an analytical function through Equation (2).

7. Conclusions

The current paper provides a comparison of commonly applied approaches for analyzing the electronic coupling in organic semiconductor crystals. This is done for the instructive example of α-quinacridone. Our study reveals shortcomings of merely considering bandwidths or transfer integrals, when the latter are based on dimer simulations. While both approaches provide certain basic insights regarding the anisotropy of the electronic coupling in molecular crystals, an analysis of bandwidths fails when dealing with comparably complex band structures. A

complication of dimer simulations (beyond the well-known issues for non-centrosymmetric structures)[32] is that they neglect the actual 3D crystalline environment. This becomes particularly problematic for the class of H-bonded chromophores. They also neglect next-nearest neighbor coupling effects mediated by a bridge molecule. Moreover, transport in specific directions can be dominated by diagonal coupling elements, and in certain directions, coupling to a sizable number of close-lying neighbors can become relevant. Finally, in situations dominated by band-transport, further complications can arise from band extrema being located neither at the Γ point nor at the Brillouin zone boundary. To overcome these problems, we recommend a fitting of the full band structure by tight-binding models considering a number of neighboring molecules, which is sufficient for mimicking the actual band structure of the crystal. This allows a straightforward extraction of transfer integrals that can be employed in hopping and dynamic disorder models. It also provides an accurate analytical expression for the band structure. The latter, for example, allows the straightforward calculation of parameters relevant for band transport (like effective masses and group velocities) at any point in reciprocal space without any numerical effort.

8. Experimental Section

For all calculations relying on periodic boundary conditions, dispersion-corrected density-functional theory (DFT) was used as implemented in VASP 5.3.3.[51–54] The exchange-correlation part was treated employing the PBE[46,47] functional in combination with the Tkatchenko–Scheffler (TS) dispersion correction method[55] to account for long-range van der Waals interactions. Furthermore, the electronic band structure of the α-polymorph was also calculated using the HSE06[56,57] functional and compared to the PBE results. This comparison was triggered by the study of Lüftner et al.,[58] who showed that for obtaining a correct ordering of the molecular orbitals of quinacridone, a proper treatment of exchange interactions is important. As far as the frontier bands are concerned, no fundamental differences between PBE and HSE06 (see Supporting Information) were observed. The recommended PAW[59] potentials (details in Supporting Information) together with a plane-wave cut-off energy of 700 eV were used for all calculations. In the self-consistent-field (SCF) procedure, the Brillouin zone was sampled in two independent steps: i) using a $32 \times 20 \times 8$ Γ-centered *k*-point grid (the charge density resulting from this calculation was also used to non-self consistently calculate the band structures in the high-symmetry directions) and ii) using a $32 \times 20 \times 8$ *k*-grid, which was shifted by a vector of (0.5, 0.5, 0.5) times the reciprocal lattice vectors. The eigenvalues obtained by these two calculations were then combined in order to densely sample the Brillouin zone. An option for larger systems would be to perform the SCF calculation for a smaller grid and then to calculate the eigenvalues to sample the Brillouin zone with a more dense grid in a non-self-consistent manner using the previously obtained charge density. This strategy was tested using a smaller $16 \times 10 \times 4$ *k*-grid in the SCF procedure, obtaining essentially the same eigenstates (for all considered *k*-points) and electronic couplings as for the full calculations. To describe the occupation of the electronic states, the Methfessel–Paxton[60] occupation scheme with a width of 0.1 eV was used. The relaxed geometry of the test system was obtained by taking the crystal structure of α-quinacridone from literature[45] and relaxing the atomic positions until the largest force component on the atoms was smaller than 0.01 eV $Å^{-1}$, while keeping the unit cell vectors fixed.

For the quinacridone dimers, which have been extracted from the relaxed crystal structure, orbital energies were obtained by performing single-point calculations using the Gaussian 09 program package[61] in combination with the PBE functional and a 6-311++G(d,p) basis set. The transfer integrals t were obtained from the orbital energies applying the ESD method.[6] The sign of the transfer integrals was determined depending on whether the bonding (positive) or antibonding (negative) linear combination of the molecular orbitals was higher in energy.

To ensure the stability of the tight-binding fits, various algorithms were tested, like conjugate-gradient, least-squares (Levenberg–Marquardt), Powell, and Nelder–Mead, all as implemented in the LMFIT[62] package for Python. Furthermore, the fitting procedure was started with randomly initialized starting guesses for the transfer integrals ranging between 0 and 5 meV. In all cases the same minimum was found regardless of the algorithm and the initial guesses.

Additionally, the stability of the fit was tested as a function of the number of *k*-points for a fixed number of transfer integrals (fit parameters). To do that, a subset of *k*-points from the high-density grid was randomly chosen and the fit was performed on these points. The fit turned out to be stable (changes of the RMSE well below 1 meV) for a *k*-grid containing only 100 points, provided that the *k*-points were homogeneously distributed in *k*-space. Here, it is, however, important to keep in mind that such results depend on the investigated material, as the minimum grid density depends on the highest-frequency component contained in the Fourier decomposition of the bands; that is, one needs to make sure that the sampling rate is such that none of the actually occurring frequency components of the band structure is above the Nyquist frequency.[63]

The crystal structures were visualized using Ovito[64] and the electronic band structures were plotted using the Python libraries NumPy[65] and Matplotlib.

Supporting Information

Supporting Information is available from the Wiley Online Library or from the author.

Acknowledgements

The authors are grateful to Oliver T. Hofmann for stimulating discussions. The work was financially supported by the TU Graz Lead Project "Porous Materials at Work" (LP-03). The computational results have been in part achieved using the Vienna Scientific Cluster (VSC3).

Conflict of Interest

The authors declare no conflict of interest.

Keywords

electronic coupling, organic semiconductors, tight-binding, transfer integrals

Received: December 21, 2018
Revised: February 8, 2019
Published online: March 28, 2019

[1] A. Mishra, P. Bäuerle, *Angew. Chem., Int. Ed.* **2012**, *51*, 2020.
[2] S. E. Root, S. Savagatrup, A. D. Printz, D. Rodriquez, D. J. Lipomi, *Chem. Rev.* **2017**, *117*, 6467.
[3] E. D. Głowacki, M. Irimia-Vladu, S. Bauer, N. S. Sariciftci, *J. Mater. Chem. B* **2013**, *1*, 3742.
[4] E. D. Głowacki, L. Leonat, M. Irimia-vladu, R. Schwödiauer, M. Ullah, H. Sitter, S. Bauer, N. S. Sariciftci, *Appl. Phys. Lett.* **2012**, *101*, 0233051.

[5] E. D. Głowacki, M. Irimia-Vladu, M. Kaltenbrunner, J. Gsiorowski, M. S. White, U. Monkowius, G. Romanazzi, G. P. Suranna, P. Mastrorilli, T. Sekitani, S. Bauer, T. Someya, L. Torsi, N. S. Sariciftci, *Adv. Mater.* **2013**, *25*, 1563.
[6] V. Coropceanu, J. Cornil, D. A. da Silva Filho, Y. Olivier, R. Silbey, J. L. Brédas, *Chem. Rev.* **2007**, *107*, 926.
[7] H. Oberhofer, K. Reuter, J. Blumberger, *Chem. Rev.* **2017**, *117*, 10319.
[8] N. Tessler, Y. Preezant, N. Rappaport, Y. Roichman, *Adv. Mater.* **2009**, *21*, 2741.
[9] S. Fratini, D. Mayou, S. Ciuchi, *Adv. Funct. Mater.* **2016**, *26*, 2292.
[10] K. Hannewald, V. M. Stojanović, J. M. T. Schellekens, P. A. Bobbert, G. Kresse, J. Hafner, *Phys. Rev. B* **2004**, *69*, 075211.
[11] F. Ortmann, K. Hannewald, F. Bechstedt, *Appl. Phys. Lett.* **2008**, *93*, 222105.
[12] F. Ortmann, K. Hannewald, F. Bechstedt, *J. Phys. Chem. B* **2009**, *113*, 7367.
[13] A. Troisi, G. Orlandi, *Phys. Rev. Lett.* **2006**, *96*, 086601.
[14] S. Ciuchi, S. Fratini, D. Mayou, *Phys. Rev. B* **2011**, *83*, 081202.
[15] S. Fratini, S. Ciuchi, *Phys. Rev. Lett.* **2009**, *103*, 266601.
[16] Y.-C. Cheng, R. J. Silbey, *J. Chem. Phys.* **2008**, *128*, 114713.
[17] F. Ortmann, F. Bechstedt, K. Hannewald, *Phys. Rev. B* **2009**, *79*, 235206.
[18] S. Fratini, S. Ciuchi, D. Mayou, G. T. De Laissardière, A. Troisi, *Nat. Mater.* **2017**, *16*, 998.
[19] R. A. Marcus, *Rev. Mod. Phys.* **1993**, *65*, 599.
[20] C. Kittel, *Introduction to Solid State Physics*, John Wiley & Sons, New York **2004**.
[21] L. Zhu, Y. Yi, Y. Li, E. G. Kim, V. Coropceanu, J. L. Brédas, *J. Am. Chem. Soc.* **2012**, *134*, 2340.
[22] K. Hummer, C. Ambrosch-Draxl, *Phys. Rev. B* **2005**, *72*, 205205.
[23] L. A. Stevens, K. P. Goetz, A. Fonari, Y. Shu, R. M. Williamson, J. L. Brédas, V. Coropceanu, O. D. Jurchescu, G. E. Collis, *Chem. Mater.* **2015**, *27*, 112.
[24] G. A. De Wijs, C. C. Mattheus, R. A. De Groot, T. T. M. Palstra, *Synth. Met.* **2003**, *139*, 109.
[25] K. Doi, K. Yoshida, H. Nakano, A. Tachibana, T. Tanabe, Y. Kojima, K. Okazaki, T. Tabata, Y. Kojima, K. Okazaki, *J. Appl. Phys.* **2005**, *98*, 113709.
[26] Y. Li, V. Coropceanu, J. L. Brédas, *J. Phys. Chem. Lett.* **2012**, *3*, 3325.
[27] L.-F. Ji, J.-X. Fan, S.-F. Zhang, A.-M. Ren, *Phys. Chem. Chem. Phys.* **2017**, *19*, 13978.
[28] H. Y. Chen, G. Schweicher, M. Planells, S. M. Ryno, K. Broch, A. J. P. White, D. Simatos, M. Little, C. Jellett, S. J. Cryer, A. Marks, M. Hurhangee, J. L. Brédas, H. Sirringhaus, I. McCulloch, *Chem. Mater.* **2018**, *30*, 7587.
[29] H.-Z. Gao, *Int. J. Quantum Chem.* **2012**, *112*, 740.
[30] O. Kwon, V. Coropceanu, N. E. Gruhn, J. C. Durivage, J. G. Laquindanum, H. E. Katz, J. Cornil, J. L. Brédas, *J. Chem. Phys.* **2004**, *120*, 8186.
[31] S. H. Wen, A. Li, J. Song, W. Q. Deng, K. L. Han, W. A. Goddard, *J. Phys. Chem. B* **2009**, *113*, 8813.
[32] E. F. Valeev, V. Coropceanu, D. A. Da Silva Filho, S. Salman, J. L. Brédas, *J. Am. Chem. Soc.* **2006**, *128*, 9882.
[33] J. L. Bredas, J. P. Calbert, D. A. da Silva Filho, J. Cornil, *Proc. Natl. Acad. Sci. U. S. A.* **2002**, *99*, 5804.
[34] V. Lemaur, D. A. Da Silva Filho, V. Coropceanu, M. Lehmann, Y. Geerts, J. Piris, M. G. Debije, A. M. Van De Craats, K. Senthilkumar, L. D. A. Siebbeles, J. M. Warman, J. L. Brédas, J. Cornil, *J. Am. Chem. Soc.* **2004**, *126*, 3271.
[35] D. A. da Silva Filho, E.-G. Kim, J.-L. Brédas, *Adv. Mater.* **2005**, *17*, 1072.
[36] H. Kobayashi, N. Kobayashi, S. Hosoi, N. Koshitani, D. Murakami, R. Shirasawa, Y. Kudo, D. Hobara, Y. Tokita, M. Itabashi, *J. Chem. Phys.* **2013**, *139*, 014707.
[37] Y. Olivier, V. Lemaur, J. L. Brédas, J. Cornil, *J. Phys. Chem. A* **2006**, *110*, 6356.
[38] V. Rühle, A. Lukyanov, F. May, M. Schrader, T. Vehoff, J. Kirkpatrick, B. Baumeier, D. Andrienko, *J. Chem. Theory Comput.* **2011**, *7*, 3335.
[39] Y. Olivier, L. Muccioli, V. Lemaur, Y. H. Geerts, C. Zannoni, J. Cornil, *J. Phys. Chem. B* **2009**, *113*, 14102.
[40] J. J. Kwiatkowski, J. Nelson, H. Li, J. L. Bredas, W. Wenzel, C. Lennartz, *Phys. Chem. Chem. Phys.* **2008**, *10*, 1852.
[41] J. Nelson, J. J. Kwiatkowski, J. Kirkpatrick, J. M. Frost, *Acc. Chem. Res.* **2009**, *42*, 1768.
[42] A. Troisi, G. Orlandi, *J. Phys. Chem. B* **2005**, *109*, 1849.
[43] Y. C. Cheng, R. J. Silbey, D. A. Da Silva Filho, J. P. Calbert, J. Cornil, J. L. Brédas, *J. Chem. Phys.* **2003**, *118*, 3764.
[44] O. K. Volkhard May, *Charge and Energy Transfer Dynamics in Molecular Systems*, Wiley-VCH, Weinheim **2011**.
[45] E. F. Paulus, F. J. J. Leusen, M. U. Schmidt, *CrystEngComm* **2007**, *9*, 131.
[46] J. P. Perdew, K. Burke, M. Ernzerhof, *Phys. Rev. Lett.* **1996**, *77*, 3865.
[47] J. P. Perdew, K. Burke, M. Ernzerhof, *Phys. Rev. Lett.* **1997**, *78*, 1396.
[48] W. B. Davis, W. A. Svec, M. A. Ratner, M. R. Wasielewski, *Nature* **1998**, *396*, 60.
[49] E. G. Petrovt, V. May, *J. Phys. Chem. A* **2001**, *105*, 10176.
[50] J. J. Hopfield, J. N. Onuchic, D. N. Beratan, *J. Phys. Chem.* **1989**, *93*, 6350.
[51] G. Kresse, J. Hafner, *Phys. Rev. B* **1993**, *47*, 558.
[52] G. Kresse, J. Hafner, *Phys. Rev. B* **1994**, *49*, 14251.
[53] G. Kresse, J. Furthmüller, *Comput. Mater. Sci.* **1996**, *6*, 15.
[54] G. Kresse, J. Furthmüller, *Phys. Rev. B* **1996**, *54*, 11169.
[55] A. Tkatchenko, M. Scheffler, *Phys. Rev. Lett.* **2009**, *102*, 073005.
[56] J. Heyd, G. E. Scuseria, M. Ernzerhof, *J. Chem. Phys.* **2003**, *118*, 8207.
[57] J. Heyd, G. E. Scuseria, M. Ernzerhof, *J. Chem. Phys.* **2006**, *124*, 219906.
[58] D. Lüftner, S. Refaely-Abramson, M. Pachler, R. Resel, M. G. Ramsey, L. Kronik, P. Puschnig, *Phys. Rev. B* **2014**, *90*, 075204.
[59] G. Kresse, D. Joubert, *Phys. Rev. B* **1999**, *59*, 1758.
[60] M. Methfessel, A. T. Paxton, *Phys. Rev. B* **1989**, *40*, 3616.
[61] M. J. Frisch, G. W. Trucks, H. B. Schlegel, G. E. Scuseria, M. A. Robb, J. R. Cheeseman, G. Scalmani, V. Barone, B. Mennucci, G. A. Petersson, H. Nakatsuji, M. Caricato, X. Li, H. P. Hratchian, A. F. Izmaylov, J. Bloino, G. Zheng, J. L. Sonnenberg, M. Hada, M. Ehara, K. Toyota, R. Fukuda, J. Hasegawa, M. Ishida, T. Nakajima, Y. Honda, O. Kitao, H. Nakai, T. Vreven, J. A. Montgomery Jr., et al., *Gaussian 09, Revision D.01*, Gaussian Inc., Wallingford, CT **2019**.
[62] M. Newville, T. Stensitzki, D. B. Allen, A. Ingargiola, *Zenodo* **2014**, https://org.doi.10.5281/zenodo.11813
[63] H. Cramér, U. Grenander, *Probability and Statistics: The Harald Cramér Volume* (Ed: U. Grenander), Almqvist & Wiksell, Stockholm**1959**.
[64] A. Stukowski, *Model. Simul. Mater. Sci. Eng.* **2010**, *18*, 015012.
[65] S. Van Der Walt, S. C. Colbert, G. Varoquaux, *Comput. Sci. Eng.* **2011**, *13*, 22.

2.3. Supporting Information

WILEY-VCH

Supporting Information for:

Analyzing the electronic coupling in molecular crystals - the instructive case of α-quinacridone

Christian Winkler, Florian Mayer, Egbert Zojer

Institute of Solid State Physics, NAWI Graz, Graz University of Technology, Petersgasse 16, 8010 Graz, Austria

1. Headers of the PAW potentials

Carbon: PAW_PBE C 08Apr2002

Hydrogen: PAW_PBE H 15Jun2001

Nitrogen: PAW_PBE N 08Apr2002

Oxygen: PAW_PBE O 08Apr2002

2. Comparison of the electronic band structures when using the PBE and the HSE06 functionals

When comparing the electronic band structure of the α-polymorph of quinacridone at the density functional theory level comparing the PBE[1,2] functional (semi-local GGA) and the HSE06[3,4] functional, we find the expected band-gap increase for HSE06. The shape of the bands, however, stays the same and the band width increases only slightly in HSE06 (see Figures S1, S2, and S3) one can find that the shape of the frontier bands, their band width and curvature shows no significant changes. Lüftner et al.[5] suggested a significant change in the orbital ordering for quinacridone for sufficient amounts of exact exchange. Therefore, we also compared orbital energies for single molecules and molecular dimers. The results can be found in Figure S4. We find that indeed the orbital ordering changes between the two functionals. The relative positions of the molecular frontier orbitals and their linear combinations are, however, not affected. Only the HOMO to HOMO-1 and LUMO to LUMO+1 splittings in the dimer case are slightly increased for HSE06.

To ensure that the character of the frontier orbitals and the electronic states in the frontier bands is the same, we also calculated the projected charge density of the respective bands (VB and CB) at the Γ-point at the PBE level (Figure S5). Comparing them to the molecular orbitals (Figure S5) we find that the VB (CB) corresponds to the HOMO (LUMO) and the VB-1 (CB+1) to the HOMO-1 (LUMO+1).

Based on all these tests we conclude that for the aspects studied in the paper, PBE and HSE06 yield the same results. Thus, we base them on the computationally far less costly PBE functional.

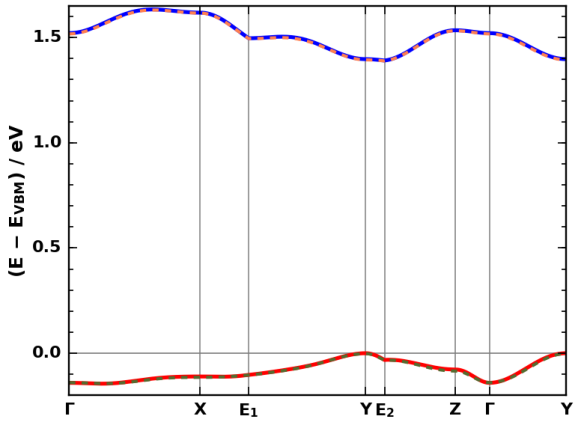

Figure S1. *Electronic band structure of the α-polymorph obtained by performing DFT calculations using the PBE functional. The dashed lines indicate the tight-binding fit which has been performed on the 3D data set and is here shown along the high-symmetry directions.*

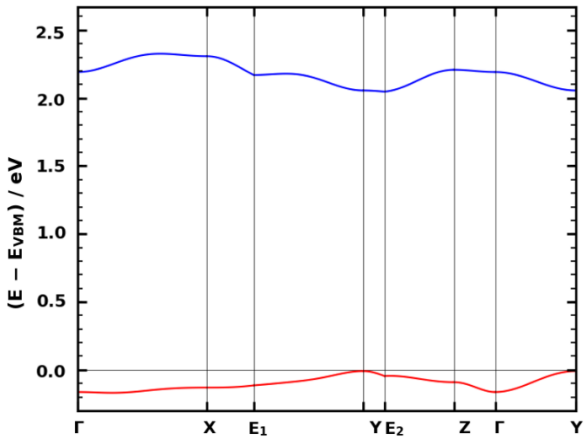

Figure S2. *Electronic band structure of the α-polymorph determined by applying the HSE06 functional.*

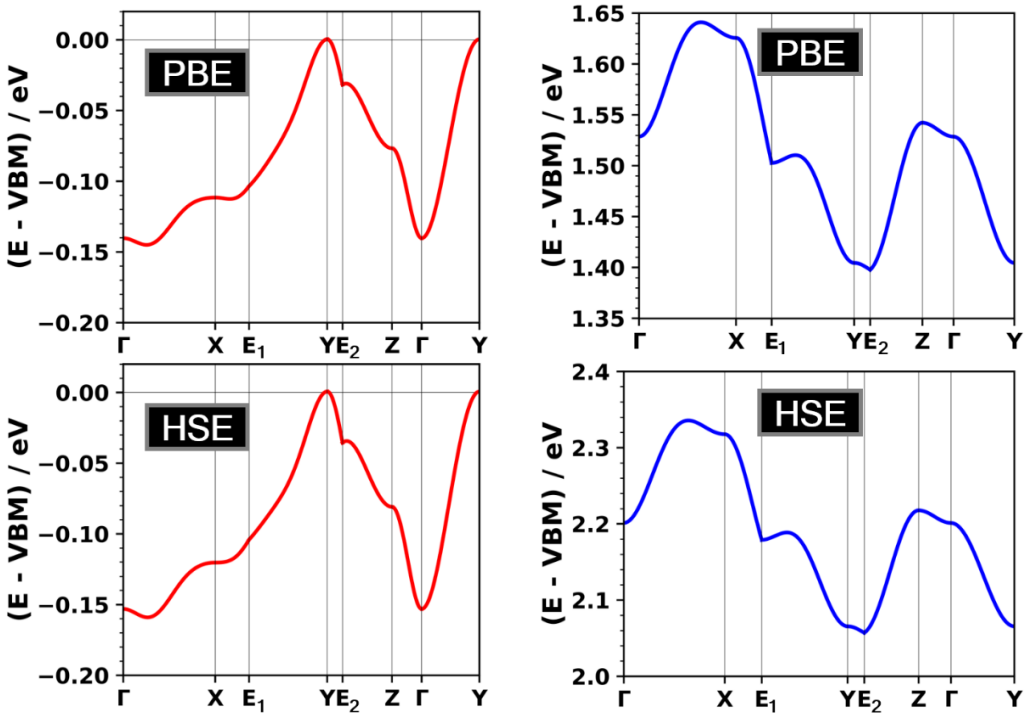

Figure S3. *Valence band (left) and conduction band (right) of α-quinacridone evaluated using PBE (top panels) and HSE06 functionals (bottom panels). The obtained results agree nicely with a minor increase of the band widths for HSE06.*

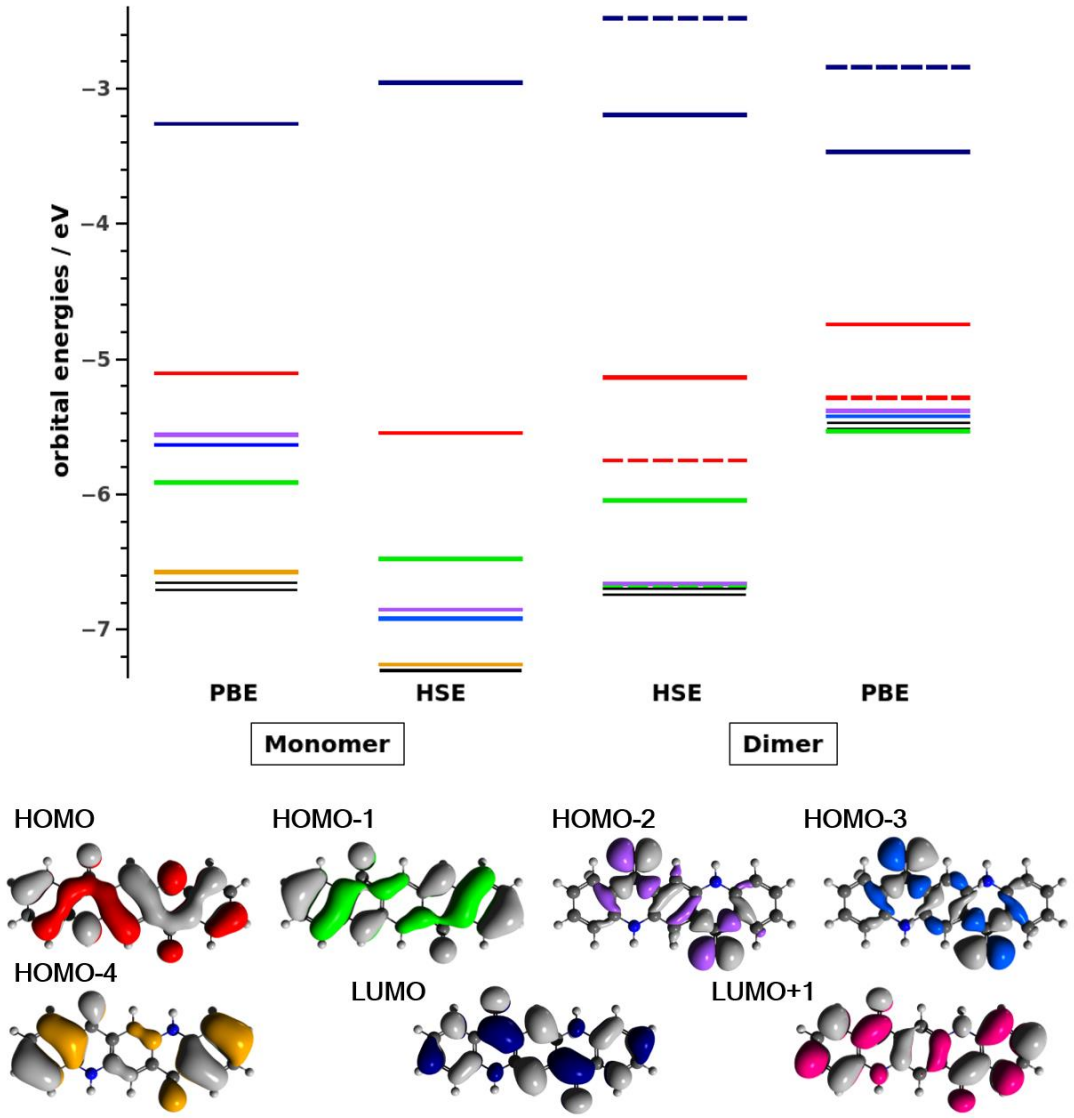

Figure S4. *Orbital energies of a single quinacridone molecule and a dimer calculated using PBE and HSE06 functionals. The orbitals shapes determined with the HSE06 functional are also shown using the same color code as for the orbital energies. In the dimer case, lines of the same color refer to related orbitals originating from bonding/antibonding linear combinations of the same molecular orbitals. Lower lying molecular orbitals of the monomer (HOMO-5 and below) are not color coded, they are shown in black whenever they are in the respective energy window, for completeness.*

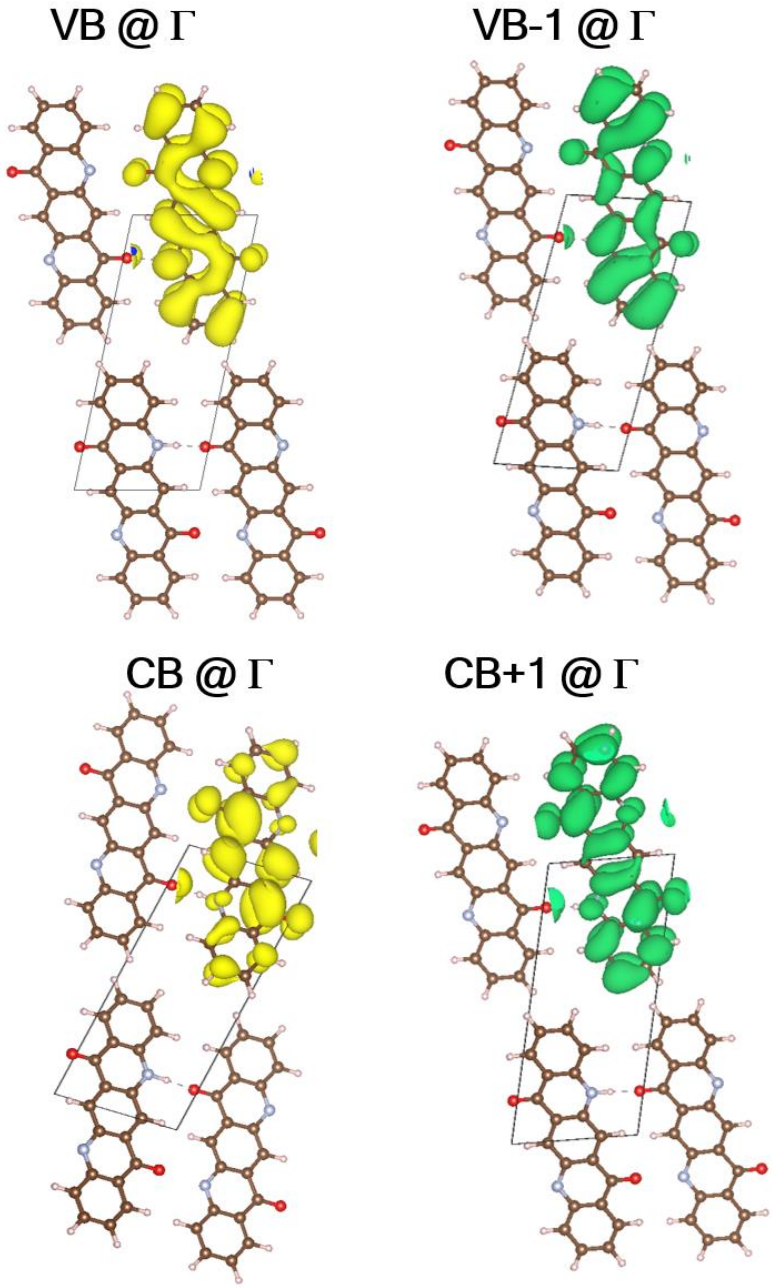

Figure S5. *Top: Partial charge density of the valence band (VB) and VB-1 at the Γ-point at a PBE level. Bottom: equivalent plot for the conduction band. For the sake of a better visibility the charge density is only shown for the one molecule in the unit cell.*

3. Stability of the tight-binding fit parameters

When comparing the obtained fit parameters (transfer integrals) for the full and the simplified model (shown in the main manuscript) one can observe that they are basically equal to each other within a sub meV spread. Here we rationalize this observation and show that this is an intrinsic property of a tight-binding model.

We start by reconsidering our tight-binding model function, which in principle is a multidimensional discrete Fourier decomposition of the energy E(**k**).

$$E(\boldsymbol{k}) = \varepsilon + \sum_{n \neq 0} e^{i\boldsymbol{k}\boldsymbol{R}_n} t_n = \sum_{n} e^{i\boldsymbol{k}\boldsymbol{R}_n} t_n$$

The right side of the equation has the form of a Fourier series with the transfer integrals t_n being the Fourier coefficients. For the sake of simplicity, we replace the above equation by its 1D equivalent. The Fourier coefficients can then be written as

$$t_R = \sum\nolimits_k E_k e^{ikR}$$

We see that each of these coefficients only depends on one specific distance R_j. All the other position vectors R_i for $i \neq j$ do not influence t_R. This is shown also explicitly for the simple case of a rectangular band structure in Figure S6. The above equation also shows that in order to get reliable results the series has to converge, which means that enough data points E_k need to be obtained from the DFT calculation.

In the main manuscript we show, how the tight-binding transfer integrals change for two different sets of considered neighboring molecules. A more detailed summary of the parameters upon increasing the number of neighboring molecules included in the fit is shown in Table S2.

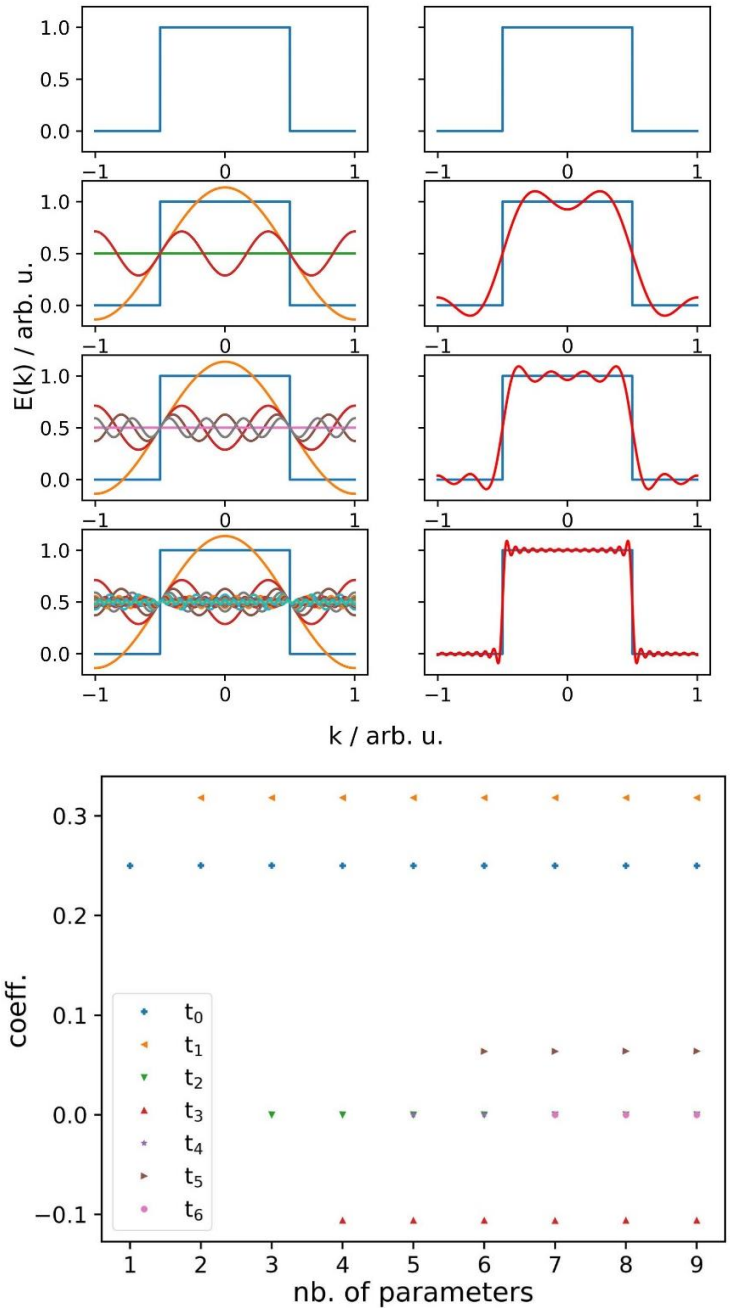

Figure S6. *Top: Fit of a rectangular band structure using our tight-binding model function. In the panels on the left one can see the original function (blue) together with the individual components of the fit. On the right the sum of the individual components is shown in red together with the original function in blue. Bottom: Evolution of the fit-parameters as a function of the number of parameters used during the fit routine.*

Table S1. *Values of the parameters (given in eV) when the model function is fitted to the DFT data of the α-phase of quinacridone. One can see that the parameters are basically unaffected by the introduction of new/additional parameters.*

# of parameters	1	2	3	4	5	6	7	8	9	10	11	12	13	14	15	16	17
χ^2 / eV	7.941241	5.999896	5.996694	3.989205	0.962418	0.962418	0.962386	0.962308	0.954439	0.737302	0.184896	0.184893	0.184891	0.184891	0.102683	0.098555	0.055273
RMSE / eV	0.038621	0.033570	0.033561	0.027373	0.013445	0.013445	0.013445	0.013444	0.013389	0.011768	0.005893	0.005893	0.005893	0.005893	0.004392	0.004303	0.003222
a1	0.004780	0.004780	0.004780	0.004780	0.004780	0.004780	0.004780	0.004780	0.004780	0.004780	0.004780	0.004780	0.004780	0.004780	0.004780	0.004780	0.004777
a1	0.004780	0.004780	0.004780	0.004780	0.004780	0.004780	0.004780	0.004780	0.004780	0.004780	0.004780	0.004780	0.004780	0.004780	0.004780	0.004780	0.004777
a2		-0.009729	-0.009729	-0.009729	-0.009729	-0.009729	-0.009729	-0.009729	-0.009729	-0.009729	-0.009729	-0.009729	-0.009729	-0.009729	-0.009729	-0.009729	-0.009729
a2		-0.009729	-0.009729	-0.009729	-0.009729	-0.009729	-0.009729	-0.009729	-0.009729	-0.009729	-0.009729	-0.009729	-0.009729	-0.009729	-0.009729	-0.009729	-0.009729
a3			0.000395	0.000395	0.000395	0.000395	0.000395	0.000395	0.000395	0.000395	0.000395	0.000395	0.000395	0.000395	0.000395	0.000395	0.000395
a3			0.000395	0.000395	0.000395	0.000395	0.000395	0.000395	0.000395	0.000395	0.000395	0.000395	0.000395	0.000395	0.000395	0.000395	0.000395
a1+a2				-0.009893	-0.009893	-0.009893	-0.009893	-0.009893	-0.009892	-0.009892	-0.009892	-0.009892	-0.009892	-0.009892	-0.009892	-0.009892	-0.009892
a1+a2				-0.009893	-0.009893	-0.009893	-0.009893	-0.009893	-0.009892	-0.009892	-0.009892	-0.009892	-0.009892	-0.009892	-0.009892	-0.009892	-0.009892
a2+a3					-0.012148	-0.012148	-0.012148	-0.012147	-0.012147	-0.012147	-0.012147	-0.012147	-0.012147	-0.012147	-0.012147	-0.012147	-0.012147
a2+a3					-0.012148	-0.012148	-0.012148	-0.012147	-0.012147	-0.012147	-0.012147	-0.012147	-0.012147	-0.012147	-0.012147	-0.012147	-0.012147
a1+a3						0.000004	0.000004	0.000004	0.000004	0.000004	0.000004	0.000004	0.000004	0.000004	0.000004	0.000004	0.000004
a1+a3						0.000005	0.000004	0.000005	0.000004	0.000005	0.000004	0.000004	0.000004	0.000004	0.000004	0.000004	0.000004
a1-a3							-0.000039	-0.000039	-0.000039	-0.000039	-0.000039	-0.000039	-0.000039	-0.000039	-0.000039	-0.000039	-0.000039
a1-a3							-0.000039	-0.000039	-0.000039	-0.000039	-0.000039	-0.000039	-0.000039	-0.000039	-0.000039	-0.000039	-0.000039
a2-a3								-0.000062	-0.000062	-0.000062	-0.000062	-0.000062	-0.000062	-0.000062	-0.000062	-0.000062	-0.000062
a2-a3								-0.000062	-0.000062	-0.000062	-0.000062	-0.000062	-0.000062	-0.000062	-0.000062	-0.000062	-0.000062
a1-a2									-0.000619	-0.000619	-0.000619	-0.000619	-0.000619	-0.000619	-0.000619	-0.000619	-0.000619
a1-a2									-0.000619	-0.000619	-0.000619	-0.000619	-0.000619	-0.000619	-0.000619	-0.000619	-0.000619
a1+a2+a3										0.003254	0.003262	0.003262	0.003262	0.003262	0.003262	0.003262	0.003262
a1+a2+a3										0.003254	0.003262	0.003262	0.003262	0.003262	0.003262	0.003262	0.003262
(-a1+a2+a3)											-0.005190	-0.005190	-0.005190	-0.005190	-0.005190	-0.005190	-0.005190
(-a1+a2+a3)											-0.005190	-0.005190	-0.005190	-0.005190	-0.005190	-0.005190	-0.005190
(a1-a2+a3)												0.000013	0.000013	0.000012	0.000013	0.000013	0.000013
(a1-a2+a3)												0.000013	0.000013	0.000013	0.000013	0.000013	0.000013
(a1+a2-a3)													0.000010	-7.332672	0.000010	0.000010	0.000010
(a1+a2-a3)													0.000010	0.106426	0.000010	0.000010	0.000010
(-a1-a2+a3)														-0.106416	/	/	/
(-a1-a2+a3)														7.332682	/	/	/
2*a1															0.002002	0.002001	0.002001
2*a1															0.002002	0.002001	0.002001
2*a2																0.000449	0.000449
2*a2																0.000449	0.000449
3*a1																	0.001446
3*a1																	0.001446

4. Orbitals of the molecular dimer formed by the nearest neighboring molecules in a_1+a_2 (H-bonding) direction

In the main manuscript we attributed the particularly strong impact of the H-bonds on the t_{a1+a2} transfer integral for the CB to the shape of the involved dimer orbital. These are shown in Figure S6, which reveal differences in the accumulation of charges close to the H-bonds and in the nodal patterns between the orbitals for occupied vs. unoccupied states.

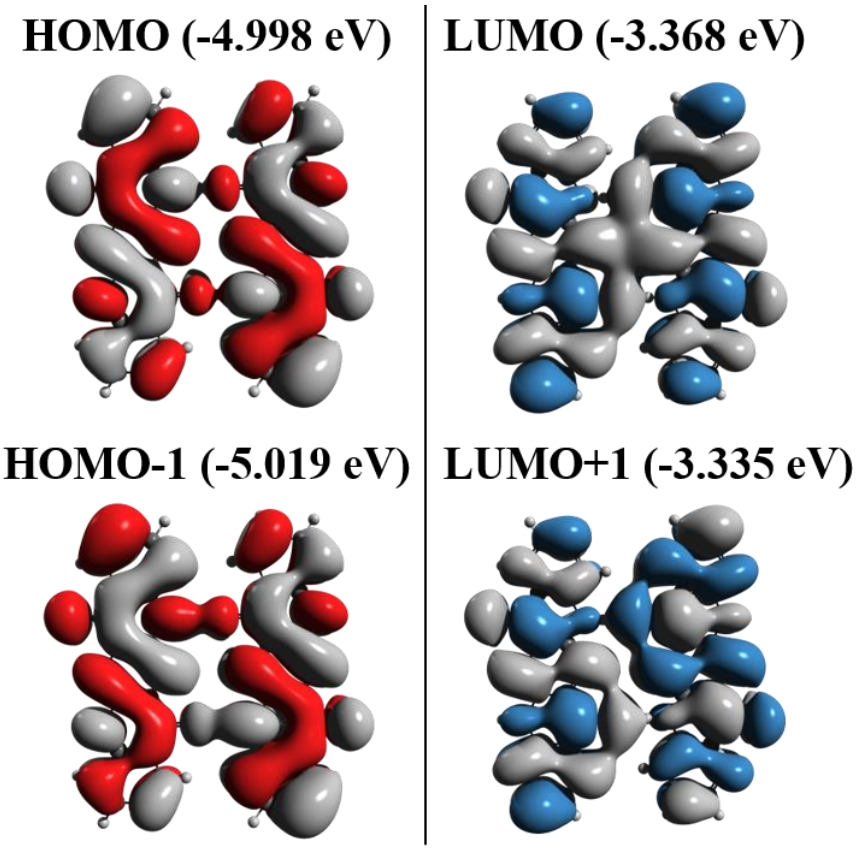

Figure S7. *Molecular orbitals of the quinacridone dimer constructed by the neighboring molecules along direction* $\boldsymbol{a_1+a_2}$.

5. Additional plots and data of the electronic band structures

Figure S8 shows the DFT calculated conduction (blue) and valence bands (red) for the considered "real space directions" discussed in section 3 of the main manuscript. Also the TB fit as described in section 4 in of the main manuscript are shown. One can see that the fitted data

agree quite well with the calculated bands. Only in direction **P** one observes a larger quantitative difference. However, the shape of this band is still nicely reproduced and the largest deviation in that direction amounts to ~4 meV, which is still comparably low. The extracted BW's (as the difference between the maximum and minimum value of the respective electronic band) are compiled in Table S2.

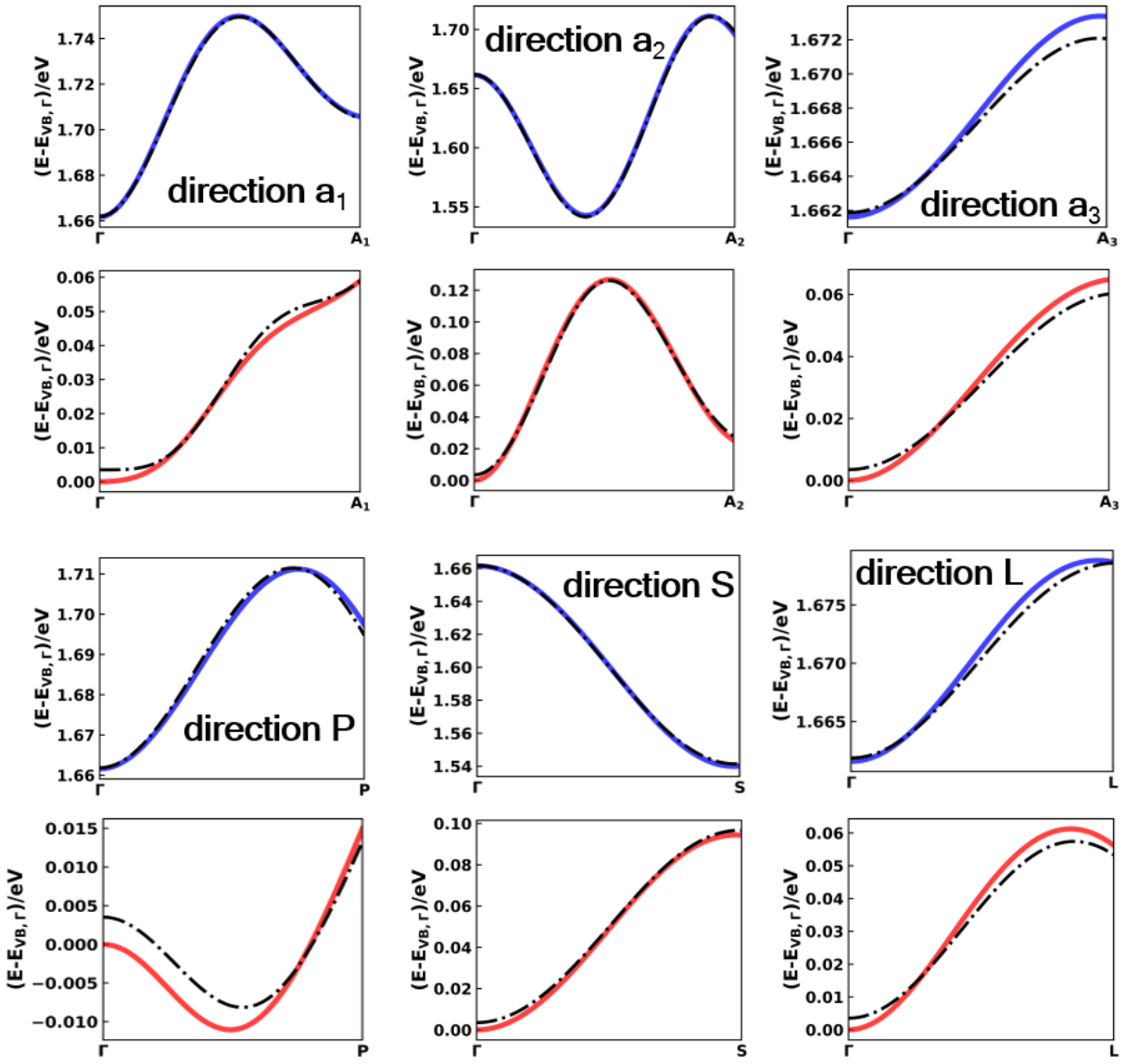

Figure S12. *Conduction (blue) and valence (red) bands along directions* ***a****1*, ***a****2*, ***a****3*, ***P***, ***S*** *and* ***L****. The tight-binding fit is shown as a black line.*

Table S2. *Band width for the highest occupied and the lowest unoccupied band of the α-phase of quinacridone along selected directions. For a description of the directions see the main text and Figure 1.*

direction	BW_{VB} (meV)	$\Delta E_{BZ,VB}$ (meV)	BW_{CB} (meV)	$\Delta E_{BZ,CB}$ (meV)
$\mathbf{a}_1$	59	59	88	44
$\mathbf{a}_2$	126	126	119	111
$\mathbf{a}_3$	65	65	12	12
P	26	15	50	36
S	95	94	122	122
L	61	56	17	17
ΓX	34	30	113	97
ΓY	141	141	124	124
ΓZ	63	63	14	14

6. Impact of the choice of fitted k-points on the performance of the tight-binding model

Here we describe the results of the "full" TB fit including only the high-symmetry directions from Fig. 2 of the main manuscript. The agreement between the TB and DFT bands along the high-symmetry directions is excellent. Figures S13 and S14 show the fitted results for directions strongly differing from the ones used in the parametrization. We find that the fit is completely wrong in this direction, which is not surprising as no data points containing information for this path have been considered during fitting. This leads to the conclusion that the whole k-space (at least for low symmetry systems) has to be included in the fitting procedure in order to be able to extract information on arbitrary k-paths and k-points.

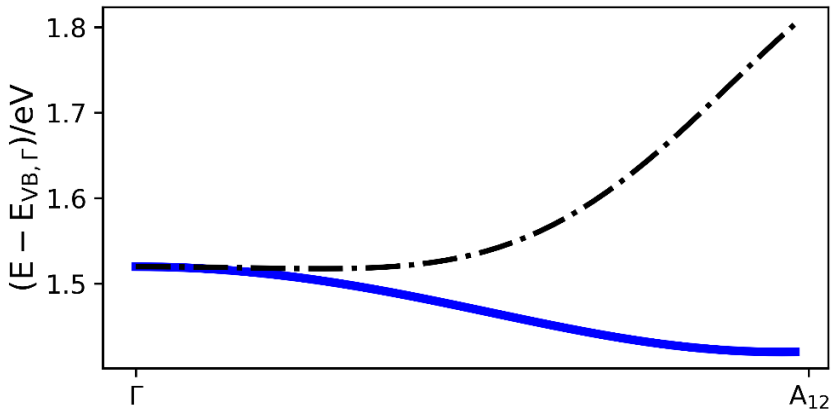

Figure S13. Conduction band in direction $\mathbf{a}_1+\mathbf{a}_2$. The DFT data are shown in blue and the TB fit on the high-symmetry directions is shown as dash-dotted black line.

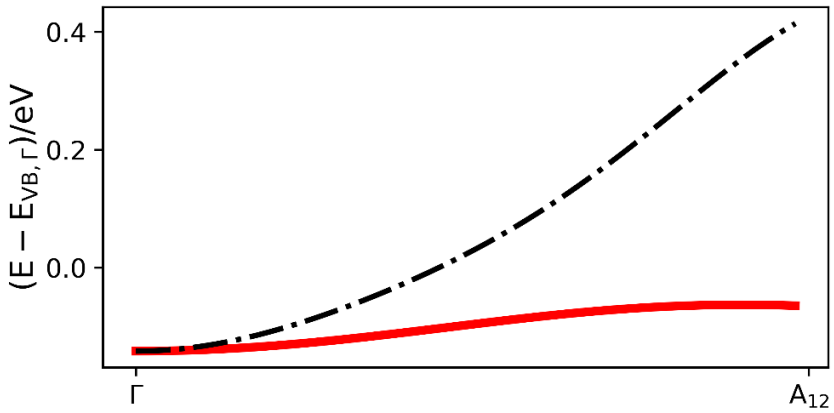

Figure S14. Valence band in direction $\mathbf{a}_1+\mathbf{a}_2$. The DFT data are shown in red and the TB fit on the high-symmetry directions is shown as dash-dotted black line.

References

[1] J. P. Perdew, K. Burke, M. Ernzerhof, *Phys. Rev. Lett.* **1996**, *77*, 3865.

[2] J. P. Perdew, K. Burke, M. Ernzerhof, *Phys. Rev. Lett.* **1997**, *78*, 1396.

[3] J. Heyd, G. E. Scuseria, M. Ernzerhof, *J. Chem. Phys.* **2003**, *118*, 8207.

[4] J. Heyd, G. E. Scuseria, M. Ernzerhof, *J. Chem. Phys.* **2006**, *124*, 219906.

[5] D. Lüftner, S. Refaely-Abramson, M. Pachler, R. Resel, M. G. Ramsey, L. Kronik, P. Puschnig, *Phys. Rev. B* **2014**, *90*, 075204.

3. Correlation between energetic stability and low intermolecular electronic couplings in molecular crystals

3.1. Author contributions

E. Zojer and O. T. Hofmann conceived the idea that for OSCs there might be a correlation between small intermolecular electronic couplings and energetic stability. C. Winkler did all DFT calculations, while A. Jeindl performed the Gaussian Process Regression. F. Mayer supported C. Winkler in fitting tight-binding models to the electronic structures of the systems. R. Tonner performed the decomposition of the interaction energy. All data were interpreted by C. Winkler, O. T. Hofmann, and E. Zojer. C. Winkler wrote a first draft of the manuscript which was then significantly revised by E. Zojer, C. Winkler, and O. T. Hofmann in several iterations. E. Zojer supervised the entire project.

The following paper is published in Chemistry of Materials and inserted here as original publication together with the Supporting Information. Reprinted with permission from " Winkler C., Jeindl A., Mayer F., Hofmann O. T., Tonner R., and Zojer E., Understanding the Correlation between Electronic Coupling and Energetic Stability of Molecular Crystal Polymorphs: The Instructive Case of Quinacridone, Chemistry of Materials, 2019, 31, 7054-7069".

3.2. Main paper

CHEMISTRY OF MATERIALS
Cite This: Chem. Mater. 2019, 31, 7054−7069
Article
pubs.acs.org/cm

Understanding the Correlation between Electronic Coupling and Energetic Stability of Molecular Crystal Polymorphs: The Instructive Case of Quinacridone

Christian Winkler,[†] Andreas Jeindl,[†] Florian Mayer,[†] Oliver T. Hofmann,[†] Ralf Tonner,[‡] and Egbert Zojer*[,†]

[†]Institute of Solid State Physics, NAWI Graz, Graz University of Technology, Petersgasse 16, 8010 Graz, Austria
[‡]Department of Chemistry, Philipps-Universität Marburg, Hans-Meerwein-Straße 4, 35032 Marburg, Germany

Supporting Information

ABSTRACT: A crucial factor determining charge transport in organic semiconductors is the electronic coupling between the molecular constituents, which is heavily influenced by the relative arrangement of the molecules. This renders quinacridone, with its multiple, structurally fundamentally different polymorphs and their diverse intermolecular interactions, an ideal test case for analyzing the correlation between the electronic coupling in a specific configuration and the configuration's energetic stability. To provide an in-depth analysis of this correlation, starting from the α-polymorph of quinacridone, we also construct a coplanar model crystal. This allows us to systematically compare the displacement dependence of the electronic coupling with that of the total energy. In this way, we identify the combination of Pauli repulsion and orbital rehybridization as the driving force steering the system toward a structure in which the electronic coupling is minimal (especially for the valence band and at small displacements). The general nature of this observation is supported by equivalent trends for an analogous pentacene model system. This underlines that the design of high-performance materials cannot rely on the "natural" assembly of the π-conjugated backbones of organic semiconductors into their most stable configurations. Rather, it must include the incorporation of functional groups that steer crystal packing toward more favorable structures, where aiming for short-axis displacements or realizing comparably large long-axis displacements appear as strategies worthy of exploring.

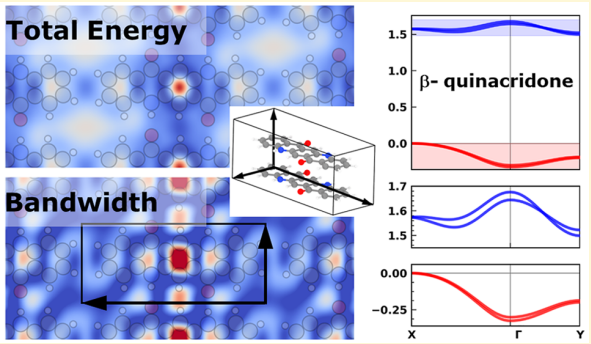

1. INTRODUCTION

Organic semiconductors (OSC) are increasingly used as active elements in (opto)electronic and photonic devices.[1−11] For most of these applications, the charge-carrier mobility, μ, of the employed materials is of paramount importance. Unfortunately, carrier mobilities in the majority of OSCs are orders of magnitude smaller than in their inorganic counterparts.[12] Improving that situation and achieving efficient charge transport is, thus, one of the key challenges for the further success of OSC-based devices. Computational modeling has the potential to significantly contribute to overcoming that challenge by explaining the experimentally observed trends and by helping to understand whether specific intermolecular interactions exist that drive molecular crystals toward low-mobility configurations. Based on such insights, it should eventually be possible to design new systems with markedly improved properties.

In order to simulate charge-carrier mobilities, many models have been developed over the years, with the limiting cases represented by fully coherent band transport (for weak electron−phonon coupling and low temperatures) and incoherent hopping (for strong electron−phonon coupling at elevated temperatures).[13−16] The popularity of the various models has varied over time, and their suitability for a given system typically depends on the type of molecules, their arrangement, the temperature range of interest, and the degree of disorder present.[13−16] Essential parameters in all models are the electronic couplings between neighboring molecules, which are typically correlated with the overlap of the associated wave functions and are often expressed via so-called transfer integrals, t. For hopping-based theories the carrier mobility, μ, is then proportional to t^2, while it is proportional to t for band-transport based models at least within a simple tight-binding picture.[13,16] For complex cases, elaborate tight-binding fits are advisable for determining the electronic coupling in the actual crystalline environment. They also allow a straightfor-

Special Issue: Jean-Luc Bredas Festschrift

Received: May 7, 2019
Revised: August 3, 2019
Published: August 6, 2019

DOI: 10.1021/acs.chemmater.9b01807
Chem. Mater. 2019, 31, 7054−7069

ward calculation of the effective mass of the charge carriers in the entire Brillouin zone.[17]

Besides small intermolecular electronic couplings, charge transport in organic crystals is also limited by factors like a particularly strong electron−phonon coupling[13−16] and the associated dynamic[18−23] and static disorder. The focus of the present study, however, is on the materials' electronic properties (considering their full 3D crystalline structures), in order to determine fundamental factors that limit the electronic coupling.

A key aspect in this context is the relative geometric arrangement of neighboring molecules, where displacements by fractions of an angstrom can easily change transfer integrals by orders of magnitude.[13,24−31] In other words, the structure of an organic semiconductor crystal crucially determines quantities describing its electronic properties, like bandwidths, transfer integrals, and effective masses. This raises the question whether a similar correlation also exists in the opposite direction, i.e., whether the magnitude of the electronic coupling between neighboring molecules in a crystal in a systematic way defines its (equilibrium) structure. To address this question, in the following we will search for correlations between intermolecular electronic couplings (i.e., transfer integrals) and the energetic stability of specific structural motifs. The primary goal of this is to understand whether there are driving forces that steer OSC crystals into equilibrium packing configurations with reduced electronic couplings. The latter is suggested by the observation that the highest mobilities are often found for metastable, high-energy phases.[32,33] In fact, based on molecular dimer simulations, Sutton et al. have already suggested a "clear correlation between the degrees of intermolecular electronic coupling and exchange repulsion".[34] Additionally, we will explore whether alternative driving forces not immediately related to intermolecular wave function overlaps, such as electrostatic or van der Waals interactions, might help mitigate this dilemma.

As the primary model system for our study, we chose the hydrogen-bonded organic pigment quinacridone, which has been successfully used in several devices, suggesting an avenue toward biocompatible electronics.[19−21] Considering the presence of polar heteroatomic groups and the prevalence of hydrogen bonds, it also promises particularly rich physics to be explored. Quinacridone exhibits three established, stable polymorphs (called α, β, and γ)[35] with fundamentally different packing motifs. Still, in all polymorphs one observes π-stacking of neighboring molecules,[35] rather than the more common herringbone arrangement.[36,37] This is insofar interesting, as a cofacial π-stacking of molecules in brickwork or slip-stacked architectures has been observed for many high-mobility materials.[28,38−40] Consequently, in the following we will focus on analyzing the electronic coupling in the π-stacking direction. In this direction the largest coupling for a given material can be achieved, provided that the molecules are suitably arranged.

On more technical grounds, in the past the magnitudes and signs of transfer integrals in OSCs have typically been rationalized based on calculations on displaced π-stacked molecular dimers together with the symmetries and nodal structures of the relevant dimer orbitals.[24−29] For quinacridone, such a π-stacked arrangement of molecules is consistent with the actual crystal structure. Consequently, starting from the α-polymorph and without breaking the intermolecular H-bonds, one can construct a representative crystalline model system with molecules arranged in parallel planes. For the sake of comparison, we also analyze an analogous model crystal built from pentacene molecules, even though pentacene crystallizes in a herringbone pattern. Displacing the molecular planes in the model systems relative to each other allows deriving the dependence of the transfer integrals on the intermolecular displacement in a realistic, crystalline environment. Importantly, in contrast to simulating dimers, these calculations also provide direct information on how the total energy of the 3D extended system depends on the displacement. This then allows identifying possible correlations between the magnitude of the transfer integral(s) and the stability of a specific crystalline structure.

2. COMPUTATIONAL METHODOLOGY

2.1. General Approach. Computationally, transfer integrals are usually either derived from molecular dimer simulations[13,24−28] or from band-structure calculations. Based on the results of the latter (relying on a simple tight-binding ansatz), transfer integrals can be directly obtained from bandwidths.[26,41] Consequently (within certain limitations),[17] also bandwidths serve as a measure for the intermolecular electronic coupling. A more advanced approach is fitting more elaborate analytic expressions derived from tight-binding models (see below) to the bands in the entire first Brillouin zone. The transfer integrals to all relevant neighbors can then be extracted from that fit.[14,17] Compared to calculations on molecular dimers, this has the advantage that the crystalline environment of the molecules is accounted for and situations can be identified in which "super exchange"-like next-nearest neighbor couplings become relevant.[17,42−45] Thus, before correlating electronic couplings and total energies, we will first explore whether simulations based on molecular dimers and calculations employing periodic boundary conditions yield consistent trends. As far as the periodic simulations are concerned, we will also test whether trends derived from bandwidths and from tight-binding parameters are consistent.

For the dimer simulations, we extracted dimer geometries from the relaxed crystal structures (see below). To calculate their electronic structure, we employed the FHI-aims code,[46] version 180424, in combination with the Perdew−Burke−Enzerhof (PBE)[47,48] functional and the default "tight" settings for the numerical parameters and basis sets (a more detailed description of the nature of the associated basis sets can be found in the Supporting Information). Transfer integrals were determined from orbital energies applying the "energy splitting in dimer" (ESD) technique.[13] As an alternative strategy, we also employed the fragment orbital (FO) approach[25] using a recently developed postprocessing tool interfaced with FHI-aims.[49] The sign of the transfer integrals was determined depending on whether the bonding (positive) or antibonding (negative) linear combination of the molecular orbitals was higher in energy. Due to the inversion symmetry of the dimers, the transfer integrals obtained with the ESD and FO approaches are essentially identical when employing the PBE functional (as is shown in the Supporting Information).

For the calculations relying on periodic boundary conditions, we used dispersion-corrected density-functional theory (DFT). Unless otherwise stated, we used VASP 5.4.4[50−53] treating exchange and correlation via the PBE functional in combination with the Tkatchenko−Scheffler (TS) dispersion correction method[54] to account for long-range van der Waals interactions. The recommended PAW[55] potentials (details in the Supporting Information) together with a plane-wave cutoff energy of 700 eV were used for all calculations. In the self-consistent-field (SCF) procedure, the Brillouin zone was sampled using a 32 × 20 × 8 Γ-centered k-point grid for α-, a 25 × 36 × 9 grid for β-, and an 8 × 32 × 8 grid for γ-quinacridone and a 25 × 25 × 25 grid for the coplanar model system. This k-point grid is significantly overconverged for determining a reliable charge density. It has been chosen here, as a particularly tight sampling of the Brillouin zone is necessary for improving the quality

DOI: 10.1021/acs.chemmater.9b01807
Chem. Mater. 2019, 31, 7054−7069

of the tight-binding fits and for determining meaningful total bandwidths (see below). Bearing this in mind, for the test of the employed methodology (functional and van der Waals correction) and for energy decompositions, less dense k-point grids have been used. To describe the occupation of the electronic states, we used the Methfessel–Paxton[56] occupation scheme with a width of 0.1 eV. The geometries of the α-, β-, and γ-polymorphs of quinacridone were obtained using the experimental unit cells[35] and relaxing the atomic positions of the molecule(s) until the largest force component on the atoms was smaller than 0.01 eV/Å.

2.2. Testing the Impact of the Type of van der Waals Correction and the Employed Functional. As far as the choice of the a posteriori van der Waals correction is concerned, in addition to the above-mentioned TS approach, we also tested the many-body dispersion (MBD) approach by Ambrosetti et al.[57] As will be shown below, the choice of the vdW correction has virtually no impact on the relative stability of the different polymorphs (Section 3.1), but it changes the order of the minima of the total energy, when calculating the coplanar model crystal as a function of intermolecular displacements (Section 3.2). Both methods applied in this test, TS as well as MBD, build on the converged charge density. For obtaining the results of the computationally much more expensive MBD approach, the same energy cutoff as in Section 2.1 has been used in VASP and we employed the following k-point grids: α-quinacridone, 16 × 10 × 4; β-quinacridone, 13 × 8 × 4; γ-quinacridone, 4 × 16 × 4; and coplanar model crystal, 12 × 12 × 12. These grids are somewhat smaller than the ones described in Section 2.1, as the MBD calculations have been used neither for determining total bandwidths nor for fitting tight-binding functions (see above). For the α-, β-, and γ-polymorphs of quinacridone, we also performed geometry optimizations using the MBD approach.

To test the impact of the employed functional (especially evaluating the role of exact exchange), we also performed calculations using the hybrid functional HSE06.[58−60] This yields equivalent results for the nature of the frontier bands, only the bandwidths obtained with HSE are somewhat larger, as will be discussed in the Results and Discussion section. The main qualitative change upon employing HSE vs PBE concerns the order of deeper-lying orbitals (see Supporting Information of ref 17), consistent with the results of Lüftner et al.[61] As we are primarily concerned with the frontier bands and since swapping the orbital ordering does not affect the electron density, this has also no effect on the quantities discussed here. Thus, we can safely rely on the (computationally much less expensive) PBE calculations.

On more technical grounds, the HSE calculations have been performed using FHI-aims for both open and periodic boundary conditions. This choice is made to be consistent with the dimer calculations. Notably, for the chosen (well converged) settings, test calculations employing the PBE functional in FHI-aims and in VASP yield identical band structures. For the HSE calculations in FHI-aims, the same well-converged k-point grids as for the MBD tests have been used for α-quinacridone, β-quinacridone, and γ-quinacridone. For the tests on the coplanar model crystal, we reduced the grid to 6 × 6 × 6 due to memory limitations.

2.3. Building the Coplanar Model Crystal. As a first step to create the model crystal with quinacridone molecules arranged in parallel planes, we constructed an orthorhombic unit cell and then placed a gas-phase optimized quinacridone molecule in this cell such that the long molecular axis was parallel to the unit cell vector $\mathbf{a}_3$, the short axis parallel to $\mathbf{a}_2$, and the stacking direction of the molecules parallel to $\mathbf{a}_1$ (see Figure 1). The length of $\mathbf{a}_1$ was set to 3.5 Å (the equilibrium distance of the quinacridone stripes in the α-polymorph).[35] The lengths of $\mathbf{a}_2$ and $\mathbf{a}_3$ were chosen such that the van der Waals surfaces of neighboring molecules touched. Next, the lengths of the unit cell vectors $\mathbf{a}_2$ and $\mathbf{a}_3$ and the molecular geometry were relaxed, where for technical reasons associated with the partially constrained relaxations we employed the FHI-aims[46] code (see Supporting Information). All geometry optimizations for the model crystal were performed combining the PBE functional with the TS van der Waals correction. Compared to simply arranging quinacridone molecules in their gas-phase geometry, this has the advantage that

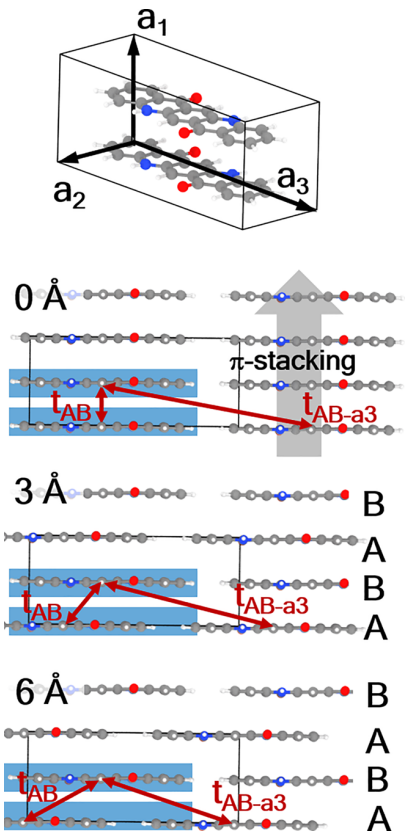

Figure 1. Unit cell of the coplanar model crystal derived from the α-phase of quinacridone. The two most important transfer integrals for transport in the π-stacking direction are sketched for three different displacements of the molecular layers.

geometric changes due to the formation of intermolecular H-bonds (i.e., a more aromatic structure of the molecules) are accounted for. In a second step, the size of the unit cell in the $\mathbf{a}_1$ direction was doubled to 7.0 Å, such that it contained two molecules in the stacking direction (c.f., Figure 1). This setup allows consecutive quinacridone layers to be easily shifted in an AB fashion; see Figure 1. In passing we note that employing this procedure has hardly any impact on the H-bonding network of quinacridone. As discussed in more detail in the Supporting Information, the H-bonding energies are reduced by less than 3% in the orthorhombic model system compared to the α-polymorph, and the bonding distances are even somewhat smaller. Notably, the procedure sketched here yields a model system that is reasonably close to the α-polymorph of quinacridone, as exemplified by the observation that the lowest-energy structure of the model system is only ca. 0.3 eV per molecule higher in energy than the α-quinacridone.

For constructing the pentacene model crystals, we adopted the same strategy with the only difference being that for the geometry optimizations we had to set the length of the $\mathbf{a}_1$ vector to a value large enough to suppress interlayer interactions (40 Å), as otherwise unrealistic geometric distortions occurred (for details see Supporting Information).

2.4. Two-Dimensional Displacement Maps, Bandwidths, and Tight-Binding Fits. When calculating the energetics and bandwidths upon displacing neighboring quinacridone or pentacene planes in the model crystals, DFT calculations employing the comparably expensive settings from Section 2.1 were performed for displacements along either the long or the short molecular axes. Doing such calculations on a sufficiently dense grid for simultaneous displacements along both axes would pose a sizable computational challenge. Thus, for such 2D displacement maps, we resorted to

DOI: 10.1021/acs.chemmater.9b01807
Chem. Mater. 2019, 31, 7054−7069

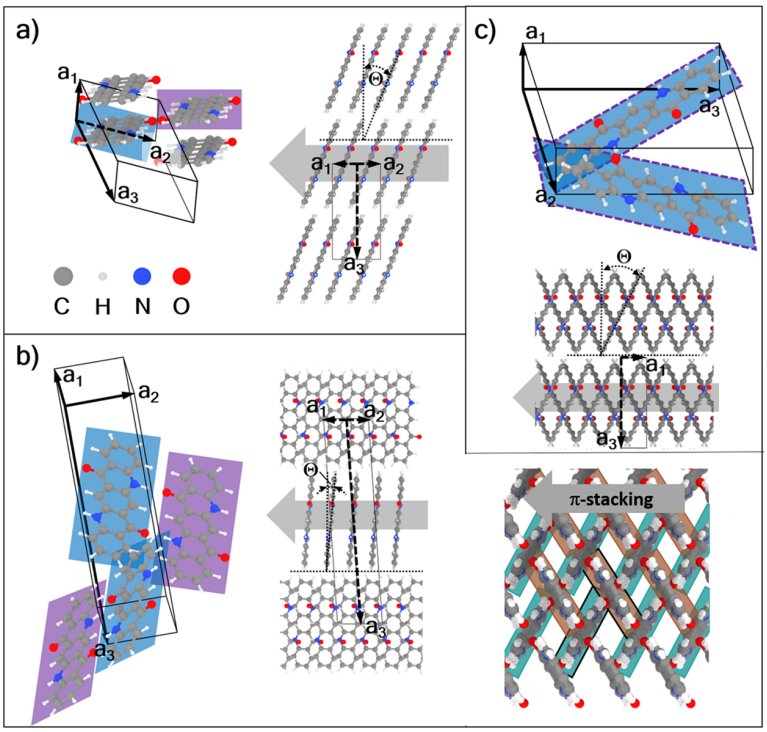

Figure 2. Crystal structures of the three quinacridone polymorphs. (a) Left: view of the unit cell of α-quinacridone with the molecule in the original cell marked by a blue rectangle and the closest H-bonding partner marked by a purple rectangle. Right: side view of the crystal structure with the viewing direction chosen such that the alignment of the H-bonded stripes is resolved most clearly. The π-stacking direction is indicated by a gray arrow. (b) Left: unit cell of β-quinacridone; again, the blue rectangles mark the (in this case two) molecules in the unit cell, and the closest H-bonding partners are highlighted in purple. The central panel again provides a side view, illustrating the alignment of the H-bonded stripes. Right: the viewing direction is perpendicular to the ($\mathbf{a}_1$, $\mathbf{a}_2$) plane to illustrate that the π-stacking direction is the same for all layers (with molecules in different layers highlighted by the cyan and brown shading). (c) Top: unit cell of γ-quinacridone containing two molecules, which are H-bonded to each other. Bottom: side view illustrating the "hunter fence" arrangement of the molecules.

Gaussian process regression. There, the model vector consisted only of the x and y positions of the shifted layer, and as kernel functions we chose linear combinations of Gaussian kernels equally distributed in the unit cell, which fulfill the periodicity constraints. To optimize the hyper-parameters, the marginal log likelihood was maximized. Gaussian process regression allows a model error to be estimated, which is visualized and discussed in the Supporting Information. The model was first trained with the data calculated for displacements along the long and short molecular axes. Then 10 additional points were chosen at the coordinates of maximum model uncertainty. During this process all system symmetries (C_2 rotation around $\mathbf{a}_1$ for quinacridone and pentacene, mirroring along $\mathbf{a}_2$ and $\mathbf{a}_3$ for pentacene) were considered and exploited.

As far as bandwidths are concerned, the total bandwidth, W, of α-quinacridone with only a single molecule in the unit cell is defined as the difference between the maximum and the minimum values of the energies of the highest occupied eigenstate for all considered k-points. Bandwidths along specific $\mathbf{k}$-paths are determined in an analogous manner. In β-quinacridone, γ-quinacridone, and the coplanar model crystals, the situation is less straightforward, as these systems all contain two molecules per unit cell, which results in a backfolding of the bands. There, to obtain values consistent with the procedure for α-quinacridone, W was determined by subtracting the maximum energy among the highest occupied eigenstates in the entire first Brillouin zone from the minimum of the second highest occupied eigenstates. For $\mathbf{k}$-paths parallel to directions in which the unit cell contains two molecules (here, along the $\mathbf{a}_1$ direction in the model crystal), the bandwidth is evaluated as the difference between the corresponding eigenstates at the Γ-point, considering the detailed evolution of the bands. This is again done for the sake of consistency, to account for the backfolding of the bands caused by the doubling of the unit cell. More details on the evaluation of the bandwidths are contained in the SI.

Regarding the tight-binding fits, the functional form of the model function differs, depending on whether there are one or two molecules in the unit cell. For α-quinacridone with only a single molecule per unit cell it reads

$$E(\mathbf{k}) = \varepsilon + \sum_j t_j \cdot e^{i\mathbf{k}\cdot\mathbf{R}_j} \tag{1}$$

Here ε denotes the on-site energy, t_j is the transfer integral for neighboring molecules along direction j, and $\mathbf{R}_j$ is the vector connecting the central molecule with the respective neighbor. Due to the inversion symmetry of α-quinacridone, the two neighbors at $\mathbf{R}_j$ and $-\mathbf{R}_j$ are equivalent, which results in identical transfer integrals t_j.

The equation becomes more complex when the unit cell contains two inequivalent molecules,[14] like in β- and γ-quinacridone and in the coplanar model system. It reads

$$E(\mathbf{k}) = \frac{H_{AA} + H_{BB}}{2} \pm \sqrt{\frac{(H_{AA} - H_{BB})^2}{4} + |H_{AB}|^2} \tag{2}$$

Here, the indices A and B denote the inequivalent molecules present in the unit cell; H_{AA} and H_{BB} are terms describing the coupling between equivalent molecules in neighboring unit cells. The couplings between inequivalent molecules, either in the same or in different unit cells, are included in the term H_{AB}. All these terms have the same functional form; only the neighbors considered in the sum are different:

$$H_{AA/BB/AB} = \sum_j t_{\mathbf{R}j,AA/BB/AB} \cdot e^{i\mathbf{k}\cdot\mathbf{R}_{j,AA/BB/AB}} \tag{3}$$

DOI: 10.1021/acs.chemmater.9b01807
Chem. Mater. 2019, 31, 7054−7069

In β- and γ-quinacridone and in the coplanar model system, for symmetry reasons H_{AA}, $t_{j,AA}$, and $\mathbf{R}_{j,AA}$ are the same as H_{BB}, $t_{j,BB}$, and $\mathbf{R}_{j,BB}$. The vectors $\mathbf{R}_{j,AB}$ differ from $\mathbf{R}_{j,AA}$ and $\mathbf{R}_{j,BB}$ by the displacement vector between the two inequivalent molecules in the unit cell. To obtain the transfer integrals, one has to fit the above expressions to the energy eigenstates of the system within the entire first Brillouin zone. In passing, we note that increasing the number of intermolecular interactions included in the tight-binding fits does not impact the values of transfer integrals determined already with fewer parameters, which is discussed in more detail in ref 17. A list containing all intermolecular interactions that have been included for the three quinacridone polymorphs and the coplanar model system can be found in the Supporting Information.

2.5. Determining the Contributions to the Bonding Energy in the Coplanar Model Crystal. A central element of the present manuscript is the analysis of the total energy of the systems (especially the total energy of the coplanar model crystal as a function of intermolecular displacements). In this context it is relevant to analyze the origin of the observed differences via energy decomposition approaches. This is frequently done for finite-size systems and molecular dimers.[34,62−71] In the present context we, however, primarily care about the 3D crystalline environment of the molecules. Therefore, we resorted to the recently developed "periodic energy decomposition analysis" (pEDA),[68,72] which decomposes the interaction energy ΔE_{int} between two fragments into several well-defined contributions.

$$\Delta E_{int} = \Delta E_{Pauli} + \Delta E_{elstat} + \Delta E_{orb} \quad (4)$$

The first is the quasi-classical electrostatic energy, ΔE_{elstat}, which considers the Coulomb interaction between the nuclei and electronic charge densities of the two fragments. This energy contribution also includes effects like charge penetration (i.e., the attractive interaction between the electron cloud of one subsystem and the nuclei of the other, which becomes relevant at small distances).[66,73,74] The ΔE_{elstat} term is (nearly) always attractive due to the larger magnitude of electron−nuclei attraction in comparison to the repulsive terms. This is also found here. ΔE_{elstat} does not yet consider modifications of the charge densities of the fragments due to the interaction. The energetic cost/gain of these modifications is split into two terms: When constructing a wave function of the joint system as a product of the eigenfunctions of the fragments, this new wave function needs to be normalized as well as antisymmetrized to obey the Pauli principle. The energetic cost for achieving that is termed Pauli repulsion energy, ΔE_{Pauli}. The second term arises from the final relaxation of the charge density to the self-consistent density of the combined system and determines the attractive orbital interaction energy, ΔE_{orb}. A final contribution to the interaction (not included in the definition of ΔE_{int} in eq 4) is the van der Waals attraction, which is calculated a posteriori, as described in Sections 2.1 and 2.2. It has been shown recently that the energy terms in the EDA analysis compare well with the results from symmetry-adapted perturbation theory analysis (SAPT) and lead to similar insights regarding the bonding situation.[75] The core advantage of the pEDA analysis is that it considers the full periodicity of the crystalline environment.

The pEDA analysis is implemented in the ADF-BAND package;[76−78] we thus employed that code (version 2018, r69431) for the energy decomposition in combination with the PBE functional, a TZ2P[79] basis set, a small frozen core, scalar relativistic effects in the ZORA approach, an SCF convergence criterion of 10^{-6} eV, and 3D periodic boundary conditions. A Γ-centered 5 × 3 × 5 k-point grid was used after checking for convergence (see SI).

The crystal structures were visualized using Ovito[80] and the molecular orbitals by Avogadro.[81]

3. RESULTS AND DISCUSSION

3.1. Crystalline α-, β-, and γ-Quinacridone. The structures of the three established polymorphs of quinacridone are shown in Figure 2. Of the α-polymorph, two variants have been discussed (α^{I} and α^{II}),[35] where only the existence of α^{I} is undisputed. Thus, in the following, this phase will be denoted as α-quinacridone. The α- and β-phases consist of H-bonded molecular stripes, which are not exactly planar but exhibit small steps between the molecules. In β-quinacridone they, for example, amount to 0.35 Å.[35] The fundamental difference between the two polymorphs is that in the α-phase all stripes run in the $\mathbf{a}_1 + \mathbf{a}_2$ direction (perpendicular to the plane of projection in the right panel of Figure 2a), while in the β-phase they run in different directions in consecutive layers ($\mathbf{a}_1 + \mathbf{a}_2$ and $\mathbf{a}_1 - \mathbf{a}_2$). Consequently, α-quinacridone contains one and β-quinacridone two molecules in the unit cell. Nevertheless, in both cases the stripes are π-stacked in the $\mathbf{a}_1$ direction, which corresponds to the shortest vector between two neighboring molecules, whose π-systems overlap (c.f., gray arrow). For the γ-phase, the packing motif is fundamentally different (Figure 2c): While for the α- and β-phases each quinacridone molecule forms two H-bonds to each of its two neighbors (causing the formation of the stripes), in γ-quinacridone every molecule has a single hydrogen bond to four different neighbors. This gives rise to a "hunter fence" structure, as shown in the bottom panel of Figure 2c. Nevertheless, one can still identify a π-stacking direction (gray arrow).

Of particular interest for the electronic couplings along the π-stacking direction (as the main topic of the present paper) is the displacement of the molecules along the short and long molecular axes in consecutive stripes. These displacements are summarized in Table 1. Consistent with the rather large inclination of the molecular stripes (Θ, see Figure 2) in the α-phase, this polymorph is characterized by a rather pronounced long-axis displacement (1.4 Å) and a smaller short-axis displacement (0.9 Å). Conversely, for β-quinacridone the long-axis displacement is negligible (0.1 Å), while the short-axis displacement amounts to 2.0 Å, which is more than twice as large as for the α-phase. For the γ-phase, due to the hunter fence arrangement of the molecules, the relative displacement of neighboring molecules is determined by the distance between the H-bonding sites on each molecule and by the equilibrium distance between the molecular backbones. Among the three different polymorphs, this results in the largest value of θ and, correspondingly, in the largest long-axis displacement of neighboring molecules (1.7 Å see Table 1). Concomitantly, the short axis displacement is the shortest of all polymorphs (0.7 Å).

Table 1. Details of the Structures of the Polymorphs of Quinacridone[a]

	long axis displacement (Å)	short axis displacement (Å)	inclination angle Θ (deg)	relative energy (meV)
α	1.4	0.9	21.5	+90 (88)
β	0.1	2.0	6.1	+5 (3)
γ	1.7	0.7	25.1	0 (0)

[a]Displacements of neighboring molecules in the π-stacking direction along their long and short molecular axes and inclination of the molecular planes relative to the normal to the quinacridone sheets, Θ, for α-, β-, and γ-quinacridone. The energies per molecule relative to the most stable conformation (γ-quinacridone) are reported. Values which have been obtained employing the many-body dispersion correction scheme are given in brackets.

Energetically, using the TS van der Waals corrections we find that the α-phase is less stable than the γ-phase by 90 meV per molecule (see Table 1), while the total energies of β-

DOI: 10.1021/acs.chemmater.9b01807
Chem. Mater. 2019, 31, 7054−7069

quinacridone and γ-quinacridone are within 5 meV. This means that (within the numerical accuracy of our simulations) the latter two phases are isoenergetic despite their fundamentally different structures. These trends also prevail when employing the MBD scheme with energetic differences of 88 and 3 meV (for more details see Supporting Information). The above values do not contain vibrational energies and entropies. Nevertheless, it is interesting to compare the calculated trends to experimental observations: For example, Lüftner et al.[61] observed the β-polymorph when growing quinacridone on Cu(111), while Paulus et al.[35] concluded that γ-quinacridone is most stable. They also successfully determined the structures of β- and γ-quinacridone but found it impossible to grow large enough single crystals of the α phase for single-crystal diffraction experiments, which massively complicated the determination of its structure.[35] They also describe that the β- and γ-phases are stable and typically do not interconvert into each other. This is not the case for α-quinacridone, which may convert into the β- and γ-phases, preventing its commercial use.[35] All these findings are in line with the above-discussed trends in total energy.

Regarding the electronic structure of the quinacridone polymorphs, a comparison of the bands in the high-symmetry directions in reciprocal space for α-, β-, and γ-quinacridone is shown in the Supporting Information. The shapes of the bands are essentially the same independent of whether one employs the PBE or the HSE06 functional. Overall, the band dispersions are comparably small for the ΓX direction, ranging between 34 and 324 meV for the valence band and between 111 and 262 meV for the conduction band in the PBE calculations. These widths only somewhat increase for the HSE-calculated bands (see Table 2). Also the total bandwidths, W, characteristic of the entire volume of the first Brillouin zone, remain rather small varying between 148 and 324 meV for the valence and between 252 and 345 meV for the conduction band (see Table 2). Interestingly, in all these cases (with the exception of the conduction band in the ΓX direction) the bandwidths are largest for the β-polymorph and rather similar for α- and γ-quinacridone. Thus, for the three established quinacridone polymorphs, there is no apparent correlation between the total widths of the frontier bands and the energetic stability of the materials.

As far as the anisotropy of the resulting electronic coupling is concerned, a detailed analysis of the situation in α-quinacridone with a focus on differences between the H-bonding, van der Waals stacking, and π-stacking directions can be found in ref 17. Here, we are primarily concerned with transport along the π-stacking direction, $\mathbf{a}_1$. Correspondingly, Figure 3 shows the valence and conduction bands of the three quinacridone polymorphs along a $\mathbf{k}$-path starting at the Γ point and running parallel to the $\mathbf{a}_1$ direction until the boundary of the Brillouin zone (Γ → A_1). Again, the bandwidths are rather small, but more importantly, compared to the total bandwidths, there are even more significant differences between the three polymorphs, especially for the valence band: It is rather flat for α-quinacridone parallel to $\mathbf{a}_1$. Consequently, W_{a1} (=59 meV) is by a factor of ∼3 smaller than the total bandwidth. This is because in α-quinacridone the valence band along $\mathbf{a}_1$ is narrower than, e.g., the band in the H-bonding direction ($\mathbf{a}_1 + \mathbf{a}_2$, i.e., along Γ → A_{12}, also shown in Figure 3). W_{a1} is intermediate for γ-quinacridone (82 meV) and largest for β-quinacridone (324 meV, see also Table 2). In β-quinacridone, W_{a1} and W are actually identical, which indicates that in this system both the maximum and the minimum of the band are found along Γ → A_1. The same trend as for W_{a1} is also found for transfer integrals between molecules displaced by $\mathbf{a}_1$. This happens independent of whether one considers the values obtained from the tight binding fits, t_{a1}, or from dimer calculations[82] within the energy splitting in dimer approach, t_{ESD}, or performing fragment orbital simulations, t_{FO} (see Table 2). Minor deviations between transfer integrals extracted from the tight-binding fits and obtained from dimer calculations are primarily attributed to the conceptual differences between the two approaches, especially the fact that the crystalline environment is only accounted for when determining t_{a1}. The latter is particularly relevant for quinacridone, where a dimer calculation misses the change in conjugation due to the H-bond formation.[83]

The situation is somewhat more involved for the conduction bands, as for the α- and β-polymorphs they display a distinctly noncosine shape (an effect that is less clearly observed also for the valence band of α-quinacridone in $\mathbf{a}_1$ direction). This is a clear evidence for "higher-frequency" components (i.e., transfer integrals beyond the nearest neighbors) playing a significant role.[17] Indeed, an analysis of the tight-binding fits shows that the corresponding transfer integrals can be associated with next-nearest neighbor couplings (t_{2a1}). This we attribute to

Table 2. Quantifying the Electronic Coupling in the Polymorphs of Quinacridone[a]

				α	β	γ
valence band	PBE	W (meV)	(PBC)	152	324	148
		$W_{ΓX}$ (meV)	(PBC)	34	324	82
		W_{a1} (meV)	(PBC)	59	324	82
		$\lvert t_{a1}\rvert$ (meV)	(TB)	5	54	22
		$\lvert t_{ESD}\rvert$ (meV)	(dimer)	4	43	20
		$\lvert t_{FO}\rvert$ (meV)	(dimer)	6	41	19
	HSE	$W_{ΓX}$ (meV)	(PBC)	39	330	99
		$\lvert t_{ESD}\rvert$ (meV)	(dimer)	6	44	24
conduction band	PBE	W (meV)	(DFT)	252	345	263
		$W_{ΓX}$ (meV)	(PBC)	113	111	262
		W_{a1} (meV)	(PBC)	88	111	262
		$\lvert t_{a1}\rvert$ (meV)	(TB)	18	31	53
		$\lvert t_{ESD}\rvert$ (meV)	(dimer)	17	21	30
		$\lvert t_{FO}\rvert$ (meV)	(dimer)	10	19	32
	HSE	$W_{ΓX}$ (meV)	(PBC)	135	112	297
		$\lvert t_{ESD}\rvert$ (meV)	(dimer)	20	19	36

[a]Total bandwidths, W, bandwidths along ΓX, $W_{ΓX}$, and bandwidths for bands running parallel to the π-stacking direction (i.e., parallel to $\mathbf{a}_1$), W_{a1}, for all three quinacridone polymorphs. The ΓX direction in reciprocal space is close to parallel to $\mathbf{a}_1$. Additionally, transfer integrals in the $\mathbf{a}_1$ direction calculated from tight-binding fits, t_{a1}, and employing molecular dimers are shown. For the latter, we compare the results of ESD, t_{ESD}, and FO, t_{FO}, calculations. Note that although the H-bonded quinacridone stripes run in different directions in consecutive quinacridone layers in the β-polymorph, the π-stacking direction in all layers is given by $\mathbf{a}_1$. (PBC) denotes results obtained in DFT calculations employing periodic boundary conditions, (TB) are values extracted from the corresponding tight-binding fits, and (dimer) refers to the results of dimer calculations. In addition to the results obtained with the PBE functional, for the sake of comparison we also show the values obtained employing the hybrid functional HSE for t_{ESD} and $W_{ΓX}$. A brief discussion of the somewhat varying HSE06 values for t_{FO} can be found in the Supporting Information.

DOI: 10.1021/acs.chemmater.9b01807
Chem. Mater. 2019, 31, 7054−7069

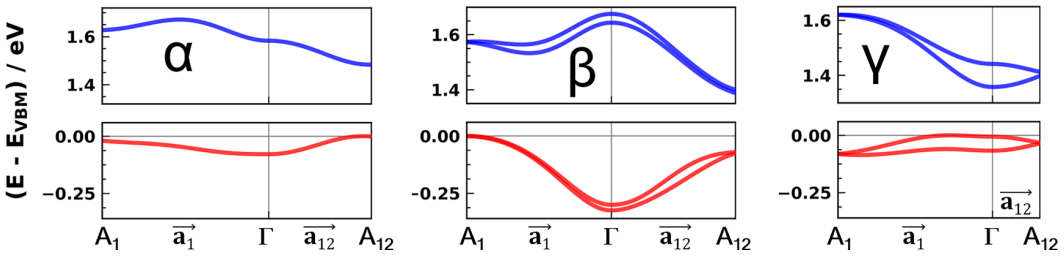

Figure 3. Electronic band structures of the three quinacridone polymorphs shown along **k**-paths originating at Γ and running parallel to the real space $\mathbf{a}_1$ and $\mathbf{a}_1 + \mathbf{a}_2$ directions until the Brillouin zone boundaries. Energies are plotted relative to the valence-band maximum.

"superexchange-like" interactions (for a more in depth discussion of this aspect in α-quinacridone see ref 17). Correspondingly, the direct correlation between bandwidths and transfer integrals is less pronounced. While this complicates the situation when analyzing electron transport, here we are mostly concerned with occupied bands, as only their properties can have an impact on the total energy of the system.

When comparing the results of the PBE and HSE simulations we find that, consistent with the similar band structures calculated in both cases, the bandwidths are also very similar. Furthermore, also the dimer-calculated transfer integrals when employing the ESD approach turn out to be quite robust against changing the exchange correlation functional.

3.2. Properties of the Coplanar Model System of Quinacridone. The above-described results for the three quinacridone polymorphs do not show a clear correlation between total energy and transfer integrals or bandwidth. Therefore, it is useful to analyze a model system whose properties can be assessed in a more systematic way. Such a system is found in the coplanar model crystal derived from α-quinacridone, which is shown in Figure 1 and whose structure is discussed in detail in the Computational Methodology section. Based on this model crystal, we will not only analyze the dependence of the electronic couplings on the intermolecular displacements but will primarily search for correlations between, on the one hand, transfer integrals and bandwidths and, on the other hand, the total energy of the system. Moreover, we will analyze the various ingredients to the total energy in order to clarify whether specific interactions exist that try to force molecular crystals toward configurations with low electronic couplings. As a first step in this quest, Figure 4 shows how the total energy, the van der Waals energy, and the total width of the valence band of the coplanar model crystal depend on the displacement of neighboring sheets.

The data in Figure 4 show that the total energy is maximized for the cofacial, zero displacement situation. Notably, all local maxima of the total energy are found for displacements along the long molecular axis, with the exception of the situation in which the quinacridone sheets are displaced by half the unit cell lengths simultaneously in the $\mathbf{a}_2$ and $\mathbf{a}_3$ directions. This maximum can be associated with a reduced van der Waals attraction between the sheets due to the minimized van der Waals contact area in this configuration (see Figure 4c). The energetically lowest configurations are also found in the vicinity of structures displaced either along the long or along the short molecular axis (the global minimum occurs for a long-axis displacement of 1.5 Å and a simultaneous minor short-axis displacement of 0.3 Å). A similar behavior is

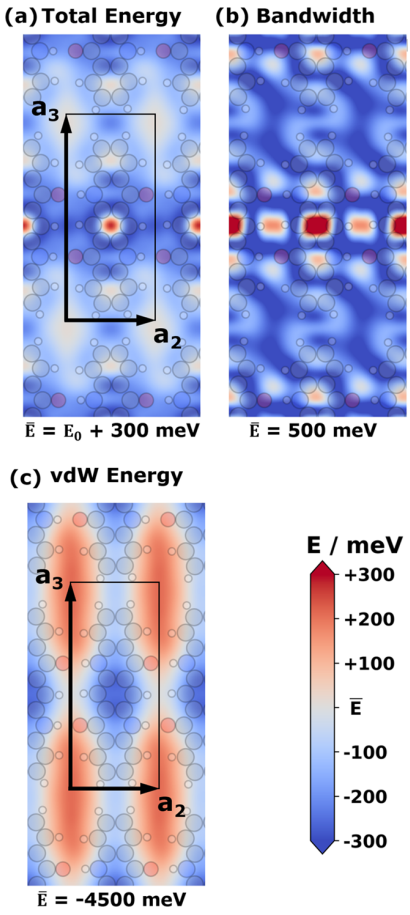

Figure 4. PBE calculated total energy (a), van der Waals energy derived from the TS approach (b), and total width of the valence band (c) as a function of the displacement of neighboring sheets. The position in the graph denotes the position of the center of a molecule in the second layer within the unit cell relative to the first layer, whose structure is indicated in the plot. All energies are given relative to an average value of the respective energy, which is specified below each of the panels. The total energy plot is additionally offset by E_0, which is the value for the lowest-energy structure. As far as the total bandwidth is concerned, the covered range is somewhat larger than indicated by the color bar, as its value varies between 140 and 1100 meV.

observed for the most pronounced maxima of the total bandwidths in Figure 4b (with by far the largest bandwidth for the cofacial, zero-displacement structure). This suggests that, for a more in depth and more quantitative discussion, it is

DOI: 10.1021/acs.chemmater.9b01807
Chem. Mater. 2019, 31, 7054−7069

useful to primarily analyze displacements either along the long or along the short molecular axis.

Displacing Consecutive Molecular Sheets along the Long Molecular Axis in Coplanar Quinacridone—Quantifying the Electronic Coupling. The results for the long-axis displacement are shown in Figure 5. Here, as a first step, we compare the trends for the most relevant parameters used in Table 1 to quantify the strength of the electronic coupling in order to determine whether a single one of them will be sufficient for the further discussion. Such a test is advisable, as when analyzing the anisotropy of coupling parameters in α-quinacridone, relevant deviations between, for example, bandwidths and transfer integrals have been observed.[17] The results for the (valence-band related) transfer integral between displaced molecular dimers obtained with the fragment orbital approach, t_{FO}, are shown in Figure 5a. They display an evolution reminiscent of the observations for rubrene,[28] anthradithiophene,[24] or sexithienyl:[26] There is a pronounced maximum for zero displacement, and subsequently t_{FO} crosses the zero line, reaches a negative maximum, and then crosses the zero line again.

Before comparing these trends to those for the corresponding transfer integral(s) obtained via the tight-binding fit, two technical aspects need to be mentioned: First, from the tight-binding fits it is not possible to extract the sign of the transfer integral describing the coupling between the two inequivalent molecules in the unit cell, t_{AB} (see Figure 1), unambiguously. This is due to symmetry reasons and the functional form of the tight-binding band structure for two molecules in the unit cell. All that can be determined is whether the signs of t_{AB} and t_{AB-a3} (see Figure 1) are the same or not. Second, the band dispersion in the $\mathbf{a}_1$ direction in the coplanar model crystal does not depend on these two transfer integrals individually but is only determined by their sum. Thus, in Figure 5b this sum, $t_{AB} + t_{AB-a3}$, is shown with the sign chosen such that it is consistent with that of t_{FO}. These aspects are discussed in detail in the Supporting Information, where also the values of the individual transfer integrals t_{AB} and t_{AB-a3} are plotted. In this context it should also be noted that especially for small displacements the contribution from t_{AB-a3} is negligible ($|t_{AB-a3}| < 5$ meV for displacements < 2.6 Å and $|t_{AB-a3}| < 20$ meV for displacements < 4.7 Å). Thus, the plot in Figure 5b for small and intermediate displacements mostly reflects the evolution of t_{AB}. As far as the overall trends are concerned, there are only minor deviations between t_{FO} and $t_{AB} + t_{AB-a3}$ concerning the magnitude of the maxima at higher displacements and their exact positions. We attribute these differences mostly to changes in the orbital structure arising from the interaction between the molecules in the actual crystalline environment.

To more easily compare the trends for the transfer integrals to those for the bandwidths, we also show the evolution for $|t_{AB} + t_{AB-a3}|$ in Figure 5b as a dashed red line. This reveals a close to perfect agreement between the evolutions of $|t_{AB} + t_{AB-a3}|$, the total width of the valence band, W, and the width of the valence band along a path starting at the Γ point and running along $\mathbf{a}_1$, W_{a1}^{VB}. The latter data are shown in Figure 5c. In passing, we note that W_{a1}^{VB} is close to zero at the displacements corresponding to zero-crossings of the transfer integrals, while this is not the case for W. This is simply due to the fact that for W also the bandwidths along other paths (e.g., parallel to the H-bonding direction) count. These are largely unaffected by the displacement of the quinacridone sheets.

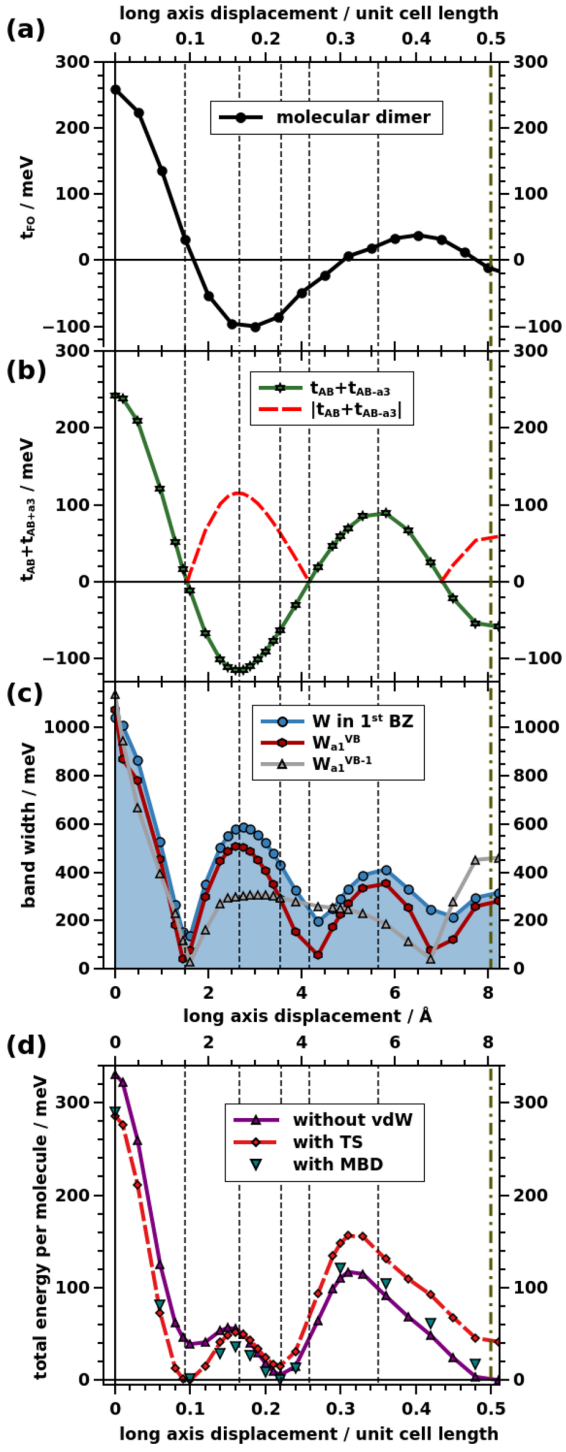

Figure 5. Dependence of the PBE-calculated electronic coupling (a–c) and the energy per molecule (d) on the long-axis displacement for quinacridone. The values in (b)–(d) have been calculated for the coplanar model crystal and those in (a) for the corresponding molecular dimer. The transfer integrals in (a) have been calculated via the fragment orbital method. Employing the energy splitting in dimer method yields the same results, as shown in the Supporting Information. In (b) the sum of the tight-binding derived transfer integrals to the two neighboring molecules in the stacking direction is shown (for details see main text) and (c) contains the total bandwidth of the valence band sampled over a tight k-point grid (area shaded in

DOI: 10.1021/acs.chemmater.9b01807
Chem. Mater. 2019, 31, 7054–7069

Figure 5. continued

blue) as well as the widths of the valence band (VB, derived from the molecular HOMO) and the next lower band (VB-1, derived from the HOMO-3) for the **k**-path running from the Γ-point to the Brillouin zone boundary in a direction parallel to $\mathbf{a}_1$. In (d) the total energies per molecule including and disregarding TS and MBD-type van der Waals interactions are shown relative to the minimum energy obtained for the long-axis displacement. The dotted vertical lines are guides to the eye, while the dashed-dotted line denotes a shift by half of the unit-cell length. On the horizontal axis, the displacements are given in Å as well as in multiples of the corresponding unit-cell length.

As far as the employed functional is concerned, using HSE leads to an increase of the maximum values of W_{a1}^{VB} by ca. 100 meV which corresponds to a relative change of ∼12%. Despite the quantitative differences, switching the functional does not affect the shapes of the bands nor the evolution of t_{FO} with the displacement (see Supporting Information).

Considering the above comparison and the overall qualitative agreement between all quantities used to determine the displacement-dependent trends in the electronic coupling, in the following we will restrict the analysis primarily to PBE-calculated bandwidths as the most straightforwardly accessible parameters for the actual crystals.

Displacing Consecutive Molecular Sheets along the Long Molecular Axis in Coplanar Quinacridone—Evolution of the Total Energy. A central observation for the present study is made when comparing the evolution of the bandwidths with that of the total energy of the system, shown in Figure 5d. Especially, for small displacements, their evolutions run parallel (c.f., refs 34 and 65), as can be seen comparing Figure 5d with Figure 5a−c. In detail, as already mentioned in the discussion of Figure 4, the largest bandwidth and the highest total energy are found when not displacing consecutive quinacridone sheets. Moreover, the total energy reaches its minimum for a total displacement of ca. 1.5 Å, where also the electronic coupling is minimized. This suggests that there is a fundamental driving force steering the crystal toward a structure with a minimized electronic coupling. In this context it is important to stress that the unfavorable situation for zero displacement is not primarily the consequence of arranging the polar carbonyl and amine groups on top of each other, as a similarly pronounced energetic maximum is observed when flipping the molecules in the second layer by 180°, placing the amines on top of the ketones.

The origin of the above-mentioned driving force minimizing the bandwidth can rather be traced back to exchange repulsion, as stressed in ref 34 and discussed for molecular dimers of acenes employing symmetry-adapted perturbation theory.[65] Qualitatively, the variation of the total energy with displacement can be understood from the following consideration: When the orbitals of two molecules overlap, bonding and antibonding linear combinations are formed, where the bonding one is stabilized less than the antibonding one is destabilized. As the energies of the occupied bands (orbitals) enter into the expression of the total energy, wave function overlap involving fully occupied orbitals, thus, results in a repulsive contribution, with the effect being particularly pronounced for large energetic splittings and, correspondingly, strong electronic couplings.

To ensure that such a destabilization of the structures by large transfer integrals is indeed a consequence of the modification of the wave functions due to the interaction between neighboring quinacridone sheets, we performed a periodic energy decomposition analysis, as described in Section 2.5 taking the two quinacridone sheets associated with the two molecules in the unit cell as the fragments for the analysis. The resulting contributions to the electronic interaction energy, ΔE_{int} (not comprising long-range van der Waals interactions),[68,72] are shown in Figure 6a relative to the values

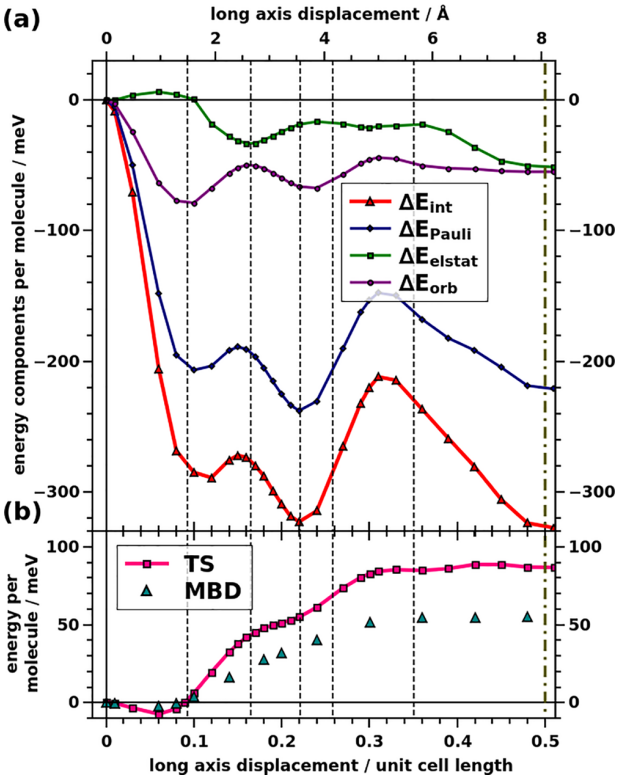

Figure 6. (a) PBE-calculated relative evolution of the electronic interaction energy, ΔE_{int} (excluding a posteriori van der Waals corrections), and its components (Pauli repulsion energy, ΔE_{Pauli}, orbital interaction energy, $\Delta E_{orbital}$, and electrostatic energy, ΔE_{elstat}, as a function of the long-axis displacement in a coplanar quinacridone model crystal). The energies are given relative to the zero-displacement situation. For the latter the following absolute values (per molecule) are obtained: ΔE_{int} = 407 meV, ΔE_{Pauli} = 870 meV, ΔE_{elstat} = −343 meV, and $\Delta E_{orbital}$ = −120 meV. As the minima for different quantities are found at different displacements, aligning them relative to the energetic minima as in Figure 5 is not advisible, as this would obscure their additive character. (b) Evolution of the TS and MBD van der Waals correction energies with displacement. At zero displacement, the following absolute values (per molecule) are obtained: $\Delta E_{vdW,TS}$ = −2375 meV and $\Delta E_{vdW,MBD}$ = −2651 meV.

obtained for zero displacement (where the latter are listed in the figure caption). One clearly sees that the evolutions of the Pauli repulsion energy, ΔE_{Pauli}, and the orbital interaction energies, ΔE_{orb}, both directly follow the trend for the total energy. That is, the modification of the wave functions in the interacting system is indeed responsible for the destabilization of the model system at large transfer integrals. This shows that for the present system attractive interactions, e.g., due to charge penetration,[66,73] are insufficient to overcome exchange repulsion. At this stage it should also be mentioned that although ΔE_{Pauli} displays an oscillatory behavior, its absolute

DOI: 10.1021/acs.chemmater.9b01807
Chem. Mater. 2019, 31, 7054−7069

value always remains large (>1.2 eV), consistent with what Sutton et al. observed for the exchange repulsion, when analyzing molecular dimers.[34]

The impact of the electrostatic interaction energy between the sheets, ΔE_{elstat}, on the relative stability of different geometries is less pronounced. It somewhat destabilizes the zero-displacement situation and stabilizes the displacement at which the total energy reaches its second maximum and a shift by half of the unit cell. Overall, the electrostatic energy, however, does not severely impact the observed trends.

As far as the long-range van der Waals contributions are concerned, several conclusions can be drawn. When considering the absolute values of the energy contributions (see the caption of Figure 5), it becomes evident that the van der Waals attraction is the force that results in the formation of the crystal, as it is the only attractive interaction that is large enough to overcome Pauli repulsion. Concerning the relative stability of different displacements, the van der Waals contribution does not change the general shape of the total energy curve (see Figure 5d). It, however, determines the relative stability of the two minima at displacements of 1.5 and 2.5 Å. Van der Waals interactions stabilize smaller displacements. Thus, for the TS van der Waals correction the first minimum is the lower one, although ΔE_{int} and the total energy excluding van der Waals corrections (Figure 5d) are smallest at the second one. The trend is also observed when using the MBD correction, although there the stabilization of the first minimum is smaller such that it becomes essentially isoenergetic to the second one.

Returning to the comparison between the bandwidth of the valence band and the total energy, two questions arise: why does the parallel evolution of the two quantities in Figure 5 not prevail for larger displacements, and why is the one-to-one correlation between bandwidth and total energy lost for most regions of Figure 4? We attribute this to the contribution of lower-lying occupied electronic bands (occupied orbitals for molecular systems). These do not impact charge transport per se, as electrons will always accumulate in the conduction band and holes in the valence band, but their contribution to the total energy is as important as that of the valence band.

As shown in Figure 7, there are various occupied bands that, for zero displacement, display widths comparable to that of the valence band. Of the bands we analyzed, this applies to all π-bands (red bars in Figure 7). Only for the second and third band below the valence band the widths are about 1 order of magnitude smaller, which is a consequence of their σ-character (black bars in Figure 7). The latter suggests that the interaction between σ-electrons has only a minor impact on the relative stability of certain displaced structures.

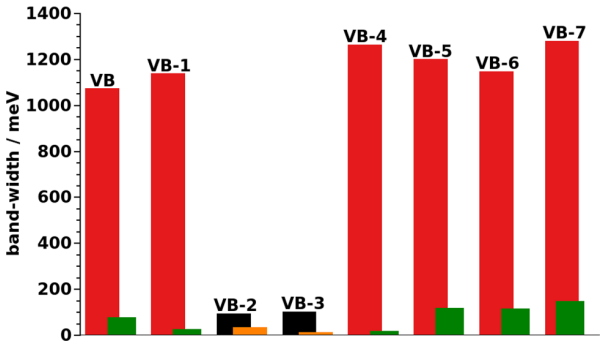

Figure 7. PBE-calculated bandwidths of the highest occupied bands of the coplanar quinacridone model crystal, evaluated as the splitting of the backfolded bands at the Γ point. π-Bands are denoted by red and green and σ-bands by black and orange bars. The widths are evaluated for zero displacement (red and black bars) and for a displacement of 0.1 times the length of the unit cell along the long molecular axis (green and orange bars).

The widths of all bands drop dramatically, when displacing consecutive quinacridone sheets by a tenth of the unit-cell length (see green and orange bars in Figure 7). This rationalizes the parallel evolutions of the valence-bandwidth and the total energy for small displacements. Notably, although the bandwidths of all considered bands become very small at a displacement of one tenth of the unit cell, the absolute value ΔE_{Pauli} remains sizable (663 meV per molecule; i.e., larger than its variation with displacement in Figure 6).

As far as the evolution of the total energy at larger displacements is concerned, the varying nodal structures of the molecular orbitals forming the lower-lying bands (see Supporting Information) result in different trends for the bandwidths at larger displacements such that they no longer follow the valence band. This is exemplarily shown for the second-highest band (VB-1) in Figure 5c. It clearly contributes to the differences in the positions of the extrema in the valence bandwidth and the total energy observed in Figure 5 for large displacements.

Short Axis Displacements in the Coplanar Quinacridone Model Crystal. As mentioned above (cf., Figure 4), additional minima in the total energy and maxima of the bandwidths are found for displacing the quinacridone sheets along the short molecular axis. The resulting evolutions of the bandwidths and energies are shown in Figure 8. Again, the bandwidth is maximized for zero displacement, drops sharply, reaching a pronounced minimum for a short-axis displacement around 1.8 Å (corresponding to a quarter of the unit cell-length in that direction), and then rises again (Figure 8a). The sharp drop at small displacements is again accompanied by a pronounced drop in the total energy (Figure 8b). For displacements of more than a quarter of the unit-cell length, the evolution of the total energy becomes very shallow. This implies that minor modifications in the interaction could easily change the position of the minimum, which would at the same time massively change the electronic coupling and the bandwidth. In fact, even in our simulations the exact position of the minimum depends on the employed van der Waals correction (see Figure 8b).

Performing an energy decomposition in analogy to the previous section reveals that electrostatic as well as van der Waals interactions favor small displacements (Figure 9). Their impact is, however, insufficient for dominating the overall evolution. Thus, again especially Pauli repulsion is responsible for the sharp drop in energy for displacements between zero and a quarter of the unit-cell length. At larger displacements it essentially compensates the evolutions of the electrostatic, the van der Waals, and the orbital interaction energies, which results in the very shallow area of the potential energy surface. The observation that in this displacement region ΔE_{Pauli} does not follow the evolution of the valence bandwidth is again attributed to different nodal structures of other occupied orbitals.

Implications for the Situation in α-, β-, and γ-Quinacridone. The structure of the α-polymorph is dominated by a displacement of neighboring quinacridone molecules

DOI: 10.1021/acs.chemmater.9b01807
Chem. Mater. 2019, 31, 7054−7069

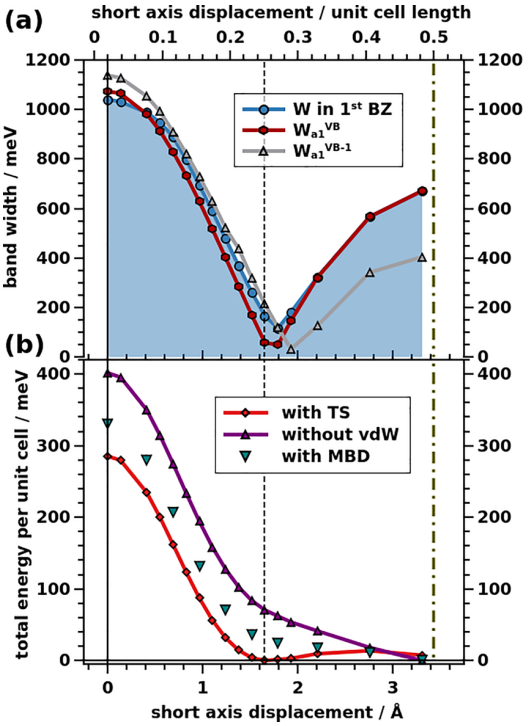

Figure 8. Dependence of the bandwidths (a) and the energies per molecule (b) on the short-axis displacement for the coplanar quinacridone model crystal. (a) contains the total bandwidth of the valence band sampled over a tight k-point grid (area shaded in blue) as well as the widths of the valence band (VB, derived from the molecular HOMO) and the next lower band (VB-1, derived from the HOMO-3) for the **k**-path running from the Γ-point to the Brillouin zone boundary in a direction parallel to $\mathbf{a}_1$. In (b) the total energies per molecule including and disregarding van der Waals interactions are shown relative to the minimum energy obtained for the short-axis displacement. The dotted vertical line is a guide to the eye, while the dashed-dotted line denotes a shift by half of the unit-cell length. On the horizontal axis, the displacements are given in Å as well as in multiples of the corresponding unit-cell length.

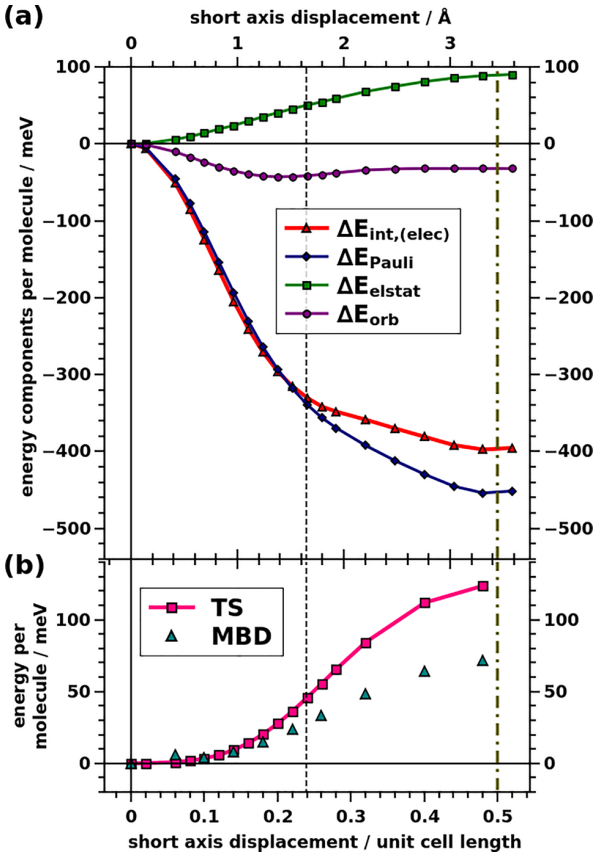

Figure 9. (a) PBE-calculated evolution of the electronic energy, ΔE_{int} (excluding a posteriori van der Waals corrections) and its components (Pauli repulsion energy, ΔE_{Pauli}, orbital interaction energy, $\Delta E_{orbital}$, and electrostatic energy, ΔE_{elstat}) as a function of the short-axis displacement in a coplanar quinacridone model crystal. The energies are given relative to the zero-displacement situation. (b) Evolution of the TS and MBD van der Waals correction energies with displacement.

along the long molecular axis (see Table 1). Intriguingly, this displacement amounts to 1.4 Å, which is very close to the zero-crossing of the transfer integrals for the model crystal upon long-axis displacement (at 1.5 Å). It also coincides with the minimum in total energy for this displacement. That is, in α-quinacridone one observes a situation where minimizing the energy also results in a vanishing transfer integral for the valence band. Interestingly, the calculated global energy minimum according to Figure 4 comprises a short-axis displacement of 0.3 Å (vide supra), which is well consistent with the experimental fact that the actual structure of α-quinacridone comprises not only a long- but also a smaller short-axis shift of the molecules (see above).

For β-quinacridone, the displacement along the short molecular axis dominates. For this direction, the coplanar crystal displays a very shallow minimum of the total energy, which does not necessarily coincide with the minimum in the electronic coupling for the valence band (see above). This suggests that even minor modifications in the crystal structure could easily result in situations with increased electronic couplings. This indeed is the case for β-quinacridone, where the equilibrium structure is characterized by a short-axis displacement of 2.0 Å, which is distinctly larger than the displacement of 1.6 Å representing the minimum bandwidth situation. This rationalizes the sharp increase of the electronic coupling in β-quinacridone compared to the α-phase (see Table 2).

The situation changes fundamentally in γ-quinacridone. Here, the total energy curve in Figure 5 is only of limited relevance due to the fundamentally different bonding motif in this polymorph, where the equilibrium displacement is strongly impacted by the position of the H-bonding sites and the equilibrium distance between two consecutive quinacridone planes (see Section 3.1). This explains the increase of the long-axis displacement by 0.3 Å compared to the α-phase, which in turn results also in a larger bandwidth consistent with the data in Table 2.

3.3. Molecular Displacements, Bandwidths, and Total Energies for a Coplanar Pentacene Model Crystal. In order to highlight the general validity of the above considerations, we performed analogous simulations for a coplanar pentacene model crystal. As shown in Figures 10 and 11, this yields similar trends as in the quinacridone case.

For the long-axis displacement, the total valence bandwidth again displays a pronounced succession of maxima and minima, where for short displacements there is a near perfect

DOI: 10.1021/acs.chemmater.9b01807
Chem. Mater. 2019, 31, 7054−7069

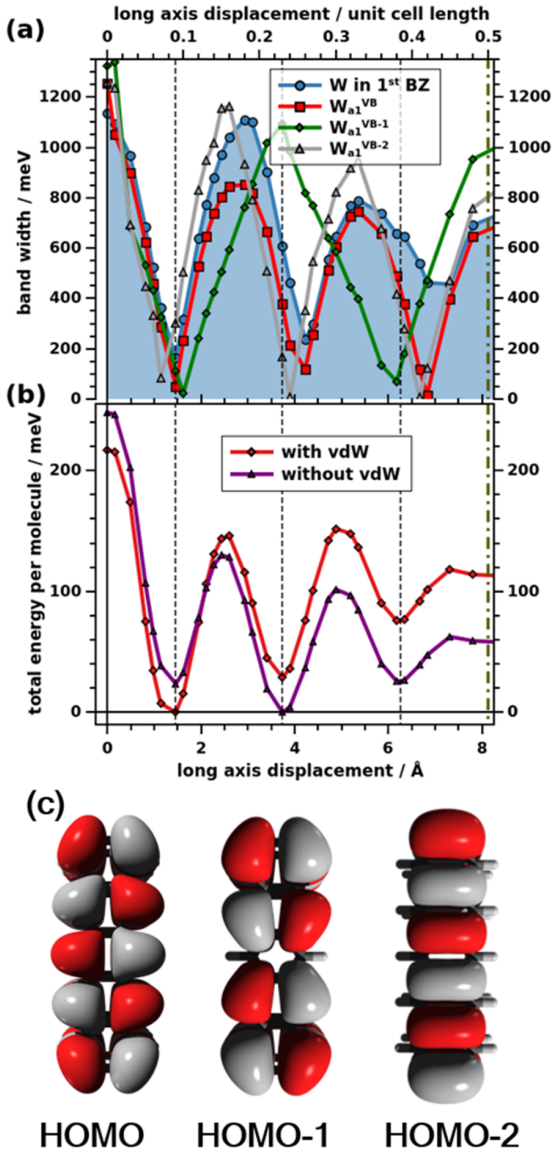

Figure 10. (a) Dependence of the bandwidths on the long-axis displacement for the coplanar pentacene model crystal. The total bandwidth of the valence band sampled over a tight k-point grid (area shaded in blue) as well as the widths of the valence band (VB, derived from the molecular HOMO) and the next two lower bands (VB-1, derived from the HOMO-1, and VB-2, derived from the HOMO-2) for the **k**-path running from the Γ-point to the Brillouin zone boundary in a direction parallel to $\mathbf{a}_1$ are shown. The values of *W* following the definition of the quantity in the Computational Methodology section underestimate the actual situation for small displacements. The reason for that is that there the bandwidths become so large that several valence bands overlap and the PBE calculated band gap vanishes (the corresponding band structure is shown in the Supporting Information). In (b), the total energies per molecule including and disregarding van der Waals interactions are plotted relative to the minimum energy obtained for long-axis displacement. The dotted vertical line is a guide to the eye, while the dashed-dotted line denotes a shift by half of the unit-cell length. On the horizontal axis, the displacements are given in Å as well as in multiples of the corresponding unit-cell length. Panel (c) contains isodensity plots of the three highest occupied molecular orbitals of pentacene.

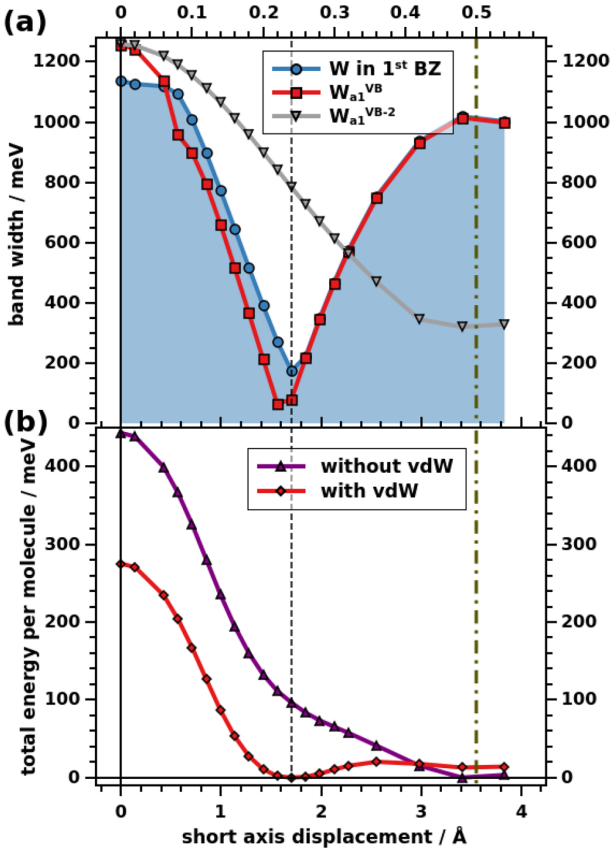

Figure 11. (a) Dependence of the bandwidths on the short-axis displacement for the coplanar pentacene model crystal. The total bandwidth of the valence band sampled over a tight k-point grid (area shaded in blue) as well as the widths of the valence band (VB, derived from the molecular HOMO) and the VB-2 (derived from the HOMO-2) for the **k**-path running from the Γ-point to the Brillouin zone boundary in a direction parallel to $\mathbf{a}_1$ are shown. The evolution for the VB-1 is not contained in the plot, as it follows that of the VB. The values of *W* following the definition of the quantity in the Computational Methodology section underestimate the actual situation for small displacements. The reason for that is that there the bandwidths become so large that several valence bands overlap and the PBE calculated band gap vanishes (the corresponding band structure is shown in the Supporting Information). In (b) the total energies per molecule including and disregarding van der Waals interactions are plotted relative to the minimum energy obtained for short-axis displacement. The dotted vertical line is a guide to the eye, while the dashed-dotted line denotes a shift by half of the unit-cell length. On the horizontal axis, the displacements are given in Å as well as in multiples of the corresponding unit-cell length.

agreement of the trend with that observed for the total energy. This correlation is once more lost for larger displacements, which also here can be rationalized by the impact of lower-lying, strongly dispersing occupied bands. In fact, as far as the latter aspect is concerned, pentacene serves as a particularly instructive example: As shown in Figure 10c, the molecular HOMO-1, which in the crystal forms the band directly below the valence band, has a smaller number of nodal planes perpendicular to the long molecular axis than the molecular HOMO (forming the valence band). Consequently, the relative displacements between consecutive minima in the bandwidth are larger. Conversely, for the molecular HOMO-2

DOI: 10.1021/acs.chemmater.9b01807
Chem. Mater. 2019, 31, 7054−7069

(and the associated band in the crystal) with an increased number of nodal planes, the number of minima increases.

As far as the short axis displacement is concerned, the overall trends are again similar to the situation in the coplanar quinacridone model crystal (see Figure 9). Particularly instructive in the pentacene case is again the evolution of the bandwidths for deeper-lying bands, in particular the VB-2 (derived from the molecular HOMO-2). There, due to the absence of a nodal plane perpendicular to the short molecular axis, the associated bandwidth reaches its minimum only, when the sheets are displaced by half the interpentacene distance. That is, they occur at twice the displacement for the minima of the VB and VB-1 (where the evolution of the latter essentially coincides with that of the valence band and, therefore, is not shown).

4. CONCLUSIONS

In the present work, we have examined the interplay between crystal packing, i.e., the relative stability of certain crystal structures, and transport relevant parameters for organic semiconductor crystals relying mostly on the instructive example of quinacridone. Comparing the electronic coupling in the three established, stable polymorphs of quinacridone, we find pronounced differences for the transfer integrals and bandwidths, which, however, do not correlate with the relative energies of the three structures. This prompted us to analyze a coplanar quinacridone model crystal, which allows relating various parameters characterizing the intermolecular electronic coupling (like bandwidths and transfer integrals) to the relative displacements of the quinacridone sheets. Even more importantly, as we simulate these displacements in a 3D periodic, crystalline environment, it is possible to correlate the evolution of the electronic coupling in the valence band with the energetic stability of specific configurations. For the sake of comparison, similar studies are performed for an analogous pentacene-based model system. These studies allow a number of conclusions: The largest bandwidths in both systems are observed for a cofacial, zero-displacement arrangement of the molecules. This configuration is, however, destabilized by Pauli repulsion and orbital rehybridization involving all electrons in the occupied π-bands. Consequently, there is a general driving force pushing the crystals toward a situation with reduced electronic couplings. This, for example, explains the particularly small transfer integrals in the π-stacking direction of α-quinacridone. For small displacements, one even observes a direct correlation between the total energy of a configuration and the width of the valence band;[34] i.e., the smaller the width of the valence band becomes the more a structure is stabilized. Thus, for realizing high-mobility materials, one cannot rely on the intrinsic interactions driving the self-assembly of the π-conjugated backbones. Instead one has to exploit, e.g., steric effects induced through chemical substitutions.[34,84−86] This is done, e.g., in the cases of rubrene[28,65,87] or TIPS-pentacene,[40] where recently efforts have been undertaken to vary packing and displacements by carefully tuning the substituents.[62,88] Alternative strategies for overcoming exchange repulsion comprise, e.g., heteroatom substitution and the inclusion of halogens in the periphery of the conjugated core, as discussed comprehensively in ref 34.

Interestingly, the direct correlation between electronic coupling in the valence band and total energy is lifted for larger displacements both in the long- and short-axis directions due to the different nodal structures of lower-lying π-bands. This means that, for structures more strongly displaced along the long molecular axis, a much smaller external stimulus (e.g., through substituents) should be enough for realizing large couplings in the valence band. Even more promising is to extrinsically control the short-axis displacement. In that case, a rather shallow local minimum in total energy as a function of the displacement is observed, as the detrimental exchange repulsion due to the valence band is more readily overcome by lower-lying bands derived from orbitals with fundamentally different nodal structures. This implies that, with only minor modifications in the intermolecular interactions, one should be able to significantly modify the relative arrangement of the molecules, which would then massively change the width of the frontier bands. In fact, this is to a certain extent already realized in β-quinacridone, where it results in an increase of the bandwidth in the π-stacking direction by nearly an order of magnitude compared to the α-phase.

■ ASSOCIATED CONTENT

Supporting Information

The Supporting Information is available free of charge on the ACS Publications website at DOI: 10.1021/acs.chemmater.9b01807.

Additional methodological details including a specification of the used PAW potentials, a detailed specification of the basis set used in the FHI-aims simulations, a description of the geometry optimization of the coplanar model crystal, a summary of how bandwidths have been calculated, a list of neighbors considered in the tight-binding fits, a description of complications arising for transfer integrals between successive quinacridone sheets in the coplanar model system, considerations regarding the stability of the tight-binding fit, data on the convergence of the k-point grid, data on the uncertainty of the machine-learning model, data on the impact of the used van der Waals correction and functional on band and orbital energies and total energies of the system, information on H-bonding energies and distances, the calculated band structures of the quinacridone polymorphs along the high symmetry directions, and additional information on deeper-lying bands and orbitals are shown in the Supporting Information (PDF)

■ AUTHOR INFORMATION

Corresponding Author

*(E.Z.) E-mail: egbert.zojer@tugraz.at.

ORCID

Oliver T. Hofmann: 0000-0002-2120-3259

Ralf Tonner: 0000-0002-6759-8559

Egbert Zojer: 0000-0002-6502-1721

Author Contributions

The manuscript was written through contributions of all authors. All authors have given approval to the final version of the manuscript.

Notes

The authors declare no competing financial interest.

■ ACKNOWLEDGMENTS

The work has been financially supported by the TU Graz Lead Project “Porous Materials at Work” (LP-03). Additional

DOI: 10.1021/acs.chemmater.9b01807
Chem. Mater. 2019, 31, 7054−7069

financial support by the Austrian Science Fund (FWF), P28631-N36, is gratefully acknowledged. The computational results have been in part achieved using the Vienna Scientific Cluster (VSC3). C.W. thanks Gernot J. Kraberger for stimulating discussions. R.T. thanks the German Science Foundation (DFG) for funding via SFB 1083. E.Z. and C.W. are grateful to Tomás Bucko and Andreas Hauser for stimulating discussions.

REFERENCES

(1) Pope, M.; Kallmann, H. P.; Magnante, P. Electroluminescence in Organic Crystals. *J. Chem. Phys.* **1963**, *38*, 2042−2043.
(2) Morel, D. L.; Ghosh, A. K.; Feng, T.; Stogryn, E. L.; Purwin, P. E.; Shaw, R. F.; Fishman, C. High-efficiency Organic Solar Cells. *Appl. Phys. Lett.* **1978**, *32*, 495−497.
(3) Barlow, S.; Brédas, J. L.; Getmanenko, Y. A.; Gieseking, R. L.; Hales, J. M.; Kim, H.; Marder, S. R.; Perry, J. W.; Risko, C.; Zhang, Y. Polymethine Materials with Solid-State Third-Order Optical Susceptibilities Suitable for All-Optical Signal-Processing Applications. *Mater. Horiz.* **2014**, *1*, 577−581.
(4) Tang, C. W. Two-layer Organic Photovoltaic Cell. *Appl. Phys. Lett.* **1986**, *48*, 183−185.
(5) Koezuka, H.; Tsumura, A.; Ando, T. Field-Effect Transistor with Polythiophene Thin Film. *Synth. Met.* **1987**, *18*, 699−704.
(6) Burroughes, J. H.; Bradley, D. D. C.; Brown, A. R.; Marks, R. N.; Mackay, K.; Friend, R. H.; Burns, P. L.; Holmes, A. B. Light-Emitting Diodes Based on Conjugated Polymers. *Nature* **1990**, *347*, 539−541.
(7) Hiramoto, M.; Fujiwara, H.; Yokoyama, M. Three-layered Organic Solar Cell with a Photoactive Interlayer of Codeposited Pigments. *Appl. Phys. Lett.* **1991**, *58*, 1062−1064.
(8) Garnier, F.; Hajlaoui, R.; Yassar, A.; Srivastava, P. All-Polymer Field-Effect Transistor Realized by Printing Techniques. *Science* **1994**, *265*, 1684−1686.
(9) Horowitz, G. Field-Effect Transistors Based on Short Organic Molecules. *J. Mater. Chem.* **1999**, *9*, 2021−2026.
(10) Hales, J. M.; Matichak, J.; Barlow, S.; Ohira, S.; Yesudas, K.; Brédas, J.-L.; Perry, J. W.; Marder, S. R. Design of Polymethine Dyes with Large Third-Order Optical Nonlinearities and Loss Figures of Merit. *Science* **2010**, *327*, 1485−1488.
(11) Gieseking, R. L.; Mukhopadhyay, S.; Shiring, S. B.; Risko, C.; Brédas, J.-L. Impact of Bulk Aggregation on the Electronic Structure of Streptocyanines: Implications for the Solid-State Nonlinear Optical Properties and All-Optical Switching Applications. *J. Phys. Chem. C* **2014**, *118*, 23575−23585.
(12) Gershenson, M. E.; Podzorov, V.; Morpurgo, A. F. Colloquium: Electronic Transport in Single-Crystal Organic Transistors. *Rev. Mod. Phys.* **2006**, *78*, 973−989.
(13) Coropceanu, V.; Cornil, J.; da Silva Filho, D. A.; Olivier, Y.; Silbey, R.; Brédas, J. L. Charge Transport in Organic Semiconductors. *Chem. Rev.* **2007**, *107*, 926−952.
(14) Oberhofer, H.; Reuter, K.; Blumberger, J. Charge Transport in Molecular Materials: An Assessment of Computational Methods. *Chem. Rev.* **2017**, *117*, 10319−10357.
(15) Tessler, N.; Preezant, Y.; Rappaport, N.; Roichman, Y. Charge Transport in Disordered Organic Materials and Its Relevance to Thin-Film Devices: A Tutorial Review. *Adv. Mater.* **2009**, *21*, 2741−2761.
(16) Fratini, S.; Mayou, D.; Ciuchi, S. The Transient Localization Scenario for Charge Transport in Crystalline Organic Materials. *Adv. Funct. Mater.* **2016**, *26*, 2292−2315.
(17) Winkler, C.; Mayer, F.; Zojer, E. Analyzing the Electronic Coupling in Molecular Crystals—The Instructive Case of A-Quinacridone. *Adv. Theory Simulations* **2019**, *2*, 1800204.
(18) Troisi, A.; Orlandi, G. Charge-Transport Regime of Crystalline Organic Semiconductors: Diffusion Limited by Thermal Off-Diagonal Electronic Disorder. *Phys. Rev. Lett.* **2006**, *96*, No. 086601.
(19) Ciuchi, S.; Fratini, S.; Mayou, D. Transient Localization in Crystalline Organic Semiconductors. *Phys. Rev. B: Condens. Matter Mater. Phys.* **2011**, *83*, No. 081202.
(20) Fratini, S.; Ciuchi, S. Bandlike Motion and Mobility Saturation in Organic Molecular Semiconductors. *Phys. Rev. Lett.* **2009**, *103*, 266601.
(21) Cheng, Y.-C.; Silbey, R. J. A Unified Theory for Charge-Carrier Transport in Organic Crystals. *J. Chem. Phys.* **2008**, *128*, 114713.
(22) Ortmann, F.; Bechstedt, F.; Hannewald, K. Theory of Charge Transport in Organic Crystals: Beyond Holstein's Small-Polaron Model. *Phys. Rev. B: Condens. Matter Mater. Phys.* **2009**, *79*, 235206.
(23) Fratini, S.; Ciuchi, S.; Mayou, D.; De Laissardière, G. T.; Troisi, A. A Map of High-Mobility Molecular Semiconductors. *Nat. Mater.* **2017**, *16*, 998−1002.
(24) Kwon, O.; Coropceanu, V.; Gruhn, N. E.; Durivage, J. C.; Laquindanum, J. G.; Katz, H. E.; Cornil, J.; Brédas, J. L. Characterization of the Molecular Parameters Determining Charge Transport in Anthradithiophene. *J. Chem. Phys.* **2004**, *120*, 8186−8194.
(25) Valeev, E. F.; Coropceanu, V.; Da Silva Filho, D. A.; Salman, S.; Brédas, J. L. Effect of Electronic Polarization on Charge-Transport Parameters in Molecular Organic Semiconductors. *J. Am. Chem. Soc.* **2006**, *128*, 9882−9886.
(26) Bredas, J. L.; Calbert, J. P.; da Silva Filho, D. A.; Cornil, J. Organic Semiconductors: A Theoretical Characterization of the Basic Parameters Governing Charge Transport. *Proc. Natl. Acad. Sci. U. S. A.* **2002**, *99*, 5804−5809.
(27) Lemaur, V.; Da Silva Filho, D. A.; Coropceanu, V.; Lehmann, M.; Geerts, Y.; Piris, J.; Debije, M. G.; Van De Craats, A. M.; Senthilkumar, K.; Siebbeles, L. D. A.; et al. Charge Transport Properties in Discotic Liquid Crystals: A Quantum-Chemical Insight into Structure-Property Relationships. *J. Am. Chem. Soc.* **2004**, *126*, 3271−3279.
(28) da Silva Filho, D. A.; Kim, E.-G.; Brédas, J.-L. Transport Properties in the Rubrene Crystal: Electronic Coupling and Vibrational Reorganization Energy. *Adv. Mater.* **2005**, *17*, 1072−1076.
(29) Kazmaier, P. M.; Hoffmann, R. A Theoretical Study of Crystallochromy. Quantum Interference Effects in the Spectra of Perylene Pigments. *J. Am. Chem. Soc.* **1994**, *116*, 9684−9691.
(30) Hoffmann, R. Die Begegnung von Chemie Und Physik Im Festkörper. *Angew. Chem.* **1987**, *99*, 871−906.
(31) Hoffmann, R. A Chemical and Theoretical Way to Look at Bonding on Surfaces. *Rev. Mod. Phys.* **1988**, *60*, 601−628.
(32) Chung, H.; Diao, Y. Polymorphism as an Emerging Design Strategy for High Performance Organic Electronics. *J. Mater. Chem. C* **2016**, *4*, 3915−3933.
(33) Diao, Y.; Lenn, K. M.; Lee, W. Y.; Blood-Forsythe, M. A.; Xu, J.; Mao, Y.; Kim, Y.; Reinspach, J. A.; Park, S.; Aspuru-Guzik, A.; et al. Understanding Polymorphism in Organic Semiconductor Thin Films through Nanoconfinement. *J. Am. Chem. Soc.* **2014**, *136*, 17046−17057.
(34) Sutton, C.; Risko, C.; Brédas, J.-L. Noncovalent Intermolecular Interactions in Organic Electronic Materials: Implications for the Molecular Packing vs Electronic Properties of Acenes. *Chem. Mater.* **2016**, *28*, 3−16.
(35) Paulus, E. F.; Leusen, F. J. J.; Schmidt, M. U. Crystal Structures of Quinacridones. *CrystEngComm* **2007**, *9*, 131−143.
(36) Klues, M.; Witte, G. Crystalline Packing in Pentacene-like Organic Semiconductors. *CrystEngComm* **2018**, *20*, 63−74.
(37) Campbell, R. B.; Robertson, J. M.; Trotter, J. IUCr. The Crystal and Molecular Structure of Pentacene. *Acta Crystallogr.* **1961**, *14*, 705−711.
(38) Park, S. K.; Jackson, T. N.; Anthony, J. E.; Mourey, D. A. High Mobility Solution Processed 6,13-Bis(Triisopropyl-Silylethynyl) Pentacene Organic Thin Film Transistors. *Appl. Phys. Lett.* **2007**, *91*, No. 063514.
(39) Reese, C.; Bao, Z. High-Resolution Measurement of the Anisotropy of Charge Transport in Single Crystals. *Adv. Mater.* **2007**, *19*, 4535−4538.
(40) Anthony, J. E.; Brooks, J. S.; Eaton, D. L.; Parkin, S. R. Functionalized Pentacene: Improved Electronic Properties from

DOI: 10.1021/acs.chemmater.9b01807
Chem. Mater. 2019, 31, 7054−7069

Control of Solid-State Order. *J. Am. Chem. Soc.* **2001**, *123*, 9482−9483.
(41) Haddon, R. C.; Siegrist, T.; Fleming, R. M.; Bridenbaugh, P. M.; Laudise, R. A. Band Structures of Organic Thin Film Transistor Materials. *J. Mater. Chem.* **1995**, *5*, 1719−1724.
(42) Volkhard May, O. K. *Charge and Energy Transfer Dynamics in Molecular Systems*, 3rd ed.; Wiley-VCH Verlag GmbH & Co. KGaA: Weinheim, Germany, 2011.
(43) Davis, W. B.; Svec, W. A.; Ratner, M. A.; Wasielewski, M. R. Molecular-Wire Behaviour in p-Phenylenevinylene Oligomers. *Nature* **1998**, *396*, 60−63.
(44) Petrov, E. G.; May, V. A Unified Description of Superexchange and Sequential Donor-Acceptor Electron Transfer Mediated by a Molecular Bridge. *J. Phys. Chem. A* **2001**, *105*, 10176−10186.
(45) Hopfield, J. J.; Onuchic, J. N.; Beratan, D. N. Electronic Shift Register Memory Based on Molecular Electron-Transfer Reactions. *J. Phys. Chem.* **1989**, *93*, 6350−6357.
(46) Blum, V.; Gehrke, R.; Hanke, F.; Havu, P.; Havu, V.; Ren, X.; Reuter, K.; Scheffler, M. Ab Initio Molecular Simulations with Numeric Atom-Centered Orbitals. *Comput. Phys. Commun.* **2009**, *180*, 2175−2196.
(47) Perdew, J. P.; Burke, K.; Ernzerhof, M. Generalized Gradient Approximation Made Simple. *Phys. Rev. Lett.* **1996**, *77*, 3865−3868.
(48) Perdew, J. P.; Burke, K.; Ernzerhof, M. Erratum: Generalized Gradient Approximation Made Simple (Physical Review Letters (1996) 77 (3865)). *Phys. Rev. Lett.* **1997**, *78*, 1396.
(49) Mayer, F. Electronic Couplings in Molecular Crystals: Development and Benchmarking of Advanced Strategies; Graz University of Technology, 2019.
(50) Kresse, G.; Hafner, J. Ab Initio Molecular Dynamics for Liquid Metals. *Phys. Rev. B: Condens. Matter Mater. Phys.* **1993**, *47*, 558−561.
(51) Kresse, G.; Hafner, J. Ab Initio Molecular-Dynamics Simulation of the Liquid-Metalamorphous- Semiconductor Transition in Germanium. *Phys. Rev. B: Condens. Matter Mater. Phys.* **1994**, *49*, 14251−14269.
(52) Kresse, G.; Furthmüller, J. Efficiency of Ab-Initio Total Energy Calculations for Metals and Semiconductors Using a Plane-Wave Basis Set. *Comput. Mater. Sci.* **1996**, *6*, 15−50.
(53) Kresse, G.; Furthmüller, J. Efficient Iterative Schemes for Ab Initio Total-Energy Calculations Using a Plane-Wave Basis Set. *Phys. Rev. B: Condens. Matter Mater. Phys.* **1996**, *54*, 11169−11186.
(54) Tkatchenko, A.; Scheffler, M. Accurate Molecular Van Der Waals Interactions from Ground-State Electron Density and Free-Atom Reference Data. *Phys. Rev. Lett.* **2009**, *102*, No. 073005.
(55) Kresse, G.; Joubert, D. From Ultrasoft Pseudopotentials to the Projector Augmented-Wave Method. *Phys. Rev. B: Condens. Matter Mater. Phys.* **1999**, *59*, 1758−1775.
(56) Methfessel, M.; Paxton, A. T. High-Precision Sampling for Brillouin-Zone Integration in Metals. *Phys. Rev. B: Condens. Matter Mater. Phys.* **1989**, *40*, 3616−3621.
(57) Ambrosetti, A.; Reilly, A. M.; Distasio, R. A.; Tkatchenko, A. Long-Range Correlation Energy Calculated from Coupled Atomic Response Functions. *J. Chem. Phys.* **2014**, *140*, 18A508.
(58) Krukau, A. V.; Vydrov, O. A.; Izmaylov, A. F.; Scuseria, G. E. Influence of the exchange screening parameter on the performance of screened hybrid functionals. *J. Chem. Phys.* **2006**, *125*, 224106.
(59) Heyd, J.; Scuseria, G. E.; Ernzerhof, M. Hybrid Functionals Based on a Screened Coulomb Potential. *J. Chem. Phys.* **2003**, *118*, 8207−8215.
(60) Heyd, J.; Scuseria, G. E.; Ernzerhof, M. Erratum: Hybrid Functionals Based on a Screened Coulomb Potential (Journal of Chemical Physics (2003) 118 (8207)). *J. Chem. Phys.* **2006**, *124*, 219906.
(61) Lüftner, D.; Refaely-Abramson, S.; Pachler, M.; Resel, R.; Ramsey, M. G.; Kronik, L.; Puschnig, P. Experimental and Theoretical Electronic Structure of Quinacridone. *Phys. Rev. B: Condens. Matter Mater. Phys.* **2014**, *90*, No. 075204.
(62) Thorley, K. J.; Finn, T. W.; Jarolimek, K.; Anthony, J. E.; Risko, C. Theory-Driven Insight into the Crystal Packing of Trialkylsilylethynyl Pentacenes. *Chem. Mater.* **2017**, *29*, 2502−2512.
(63) Mitoraj, M. P.; Michalak, A.; Ziegler, T. A Combined Charge and Energy Decomposition Scheme for Bond Analysis. *J. Chem. Theory Comput.* **2009**, *5*, 962−975.
(64) Ryno, S. M.; Risko, C.; Brédas, J. L. Noncovalent Interactions and Impact of Charge Penetration Effects in Linear Oligoacene Dimers and Single Crystals. *Chem. Mater.* **2016**, *28*, 3990−4000.
(65) Sutton, C.; Marshall, M. S.; Sherrill, C. D.; Risko, C.; Brédas, J. L. Rubrene: The Interplay between Intramolecular and Intermolecular Interactions Determines the Planarization of Its Tetracene Core in the Solid State. *J. Am. Chem. Soc.* **2015**, *137*, 8775−8782.
(66) Sherrill, C. D. Energy Component Analysis of π Interactions. *Acc. Chem. Res.* **2013**, *46*, 1020−1028.
(67) Pastorczak, E.; Corminboeuf, C. Perspective: Found in Translation: Quantum Chemical Tools for Grasping Non-Covalent Interactions. *J. Chem. Phys.* **2017**, *146*, 120901.
(68) Pecher, L.; Tonner, R. Deriving Bonding Concepts for Molecules, Surfaces, and Solids with Energy Decomposition Analysis for Extended Systems. *Wiley Interdiscip. Rev. Comput. Mol. Sci.* **2019**, *9*, No. e1401.
(69) Ziegler, T.; Rauk, A. On the Calculation of Bonding Energies by the Hartree Fock Slater Method - I. *Transition State Method. Theor. Chim. Acta* **1977**, *46*, 1−10.
(70) Bickelhaupt, F. M.; Baerends, E. J. Kohn-Sham Density Functional Theory: Predicting and Understanding Chemistry. In *Reviews in computational chemistry*; Wiley-VCH: Verlag, 2007; Vol. *15*, pp 1−86.
(71) Zhao, L.; von Hopffgarten, M.; Andrada, D. M.; Frenking, G. Energy Decomposition Analysis. *Wiley Interdiscip. Rev. Comput. Mol. Sci.* **2018**, *8*, No. e1345.
(72) Raupach, M.; Tonner, R. A Periodic Energy Decomposition Analysis Method for the Investigation of Chemical Bonding in Extended Systems. *J. Chem. Phys.* **2015**, *142*, 194105.
(73) Sinnokrot, M. O.; Sherrill, C. D. Substituent Effects in π-π Interactions: Sandwich and t-Shaped Configurations. *J. Am. Chem. Soc.* **2004**, *126*, 7690−7697.
(74) Wheeler, S. E. Local Nature of Substituent Effects in Stacking Interactions. *J. Am. Chem. Soc.* **2011**, *133*, 10262−10274.
(75) Stasyuk, O. A.; Sedlak, R.; Guerra, C. F.; Hobza, P. Comparison of the DFT-SAPT and Canonical EDA Schemes for the Energy Decomposition of Various Types of Noncovalent Interactions. *J. Chem. Theory Comput.* **2018**, *14*, 3440−3450.
(76) te Velde, G.; Bickelhaupt, F. M.; Baerends, E. J.; Fonseca Guerra, C.; van Gisbergen, S. J. A.; Snijders, J. G.; Ziegler, T. Chemistry with ADF. *J. Comput. Chem.* **2001**, *22*, 931−967.
(77) Fonseca Guerra, C.; Snijders, J. G.; Te Velde, G.; Baerends, E. J. Towards an Order-N DFT Method. *Theor. Chem. Acc.* **1998**, *99*, 391−403.
(78) Baerends, E. J.; Ziegler, T.; Atkins, A. J.; Autschbach, J.; Bashford, D.; Baseggio, O.; Bérces, A.; Bickelhaupt, F. M.; Bo, C.; Boerritger, P. M.; et al. *ADF2018, SCM, Theoretical Chemistry*; Vrije Universiteit: Amsterdam, The Netherlands, https://www.scm.com.
(79) Van Lenthe, E.; Baerends, E. J. Optimized Slater-Type Basis Sets for the Elements 1−118. *J. Comput. Chem.* **2003**, *24*, 1142−1156.
(80) Stukowski, A. Visualization and Analysis of Atomistic Simulation Data with OVITO−the Open Visualization Tool. *Modell. Simul. Mater. Sci. Eng.* **2010**, *18*, No. 015012.
(81) Hanwell, M. D.; Curtis, D. E.; Lonie, D. C.; Vandermeersch, T.; Zurek, E.; Hutchison, G. R. Avogadro: An Advanced Semantic Chemical Editor, Visualization, and Analysis Platform. *J. Cheminf.* **2012**, *4*, 17.
(82) Gao, H. Z. Theoretical Study on Charge Transport of Quinacridone Polymorphs. *Int. J. Quantum Chem.* **2012**, *112*, 740−746.
(83) Głowacki, E. D.; Leonat, L.; Irimia-vladu, M.; Schwödiauer, R.; Ullah, M.; Sitter, H.; Bauer, S.; Sariciftci, N. S. Intermolecular Hydrogen-Bonded Organic Semiconductors — Quinacridone versus

DOI: 10.1021/acs.chemmater.9b01807
Chem. Mater. 2019, 31, 7054−7069

Pentacene Intermolecular Hydrogen-Bonded Organic Semiconductors — Quinacridone versus Pentacene. *Appl. Phys. Lett.* **2012**, *101*, 023305.
(84) Mei, J.; Diao, Y.; Appleton, A. L.; Fang, L.; Bao, Z. Integrated Materials Design of Organic Semiconductors for Field-Effect Transistors. *J. Am. Chem. Soc.* **2013**, *135*, 6724−6746.
(85) Anthony, J. E. Functionalized Acenes and Heteroacenes for Organic Electronics. *Chem. Rev.* **2006**, *106*, 5028−5048.
(86) Okamoto, T.; Nakahara, K.; Saeki, A.; Seki, S.; Oh, J. H.; Akkerman, H. B.; Bao, Z.; Matsuo, Y. Aryl-Perfluoroaryl Substituted Tetracene: Induction of Face-to-Face π-π Stacking and Enhancement of Charge Carrier Properties. *Chem. Mater.* **2011**, *23*, 1646−1649.
(87) McGarry, K. A.; Xie, W.; Sutton, C.; Risko, C.; Wu, Y.; Young, V. G.; Brédas, J.-L. L.; Frisbie, C. D.; Douglas, C. J. Rubrene-Based Single-Crystal Organic Semiconductors: Synthesis, Electronic Structure, and Charge-Transport Properties. *Chem. Mater.* **2013**, *25*, 2254−2263.
(88) Sorli, J. C.; Ai, Q.; Granger, D. B.; Gu, K.; Parkin, S.; Jarolimek, K.; Telesz, N.; Anthony, J. E.; Risko, C.; Loo, Y.-L. L. Impact of Atomistic Substitution on Thin-Film Structure and Charge Transport in a Germanyl-Ethynyl Functionalized Pentacene. *Chem. Mater.* **2019**, DOI: 10.1021/acs.chemmater.9b00546.

DOI: 10.1021/acs.chemmater.9b01807
Chem. Mater. 2019, 31, 7054−7069

3.3. Supporting Information

Supporting Information for:

Understanding the correlation between electronic coupling and energetic stability of molecular crystal polymorphs: The instructive case of quinacridone

*Christian Winkler,[1] Andreas Jeindl,[1] Florian Mayer,[1] Oliver T. Hofmann,[1] Ralf Tonner,[2] and Egbert Zojer[1]**

[1]Institute of Solid State Physics, NAWI Graz, Graz University of Technology, Petersgasse 16, 8010 Graz, Austria

[2]Department of Chemistry, Philipps-Universität Marburg, Hans-Meerwein-Straße 4, 35032 Marburg, Germany

1. Additional methodological details

1.1 Overview of PAW potentials used in the VASP calculations

The following list contains the headers of all used PAW potentials, which allows their unambiguous dentification:

Carbon: PAW_PBE C 08Apr2002

Hydrogen: PAW_PBE H 15Jun2001

Nitrogen: PAW_PBE N 08Apr2002

Oxygen: PAW_PBE O 08Apr2002

1.2 Overview of basis functions used in FHI-AIMS

Table S1. *Basis functions that have been used for all calculations performed with FHI-AIMS. The abbreviations read as follows: H(nl,z), where H describes the type of the basis function where H stands for hydrogen-like type function, n is the main quantum number, l denotes the angular momentum quantum number, and z denotes an effective nuclear charge which scales the radial function in the defining Coulomb potential.*[1]

	H	C	N	O
Minimal	1s	[He]+2s2p	[He]+2s2p	[He]+2s2p
Tier 1	H(2s,2.1) H(2p,3.5)	H(2p,1.7) H(3d,6) H(2s,4.9)	H(2p,1.8) H(3d,6.8) H(3s,5.8)	H(2p,1.8) H(3d,7.6) H(3s,6.4)
Tier 2	H(1s,0.85) H(2p,3.7) H(2s,1.2) H(3d,7)	H(4f,9.8) H(3p,5.2) H(3s,4.3) H(5g,14.4) H(3d,6.2)	H(4f,10.8) H(3p,5.8) H(1s,0.8) H(5g,16) H(3d,4.9)	H(4f,11.6) H(3p,6.2) H(3d,5.6) H(5g,17.6) H(1s,0.75)

1.3. Details of the geometry optimizations of the coplanar model systems for quinacridone and pentacene.

As constraining only individual lattice constants in geometry optimizations is not straightforward in the VASP code, we employed FHI-aims[1] for optimizing the structures of the coplanar model crystals. Also here, we used the PBE[2,3] exchange correlation functional with a tight basis set and the TS[4] dispersion correction.

For quinacridone we performed the constrained geometry optimization on the unit cell constructed as described in the main manuscript employing a 2×2×2 k-point grid and a force threshold of 0.05eV/Å threshold. Doing the same for pentacene in the tight crystal packing configuration resulted in an artificial stabilization of the zero-displacement geometry, when subsequently analysing the impact of inter-molecular displacements by means of single-point calculations. This is shown below in the evolution of the total energy as a function of the long-axis displacement. Notably no such stabilization was observed for quinacridone. The situation also could not be resolved by tilting the $\mathbf{a}_1$ vector in the optimization, i.e., optimizing a densely-packed system with molecules displaced by 0.5 Å. Therefore, we increased the force-convergence criterion to 0.01eV/Å decoupled consecutive pentacene sheets by increasing the inter-layer distance to 40 Å and switched to a 25×25×1 k-point grid. When the resulting molecular geometry and then performing single-point calculations for a densely-packed system at varying displacements, this led to the expected behaviour ("free-standing monolayer" in Figure S1). At this stage, we do not fully understand the problems encountered when optimizing the densely packed layer and subsequently using the such-optimized geometry of the pentacene molecule for further studies, but hypothesize that it might be related to the observation that coplanar pentacene at small displacements becomes metallic when employing the PBE functional. This notion is further supported by the finding that when building the coplanar model crystal from pentacene molecules in their gas-phase configuration, the results equivalent to those for the "free-standing monolayer" have been obtained.

Finally, we compared the dependence of the total energy on the long axis displacement in quinacridone for molecular geometries obtained via the bulk crystal and the free-standing monolayer approach and observed differences of only at the most 5 meV.

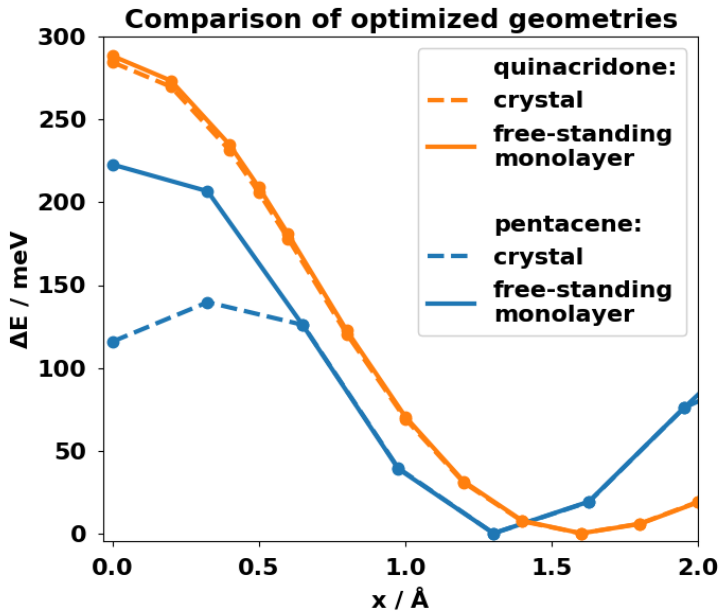

Figure S1. *Total energies of coplanar quinacridone and pentacene model crystals for a distance of 3.5 Å between the sheets. The curves differ in the way the geometries of the molecules building up the crystal have been obtained. In the "crystal" case, they have been optimized for a densely-packed system with an inter-sheet distance of 3.5 Å, while in the "free-standing monolayer" case, they have been optimized for quasi-isolated molecular sheets. For the single-point calculations in this test a 2×2×5 k-point grid in conjunction with FHI-aims has been used.*

1.4. k-point convergence for the orthorhombic model system

Table S2. *VASP calculated total energies of the orthorhombic model system as a function of the employed k-grid. Two displacements (given in multiples of the unit-cell lengths) have been evaluated and the absolute values as well as their difference are given in eV.*

displacement	**Γ**	**2x2x2**	**5x3x5**	**6x6x6**	**12x12x12**	**25x25x25**	
0.0	-514.898	-515.789	-515.795	-515.795	-515.795	-515.795	vdW TS
0.1	-516.121	-516.365	-516.366	-516.366	-516.366	-516.366	
Δ	-1.223	-0.576	-0.571	-0.571	-0.571	-0.571	
0.0	-510.185	-511.04	-511.045	-511.045	-511.045	-511.045	no vdW
0.1	-511.402	-511.628	-511.629	-511.629	-511.629	-511.629	

Δ	-1.217	-0.588	-0.584	-0.584	-0.584	-0.584	

Table S3. *ADF-BAND calculated total energies of the orthorhombic model system as a function of the employed k-grid. Two displacements have been evaluated and the absolute values as well as their difference are given in eV.*

displacement	Γ	5x3x5	6x6x6
0.0	-515.778	-516.635	-516.635
0.1	-516.941	-517.180	-517.181
Δ	-1.163	0.545	0.546

1.5. Evaluation of the Band Width (W)

Two different procedures had to be used for evaluating the band width. Here we start with the simpler and more common one: One can calculate the electronic band structure along a certain path connecting high-symmetry k-points, then follow the bands of interest (VB and CB here) along that path and extract the band width as the difference between the maximum and minimum values of the energies along that **k**-path. Here, because of the two molecules in the unit cell, in some cases there is a backfolding of the electronic bands in one direction and therefore we have to take this into account. This is particularly relevant for the coplanar model system, where the doubling of the size of the unit cell occurs in the direction that is further analyzed (the $\mathbf{a}_1$ direction). In such a case, we plot the band and then follow it along a path from Γ to X and back to Γ. This helps us to determine which eigenvalue at Γ belongs to which band (including the backfolding). We then define the band width in a specific direction as the energetic splitting between these two energies at the Γ-point. For simple (cosine shaped) bands the such defined band width directly corresponds to the range of energies covered by the band in the chosen direction. Only close to the maxima of the band widths there can be some minor deviations as then the shape of the band can potentially deviate from a simple cosine. However, these deviations do not have any qualitative influence on the evolution of the band-widths as a function of the molecular displacement. This procedure is illustrated for several exemplary displacements in Figure S2.

In this way, we can account for band crossings when analyzing individual k-paths. This is, however, not possible when determining the total band width in the entire first Brillouin zone, as

there it is not possible to visually follow an individual band and determine, whether or not band crossings play a role. Therefore, we define the total band width (of the valence band) as the difference between the maximum amongst all k-points of the highest occupied eigenstate and the minimum amongst all k-points of the second highest eigenstate. The highest- and the second-highest eigenstates are both considered to again account for the backfolding of the band resulting from the doubling of the unit-cell size. As long as the band widths are not too large, this procedure works perfectly, but as soon as the bands start crossing for particularly large couplings, the total range of energies covered by the valence band is larger than the total band widths determined by the procedure described above.

Due to the different definitions, in such cases the total band width can even become smaller than the band widths along specific high-symmetry directions, where band crossings can be identified. The situation becomes particularly involved for pentacene at zero displacement. There, the band widths become so large that several valence bands overlap and the PBE gap vanishes. This leads to an even larger “underestimation” of the total band width when employing the above procedure, but can again be accounted for when evaluating the band widths along a certain k-path “by hand”.

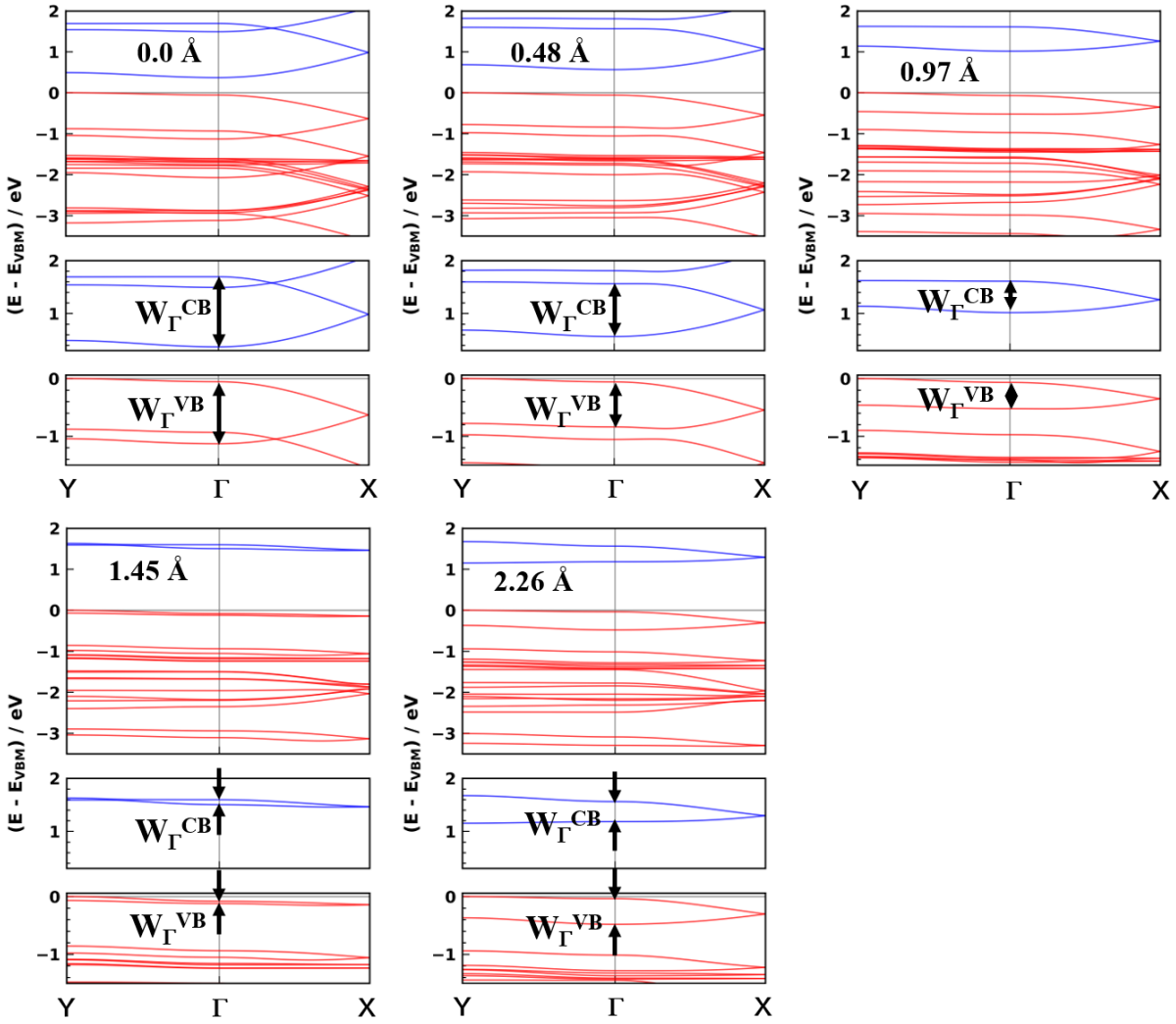

Figure S2. *Electronic band structure of the coplanar model crystal for various long axis displacements. The lower panels show a zoom in to the region around the valence and conduction band. The band-widths for k-paths along the Γ-X direction following the above definition are indicated by the black arrows.*

1.6. List of neighbors included in the set-up of the tight-binding model function

Table S4. *Transfer integrals (neighboring molecules) included in the tight-binding fits for the valence band. The neighbors which are included are marked by an X.*

	Polymorph			
coordinate	**α**	**β**	**γ**	**model crystal**
$\mathbf{a}_1$	X	X	X	X
$\mathbf{a}_2$	X	X	X	X
$\mathbf{a}_3$	X	X	X	X
$\mathbf{a}_1+\mathbf{a}_2$	X	X	X	X
$\mathbf{a}_1-\mathbf{a}_2$	X	X	X	X
$\mathbf{a}_2+\mathbf{a}_3$	X	X	X	-
$\mathbf{a}_2-\mathbf{a}_3$	X	X	X	-
$2\times\mathbf{a}_1$	X	-	-	-
$\mathbf{a}_1+\mathbf{a}_2+\mathbf{a}_3$	X	-	-	-
		All above expressions + $\mathbf{R}_{AB}$		

1.7. Complications arising for transfer integrals between successive quinacridone sheets in the coplanar model system

For the coplanar model system, we are mostly concerned with the bands running in the π-stacking direction and in the direction perpendicular to the 2D quinacridone sheets (Figure 1d, i.e., parallel to $\mathbf{a}_1$). The valence band will be dominated by the couplings to molecules displaced in **AB** and in

AB-a$_3$ direction (see Figure 1 in the main manuscript). If only these couplings are considered, Equations (2) and (3) simplify to

$$\varepsilon = \varepsilon_0 \pm 2\left|cos\left(\frac{\boldsymbol{ka_1}}{2}\right)\right|\sqrt{\left(t_{\boldsymbol{AB}}^2 + t_{\boldsymbol{AB-a3}}^2 + 2t_{\boldsymbol{AB}}t_{\boldsymbol{AB-a3}}cos(\boldsymbol{ka_3})\right)} \qquad \text{(S1).}$$

From this equation it becomes apparent that the signs of t_{AB} and and $t_{AB\text{-}a3}$ no longer count independently, but that all that matters is, whether they are the same or different. Equation (S1) can be further simplified for the band running parallel to the $\mathbf{a}_1$ direction, as then $\mathbf{k}\cdot\mathbf{a}_3$ vanishes. The expression for the energy then reads:

$$\varepsilon_{\boldsymbol{a1}} = \varepsilon_0 \pm 2\left|cos\left(\frac{\boldsymbol{ka_1}}{2}\right)\right|\left|t_{\boldsymbol{AB}} + t_{\boldsymbol{AB-a3}}\right| \qquad \text{(S2)}$$

I.e., for the dispersion of that band only the absolute value of the sum of $\mathbf{t}_{AB}$ and $\mathbf{t}_{AB\text{-}a3}$ counts. Therefore, only that sum is displayed in the main manuscript in Figure 5. The absolute values of the individual components $\mathbf{t}_{AB}$ and $\mathbf{t}_{AB\text{-}a3}$ are displayed in Figure S3.

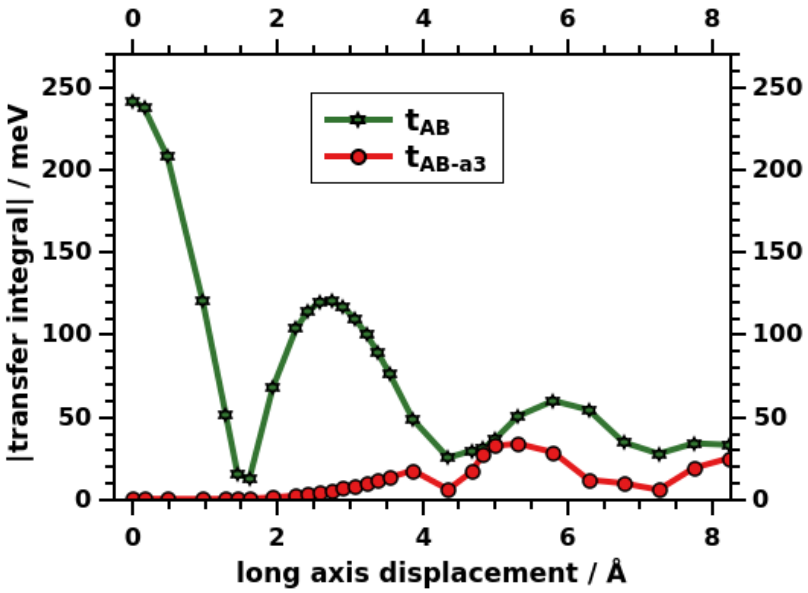

Figure S3. *Evolution of transfer integrals* t_{AB} *and* $t_{AB\text{-}a3}$ *of the coplanar quinacridone model system as a function of the long axis displacement.*

1.8. Stability of the tight-binding fit parameters

Whenever employing the more complex tight-binding model which considers two inequivalent molecules in the unit cell, the choice of the starting values for the fit-parameters (transfer integrals) becomes crucial. Employing standard fit algorithms like least squares, or Levenberg Marquard and not paying attention to the starting values one can easily end up in a local minimum. Choosing the starting values for the transfer integrals close to the absolute values of a molecular dimer solved this problem for the quinacridone polymorphs and the quinacridone model system. However, it is highly advisable to pay close attention to the starting values and to test, whether one actually has converged to the correct minimum.

1.9. Uncertainty of the machine learning model

Gaussian process regression allows to evaluate the uncertainty of the model prediction (as a standard deviation) at each point, resulting in an uncertainty map. Those uncertainties have a maximum value of around 50 meV and correspond roughly to the real error when adding a new point at a position with high uncertainty. Figure S4 shows such an uncertainty map for the total energy of quinacridone. One can see that, at all trained points, the uncertainty is very low, while for some other areas the uncertainty rises up to 50 meV. The uncertainty along the main axes is so low, because we used all 1D-sweep data points from Figures 5 and 8 of the main manuscript for the training.

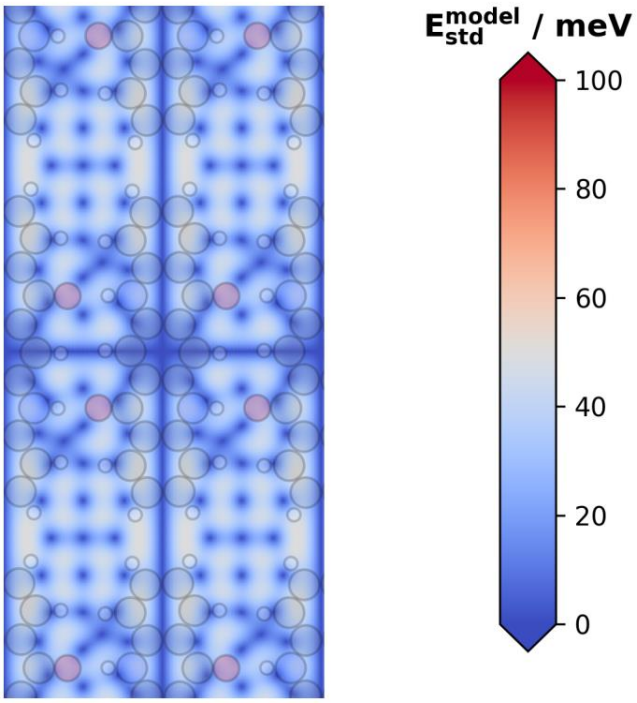

Figure S4. *Uncertainty map for the total energy of quinacridone. The blue areas are positions where a data point has been calculated.*

2 Evaluating the impact of the employed functional and van der Waals correction

2.1 Band structures of quinacridone polymorphs calculated using PBE and HSE.

When calculating the electronic band structure of the three quinacridone polymorphs with the PBE functional[2,3] (semi-local GGA) and also with HSE06[5,6] (range-separated hybrid functional) we find the expected increase of the band gap when using HSE06 instead of PBE. The PBE results have been obtained using VASP (5.4.4) and the HSE06 results by using FHI-aims.[1] As far as the shapes, widths and curvatures of the frontier bands are concerned, a comparison of the top and bottom panels of Figures S5, S6, and S7 shows that no fundamental changes occur. The overall evolution of the bands is independent of the used functional. Furthermore, when comparing the band widths

obtained by PBE (red) to the ones for HSE06 (black) one can see that for most directions these values agree quite well, with the HSE06 widths being typically by ~15 % larger. The only exception is direction XΓ for the α-polymorph. There, the band width increases by almost 80% when using HSE06 instead of PBE, but here the values are very small such that a large relative change translates in an increase of the band width of only 17 meV. Most importantly, in none of the cases the qualitative trends are impacted by the choice of the functional. Furthermore, when considering the orthorhombic model crystal at 0.00 and 0.10 long axis displacement we find that by using PBE instead of the hybrid functional HSE06 we underestimate the band-width by about 15 %, similar to the results for the polymorphs. However, despite this underestimation, the overall evolution of the electronic frontier bands agrees quite well for PBE and HSE06. Based on these data one can conclude that the use of the much cheaper PBE functional is justified.

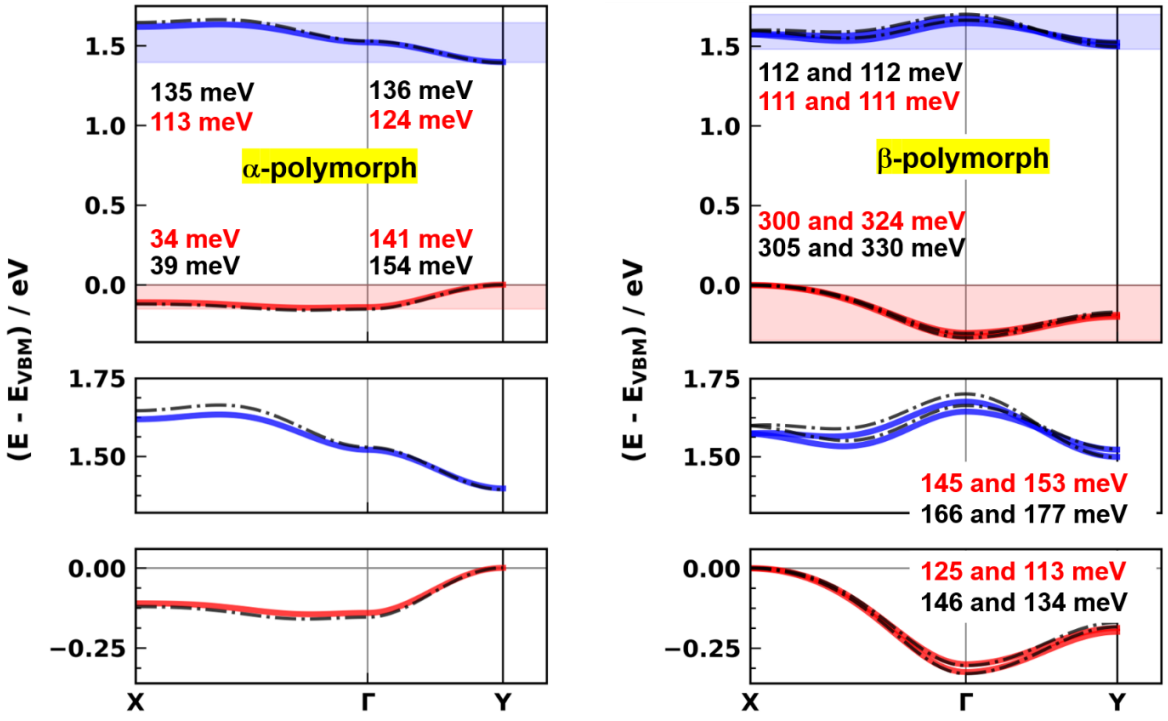

Figure S5. *Electronic band structure of the α- and β-polymorph of quinacridone obtained by performing DFT calculations using the PBE functional (solid lines) and the HSE functional (dash dotted). The electronic bands have been calculated for the high-symmetry k-path XΓY. The values of the corresponding band-widths are also given in these plots. The red values correspond to the*

PBE functional and the black ones to the HSE06 functional. All valence bands (conduction bands) are aligned to the respective valence band maximum (conduction band minimum) of the PBE calculation. Concerning the band gaps of the three polymorphs, we find that they increase when HSE06 is used instead of PBE. This is what can be expected when going from a semi-local GGA functional to a hybrid functional. The values of the band gaps are PBE(HSE): α-polymorph 1.39 eV (2.05 eV), β-polymorph 1.34 eV (2.05 eV) and γ-polymorph 1.35 eV (1.99 eV).

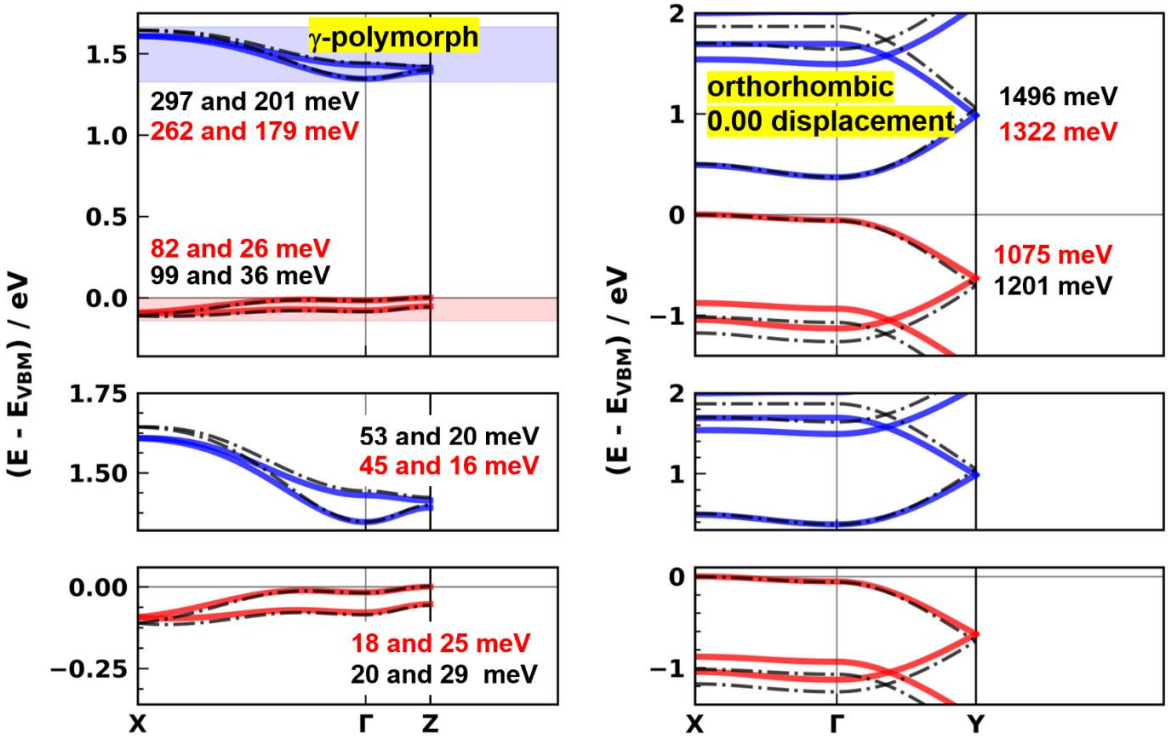

Figure S6. *Electronic band structure of the γ-polymorph of quinacridone and the orthorhombic model crystal at 0.00 long axis displacement. The results were obtained by performing DFT calculations using the PBE functional (solid lines) and the HSE functional (dash dotted). The electronic bands have been calculated for the high-symmetry k-path XΓZ for γ and XΓY for the orthorhombic system. The values of the corresponding band-widths are also given in these plots. The red values correspond to the PBE functional and the black ones to the HSE06 functional. All valence bands (conduction bands) are aligned to the respective valence band maximum (conduction band minimum) of the PBE calculation.*

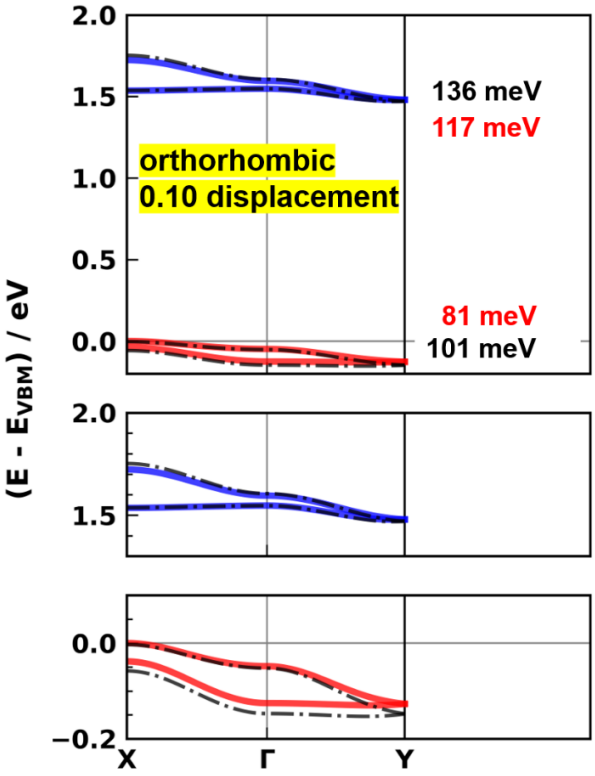

Figure S7. *Electronic band structure of the orthorhombic model crystal at 0.10 long axis displacement. The results were obtained by performing DFT calculations using the PBE functional (solid lines) and the HSE functional (dash dotted). The electronic bands have been calculated for the high-symmetry k-path XΓY for the orthorhombic system. The values of the corresponding band-widths are also given in these plots. The red values correspond to the PBE functional and the black ones to the HSE06 functional. All valence bands (conduction bands) are aligned to the respective valence band maximum (conduction band minimum) of the PBE calculation.*

2.2 Calculation of transfer integrals as a function of the long-axis displacement comparing PBE and HSE06

When calculating the transfer integrals for the molecular dimer as a function of long axis displacement (Figure S8) we find that they are qualitatively the same for PBE and HSE06. Generally, the HSE06 transfer integrals are larger than the PBE ones. Notably, for the PBE functional, ESD and FO yield identical results. When using the hybrid HSE functional, the FO

values are somewhat larger than the ESD ones. The origin of this difference is not fully understood at this point and will require further analysis. In passing we note that a similar observation is also made when calculating the three polymorphs of quinacridone: Also there the ESD calculated transfer integrals are very similar for PBE and HSE (Table 2 of the main manuscript), while the FO values show a larger deviation especially for the α- and γ-polymorphs (with $t_{FO,HSE,\alpha}$=19 meV, $t_{FO,HSE,\beta}$=39 meV, $t_{FO,HSE,\alpha}$=39 meV).

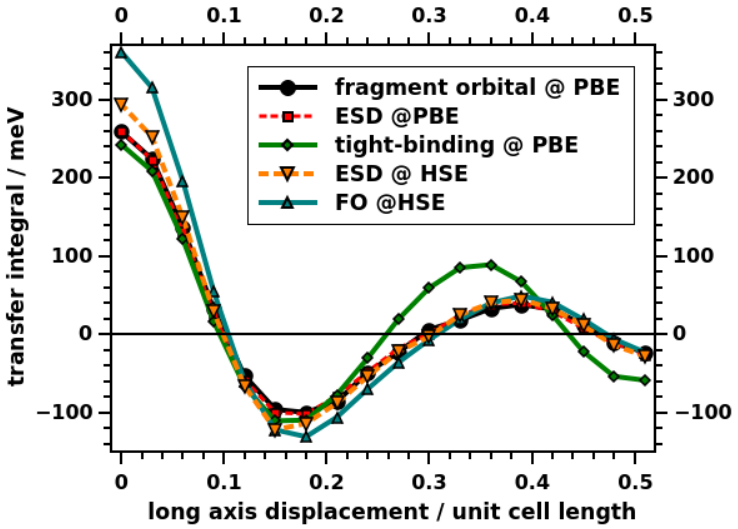

Figure S8. *Transfer integrals for the molecular crystal and the corresponding dimer as a function of displacement along the long molecular axis. The transfer integrals for the dimer have been evaluated using the fragment orbital method for the PBE and HSE06 calculations and additionally also by ESD for the PBE calculations. The tight binding transfer integrals evaluated for the PBE band structure are also given.*

2.3 Impact of the choice of the functional on the ordering of the quinacridone orbitals

As a last step we also checked the dependence of the orbital ordering of the frontier states on the choice of the exchange correlation functional. We find that for the single molecule, PBE reproduces the supposedly correct ordering of the HSE orbitals only for the two frontier states (HOMO and LUMO). Notably, also for the dimer the ordering of the associated orbitals (HOMO,

HOMO-1, LUMO, and LUMO+1) is correctly described by PBE. Therefore, as long as we are only concerned about the behavior of the frontier states, i.e. the corresponding transfer integrals, the use of PBE is justified. A more in depth discussion of these aspects can be found in the Supporting Information section of Ref. [7].

2.4 Impact of the type of van der Waals correction on the relative energetics of the three quinacridone polymorphs

To check the influence of the dispersion interaction on the relative energetic stability of the three polymorphs we compare the results obtained by using the pairwise TS correction scheme[4] to many body dispersion interactions[8] (MBD, as implemented in FHI-aims and VASP). The data are shown in Table S5. From these one can see that the relative energetic stability of the three polymorphs is only very weakly affected by the use of different dispersion correction concepts. The variation of the relative energies is on the order of a few meV upon the usage of different dispersion correction schemes for the calculations. Also using the MBD scheme to reoptimize the atomic positions of the atoms and then calculating the energetic stability does not show a significant change.[1] Therefore, we conclude that the use of the pairwise TS correction scheme gives qualitatively correct results concerning the energetic stability of the polymorphs. Notably, the variations between different codes are of similar magnitude as the variations between different methods. This is insofar not surprising, as errors in the total energy on the order of a few meV correspond to the accuracy of the numerical settings.[9]

Table S5. *Absolute and relative total energies of the three quinacridone polymorphs obtained by using the pairwise TS correction scheme as well as many body dispersion to account for van der Waals interactions. The abbreviation reads as follows: XX@YY,ZZ. Here XX describes the dispersion correction used for calculating the total energy. YY describes the exchange correlation*

[1] The average change in the atomic positions upon optimization including MBD corrections ranges between 0.006 and 0.058 Å.

functional used during the geometry optimizations and the single point calculations and finally ZZ stands for the dispersion correction used during the geometry optimization.

	MBD@PBE,TS	**Δ(min)**	**TS@PBE,TS**	**Δ(min)**	**MBD@PBE,MBD**	**Δ(min)**	**Δ(min)**
	FHI-Aims		VASP		FHI-Aims		VASP
α	-28013.8725 eV	84 meV	-258.5086 eV	90 meV	-28013.8753 eV	86 meV	88 meV
β	-28013.9523 eV	4 meV	-258.5943 eV	5 meV	-28013.9544 eV	7 meV	3 meV
γ	-28013.9561 eV	0 meV	-258.5988 eV	0 meV	-28013.9611 eV	0 meV	0 meV

3. Additional data on the electronic structure of quinacridone

3.1 Hydrogen bonding energies for molecular dimers extracted from the crystals of the quinacridone polymorphs and the orthorhombic model crystal.

As hydrogen bonds are a major driving force for the packing of quinacridone and the molecular packing of all the considered systems is quite different, it is interesting to analyze the impact of different molecular arrangements on the hydrogen-bonding energies. To estimate these energies, we extracted clusters from the corresponding crystal structures and then calculated the total energies of these clusters as well as those of the individual fragments (see Table S6). All calculations were done using the same settings as for the molecular dimer calculations presented in the main manuscript. For the α- and β-phases, as well as for the orthorhombic model crystal, the clusters consist of two neighboring molecules in H-bonding direction. This is a result of the formation of H-bonded stripes in these systems. Thus, in these crystals, each molecule has two identical neighbors in H-bond direction. For the γ-phase the situation is a bit more difficult, as in this crystal structure the molecule has 4 H-bonding partners (2 on each side). As only pairs of bonding partners are equivalent, one has to calculate a molecular trimer in order to estimate the H-bonding energy E_H. Comparing the obtained H-bonding energies we find essentially the same values for α- and β-quinacridone, i.e. the difference is about 1 meV. For γ quinacridone, E_H is

about 200 meV larger compared to E_H for α and β quinacridone. This finding agrees quite well with γ-quinacridone being the energetically most stable one of the three polymorphs, although we cannot exclude that the three- vs. two-molecule model clusters also have an impact. Interestingly, the H-bonding energy in the coplanar model crystal agrees well with the α- and β-polymorphs. This shows that the construction of the model system does not disrupt the H-bonding network. This is insofar relevant as the H-bonded molecular stripes in α- and β-quinacridone are not exactly planar, but exhibit small steps between the molecules,[10] which do not occur in the model system. In this context it is, however, worthwhile mentioning, that already Paulus et al.[10] hypothesized that the steps are not caused by the H-bonds per se, but rather by the crystal packing.

Beyond the H-bonding energies, we also analyzed bond lengths (in the optimized crystal structures). Correspondingly, the distances between N, H, and O, which are the closest atoms forming the H-bonds, are reported in Table S7. Similar to the trends for the energies, the H-O and N-O distances for α and β quinacridone are very similar. For γ and the orthorhombic system these distances are even smaller by about 0.1 Å.

Table S6. *Total energies of molecular clusters of the three quinacridone polymorphs and the orthorhombic model crystal (dimer for α–, and β– quinacridone and for the orthorhombic, coplanar model crystal structures and trimer for and γ-quinacridone), energies of the monomers and H-bonding energy evaluated as the difference of the total energy of the combined system and the energy of the fragments. The H-bonding energies have been evaluated using the TS and MBD methods.*

	System AB / eV	**Fragment A / eV**	**Fragment B / eV**	**E_H = AB – A – B / eV**
TS vdW correction				
α	-56022.784	-28010.893	equivalent	-0.100
β	-56022.805	-28010.902	equivalent	-1.001
ortho	-56022.816	-28010.922	equivalent	-0.973
γ	-84034.735	-28010.871	-56022.656	-1.207
MBD vdW correction				

α	-56024.078	-28011.535	equivalent	-1.009
β	-56024.105	-28011.544	equivalent	-1.017
ortho	-56024.122	-28011.565	equivalent	-0.992
γ	-84036.340	-56023.640	-28011.513	-1.188

Table S7. *Distances between the H, N and O atoms forming the intermolecular H-bonds. These distances have been measured as the length of the connection vector.*

crystal	**H-O distance / Å**	**N-O distance / Å**
α	1.848	2.850
β	1.853	2.861
ortho	1.762	2.793
γ	1.719	2.739

3.2. Electronic band structures of the three quinacridone polymorphs

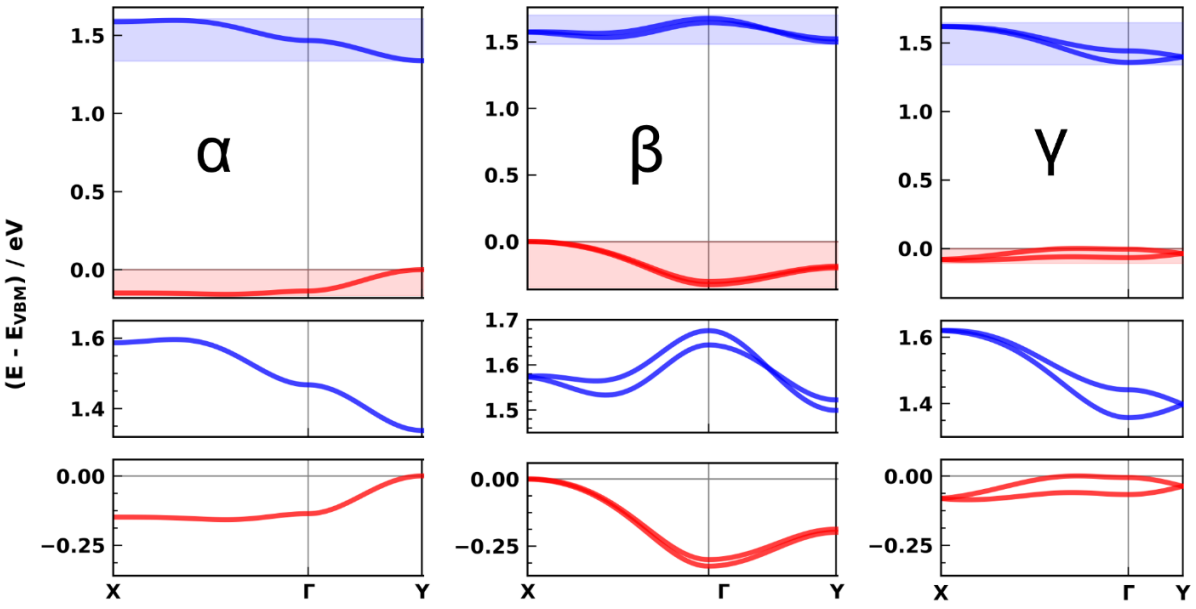

Figure S9. *Electronic band structures of the three quinacridone polymorphs (α, β, and γ) along a high-symmetry path from X to Γ to Y. Valence and conduction bands are shown. The bands are aligned to the respective valence band maximum.*

3.3 Additional information on deeper-lying bands and orbitals

Figure 7 in the main manuscript reports the band widths for the eight highest occupied bands of the coplanar model crystal at zero displacement and for a displacement along the long molecular axis by one tenth of the unit cell length. Figure S10 below shows the corresponding band structures.

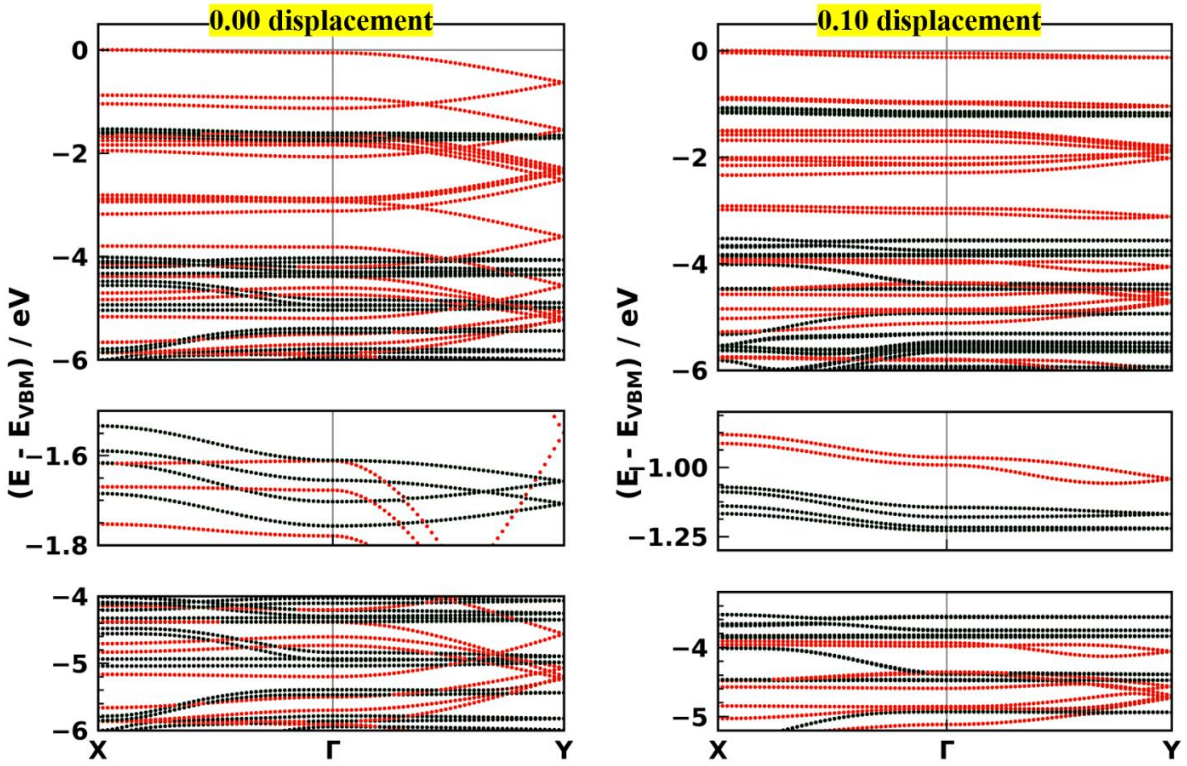

Figure S10. *Band structures of the orthorhombic model crystal for displacements 0.00 and 0.10 times the long molecular axis. The bands are additionally resolved according to their character. Bands which are black have mainly σ- and bands which are red have a dominant π-character. All bands are aligned to the corresponding valence band maximum.*

Further insight can be gained by analyzing the orbitals forming these bands in isolated molecules and molecular dimers. Considering that the results in Figure 7 of the main manuscript show that only π-orbitals are relevant here, in the following we will also discuss only those. Notably, the energetic splitting between the two dimer orbitals originating from linear combinations of identical orbitals on the two molecules are very similar in all systems (see Figure S11) in line with the similar widths of the corresponding bands from Figure 7 of the main manuscript. Here it should be noted that in the dimer case the HOMO-1 is a σ-orbital, while the VB-1 in the crystal is a π-band. This change in order is primarily a consequence of the band dispersion in the periodic case.

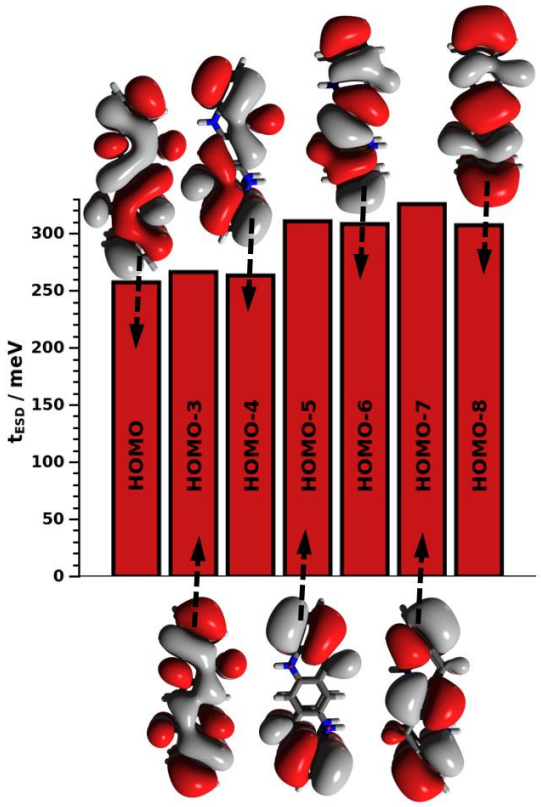

Figure S11. *Transfer integrals calculated for cofacial molecular dimers employing the ESD method for the highest-lying occupied π-orbital pairs derived from the molecular HOMO, the*

HOMO-3, and the HOMO-4 to HOMO-8. The pairs derived from HOMO-1 and HOMO-2 are not considered here, as the associated transfer integrals are negligibly small due to the σ-character of the orbitals in the PBE calculations. Top-views of the dimer orbitals highlighting the nodal pattern of the parent orbitals are also shown.

REFERENCES

(1) Blum, V.; Gehrke, R.; Hanke, F.; Havu, P.; Havu, V.; Ren, X.; Reuter, K.; Scheffler, M. Ab Initio Molecular Simulations with Numeric Atom-Centered Orbitals. *Comput. Phys. Commun.* **2009**, *180*, 2175–2196.

(2) Perdew, J. P.; Burke, K.; Ernzerhof, M. Generalized Gradient Approximation Made Simple. *Phys. Rev. Lett.* **1996**, *77*, 3865–3868.

(3) Perdew, J. P.; Burke, K.; Ernzerhof, M. Erratum: Generalized Gradient Approximation Made Simple (Physical Review Letters (1996) 77 (3865)). *Physical Review Letters*, 1997, *78*, 1396.

(4) Tkatchenko, A.; Scheffler, M. Accurate Molecular Van Der Waals Interactions from Ground-State Electron Density and Free-Atom Reference Data. *Phys. Rev. Lett.* **2009**, *102*, 073005.

(5) Heyd, J.; Scuseria, G. E.; Ernzerhof, M. Hybrid Functionals Based on a Screened Coulomb Potential. *J. Chem. Phys.* **2003**, *118*, 8207–8215.

(6) Heyd, J.; Scuseria, G. E.; Ernzerhof, M. Erratum: Hybrid Functionals Based on a Screened Coulomb Potential (Journal of Chemical Physics (2003) 118 (8207)). *Journal of Chemical Physics*, 2006, *124*, 219906.

(7) Winkler, C.; Mayer, F.; Zojer, E. Analyzing the Electronic Coupling in Molecular Crystals—The Instructive Case of A-Quinacridone. *Adv. Theory Simulations* **2019**, *2*, 1800204.

(8) Ambrosetti, A.; Reilly, A. M.; Distasio, R. A.; Tkatchenko, A. Long-Range Correlation Energy Calculated from Coupled Atomic Response Functions. *J. Chem. Phys.* **2014**, *140*, 18A508.

(9) Lejaeghere, K.; Bihlmayer, G.; Björkman, T.; Blaha, P.; Blügel, S.; Blum, V.; Caliste, D.; Castelli, I. E.; Clark, S. J.; Dal Corso, A.; *et al.* Reproducibility in Density Functional Theory Calculations of Solids. *Science* **2016**, *351*, aad3000.

(10) Paulus, E. F.; Leusen, F. J. J.; Schmidt, M. U. Crystal Structures of Quinacridones. *CrystEngComm* **2007**, *9*, 131–143.

4. Structure-to-Property Relationships in Electrically Conductive Metal-Organic Frameworks

4.1. Author contributions

E. Zojer and C. Winkler conceived the idea to transfer knowledge on charge transport within OSCs to the MOF-field. C. Winkler performed all calculations together with a primary analysis of the data. This data was then discussed by C. Winkler and E. Zojer and further analysis was performed by the two. C. Winkler also wrote the first version of the manuscript and prepared all figures. C. Winkler and E. Zojer revised the manuscript in several iterations. The project was supervised by E. Zojer.

The following paper is published in Nanomaterials and inserted here as original publication together with the Supporting Information. Furthermore, this paper has recently been selected to be part of the *Editor's Choice* section of Nanomaterials. Reprinted with permission from "Winkler C., and Zojer E., Strategies for Controlling Through-Space Charge Transport in Metal-Organic Frameworks via Structural Modifications , Nanomaterials, 2020, 10, 2372". MDPI 2020.

4.2. Main Paper

nanomaterials

MDPI

Article

Strategies for Controlling Through-Space Charge Transport in Metal-Organic Frameworks via Structural Modifications

Christian Winkler and Egbert Zojer *

Institute of Solid State Physics, NAWI Graz, Graz University of Technology, Petersgasse 16, 8010 Graz, Austria; christian.winkler@student.tugraz.at

* Correspondence: egbert.zojer@tugraz.at

Received: 12 November 2020; Accepted: 26 November 2020; Published: 28 November 2020

Abstract: In recent years, charge transport in metal-organic frameworks (MOFs) has shifted into the focus of scientific research. In this context, systems with efficient through-space charge transport pathways resulting from π-stacked conjugated linkers are of particular interest. In the current manuscript, we use density functional theory-based simulations to provide a detailed understanding of such MOFs, which, in the present case, are derived from the prototypical Zn_2(TTFTB) system (with $TTFTB^{4-}$ corresponding to tetrathiafulvalene tetrabenzoate). In particular, we show that factors such as the relative arrangement of neighboring linkers and the details of the structural conformations of the individual building blocks have a profound impact on bandwidths and charge transfer. Considering the helical stacking of individual tetrathiafulvalene (TTF) molecules around a screw axis as the dominant symmetry element in Zn_2(TTFTB)-derived materials, the focus, here, is primarily on the impact of the relative rotation of neighboring molecules. Not unexpectedly, changing the stacking distance in the helix also plays a distinct role, especially for structures which display large electronic couplings to start with. The presented results provide guidelines for achieving structures with improved electronic couplings. It is, however, also shown that structural defects (especially missing linkers) provide major obstacles to charge transport in the studied, essentially one-dimensional systems. This suggests that especially the sample quality is a decisive factor for ensuring efficient through-space charge transport in MOFs comprising stacked π-systems.

Keywords: metal-organic frameworks; charge transport; through-space pathways

1. Introduction

Metal-organic frameworks (MOFs) are porous, highly crystalline solids consisting of inorganic nodes connected by organic linkers [1–3]. They have been investigated extensively for various applications in fields such as gas storage, [4–6] catalysis, [7–9], and gas separation [10,11]. Until recently, comparably little attention has been paid to the electronic properties of MOFs, [12] although electrically conductive MOFs can be relevant as active materials for several applications, such as electrocatalysis, [13–17] chemiresistive sensing, [18–23] and energy storage [24–26]. Therefore, in recent years, interest in controlling and modifying the electronic properties of MOFs has gained considerable attention [12,27,28].

On more fundamental grounds, the electronic (and also the optical) properties of a solid are determined (in a first approximation) by its electronic band structure, where MOFs usually show rather flat bands [27]. This is a consequence of the commonly observed weak hybridization between states localized on the organic linkers and states localized on the inorganic secondary building units. A second reason is the small overlap of the *π-systems* of neighboring organic linkers. This assessment already comprises two strategies for changing the electronic properties of MOFs: one can either focus

on improving the bonding between the metal and the ligands (through-bond coupling), or one can try to improve the overlap of the *π-systems* in neighboring linkers (through-space coupling) [12,27,29]. In the present contribution, we will focus on the latter approach, where a large overlap of neighboring π-electron systems can result in the formation of bands displaying a large dispersion and generating through-space charge transport pathways.

The impact of the packing motif of organic *π-systems* on intermolecular electronic couplings (expressed via transfer integrals and band dispersions) has been thoroughly studied for organic semiconductors, OSCs. Crucial factors identified for these materials are the stacking distance of neighboring molecules (i.e., neighboring π-systems) and the arrangement of neighboring molecules in terms of relative displacements and rotations [30–37]. All these structural changes lead to changes in the orbital overlap between consecutive molecules, which, in turn, change the intermolecular electronic couplings. For example, considering dimers of acenes (or quinacridone) and shifting the molecules relative to each other along their long molecular axis, one finds that the transfer integrals oscillate as a function of the displacement [30–34,36,38]. The influence of relative rotations of molecular dimers has been investigated primarily in the context of discotic liquid crystals. There, it has been found that the transfer integral varies as a function of the rotation angle [35,37,39–42]. Importantly, independent of whether neighboring molecules are shifted or rotated relative to each other, what counts for the intermolecular electronic coupling (transfer integral) is the overlap of the frontier orbitals. This overlap is determined by the orbitals' shape and symmetry. In this context, it has been suggested that when organic semiconductors can assemble without pronounced sterical constraints, exchange repulsion acts as an intrinsic driving force, favoring molecular arrangements with particularly small electronic couplings [32,33]. Therefore, developing design strategies "extrinsically" enforcing favorable molecular arrangements have shifted into the focus of current research [32,33,43–46]. Here, MOFs are of particular appeal, as the framework structure offers an additional level of control over the stacking sequence of neighboring molecules, which goes far beyond what is typically achievable in organic semiconductors. Similar to OSCs, it has been predicted also for layered MOFs that their electronic band structure depends on the proximity [47] of the layers as well as on interlayer displacements [48–50]. For MOFs comprising 3D networks, such structure-to-property relations for charge transport are, however, hardly developed.

Material-wise, particularly promising MOFs showing through-space charge-transport pathways are frameworks consisting of ligands based on tetrathiafulvalene (TTF) [12]. Especially for a subgroup of these MOFs in which the TTF units form helical stacks with comparably close π-stacking one observes relatively large electrical conductivities [12,51]. For such systems, it has also been shown that reducing the S ... S stacking distance within the TTF stacks results in significantly increased conductivities [52–54].

In this work, we will apply dispersion-corrected density functional theory (DFT) calculations to show, how the electronic coupling in such TTF-based MOFs can be controlled by additional structural parameters, such as the relative rotation or slip of neighboring TTF units. The goal of these calculations is to identify stacking motives that maximize through-space charge-carrier mobilities. Moreover, we will address the impact of defects such as missing linkers, pair formation, and shifted molecules.

1.1. Systems of Interest

The starting point for this study is the stacking of the TTF cores of Zn_2(TTFTB) [51], shown in Figure 1. The linkers ($TTFTB^{4-}$ = tetrathiafulvalene tetrabenzoate) and the metal nodes (forming Zn_2(TTFTB)) crystallize in the $P6_5$ space group with a hexagonal unit cell (a = b= 19.293 Å and c = 20.838 Å). This results in helical TTF stacks (six TTF molecules per unit cell), where neighboring TTF molecules are rotated by 60° relative to each other and translated by 3.473 Å in stacking direction (see Figure 1). The stacks themselves are arranged in a hexagonal pattern and connected by the nodes, as illustrated in Figure 1a. Notably, the 6_5 screw axis is offset from the central ethylene unit of the TTF cores (see Figure 1b,c). This induces an additional shift of neighboring molecules relative to each other,

which is perpendicular to the screw axis [51]. As a consequence, the centers of the TTF molecules are arranged on a helix, whose projection onto the x,y-plane (the plane perpendicular to the stacking direction, z) becomes a circle with a radius r of ~1.6 Å. This stacking motif of the TTF cores is determined by the arrangement of the Zn nodes and the carboxylic acid groups. The MOF structure discussed in the main manuscript contains neither solvent molecules nor water molecules (i.e., the MOF is desolvated and dehydrated). For comparison, a MOF with water molecules coordinating to the Zn atoms was also calculated. The water molecules cause only very minor changes in the atomic coordinates and the electronic structure (see Supplementary Materials).

For analyzing the impact of structural changes on the electronic properties of the TTF stacks, we first constructed helical model TTF and TTFTB stacks consisting of molecules exhibiting the same geometry and stacking motif as in the MOF. These stacks were then arranged in the same pattern as in the MOF, as shown in Figure 1a.

For generating TTF stacks with different numbers of molecules in the unit cell, N, we replicated individual molecules (in the geometries adopted in the stacks), rotated them around the central screw axis by angles of 360°/N, and arranged them at distances of 3.473 Å. Laterally, these stacks were then, again, arranged consistent with the experimental structure of Zn_2(TTFTB), while the unit cell in the stacking direction was set to N*3.473 Å. To verify the construction procedure, we compared the electronic structure of the N = 6 TTF model stack to the system extracted directly from the MOF structure, observing only negligible differences (see Table 1 in Section 3.2). A detailed description of the construction of the parent TTF stacks and the model systems with modified rotation angles can be found in the Supplementary Materials.

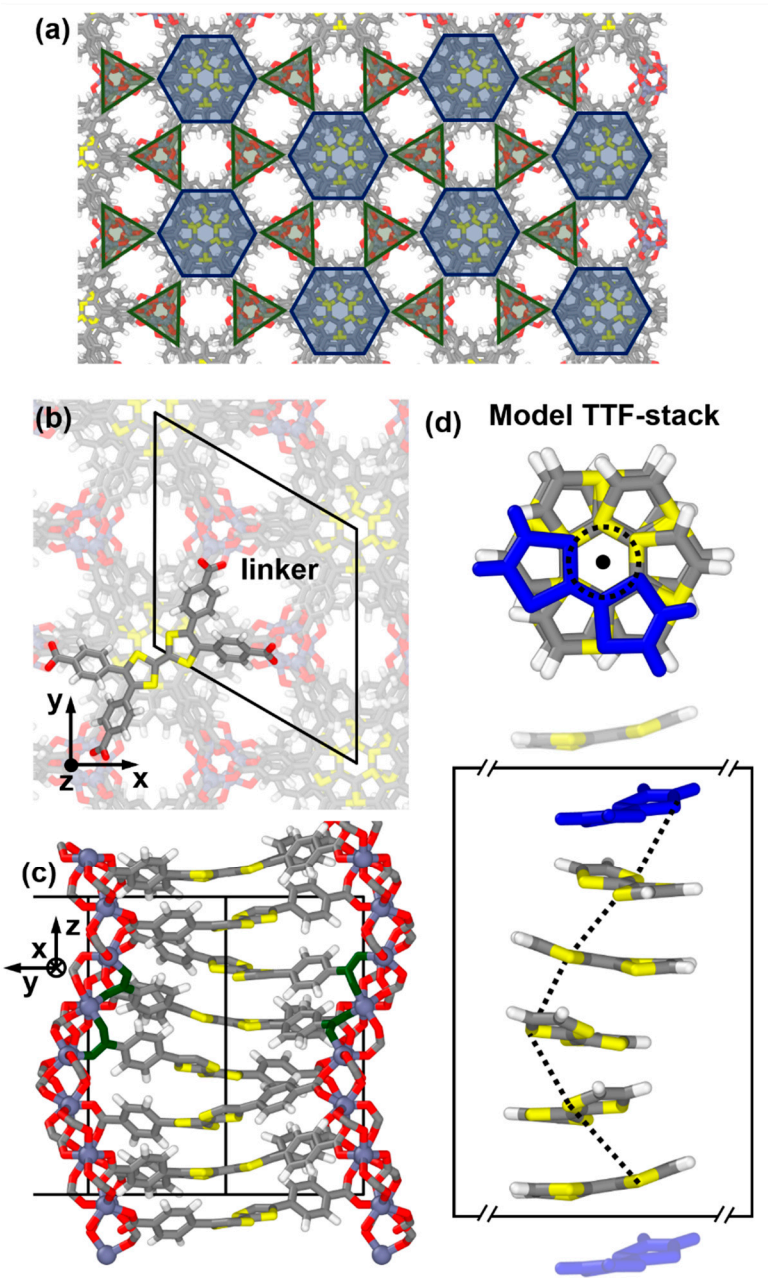

Figure 1. Structure of Zn_2(TTFTB) and the constructed tetrathiafulvalene (TTF) model system. Panel (**a**) shows the connectivity between linkers (blue hexagons) and nodes (green triangles) within the Zn_2(TTFTB) metal-organic framework (MOF). Panels (**b**,**c**) contain a more detailed illustration structure of the Zn_2(TTFTB) MOF (top and side view). The linker is highlighted in (**b**), and in panel (**c**), the carboxyl groups of neighboring linkers are colored in green to indicate how linkers and metal nodes are connected on an atomistic level. The unit cell of the MOF is represented by thick black lines. Panel (**d**) contain the top and side views of the model system used for describing the one-dimensional charge transport in these materials. The top TTF molecule in the model system is marked in blue, and the rotation axis is indicated by the black dot in the center of the top structure in panel (**d**). The dashed black line in the model system indicates the rotation of the molecules around the screw axis. The periodic boundary conditions are indicated by the frame around the repeat unit of the TTF model system. C—grey, H—white, S—yellow, Zn—purple, O—red.

Table 1. Valence bandwidths (VBW) and effective masses at the valence band maxima for transport in (001) direction for all considered MOFs (i.e., the parent MOF Zn_2(TTFTB), the MOF with Zn replaced by Cd, and the MOF with S replaced by Se) and for model TTF stacks with 1, 6, and 12 TTF molecules per unit cell (i.e., with rotation angles of 0°, 60°, and 30°). The systems TTF and TTFTB listed under MOFs are the stacks extracted from the Zn_2(TTFTB) structure. For the model stacks, we compare systems generated with different geometries of the individual molecules. Here, (MOF) refers to TTF conformations extracted from the MOF structure, (relaxed) to geometries relaxed in the stack, (boat) to gas-phase relaxed TTF geometries in boat conformation, and (planar) to planar TTF molecules for which only the *x*- and *y*-coordinates have been relaxed in the gas phase.

	MOFs					
	VBW/meV			**m^*/m_e**		
Zn_2(TTFTB)	371			2.05		
Zn_2(TSFTB)	641			1.05		
Cd_2(TTFTB)	333			2.21		
TTFTB	373			2.10		
TTF	303			2.40		
	Model Stacks					
	VBW/meV			**m^*/m_e**		
	N = 1	**N = 6**	**N = 12**	**N = 1**	**N = 6**	**N = 12**
TTF (MOF)	1337	298	650	0.93	2.48	1.84
TTF (relaxed)	1047	207	609	1.89	3.02	1.86
TTF (boat)	1269	72	348	1.23	7.29	4.35
TTF (planar)	1804	117	666	0.51	4.33	1.75

Additionally, molecular dimers were designed in analogy to the construction described in the previous paragraph. As these dimers were simulated using open boundary conditions, any value could be chosen for the rotation angle around the off-center screw axis, allowing us to generate smooth evolutions of the dimer electronic couplings with rotation angle.

To investigate the impact of chemical modifications, we also considered Cd_2(TTFTB), which has been reported to be isostructural to Zn_2(TTFTB) but shows a higher electrical conductivity [53]. Moreover, we replaced TTF with tetraselenafulvalene (TSF, $C_6H_4Se_4$, yielding Zn_2(TSFTB)) to test the extent to which the increased p_z-orbital overlap for Se would result in a larger valence bandwidth.

1.2. Describing Through-Space Charge Transport in Pristine MOFs

Before considering the electronic band structure of Zn_2(TTFTB) and how it is affected by changes in the structure of the TTF stack, it is useful to realize that through-space charge transport in porous materials is strongly reminiscent of the situation in (one-dimensional) organic semiconductors, [31,55–57] for which various models for describing charge transport have been proposed over the past few decades. These models comprise fully coherent band transport and incoherent hopping transport as limiting cases and also include more recent developments, such as the highly successful dynamic disorder model [58–62]. For all these models, the intermolecular electronic couplings between neighboring molecules are essential parameters [31,55–57]. These electronic couplings are typically expressed via transfer integrals t, which enter linearly (quadratically) into the expressions for band (hopping) mobilities [31,57]. Such transfer integrals can, for example, be extracted from studying suitably arranged dimers [31,34–37,63] or from fitting tight-binding models to electronic band structures [64]. In fact, within a tight-binding picture, the magnitudes of the transfer integrals can be intimately related to the widths of the frontier bands. This suggests that general trends for the dependence of charge-carrier mobilities on structural parameters can be gained from calculating electronic band structures, even in cases in which band transport is not the dominant mechanism. Therefore, in the following, we will primarily analyze such band structures calculated by dispersion

corrected density functional theory (with the discussion primarily based on band widths and the derived transfer integrals). We acknowledge that in this way, the role of the material's phonon properties (such as the occurrence of "killer phonon" modes) [65] is not revealed. Nevertheless, the analysis provides crucial insights into the structure-to-property relationships for the electronic MOF properties which determine through-space charge transport.

2. Methods

For investigating the structural and electronic properties of the MOFs, the periodic model systems, and the molecular dimers, we employed the dispersion-corrected density functional theory, DFT, which, in a recent review, was highlighted as a viable method for gaining an in-depth understanding of the electronic structure of MOFs [66]. The simulations were performed with the FHI-aims code (version 190906, Berlin, Germany) [67]. Exchange and correlation were treated by the PBE functional [68,69], and the Tkatchenko–Scheffler [70] scheme was used as an a posteriori van der Waals correction. We employed the default tight basis sets of FHI-aims for periodic and molecular simulations. Further details on the employed basis functions are provided in the Supplementary Materials. For Zn_2(TTFTB), the electronic band structure was also calculated with the hybrid functional HSE06 [71,72] to ensure that the introduction of Hartree–Fock exchange has a negligible influence on the valence bandwidth as the primary quantity of interest for the present study.

During the geometry optimizations, all atomic positions were relaxed until the largest remaining force component on any atom was smaller than 0.01 eV/Å. For all MOF systems, a $3 \times 3 \times 3$ k-point grid was used for sampling reciprocal space during the geometry relaxations. During the electronic structure calculations, a $4 \times 4 \times 4$ k-point grid was employed. For both grids, the total energy was converged to within less than 1 meV. The smaller grid in the more time-consuming geometry relaxations was used to speed up the calculations. For the periodic stacks, we used a $1 \times 1 \times 12$ k-point grid, which is already converged, even for the smallest system (with the largest reciprocal space vector along the stacking direction). The effective masses were calculated from the (inverse) curvature of the band structure at the top of the valence band in the (001) direction to describe transport in the TTF stacking direction. Technically, the band curvature was determined by fitting a cosine function to the dispersion relation E(k), including the 10 k-points closest to the valence band maximum, with a spacing between neighboring k-points of 0.005 $Å^{-1}$. A cosine function was chosen for the fit to be consistent with the best-suited tight-binding band model for the systems studied here (see below). The structures of the MOFs and the molecular systems were visualized using Ovito (version 3.2.1) [73] and the molecular orbitals were rendered using Avogadro (version 1.2.0) [74].

3. Results and Discussion

3.1. Electronic Structure of Zn_2(TTFTB) and the Extracted Model Stack

As a first step, we analyzed the electronic structure of Zn_2(TTFTB), for which the frontier bands are shown in Figure 2a. Figure 2b contains a zoom into the valence band region. In the following, we will be primarily concerned with bands in the ΓA direction, as this corresponds to the stacking direction of the TTF molecules. Moreover, the valence and conduction bands are flat in directions perpendicular to ΓA (with bandwidths around 1 meV in AL and even less in ΓK directions). This indicates that there is virtually no electronic coupling between individual TTF stacks within the MOF, resulting in essentially one-dimensional charge transport in Zn_2(TTFTB). This is supported by measurements by Sun et al., who observed that the electrical conductivity in the direction of the stacks is 2–3 orders of magnitude larger than perpendicular to them [75].

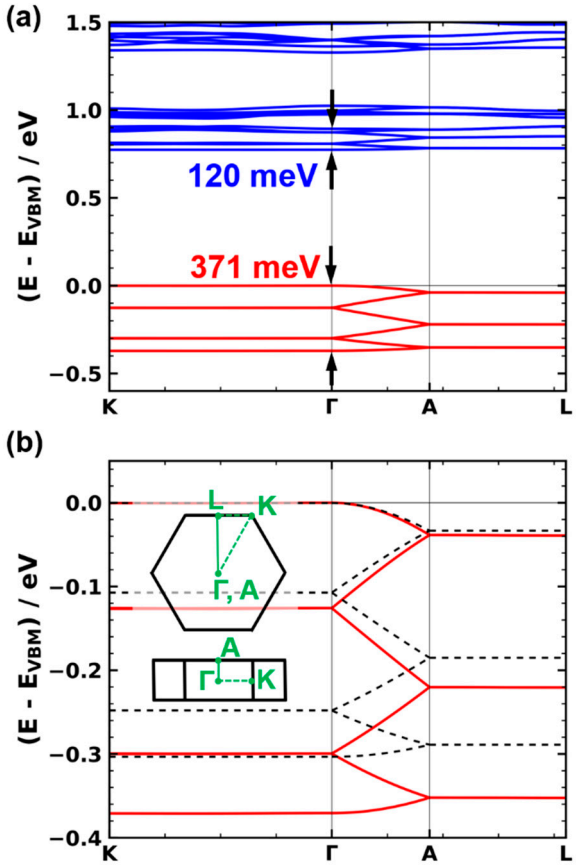

Figure 2. Electronic structure of the Zn_2(TTFTB) MOF and the corresponding TTF model stack: (**a**) electronic band structure of Zn_2(TTFTB) along the selected high-symmetry directions. The energy scale is aligned to the valence band maximum. (**b**) Zoom into the valence band of Zn_2(TTFTB) (solid red line) and of the TTF model stack (dashed black line). The first Brillouin zone together with the relevant directions in k-space are shown as an inset.

As far as the ΓA direction is concerned, one can identify a six-times backfolded band, which is particularly well resolved for the valence band in Figure 2b. This backfolding is related to the crystallographic unit cell (determining the shape and size of the first Brillouin zone). It contains six TTF-based linkers as translational repeat units, whose repetition yields the infinitely extended TTF stack. What counts from an electronic point of view is, however, not only the translational symmetry but also the screw axis in the middle of the TTF stack (see Figure 1). With respect to that screw axis, each TTF molecule has an identical electronic environment. Thus, one can view a single TTF molecule as the "electronic" repeat unit of the TTF stack in Zn_2(TTFTB). This is supported by the observation that for the perfectly symmetric structure, no band gaps open for the backfolded bands at the Γ and A points. In passing, we note that this situation changes when defects disturb the perfect symmetry, as will be discussed in Section 3.4.

As a consequence of a single TTF molecule serving as an "electronic" repeat unit, the electronic bands in the ΓA direction can be conveniently described by a tight-binding model with a single molecule per unit cell. These considerations imply that for judging the electronic coupling between neighboring TTF molecules, one needs to consider the width of the entire, six-times backfolded band, as indicated by the arrows in Figure 2a. Based on the 1D nearest-neighbor tight-binding model mentioned above, the total band width of the six-times backfolded band then corresponds to $4 \times t$ (with t representing the intermolecular transfer integral in stacking direction). This extraction of t from the band structure is confirmed by the data shown in Figure 3, where the dimer-derived bandwidths are compared to the results for the actual TTF stacks. Additional validation data are contained in the

Supplementary Materials. Conversely, the width of the valence band between Γ and A is a measure for the electronic coupling between adjacent groups of six TTF units (i.e., between the entirety of the TTF molecules in adjacent unit cells).

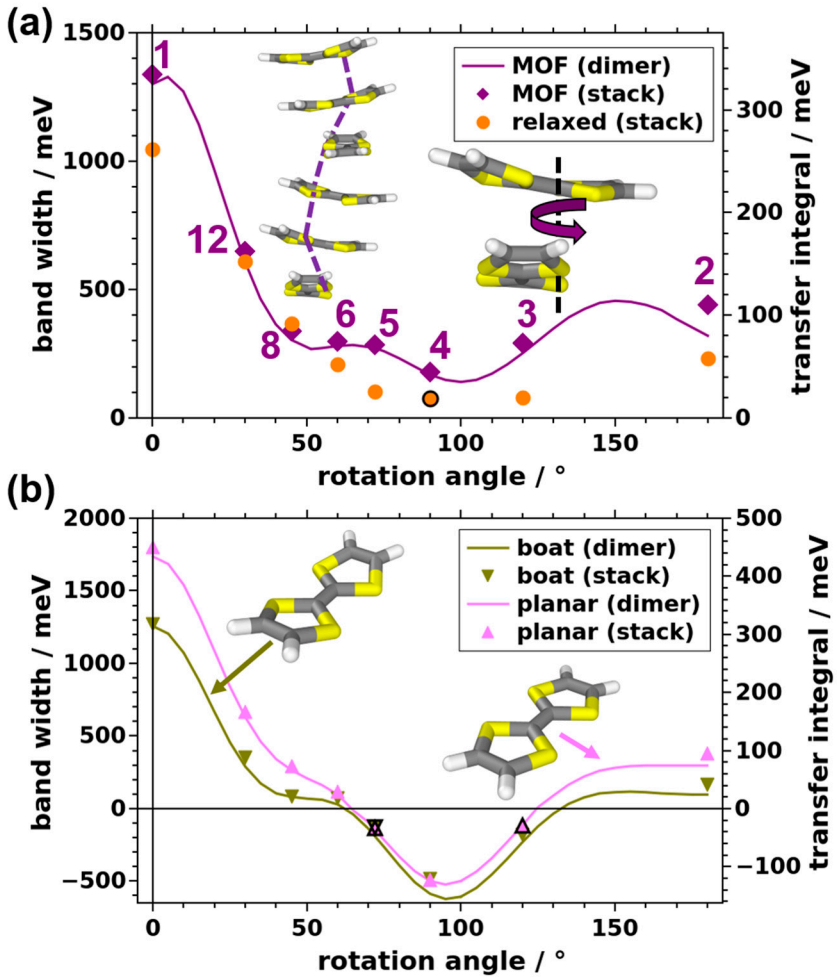

Figure 3. Evolution of the width of the valence band in the (001) direction and of the transfer integrals between neighboring TTF molecules in the stacking direction as a function of the rotation angle between neighboring molecules. Panel (**a**) shows the situation for stacks and dimers with molecular geometries taken from Zn_2(TTFTB) (purple diamonds and line) and for stacks with optimized geometries (orange circles; for details, see main text). In panel (**b**), the results for fully gas-phase optimized (dark yellow down-facing triangles and line) and for planar molecules (light magenta up-facing triangles and line) are shown. Symbols denote data points calculated for infinitely extended TTF stacks, where the rotation angles are set by varying the number of TTF molecules in each unit cell (see numbers in panel (**a**)). The solid lines have been calculated for dimers with rotation angles varied in steps of 5° (individual data points not shown). In panel (**b**), bandwidths are set to negative values whenever the signs of the dimer-calculated transfer integrals are also negative. Points marked with a black frame comprise band structures deviating from a simple 1D tight-binding system and are discussed in the Supplementary Materials.

On more quantitative grounds, the valence bandwidth, VBW, for the backfolded band amounts to 371 meV in the PBE calculations (400 meV when using the HSE06 functional), as indicated by the arrows in Figure 2a. This is significantly larger than the width of the conduction band, which is 120 meV. This finding suggests that Zn_2(TTFTB) is preferentially a hole conductor [53], which is in line with the notion of organosulfur compounds, such as TTF, being good electron donors [76,77].

An analysis of the contributions of the different parts of the MOF to the valence and conduction bands suggests that especially hole transport (which is particularly relevant for TTF-based systems; see above) should be described well by the model TTF stack. This notion is confirmed by the comparison of the valence band structure of the actual Zn_2(TTFTB) MOF (solid line) and the band structure of the model TTF stack in Figure 2b; qualitatively, the two band structures are the same. The only apparent difference is a somewhat smaller bandwidth of 303 meV in the model system (which amounts to ~82% of the bandwidth of the actual MOF). This leads to a comparably small change in the effective mass at the valence band maximum (VBM) from 2.05 to 2.40 m_e (with m_e being the mass of a free electron). We attribute this difference to the overlap of the π-orbitals of neighboring phenylenes in the H_4TTFTB linkers in the actual MOF, which is not captured by the model system (see systems TTF and TTFTB in Table 1 and further details in the Supplementary Materials). These quantitative differences are, however, rather small compared to the effects discussed below, rendering the TTF stack a useful model system.

3.2. Dependence of Bandwidth and Transfer Integral on the Relative Rotation of Consecutive TTF Units

With a reliable model system at hand, we can now turn to studying the impact of changes in the structure of the TTF stacks on the electronic coupling. It has been shown, for a variety of molecular dimers, that the relative rotation of neighboring molecules has a tremendous effect on intermolecular electronic couplings [35,37,39–42]. As this effect is a consequence of changes in the orbital overlap upon rotation, one can expect similar effects for the TTF stacks considered in this work. Following the construction procedure for TTF stacks described in Section 1.1 and in the Supplementary Materials, it is apparent that the number of stacked molecules in the unit cell determines their relative rotation. Thus, we consider unit cells containing 1, 2, 3, 4, 5, 6, 8, and 12 molecules (corresponding to rotations of 0°, 180°, 120°, 90°, 72°, 60°, 45°, and 30°, respectively).

The resulting band structures are shown in the Supplementary Materials. They reveal that the cofacial arrangement with one repeat unit exhibits the largest valence band width of 1337 meV, corresponding to a transfer integral between neighboring molecules of 334 meV (see data points in Figure 3a and values in Table 1). The bandwidth decreases by a factor of nearly three to 447 meV when considering the system with two molecules per unit cell (N = 2, or a relative rotation between consecutive TTF molecules of 180°). The bandwidth further decreases for three TTF molecules (120° rotation) and reaches a minimum of 180 meV (a transfer integral of 45 meV) for the system containing four molecules in the unit cell (see Figure 3a). Upon further increasing the number of repeat units, the bandwidth again increases slightly (to between 235 and 337 meV for N = 5, 6, and 8). A steep increase is then observed for 12 molecules per unit cell (i.e., for a relative rotation angle of 30°). Here, a valence bandwidth of 650 meV means a doubling compared to the reference system with N = 6, which mimics the situation in the actual Zn_2(TTFTB) MOF. Concomitantly, the effective mass of the holes increases from 0.93 m_e for N = 1 to 2.48 m_e for the reference system with N = 6 and then drops again to 1.84 m_e for N = 12. These considerations show that changing the relative twist between consecutive molecules, indeed, has a profound impact on the electronic coupling in the TTF stack and that the situation in Zn_2(TTFTB) is far from ideal for hole transport.

For obtaining values at intermediate rotation angles we considered model dimers, extracting transfer integrals via the fragment orbital method [78]. The valence bandwidth for one molecule as "electronic repeat unit" is then obtained as $W = 4 \times t$ employing a 1D tight-binding model. At rotation angles at which data for actual stacks and from dimers are available, one typically observes an excellent agreement. This suggests that dimer calculations can, indeed, be used as an efficient tool for predicting and explaining general trends.

As a next step, we discuss the role of the conformation of the molecules within the stack. First, we fully relaxed the geometries of the molecules in the stacks, fixing only the positions of the central C=C atoms to maintain the overall structure. This yields an evolution of the valence bandwidths comparable to that of the TTF stacks with molecules in MOF geometry (see above), although the

bandwidths are consistently smaller in the relaxed case (with the exception of the N = 8 system; see Figure 3a). The reduction in the bandwidth is particularly pronounced for N between 2 and 5, such that the overall variation between the largest and the smallest bandwidths amounts to a factor of almost 14.

For the relaxed stacks, it is also sensible to compare the total energies of the systems. Interestingly, for N between 3 and 12 these are within 35 meV per molecule (i.e., only somewhat larger than k_BT; see Supplementary Materials). This occurs despite variations in the bandwidths (transfer integrals) by a factor of 8. Only for N = 1 and 2, the total energy increases by 232 and 121 meV, respectively. This suggests that from a TTF-stacking point of view, there is no strong driving force preventing structures with comparably large bandwidths (such as for N = 12), which is in sharp contrast to observations for various molecular crystals [32,33].

Notably, in the stacks discussed so far (fully optimized or built from molecules in MOF conformation), the TTF molecules are slightly tilted around their long and short molecular axes. To assess the role of those tilts, we also studied two model systems in which such tilts do not occur, starting from a gas-phase optimized TTF molecule either in boat conformation (actual minimum structure) or forced to be planar. In the stacks, these molecules are then aligned such that all S atoms of each molecule are in a plane perpendicular to the screw axis. The infinitely extended stacks are then constructed following the procedure described in Section 1.1 and in the Supplementary Materials. The results for these stacks are complemented by calculations for corresponding molecular dimers. As shown in Figure 3b, the obtained data, at first glance, appear to directly correlate to the data for the MOF-derived structure (purple diamonds and line in Figure 3a). A closer inspection, however, reveals that there is a fundamental difference: the signs of the dimer transfer integrals come out negative for rotation angles Θ between ~65° and ~125° (where, for the sake of consistency, we also plot the bandwidths with a negative sign in that range of rotation angles). The zero-crossing of transfer integrals and bandwidths has a profound impact on charge transport properties. As for systems like the present one primarily the absolute value of the bandwidth counts, for the cases shown in Figure 3b the carrier mobility in stacking direction is expected to be close to a local maximum for the N = 4 system (rather than close to the global minimum, as for the systems shown in Figure 3a). Conversely, the valence bands become completely flat for rotation angles around ~65° and ~125°, implying a vanishingly small carrier mobility in for these angles.

The evolution of the transfer integrals with rotation angle (including the zero-crossing) can be explained by the shapes of the involved molecular orbitals. This is most straightforwardly seen for the bonding and antibonding linear combinations of the highest occupied molecular orbitals (HOMOs) of the two TTF molecules in the dimer calculations. They can be derived from linear combinations of the HOMOs of individual TTF molecules, and (for centrosymmetric systems) their splitting determines the magnitude of the transfer integral [31]. The evolutions of the orbital shapes and orbital energies with rotation angle are exemplarily shown in Figure 4 for the dimers consisting of planar molecules.

For the cofacial arrangement of the molecules, the antisymmetric linear combination of the TTF HOMOs is lowest in energy and the symmetric linear combination is highest (Figure 4b, 0°). This is exactly what one would expect considering the fully bonding nature of the hybrid orbital in the antisymmetric case (non-zero value of the wavefunction between molecules or even a local maximum) and its fully antibonding nature in the symmetric case (vanishing wavefunction between the molecules). Upon increasing the rotation angle, the HOMO-1 becomes increasingly destabilized and the HOMO gets stabilized, which reduces their energetic splitting and, concomitantly the associated transfer integral. This can be understood by the appearance of antibonding contributions for the antisymmetric and bonding contributions for the symmetric linear combinations. At a rotation angle of 65°, both linear combinations display nearly equal amounts of bonding and antibonding regions. Consequently, the two orbitals are essentially isoenergetic, resulting in a vanishing transfer integral. Upon further increasing the rotation angle, the nature of the HOMO and HOMO-1 is switched, resulting in a change of the sign of the transfer integral. The stabilization of the originally antisymmetric linear combination

of the molecular orbitals is maximized at a rotation angle of 95° and the trend is reversed for systems with larger rotations. In passing, we note that the reason for the much smaller HOMO-to-HOMO-1 splitting at 180° compared to the cofacial situation (i.e., 0°) is the reduced spatial overlap of the molecules following from the screw axis not coinciding with the center of the TTF molecules (see Figure 1).

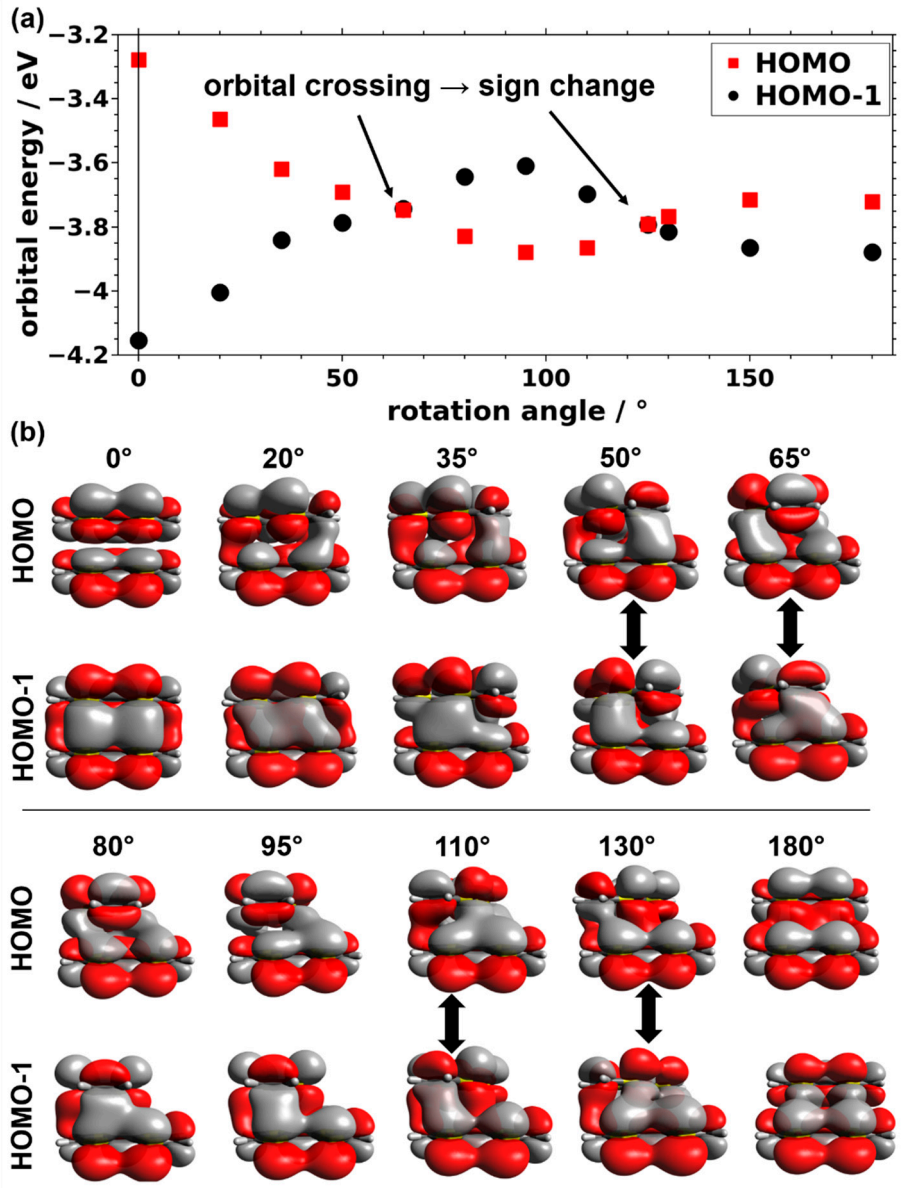

Figure 4. (**a**) Orbital energies of the planar TTF dimer as a function of the rotation angle and (**b**) corresponding plots showing the respective molecular orbitals. The dimers at the angles between which the two frontier orbitals change their order are highlighted by thick, vertical black arrows in panel (**b**).

Similar trends are observed for the other three molecular conformations. The lack of a zero-crossing of the bandwidths and transfer integrals for the MOF-derived and optimized geometries (i.e., the systems shown in Figure 3a) arises from the fact that due to the twisting of the molecules around the long and short molecular axes, certain regions of neighboring molecules get particularly close. This strongly amplifies the contributions of these regions to the orbital energies, such that the cancellation effects discussed above do not occur any more.

To conclude this section, it should be noted that, of course, also the location of the screw axis relative to the center of the TTF molecules impacts the wavefunction overlap, as discussed in detail in the Supplementary Materials. In short, the resulting overall situation is similar to the cases discussed above, although in that case, there is no zero-crossing of the transfer integral for the planar molecular conformation.

3.3. Impact of the Intermolecular Distance and of Chemical Modifications on the Bandwidth

Another structural parameter that is expected to change the intermolecular electronic coupling is the distance between neighboring TTF molecules. In fact, for layered MOFs, a profound impact of the layer proximity on the electronic band structure has been predicted [47]. For periodic stacks, such as the ones studied here, the distance between neighboring TTF molecules can simply be changed by modifying the unit cell length in the stacking direction. The impact of changing the stacking distance by ±0.1 Å per molecule is shown in Figure 5a for molecules adopting the same conformation as in the MOF and in Figure 5b for planar molecules. Not unexpectedly, the bandwidth typically increases upon decreasing the inter-molecular distance and vice versa. The data in Figure 5 also show that, typically, the absolute change in bandwidths and transfer integrals with stacking distance is more pronounced for situations in which these quantities are already large to start with. This can be rationalized based on the discussion of Figure 4 in the previous section; in cases in which bonding and antibonding contributions for certain hybrid orbitals largely cancel, the situation is not fundamentally modified upon changing the stacking distance. Conversely, when hybrid orbitals are either fully antibonding or fully bonding (as in the case of the cofacial dimer), changing the stacking distance has a maximal impact.

Notably, for the N = 6 stack, which directly mimics the stacking of the TTF molecules in the actual Zn_2(TTFTB) MOF, the increase in the valence bandwidth for a reduction in the stacking distance by 0.1 Å amounts to only 33 meV (~11%). This is, insofar, relevant, as it has been reported that changing the stacking distance for TTFTB-based MOFs results in massive changes in the measured electrical conductivities [53]. Especially when replacing the Zn^{2+} cations in the synthesis with Cd^{2+}, an increase in the electrical conductivity by two orders of magnitude has been observed. Originally, this was attributed to the lowered S . . . S distances for neighboring TTF units, which decreased by 0.103 Å [53]. Such a massive change in conductivities, however, cannot be explained by the trends discussed above. This raises the question of whether there are relevant structural changes between the Zn_2(TTFTB) and Cd_2(TTFTB) MOFs beyond a change in the stacking distance. Therefore, we compared the full electronic band structures of Zn_2(TTFTB) and Cd_2(TTFTB) (see Supplementary Materials), but also, in this case, the changes in bandwidths and effective masses for the valence band are comparably minor, as summarized in Table 1. In fact, the valence bandwidth is even smaller in Cd_2(TTFTB) than in Zn_2(TTFTB).

A different approach for increasing the valence bandwidth could be to increase the orbital overlap by exchanging TTF with tetraselenafulvalene ($C_6H_4Se_4$). In our calculations, this results in an increase in the valence bandwidth by a factor of almost two (from 371 to 641 meV). Considering that we observe only minor structural changes between the S-based Zn_2(TTFTB) and the Se-based Zn_2(TSFTB), we attribute that to the larger spatial extent of the p_z-orbitals of Se, which result in an increased wavefunction overlap. Nevertheless, such chemical modifications also do not change hole mobilities by orders of magnitude.

An additional factor that would influence the mobility of holes would be changes in the vibrational properties of the MOF, which impact charge transport through dynamic disorder effects [57,58,65]. Such effects are not explicitly considered here, but it is hard to imagine that they could be responsible for the orders of magnitude changes in transport properties between Zn_2(TTFTB) and Cd_2(TTFTB).

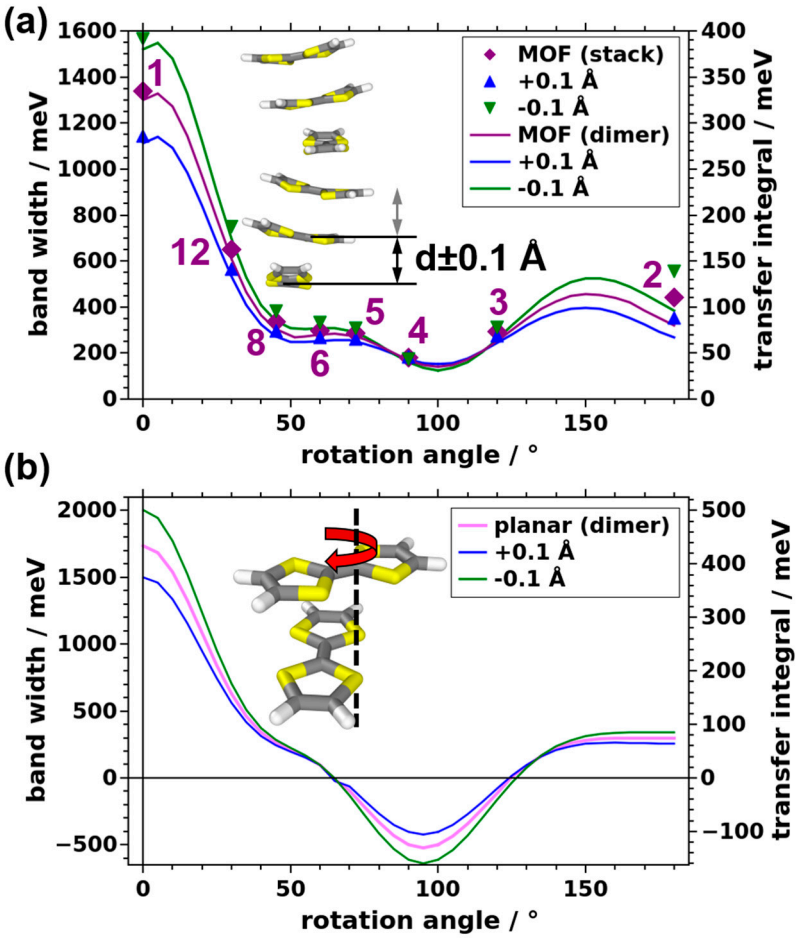

Figure 5. Evolution of the valence bandwidth and the transfer integral with the rotation angle as a function of the stacking distance. (**a**) Results obtained for TTF stacks and corresponding dimers based on the MOF geometry. (**b**) Dimer results based on the planar TTF conformation.

There could, however, be several other explanations for the above-mentioned differences. First, one has to keep in mind that in [53], the authors did not report carrier mobilities but electrical conductivities (which, to date, is still common for metal-organic frameworks [75]). These are crucially impacted not only by carrier mobilities but also by the densities of mobile carriers. As far as the latter are concerned, it has been argued in the past that they can be massively impacted by the nature of the metal ions in the nodes [12,79]. Another factor massively changing free carrier concentrations in any type of semiconductor is the presence of extrinsic impurities (i.e., dopants) [12,27,80–83].

Besides chemical imperfections influencing the carrier concentration, structural imperfections can also have a tremendous impact—in this case, also on the carrier mobilities. The impact of some of these imperfections on the electronic coupling in Zn_2(TTFTB) type systems is, therefore, discussed in the following section.

3.4. Role of Defects

A consequence of the flat electronic bands along reciprocal space directions perpendicular to the TTF stacks (see Section 3.1) is that charge transport is essentially one-dimensional. It is well established for molecular semiconductors that transport in 1D systems is severely affected by either static or dynamic disorder [58]. This is not surprising, considering that an "obstacle" along a 1D transport path cannot be simply bypassed via neighboring sites. In the context of MOFs, it has, actually, been found that defects can lead to bands with almost no dispersion [49]. For the present systems, we considered several types of static defects. As mentioned above, dynamic disorder caused by vibrations of the

MOF lattice is not considered here, although the defects discussed in the following, in some sense, also mimic what could happen as a function of the thermal motion of the MOF constituents.

The static defect with the most dramatic consequences is a missing linker defect. We realized such a defect by removing one TTF linker from either the Zn_2(TTFTB) unit cell or from the corresponding model stack (see Figure 6a). To describe pair formation as another type of defect, we displaced one molecule in the unit cell, such that it moved towards one of its neighbors by $-\Delta d$ and away from the other neighbor by $+\Delta d$ (see Figure 6b). A "displaced molecule" defect is characterized by one of the molecules in the unit cell being shifted from its equilibrium position along a vector parallel to the xy-plane (Figure 6c). In fact, it has been predicted for layered MOFs that interlayer displacements significantly affect the materials' band structures [48–50]. For OSCs, it is also well known that changes in the intermolecular interactions induced upon variations of the involved molecule's relative displacements depend on the actual shift direction [33–36,38]. In the present contribution, we focused on displacements along the x-direction (Figure 6b) as a representative example, highlighting the potential impact of such defects. For the final defect that is explicitly considered, the "misrotated" molecule case, the rotation angle of one of the molecules in the unit cell is changed by a value of $\Delta\Theta$ (Figure 6d). Considering the structure of the MOF and identifying the degrees of freedom of each TTF moiety, one could actually identify several more structural defects. Examples are tilts of the molecules around the long and short molecular axes, changes in the bending of the molecules, or torsions around the central C=C bonds, to name a few. Therefore, a missing linker, pair formation, a "displaced molecule", and misrotation of a molecule primarily serve as instructive examples for the possible impact of such structural defects on the electronic structure of the systems. Notably, the qualitative impact of all of the considered defects on the electronic structure of the model stacks is similar. They cause a loss of symmetry around the 6_5 screw axis in the center of the stack. Consequently, the notion of a single TTF molecule as the "electronic" repeat unit of the stack no longer applies. In the band structure, this results in an opening of gaps at the Brillouin zone boundary and at the Γ point (see Figure 7 for the missing linker, pair formation, and misrotated molecule defects). Thus, for the defective structures, it is not sensible to report the width of the six-times backfolded valence band and we will instead focus on the effective masses at the valence band maximum. Additionally, in the spirit of hopping transport, we will report the smallest transfer integrals between neighboring molecules found in all inequivalent dimers extracted from each of the defective TTF stacks.

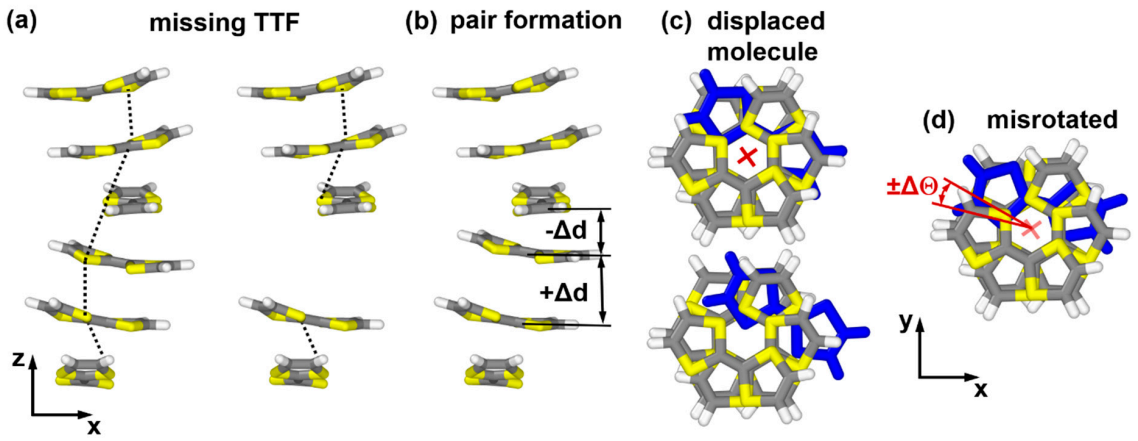

Figure 6. Instructive examples for possible structural defects in TTFTB-based MOFs. (**a**) Ideal model stack plus system with a missing TTF molecule; (**b**) structure of the system upon pair formation between neighboring TTFs; (**c**) displaced molecule defect realized by displacing one molecule along x; (**d**) structure of a misrotated molecule defect. It should be noted that for infinitely extended stacks, due to the employed periodic boundary conditions, a defect occurs in every unit cell.

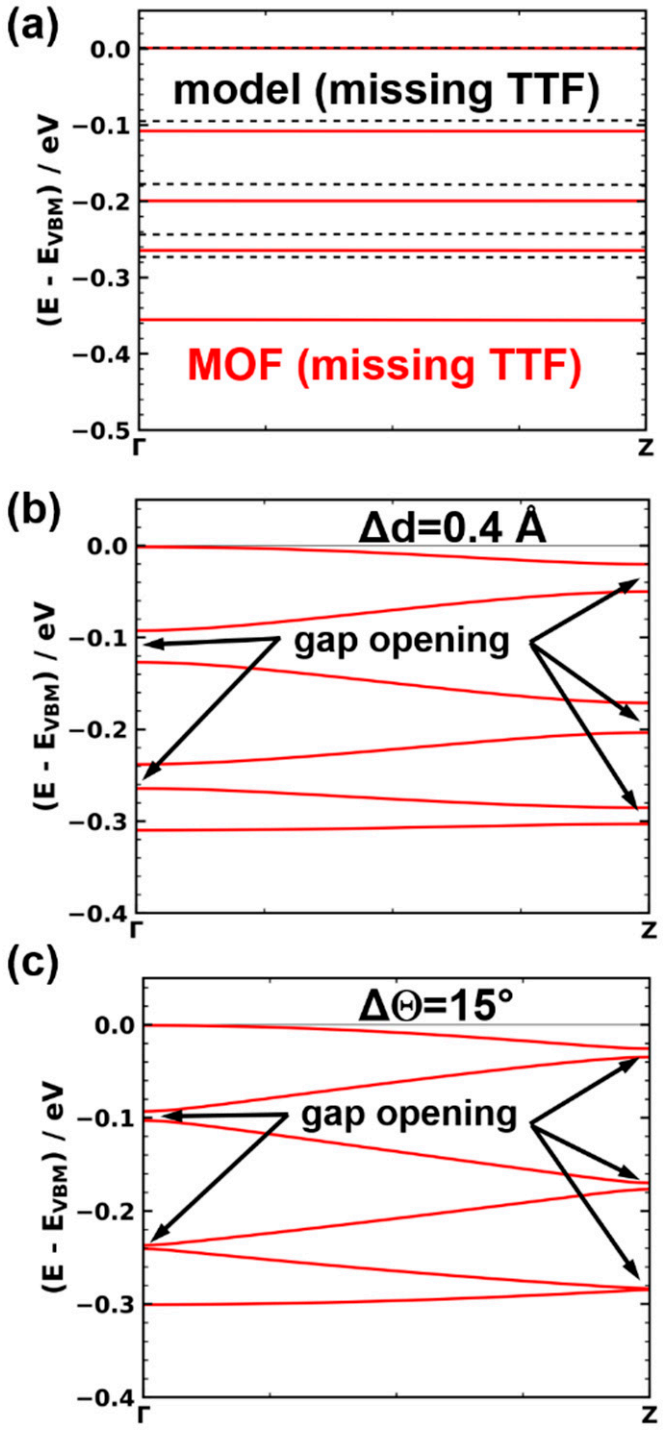

Figure 7. Electronic structure of the defective systems. (**a**) Electronic band structure in the stacking direction for Zn_2(TTFTB) with a missing linker defect (red solid line). The results for the corresponding TTF stack are shown as dashed black lines. (**b**) Electronic band structure for the model TTF stack with a pair formation defect with a displacement of Δd = 0.4 Å. (**c**) Electronic band structure for the model TTF stack with a misrotated molecule defect of ΔΘ = 15°.

The missing linker defect has the most dramatic impact. It results in essentially flat bands (see Figure 7a), the minimum transfer integral drops to 1 meV, and the effective mass skyrockets to 22 m_e. This shows that such a defect nearly stops charge transport along the affected TTF stack. As shown in Figure 8, also pair formation and displaced molecule defects result in an increased

effective mass and a decreased transfer integral (with the exception of a minor decrease in m* for a very small dimerization of Δd = 0.05 Å, which is in the range of the uncertainty of the fitting procedure). The magnitude of the change increases with increasing displacement. Additional data on the impact of the other defects can be found in the Supplementary Materials. As a consequence, charge transport is hindered within defective TTF stacks. Interestingly, for pair formation as well as for the displaced molecule defect, the minimum transfer integral decreases almost linearly with the displacement, while the effective mass experiences a roughly quadratic increase. The latter is more pronounced in the displaced molecule case. The overall impact of these defects is, however, rather moderate (especially compared to the missing-linker case). For example, a lateral displacement of a TTF molecule by a rather sizable distance of Δx = 0.3 Å leads to an increase in m* by a moderate 0.42 m_e (or 17%).

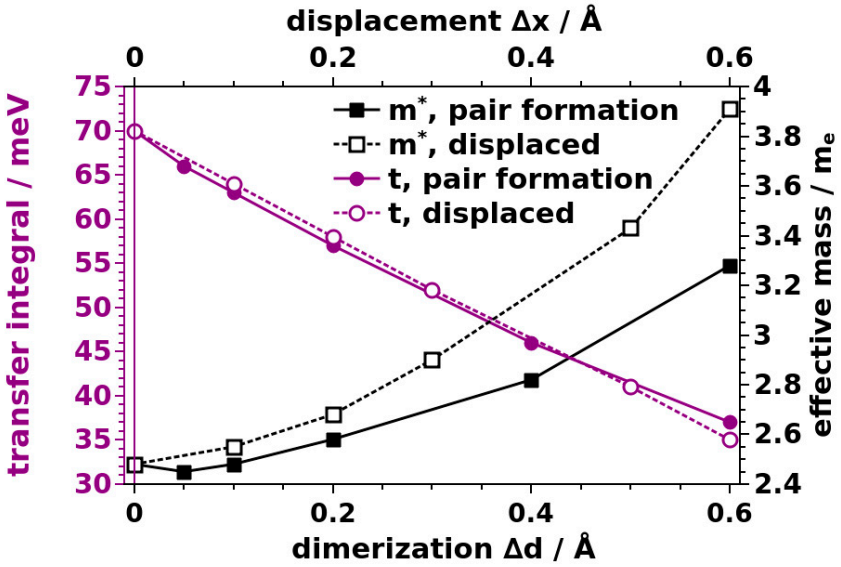

Figure 8. Evolution of the effective mass and the smallest transfer integral of the model TTF stack as a function of the dimerization displacement Δd and displacement Δx.

In this context it, however, has to be considered that our test of defective structures is not exhaustive. Additionally, several defects might occur simultaneously, further worsening the situation. Nevertheless, the above considerations suggest that for changing the carrier mobilities by orders of magnitude, mere displacements of molecules might not be sufficient and more serious defects, such as missing linkers, are required. To the best of our knowledge, no systematic experimental study on the interplay between defect densities and (through-space) charge transport properties of MOFs has been carried out to date. However, especially for Zr-based MOFs (in particular for UiO-66) it is well known how to control the defect density, and extensive experimental and computational studies on the influence of the defect density on energy gaps, the redox conductivity, and the (photo-)catalytic activity have been carried out [84–88]. Therefore, such systems appear as prime candidates for also studying the impact of defects on charge-transport properties.

4. Conclusions

The present paper describes a variety of aspects concerning through-space charge transport in metal-organic frameworks in general and tetrathiafulvalene-based MOFs in particular. First, it is shown that the electronic band structure of the helical TTF stack contained in Zn_2(TTFTB) largely determines the valence band structure of the entire MOF. In fact, we find that the electronic bands perpendicular to the TTF stacking direction are essentially flat. This highlights the negligible electronic coupling between neighboring stacks and establishes that Zn_2(TTFTB) is a truly one-dimensional conductor. In the perfectly periodic MOF with six molecules in the crystallographic unit cell, the valence band is

backfolded six times (without any gaps at the Γ-point or at the Brillouin zone boundary). This suggests that the symmetry element relevant for the electronic structure of the MOF is the six-fold screw axis parallel to the stacking direction. Therefore, a single TTF molecule acts as an "electronic" repeat unit of the MOF, with the consequence that the electronic parameter determining charge transport in Zn_2(TTFTB) is the transfer integral between two neighboring TTF molecules.

This permits the use of stacks with varying numbers of molecules in the crystallographic unit cell to study the impact of the relative rotation of the TTF molecules. It turns out that decreasing the rotation angle of neighboring TTF molecules compared to the parent Zn_2(TTFTB) system significantly increases the valence bandwidth, while increasing the rotation in a four-TTFs-per-unit-cell stack yields a significantly reduced electronic coupling. These results are corroborated by simulations on TTF dimers, which also allow us to trace the observations back to the shapes of the hybrid orbitals determining the valence band. Additionally, we found that the actual value of the transfer integral is extremely sensitive to the specific conformation of the TTF molecules. For example, for stacks of flat TTF molecules, the electronic coupling essentially disappears for the 60° rotation angles found in Zn_2(TTFTB) and the associated transfer integral even changes sign at larger angles.

Interestingly, changes in the relative rotation and molecular conformation of the TTF molecules have a more pronounced impact on the observed bandwidth than "moderate" modifications in the stacking distance, which have been realized experimentally by replacing Zn with Cd atoms in the metal nodes of the MOFs. Thus, we hypothesize that the two-orders of magnitude increase in the electrical conductivity of Cd_2(TTFTB) compared to Zn_2(TTFTB) [53] must either be the consequence of significantly modified concentrations of mobile carriers or must be due to different defect densities in the two systems.

As far as static defects are concerned, we have, thus, investigated several scenarios, including displaced molecules, molecular pairing along the stack, or misrotations of specific molecules. The impact of these defects turned out to be rather moderate. This, however, changes when also considering missing linker defects, where we find that due to the 1D nature of the TTF stacks, such a missing linker is a massive obstacle for charge transport. This is manifested, e.g., in an increase in the effective mass by a factor of ~10 compared to the perfectly ordered parent MOF.

Overall, these results show that on the one hand, there is still considerable room for improvement for through-space charge transport in MOFs through clever structural design. On the other hand, the 1D nature of systems, such as the ones discussed here, makes their expected charge-transport properties particularly sensitive to structural imperfections and, thus, extremely dependent on sample quality.

Supplementary Materials: Additional data on the electronic structures of the considered systems as well as a description of the basis employed during the DFT calculations, details on the construction of the model systems, and validation of the simple tight-binding model are available online at http://www.mdpi.com/2079-4991/10/12/2372/s1. All calculations are available from the NOMAD database under https://dx.doi.org/10.17172/NOMAD/2020.11.25-1.

Author Contributions: C.W. performed all simulations, conceived the first interpretation of the data, and provided an initial draft of the manuscript. E.Z. supported the interpretation of the data, helped with planning the research, and contributed significantly to writing the present article. All authors have read and agreed to the published version of the manuscript.

Funding: This research was funded by the TU Graz Lead Project "Porous Materials at Work" (LP-03).

Acknowledgments: The work was financially supported by the TU Graz Lead Project "Porous Materials at Work" (LP-03). The computational results have been achieved in part using the Vienna Scientific Cluster (VSC3). Open Access Funding by the Graz University of Technology is acknowledged.

Conflicts of Interest: The authors declare no conflict of interest.

References

1. James, S.L. Metal-organic frameworks. *Chem. Soc. Rev.* **2003**, *32*, 276–288. [CrossRef]
2. Rowsell, J.L.C.; Yaghi, O.M. Metal-organic frameworks: A new class of porous materials. *Microporous Mesoporous Mater.* **2004**, *73*, 3–14. [CrossRef]
3. Furukawa, H.; Cordova, K.E.; O'Keeffe, M.; Yaghi, O.M. The chemistry and applications of metal-organic frameworks. *Science* **2013**, *341*, 1230444. [CrossRef] [PubMed]
4. Eddaoudi, M.; Kim, J.; Rosi, N.; Vodak, D.; Wachter, J.; O'Keeffe, M.; Yaghi, O.M. Systematic design of pore size and functionality in isoreticular MOFs and their application in methane storage. *Science* **2002**, *295*, 469–472. [CrossRef] [PubMed]
5. Murray, L.J.; Dinc, M.; Long, J.R. Hydrogen storage in metal-organic frameworks. *Chem. Soc. Rev.* **2009**, *38*, 1294–1314. [CrossRef]
6. Rowsell, J.L.C.; Yaghi, O.M. Effects of functionalization, catenation, and variation of the metal oxide and organic linking units on the low-pressure hydrogen adsorption properties of metal-organic frameworks. *J. Am. Chem. Soc.* **2006**, *128*, 1304–1315. [CrossRef]
7. Pascanu, V.; González Miera, G.; Inge, A.K.; Martín-Matute, B. Metal-Organic Frameworks as Catalysts for Organic Synthesis: A Critical Perspective. *J. Am. Chem. Soc.* **2019**, *141*, 7223–7234. [CrossRef]
8. Zhu, L.; Liu, X.Q.; Jiang, H.L.; Sun, L.B. Metal-Organic Frameworks for Heterogeneous Basic Catalysis. *Chem. Rev.* **2017**, *117*, 8129–8176. [CrossRef]
9. Liu, J.; Chen, L.; Cui, H.; Zhang, J.; Zhang, L.; Su, C.Y. Applications of metal-organic frameworks in heterogeneous supramolecular catalysis. *Chem. Soc. Rev.* **2014**, *43*, 6011–6061. [CrossRef]
10. Bloch, E.D.; Queen, W.L.; Krishna, R.; Zadrozny, J.M.; Brown, C.M.; Long, J.R. Hydrocarbon separations in a metal-organic framework with open iron(II) coordination sites. *Science* **2012**, *335*, 1606–1610. [CrossRef]
11. Chen, B.; Liang, C.; Yang, J.; Contreras, D.S.; Clancy, Y.L.; Lobkovsky, E.B.; Yaghi, O.M.; Dai, S. A microporous metal-organic framework for gas-chromatographic separation of alkanes. *Angew. Chem.-Int. Ed.* **2006**, *45*, 1390–1393. [CrossRef] [PubMed]
12. Xie, L.S.; Skorupskii, G.; Dincă, M. Electrically Conductive Metal-Organic Frameworks. *Chem. Rev.* **2020**, *120*, 8536–8580. [CrossRef] [PubMed]
13. Clough, A.J.; Yoo, J.W.; Mecklenburg, M.H.; Marinescu, S.C. Two-dimensional metal-organic surfaces for efficient hydrogen evolution from water. *J. Am. Chem. Soc.* **2015**, *137*, 118–121. [CrossRef] [PubMed]
14. Miner, E.M.; Fukushima, T.; Sheberla, D.; Sun, L.; Surendranath, Y.; Dincə, M. Electrochemical oxygen reduction catalysed by Ni3 (hexaiminotriphenylene)2. *Nat. Commun.* **2016**, *7*, 10942. [CrossRef]
15. Dong, R.; Zheng, Z.; Tranca, D.C.; Zhang, J.; Chandrasekhar, N.; Liu, S.; Zhuang, X.; Seifert, G.; Feng, X. Immobilizing Molecular Metal Dithiolene–Diamine Complexes on 2D Metal-Organic Frameworks for Electrocatalytic H2Production. *Chem.-A Eur. J.* **2017**, *23*, 2255–2260. [CrossRef]
16. Downes, C.A.; Clough, A.J.; Chen, K.; Yoo, J.W.; Marinescu, S.C. Evaluation of the H2 Evolving Activity of Benzenehexathiolate Coordination Frameworks and the Effect of Film Thickness on H2 Production. *ACS Appl. Mater. Interfaces* **2018**, *10*, 1719–1727. [CrossRef]
17. Miner, E.M.; Wang, L.; Dincă, M. Modular O2 electroreduction activity in triphenylene-based metal-organic frameworks. *Chem. Sci.* **2018**, *9*, 6286–6291. [CrossRef]
18. Campbell, M.G.; Liu, S.F.; Swager, T.M.; Dincə, M. Chemiresistive Sensor Arrays from Conductive 2D Metal-Organic Frameworks. *J. Am. Chem. Soc.* **2015**, *137*, 13780–13783. [CrossRef]
19. Campbell, M.G.; Sheberla, D.; Liu, S.F.; Swager, T.M.; Dincə, M. Cu3(hexaiminotriphenylene)2: An electrically conductive 2D metal-organic framework for chemiresistive sensing. *Angew. Chem.-Int. Ed.* **2015**, *54*, 4349–4352. [CrossRef]
20. Meng, Z.; Aykanat, A.; Mirica, K.A. Welding Metallophthalocyanines into Bimetallic Molecular Meshes for Ultrasensitive, Low-Power Chemiresistive Detection of Gases. *J. Am. Chem. Soc.* **2019**, *141*, 2046–2053. [CrossRef]
21. Smith, M.K.; Mirica, K.A. Self-Organized Frameworks on Textiles (SOFT): Conductive Fabrics for Simultaneous Sensing, Capture, and Filtration of Gases. *J. Am. Chem. Soc.* **2017**, *139*, 16759–16767. [CrossRef] [PubMed]

22. Rubio-Giménez, V.; Almora-Barrios, N.; Escorcia-Ariza, G.; Galbiati, M.; Sessolo, M.; Tatay, S.; Martí-Gastaldo, C. Origin of the Chemiresistive Response of Ultrathin Films of Conductive Metal-Organic Frameworks. *Angew. Chem.-Int. Ed.* **2018**, *57*, 15086–15090. [CrossRef] [PubMed]
23. Aubrey, M.L.; Kapelewski, M.T.; Melville, J.F.; Oktawiec, J.; Presti, D.; Gagliardi, L.; Long, J.R. Chemiresistive Detection of Gaseous Hydrocarbons and Interrogation of Charge Transport in Cu[Ni(2,3-pyrazinedithiolate) 2] by Gas Adsorption. *J. Am. Chem. Soc.* **2019**, *141*, 5005–5013. [CrossRef] [PubMed]
24. Sheberla, D.; Bachman, J.C.; Elias, J.S.; Sun, C.J.; Shao-Horn, Y.; Dincă, M. Conductive MOF electrodes for stable supercapacitors with high areal capacitance. *Nat. Mater.* **2017**, *16*, 220–224. [CrossRef] [PubMed]
25. Park, J.; Lee, M.; Feng, D.; Huang, Z.; Hinckley, A.C.; Yakovenko, A.; Zou, X.; Cui, Y.; Bao, Z. Stabilization of Hexaaminobenzene in a 2D Conductive Metal-Organic Framework for High Power Sodium Storage. *J. Am. Chem. Soc.* **2018**, *140*, 10315–10323. [CrossRef] [PubMed]
26. Shinde, S.S.; Lee, C.H.; Jung, J.Y.; Wagh, N.K.; Kim, S.H.; Kim, D.H.; Lin, C.; Lee, S.U.; Lee, J.H. Unveiling dual-linkage 3D hexaiminobenzene metal-organic frameworks towards long-lasting advanced reversible Zn-air batteries. *Energy Environ. Sci.* **2019**, *12*, 727–738. [CrossRef]
27. Stassen, I.; Burtch, N.; Talin, A.; Falcaro, P.; Allendorf, M.; Ameloot, R. An updated roadmap for the integration of metal-organic frameworks with electronic devices and chemical sensors. *Chem. Soc. Rev.* **2017**, *46*, 3185–3241. [CrossRef]
28. Medina, D.D.; Mähringer, A.; Bein, T. Electroactive Metalorganic Frameworks. *Isr. J. Chem.* **2018**, *58*, 1089–1101. [CrossRef]
29. Sun, L.; Campbell, M.G.; Dincă, M. Electrically Conductive Porous Metal-Organic Frameworks. *Angew. Chem. Int. Ed.* **2016**, *55*, 3566–3579. [CrossRef]
30. Kazmaier, P.M.; Hoffmann, R. A Theoretical Study of Crystallochromy. Quantum Interference Effects in the Spectra of Perylene Pigments. *J. Am. Chem. Soc.* **1994**, *116*, 9684–9691. [CrossRef]
31. Coropceanu, V.; Cornil, J.; da Silva Filho, D.A.; Olivier, Y.; Silbey, R.; Brédas, J.L. Charge transport in organic semiconductors. *Chem. Rev.* **2007**, *107*, 926–952. [CrossRef] [PubMed]
32. Sutton, C.; Risko, C.; Brédas, J.-L. Noncovalent Intermolecular Interactions in Organic Electronic Materials: Implications for the Molecular Packing vs Electronic Properties of Acenes. *Chem. Mater.* **2016**, *28*, 3–16. [CrossRef]
33. Winkler, C.; Jeindl, A.; Mayer, F.; Hofmann, O.T.; Tonner, R.; Zojer, E. Understanding the Correlation between Electronic Coupling and Energetic Stability of Molecular Crystal Polymorphs: The Instructive Case of Quinacridone. *Chem. Mater.* **2019**, *31*, 7054–7069. [CrossRef]
34. Kwon, O.; Coropceanu, V.; Gruhn, N.E.; Durivage, J.C.; Laquindanum, J.G.; Katz, H.E.; Cornil, J.; Brédas, J.L. Characterization of the molecular parameters determining charge transport in anthradithiophene. *J. Chem. Phys.* **2004**, *120*, 8186–8194. [CrossRef]
35. Lemaur, V.; Da Silva Filho, D.A.; Coropceanu, V.; Lehmann, M.; Geerts, Y.; Piris, J.; Debije, M.G.; Van De Craats, A.M.; Senthilkumar, K.; Siebbeles, L.D.A.; et al. Charge Transport Properties in Discotic Liquid Crystals: A Quantum-Chemical Insight into Structure-Property Relationships. *J. Am. Chem. Soc.* **2004**, *126*, 3271–3279. [CrossRef]
36. Bredas, J.L.; Calbert, J.P.; da Silva Filho, D.A.; Cornil, J. Organic semiconductors: A theoretical characterization of the basic parameters governing charge transport. *Proc. Natl. Acad. Sci. USA* **2002**, *99*, 5804–5809. [CrossRef]
37. Brédas, J.L.; Beljonne, D.; Coropceanu, V.; Cornil, J. Charge-transfer and energy-transfer processes in π-conjugated oligomers and polymers: A molecular picture. *Chem. Rev.* **2004**, *104*, 4971–5003. [CrossRef]
38. da Silva Filho, D.A.; Kim, E.-G.; Brédas, J.-L. Transport Properties in the Rubrene Crystal: Electronic Coupling and Vibrational Reorganization Energy. *Adv. Mater.* **2005**, *17*, 1072–1076. [CrossRef]
39. Tant, J.; Geerts, Y.H.; Lehmann, M.; De Cupere, V.; Zucchi, G.; Laursen, B.W.; Bjørnholm, T.; Lemaur, V.; Marcq, V.; Burquel, A.; et al. Liquid crystalline metal-free phthalocyanines designed for charge and exciton transport. *J. Phys. Chem. B* **2005**, *109*, 20315–20323. [CrossRef]
40. Cornil, J.; Lemaur, V.; Calbert, J.P.; Brédas, J.L. Charge transport in discotic liquid crystals: A molecular scale description. *Adv. Mater.* **2002**, *14*, 726–729. [CrossRef]
41. Lehmann, M.; Kestemont, G.; Aspe, R.G.; Buess-Herman, C.; Koch, M.H.J.; Debije, M.G.; Piris, J.; De Haas, M.P.; Warman, J.M.; Watson, M.D.; et al. High charge-carrier mobility in π-deficient discotic mesogens: Design and structure-property relationship. *Chem.-A Eur. J.* **2005**, *11*, 3349–3362. [CrossRef] [PubMed]

42. Idé, J.; Méreau, R.; Ducasse, L.; Castet, F.; Olivier, Y.; Martinelli, N.; Cornil, J.; Beljonne, D. Supramolecular organization and charge transport properties of self-assembled π-π Stacks of perylene diimide dyes. *J. Phys. Chem. B* **2011**, *115*, 5593–5603. [CrossRef] [PubMed]
43. Mei, J.; Diao, Y.; Appleton, A.L.; Fang, L.; Bao, Z. Integrated materials design of organic semiconductors for field-effect transistors. *J. Am. Chem. Soc.* **2013**, *135*, 6724–6746. [CrossRef] [PubMed]
44. Anthony, J.E. Functionalized acenes and heteroacenes for organic electronics. *Chem. Rev.* **2006**, *106*, 5028–5048. [CrossRef] [PubMed]
45. Okamoto, T.; Nakahara, K.; Saeki, A.; Seki, S.; Oh, J.H.; Akkerman, H.B.; Bao, Z.; Matsuo, Y. Aryl-perfluoroaryl substituted tetracene: Induction of face-to-face π-π Stacking and enhancement of charge carrier properties. *Chem. Mater.* **2011**, *23*, 1646–1649. [CrossRef]
46. Sorli, J.C.; Ai, Q.; Granger, D.B.; Gu, K.; Parkin, S.; Jarolimek, K.; Telesz, N.; Anthony, J.E.; Risko, C.; Loo, Y.L. Impact of Atomistic Substitution on Thin-Film Structure and Charge Transport in a Germanyl-ethynyl Functionalized Pentacene. *Chem. Mater.* **2019**, *31*, 6615–6623. [CrossRef]
47. Kuc, A.; Springer, M.A.; Batra, K.; Juarez-Mosqueda, R.; Wöll, C.; Heine, T. Proximity Effect in Crystalline Framework Materials: Stacking-Induced Functionality in MOFs and COFs. *Adv. Funct. Mater.* **2020**, *30*, 1908004. [CrossRef]
48. Foster, M.E.; Sohlberg, K.; Spataru, C.D.; Allendorf, M.D. Proposed Modification of the Graphene Analogue Ni3(HITP)2 To Yield a Semiconducting Material. *J. Phys. Chem. C* **2016**, *120*, 15001–15008. [CrossRef]
49. Foster, M.E.; Sohlberg, K.; Allendorf, M.D.; Talin, A.A. Unraveling the Semiconducting/Metallic Discrepancy in Ni 3 (HITP) 2. *J. Phys. Chem. Lett.* **2018**, *9*, 481–486. [CrossRef]
50. Clough, A.J.; Skelton, J.M.; Downes, C.A.; De La Rosa, A.A.; Yoo, J.W.; Walsh, A.; Melot, B.C.; Marinescu, S.C. Metallic Conductivity in a Two-Dimensional Cobalt Dithiolene Metal-Organic Framework. *J. Am. Chem. Soc.* **2017**, *139*, 10863–10867. [CrossRef]
51. Narayan, T.C.; Miyakai, T.; Seki, S.; Dincă, M. High charge mobility in a tetrathiafulvalene-based microporous metal-organic framework. *J. Am. Chem. Soc.* **2012**, *134*, 12932–12935. [CrossRef] [PubMed]
52. Xie, L.S.; Dincă, M. Novel Topology in Semiconducting Tetrathiafulvalene Lanthanide Metal-Organic Frameworks. *Isr. J. Chem.* **2018**, *58*, 1119–1122. [CrossRef]
53. Park, S.S.; Hontz, E.R.; Sun, L.; Hendon, C.H.; Walsh, A.; Van Voorhis, T.; Dincə, M. Cation-dependent intrinsic electrical conductivity in isostructural tetrathiafulvalene-based microporous metal-organic frameworks. *J. Am. Chem. Soc.* **2015**, *137*, 1774–1777. [CrossRef] [PubMed]
54. Xie, L.S.; Alexandrov, E.V.; Skorupskii, G.; Proserpio, D.M.; Dincă, M. Diverse π-π Stacking motifs modulate electrical conductivity in tetrathiafulvalene-based metal-organic frameworks. *Chem. Sci.* **2019**, *10*, 8558–8565. [CrossRef] [PubMed]
55. Oberhofer, H.; Reuter, K.; Blumberger, J. Charge Transport in Molecular Materials: An Assessment of Computational Methods. *Chem. Rev.* **2017**, *117*, 10319–10357. [CrossRef] [PubMed]
56. Tessler, N.; Preezant, Y.; Rappaport, N.; Roichman, Y. Charge transport in disordered organic materials and its relevance to thin-film devices: A tutorial review. *Adv. Mater.* **2009**, *21*, 2741–2761. [CrossRef]
57. Fratini, S.; Mayou, D.; Ciuchi, S. The transient localization scenario for charge transport in crystalline organic materials. *Adv. Funct. Mater.* **2016**, *26*, 2292–2315. [CrossRef]
58. Fratini, S.; Ciuchi, S.; Mayou, D.; De Laissardière, G.T.; Troisi, A. A map of high-mobility molecular semiconductors. *Nat. Mater.* **2017**, *16*, 998–1002. [CrossRef]
59. Troisi, A.; Orlandi, G. Charge-Transport Regime of Crystalline Organic Semiconductors: Diffusion Limited by Thermal Off-Diagonal Electronic Disorder. *Phys. Rev. Lett.* **2006**, *96*, 086601. [CrossRef]
60. Ciuchi, S.; Fratini, S.; Mayou, D. Transient localization in crystalline organic semiconductors. *Phys. Rev. B* **2011**, *83*, 081202. [CrossRef]
61. Fratini, S.; Ciuchi, S. Bandlike motion and mobility saturation in organic molecular semiconductors. *Phys. Rev. Lett.* **2009**, *103*, 266601. [CrossRef] [PubMed]
62. Cheng, Y.-C.; Silbey, R.J. A unified theory for charge-carrier transport in organic crystals. *J. Chem. Phys.* **2008**, *128*, 114713. [CrossRef] [PubMed]
63. Valeev, E.F.; Coropceanu, V.; Da Silva Filho, D.A.; Salman, S.; Brédas, J.L. Effect of electronic polarization on charge-transport parameters in molecular organic semiconductors. *J. Am. Chem. Soc.* **2006**, *128*, 9882–9886. [CrossRef] [PubMed]

64. Winkler, C.; Mayer, F.; Zojer, E. Analyzing the Electronic Coupling in Molecular Crystals—The Instructive Case of α-Quinacridone. *Adv. Theory Simul.* **2019**, *2*, 1800204. [CrossRef]
65. Schweicher, G.; D'Avino, G.; Ruggiero, M.T.; Harkin, D.J.; Broch, K.; Venkateshvaran, D.; Liu, G.; Richard, A.; Ruzié, C.; Armstrong, J.; et al. Chasing the "Killer" Phonon Mode for the Rational Design of Low-Disorder, High-Mobility Molecular Semiconductors. *Adv. Mater.* **2019**, *31*, 1902407. [CrossRef] [PubMed]
66. Mancuso, J.L.; Mroz, A.M.; Le, K.N.; Hendon, C.H. Electronic Structure Modeling of Metal-Organic Frameworks. *Chem. Rev.* **2020**, *120*, 8641–8715. [CrossRef]
67. Blum, V.; Gehrke, R.; Hanke, F.; Havu, P.; Havu, V.; Ren, X.; Reuter, K.; Scheffler, M. Ab initio molecular simulations with numeric atom-centered orbitals. *Comput. Phys. Commun.* **2009**, *180*, 2175–2196. [CrossRef]
68. Perdew, J.P.; Burke, K.; Ernzerhof, M. Generalized Gradient Approximation Made Simple. *Phys. Rev. Lett.* **1996**, *77*, 3865–3868. [CrossRef]
69. Perdew, J.P.; Burke, K.; Ernzerhof, M. Erratum: Generalized gradient approximation made simple (Physical Review Letters (1996) 77 (3865)). *Phys. Rev. Lett.* **1997**, *78*, 1396. [CrossRef]
70. Tkatchenko, A.; Scheffler, M. Accurate Molecular Van Der Waals Interactions from Ground-State Electron Density and Free-Atom Reference Data. *Phys. Rev. Lett.* **2009**, *102*, 073005. [CrossRef]
71. Heyd, J.; Scuseria, G.E.; Ernzerhof, M. Hybrid functionals based on a screened Coulomb potential. *J. Chem. Phys.* **2003**, *118*, 8207–8215. [CrossRef]
72. Heyd, J.; Scuseria, G.E.; Ernzerhof, M. Erratum: Hybrid functionals based on a screened Coulomb potential (Journal of Chemical Physics (2003) 118 (8207)). *J. Chem. Phys.* **2006**, *124*, 219906. [CrossRef]
73. Stukowski, A. Visualization and analysis of atomistic simulation data with OVITO–the Open Visualization Tool. *Model. Simul. Mater. Sci. Eng.* **2010**, *18*, 015012. [CrossRef]
74. Hanwell, M.D.; Curtis, D.E.; Lonie, D.C.; Vandermeersch, T.; Zurek, E.; Hutchison, G.R. Avogadro: An advanced semantic chemical editor, visualization, and analysis platform. *J. Cheminform.* **2012**, *4*, 17. [CrossRef] [PubMed]
75. Sun, L.; Park, S.S.; Sheberla, D.; Dincă, M. Measuring and Reporting Electrical Conductivity in Metal-Organic Frameworks: Cd2(TTFTB) as a Case Study. *J. Am. Chem. Soc.* **2016**, *138*, 14772–14782. [CrossRef] [PubMed]
76. Wudl, F.; Smith, G.M.; Hufnagel, E.J. Bis-1,3-dithiolium chloride: An unusually stable organic radical cation. *J. Chem. Soc. D Chem. Commun.* **1970**, *21*, 1453–1454. [CrossRef]
77. Ferraris, J.; Cowan, D.O.; Walatka, V.; Perlstein, J.H. Electron Transfer in a New Highly Conducting Donor-Acceptor Complex. *J. Am. Chem. Soc.* **1973**, *95*, 948–949. [CrossRef]
78. Senthilkumar, K.; Grozema, F.C.; Bickelhaupt, F.M.; Siebbeles, L.D.A. Charge transport in columnar stacked triphenylenes: Effects of conformational fluctuations on charge transfer integrals and site energies. *J. Chem. Phys.* **2003**, *119*, 9809–9817. [CrossRef]
79. Sun, L.; Hendon, C.H.; Park, S.S.; Tulchinsky, Y.; Wan, R.; Wang, F.; Walsh, A.; Dincă, M. Is iron unique in promoting electrical conductivity in MOFs? *Chem. Sci.* **2017**, *8*, 4450–4457. [CrossRef]
80. Kobayashi, Y.; Jacobs, B.; Allendorf, M.D.; Long, J.R. Conductivity, doping, and redox chemistry of a microporous dithiolene-based metal-organic framework. *Chem. Mater.* **2010**, *22*, 4120–4122. [CrossRef]
81. Lee, D.Y.; Kim, E.K.; Shrestha, N.K.; Boukhvalov, D.W.; Lee, J.K.; Han, S.H. Charge Transfer-Induced Molecular Hole Doping into Thin Film of Metal-Organic Frameworks. *ACS Appl. Mater. Interfaces* **2015**, *7*, 18501–18507. [CrossRef] [PubMed]
82. Xie, L.S.; Sun, L.; Wan, R.; Park, S.S.; Degayner, J.A.; Hendon, C.H.; Dincă, M. Tunable Mixed-Valence Doping toward Record Electrical Conductivity in a Three-Dimensional Metal-Organic Framework. *J. Am. Chem. Soc.* **2018**, *140*, 7411–7414. [CrossRef] [PubMed]
83. Wentz, H.C.; Skorupskii, G.; Bonfim, A.B.; Mancuso, J.L.; Hendon, C.H.; Oriel, E.H.; Sazama, G.T.; Campbell, M.G. Switchable electrical conductivity in a three-dimensional metal-organic framework: Via reversible ligand n-doping. *Chem. Sci.* **2020**, *11*, 1342–1346. [CrossRef]
84. Shimoni, R.; He, W.; Liberman, I.; Hod, I. Tuning of Redox Conductivity and Electrocatalytic Activity in Metal-Organic Framework Films Via Control of Defect Site Density. *J. Phys. Chem. C* **2019**, *123*, 5531–5539. [CrossRef]
85. Svane, K.L.; Bristow, J.K.; Gale, J.D.; Walsh, A. Vacancy defect configurations in the metal–organic framework UiO-66: Energetics and electronic structure. *J. Mater. Chem. A* **2018**, *6*, 8507–8513. [CrossRef]

86. De Vos, A.; Hendrickx, K.; Van Der Voort, P.; Van Speybroeck, V.; Lejaeghere, K. Missing Linkers: An Alternative Pathway to UiO-66 Electronic Structure Engineering. *Chem. Mater.* **2017**, *29*, 3006–3019. [CrossRef]
87. Xiang, W.; Zhang, Y.; Chen, Y.; Liu, C.J.; Tu, X. Synthesis, characterization and application of defective metal-organic frameworks: Current status and perspectives. *J. Mater. Chem. A* **2020**, *8*, 21526–21546. [CrossRef]
88. Taddei, M.; Schukraft, G.M.; Warwick, M.E.A.; Tiana, D.; McPherson, M.J.; Jones, D.R.; Petit, C. Band gap modulation in zirconium-based metal-organic frameworks by defect engineering. *J. Mater. Chem. A* **2019**, *7*, 23781–23786. [CrossRef]

4.3. Supporting Information

nanomaterials

MDPI

Supplementary Material

Strategies for Controlling Through-Space Charge Transport in Metal-Organic Frameworks via Structural Modifications

Christian Winkler and Egbert Zojer *

Institute of Solid State Physics, NAWI Graz, Graz University of Technology, Petersgasse 16, 8010 Graz, Austria; christian.winkler@student.tugraz.at

* Correspondence: egbert.zojer@tugraz.at

1. Additional methodological details

1.1. Overview of basis functions used in FHI-AIMS

Table 1. Basis functions that have been used for all calculations performed with FHI-AIMS. The abbreviations read as follows: H(nl,z), where H describes the type of the basis function where H stands for hydrogen-like type function, n is the main quantum number, l denotes the angular momentum quantum number, and z denotes an effective nuclear charge which scales the radial function in the defining Coulomb potential.[1].

	H	**C**	**S**	**O**	**Zn**	**Se**	**Cd**
Minimal	1s	[He]+2s2p	[Ne]+3s3p	[He]+2s2p	[Ar]+4s3p3d	[Ar]+4s3d4p	[Kr]+4d5s
Tier 1	H(2s,2.1) H(2p,3.5)	H(2p,1.7) H(3d,6) H(2s,4.9)	ionic(3d,auto) H(2p,1.8) H(4f,7) ionic(3s,auto)	H(2p,1.8) H(3d,7.6) H(3s,6.4)	H(2p,1.7) H(3s,2.9) H(4p,5.4) H(4f,7.8) H(3d,4.5)	H(3d,4.3) H(2p,1.6) H(4f,7.2) ionic(4s, auto)	H(2p,1.6) H(4f,7) H(3s,2.8) H(3p,5.2) H(5g,10) H(3d,3.8)
Tier 2	H(1s,0.85) H(2p,3.7) H(2s,1.2) H(3d,7)	H(3p,5.2) H(3s,4.3) H(3d,6.2)	H(4d,6.2) H(4p,4.9) H(1s,0.8)	H(3p,6.2) H(3d,5.6) H(1s,0.75)		H(4p,4.5) H(4d6.2) H(1s,0.5)	

1.2. Construction of TTF and TTFTB model systems

Additional details on the construction of several model systems discussed in the main manuscript are give below.

First, based on the relaxed structure of desolvated and dehydrated Zn_2(TTFTB), we constructed helical model TTF and TTFTB stacks by removing all atoms within the MOF structure apart from the TTF cores. The latter were then saturated by attaching H atoms. Subsequently, the positions of these H atoms were relaxed while keeping all other atomic positions fixed. This results in TTF molecules exhibiting the same geometry and stacking motif as in the MOF. These stacks were then arranged in the same pattern as in the MOF as shown in Fig. 1a of the main manuscript. In a similar way also the TTFTB model stack has been constructed: All atoms apart from the TTF core and the connected phenylene rings were removed. In essence, this means that the carboxyl groups have been removed from the linker in the MOF structure and replaced by H atoms. The positions of these H atoms then were relaxed in a subsequent step.

Second, for generating TTF stacks with different numbers of repeat units N, we simply picked one of the symmetry equivalent molecules of the parent stack discussed in the previous paragraph. This molecule was then duplicated, and rotated by the respective rotation angle ((n/N)*360°) around the off-center rotation axis (with n being an integer between 1 and N-1). Then the molecule was shifted in z-direction by n*3.473 Å. This procedure was repeated N-1 times to generate the unit cell for the simulations. For example, for 3 repeat units (N=3) we have in total three TTF molecules per unit cell including the molecule at the bottom of the cell (n=0) and its replicas at n=1 and n=2. The lateral extent of the unit cell of the model system is the same as that observed experimentally for Zn_2(TTFTB), while the extent of the unit cell in stacking direction amounts to N*3.473 Å. To verify the construction procedure we compared the electronic structure of the N=6 TTF model stack to the system extracted directly from the MOF structure. The identified differences are almost negligible (see Table 1) and can be assigned to subtle changes in the geometry of individual TTF molecules within the MOF-extracted system.

1.3. Comparison of a simple tight-binding model to the electronic band structure of Zn_2(TTFTB)

Here, we investigate whether a simple, one-dimensional tight-binding model with one "electronic" repeat unit can reproduce the 6-times backfolded band structure of the model stacks (shape and band width). This is relevant, as the transfer integrals reported in the main manuscript have been extracted from calculated actual band widths employing that approach. The model reads $E(k) = 2t * cos(k * R)$, with R being the shift between adjacent TTF molecules in the direction of the screw axis, i.e., the distance between electronic repeat units in stacking direction (R = 3.473 Å). From the electronic band structure of the 6 repeat unit TTF stack we extracted the transfer integral as (1/4)×W, with W being the calculated band width. Using W=298 meV we then calculated the electronic band structure of the model. In order to compare it to the 6 times backfolded band structure of the TTF stack we folded the resulting band back into the crystallographic unit cell of the TTF stack containing 6 molecules. Comparing the two band structures (green for model and red for TTF stack in Figure S1a), we find an excellent qualitative agreement. I.e., the simple tight-binding model with a single TTF molecule as "electronic repeat units" provides a physically meaningful model for the valence band of the TTF stack. Also the quantitative agreement is reasonably good, which supports the use of t = W/4 for depicting the trends for the transfer integrals in the main manuscript.

In the actual stack, there might, of course, also be couplings to next nearest neighbors which might play a role. Such couplings could be hyperexchange-like, as we observed it in quinacridone, a prototypical H-bonded organic semiconductor.[2] Therefore, we also considered a slightly modified model, where we considered next-nearest neighbor couplings as well. It reads: $E(k) = 2t * cos(k * R) + b * 2t * cos(2 * k * R)$. The coupling between these sites was estimated to be around 10% of the nearest neighbor couplings (~8 meV) where b actually is a fit parameter (smallest RMSE for b=0.1). A comparison between the bands resulting from this model and the actual TTF stack is shown in Figure S1b. There, we observe a further improved agreement between the simple tight-binding model and the data of the actual TTF stack, especially at the band extrema.

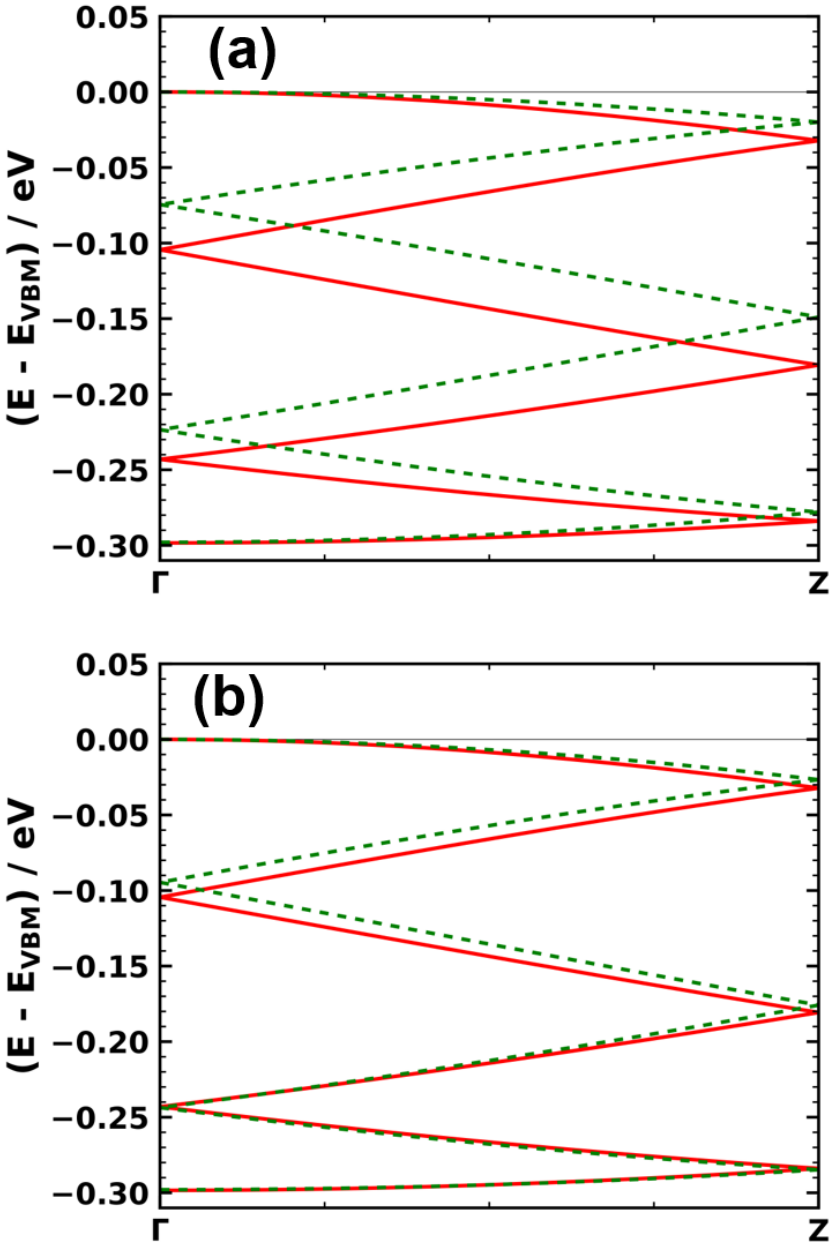

Figure S1. Comparison of band structures resulting from simple tight-binding models (green dashed line) and the 6 repeat unit TTF stack (solid red line). (a) One-dimensional tight-binding model with only nearest neighbor couplings considered. (b) One-dimensional tight-binding model with next-nearest neighbor couplings also included.

2. Additional data for Zn_2(TTFTB) and the TTF model systems

2.1. Species projected and angular momentum resolved density of states of Zn_2(TTFTB)

For a further in-depth analysis, we projected the density of states onto individual parts of the MOF: the central TTF stack (TTF), the phenylene rings (rings) and the metal nodes (frame). Similar to the findings in Ref [3], this projected density of states (pDOS, displayed in bottom-right panel of Figure S2) shows that the valence band is primarily formed from states localized on the TTF stacks. Analyzing the angular momentum resolved species projected DOS also shown in Figure S2 we find that these states are of p-character. The phenylene rings contribute only weakly to the valence band. This is consistent with the notion that the valence band describes a through-space pathway for holes along the helical stack of TTF molecules. In contrast, for the conduction band, one can see non-negligible contributions from the phenylene rings as well as from the metal nodes. This means that electron transport also involves other parts of the MOF besides the central TTF stack. For the conduction band also O p-states and a small contribution from Zn p-states are important.

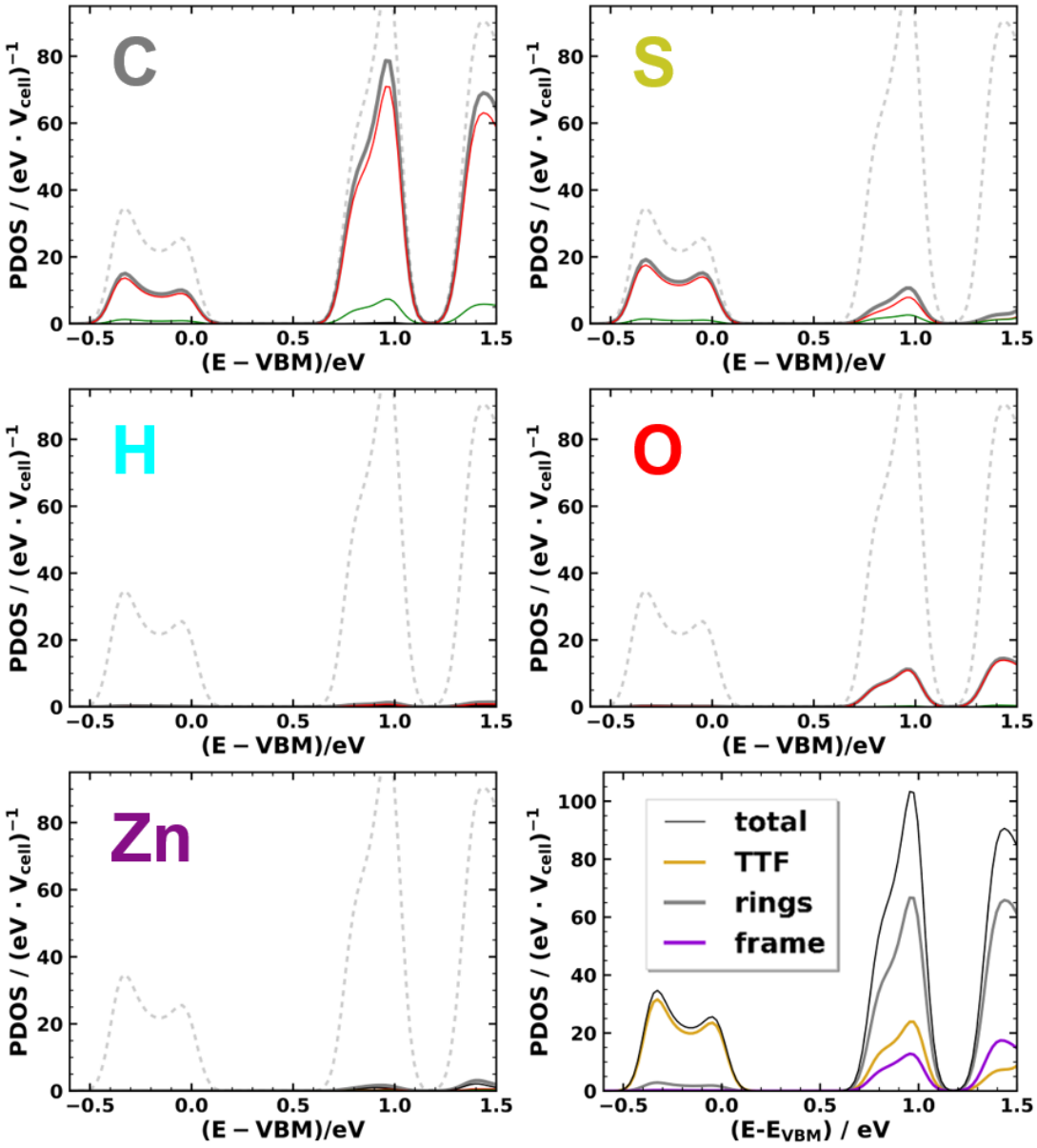

Figure S2. Species-projected and angular momentum resolved density of states for Zn_2(TTFTB). Grey is the total contribution of the individual species, black indicates s-states, red p-states and green d-states. Bottom right panel: Density of states of Zn_2(TTFTB) projected onto individual parts of the

MOF. "TTF" refers to the TTF units, "rings" to the attached phenylene rings and "frame" to the nodes. The total density of states (as the sum of the individual contributions) is given by the black line.

2.2. Electronic structure of Zn_2(TTFTB) calculated with HSE06

To see how the electronic structure of the MOF would be affected by the choice of the actual functional (in particular the treatment of exchange and correlation), we also employed the range separated hybrid functional HSE06 to calculate the electronic structure of Zn_2(TTFTB) (Figure S3). As expected for hybrid functionals, this results in an increased band gap (0.773 eV for PBE and 1.483 eV for HSE), which is, however, of no relevance for the discussion in the present manuscript. More relevant is the slightly larger width of the valence band obtained with HSE, but the overall effect is rather minor. These two differences aside, there is virtually no difference between the PBE and the HSE calculations.

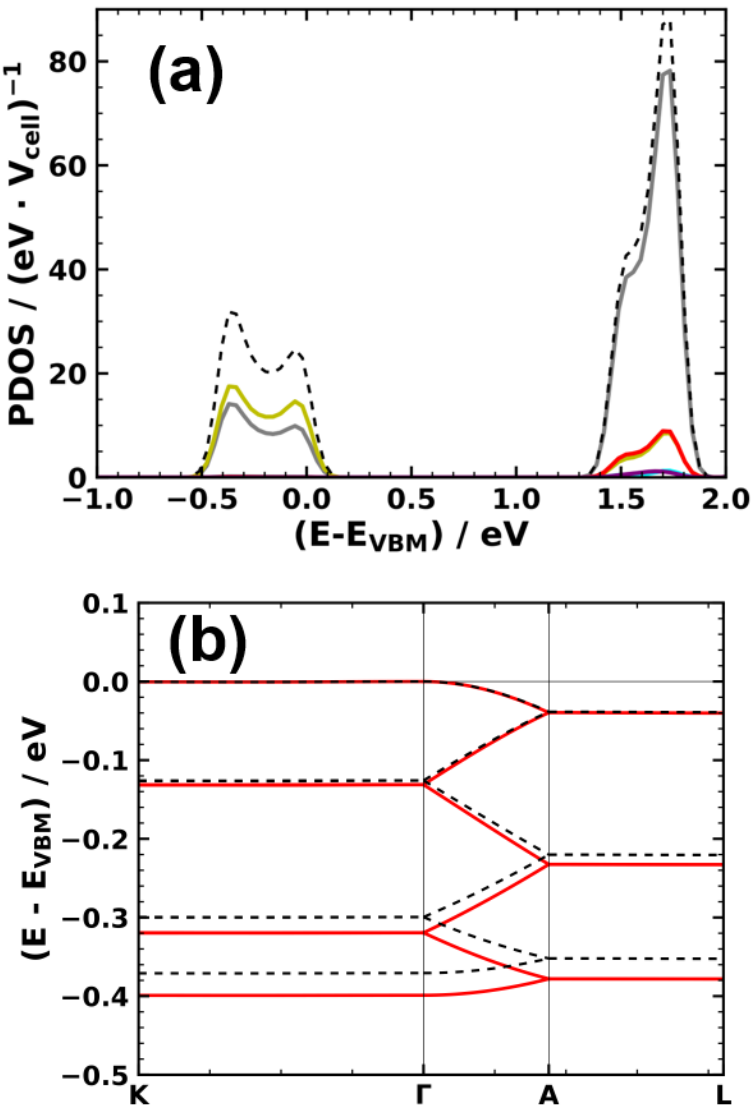

Figure S3. Electronic structure of Zn_2(TTFTB) calculated employing the HSE06 functional and using a PBE-optimized geometry. (a) Species projected density of states (C—grey, H—cyan, O—red, Se—yellow, Zn—purple) and (b) Electronic band structure of the valence band as obtained with HSE06 (red) compared to the PBE result (black, dashed).

2.3. Valence band of Zn_2(TTFTB) along additional high-symmetry k-space directions

To investigate whether the valence band is flat for all directions apart from those associated with the stacking direction of the TTF cores (GA and LM), we calculated the electronic band structure along a path considering all relevant high-symmetry k-space directions (see Figure S4). Indeed we find that only for directions parallel to the stacking direction of TTF the valence band shows a significant dispersion.

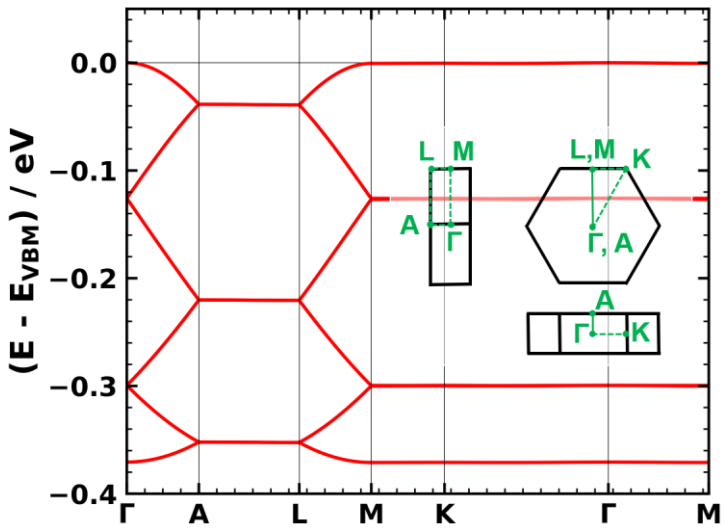

Figure S4. Electronic band structure for Zn_2(TTFTB) for a path covering all relevant high-symmetry directions in the first Brillouin zone. The first Brillouin zone is shown as an inset.

2.4. Geometrical and electronic structure of Zn_2(TTFTB) containing water

To investigate the influence of water molecules coordinated to the Zn atoms in the Zn_2(TTFTB) MOF, we considered the initial structure extracted from the cif-file from reference [3], removed the solvent molecules and calculated the electronic structure of this system. The used geometry and the obtained electronic structure are shown in the left panel of Figure S5. In the top panel, the structure with the water molecules extracted from the cif file is compared to the structure that has been obtained by relaxing the atomic positions of Zn_2(TTFTB) without water (green). One can see that there are only slight differences in the geometric structure of the systems. Considering the electronic band structure of the valence band for this geometry we find a valence band width of 353 meV and a corresponding effective mass of 1.97 m_e. Both compare well to the 371 meV and 2.05 m_e obtained for the optimized Zn_2(TTFTB) structure without water.

The results for the fully relaxed atomic positions calculated including the water molecules are compared to the relaxed geometry of the system without water (right panel in Figure S5 and Figure S6 a). We find that the central TTF core is hardly affected by the presence of water molecules at the Zn coordination sites, while the phenyl rings indeed show structural changes. As outlined in the main manuscript also these phenyl rings contribute to the valence band. Thus, considering the electronic structure of the relaxed MOF with water we find that this system exhibits a larger band width of 411 meV (1.76 m_e) compared to the system without water (see Figure S6 a for band structures). Nevertheless, these changes are quite minor. Therefore, the system without water can serve as a prototypical example for the influence of structural effects on the charge transport properties. Additionally we tested, whether one can use a TTF model system (constructed according to section 3.2 in the main paper) for describing the valence band of the relaxed system with water (dashed black line in Figure S5). Indeed we find that such a TTF stack can serve as a viable model system, only slightly underestimating the resulting valence band width of the actual MOF. For the sake of completeness we also report the species projected DOS of the relaxed Zn_2(TTFTB) MOF with water molecules coordinating to Zn in Figure S6.

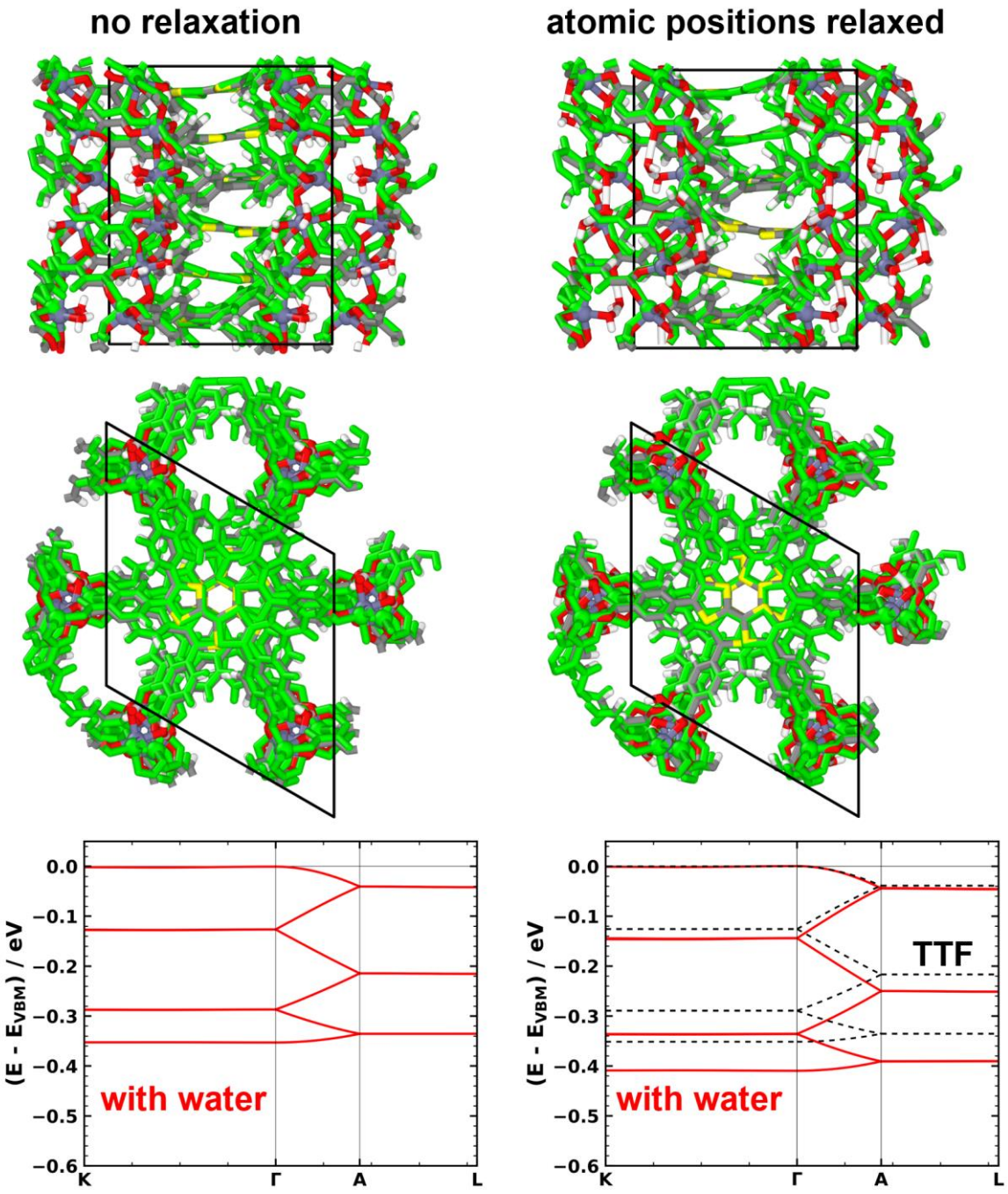

Figure S5. Geometric structure and electronic band structure of Zn_2(TTFTB) with and without water molecules coordinated to the Zn metal atoms. Two systems are considered and compared to the structure obtained by relaxing the atomic positions without water molecules present (green): The left panels show data for a structure with water, as reported in literature cif file (i.e., without a further geometry relaxation). The electronic band structure is shown below the crystallographic structure. The right panel shows the structure with water after performing a geometry relaxation of the atomic positions. In the bottom panel the electronic band structure of that system is shown in red. The dashed black line corresponds to the data for the saturated TTF stack including water molecules. The unit cell is shown by the solid black lines in the geometric structures.

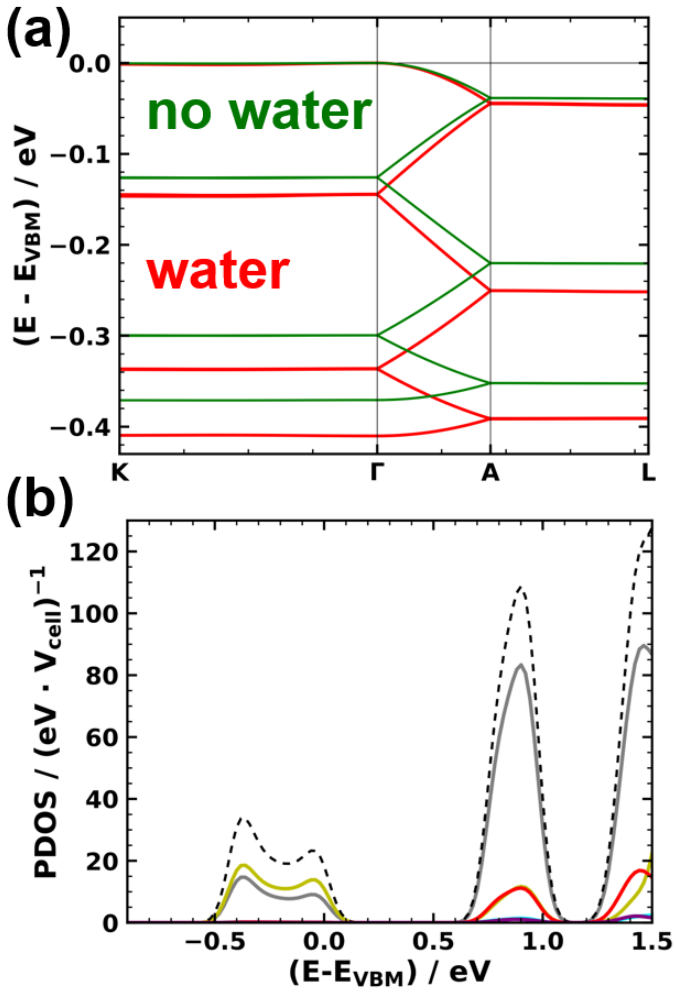

Figure S6. Electronic structure of Zn2(TTFTB) of relaxed Zn_2(TTFTB) with water molecules coordinated to Zn. (a) Electronic band structure of Zn_2(TTFTB) with water (red) compared to Zn_2(TTFTB) without water (green). (b) Species projected density of states of Zn_2(TTFTB) (C—grey, H—cyan, O—red, Se—yellow, Zn—purple, total—dashed).

2.5. Conduction band of Zn_2(TTFTB) and model TTF stacks

Considering the conduction band of Zn_2(TTFTB) (without water; mFigure S7) we find that it has a significantly smaller band width than the valence band. This has already been discussed in the main manuscript. Additionally, we can observe that bands along directions perpendicular to the stacking direction (KΓ and AL) exhibit small dispersions of around 20 meV. This means that unlike for the valence band, for the conduction there is a small coupling between neighboring TTF stacks. This coupling is potentially mediated by Zn and O p-states, as can be rationalized by these atoms'/orbitals' contributions to the conduction band.

Considering that not solely states arising from the central TTF core contribute to the conduction band it is not surprising that a model stack consisting only of TTF molecules cannot reproduce the conduction bands of the actual MOF (see dashed line in Figure S7).

Interestingly, for the system with water (after relaxing the atomic positions), we find that the dispersion along KΓ and AL is significantly reduced (see Figure S8). This indicates a weaker coupling between neighboring TTF stacks for the conduction band in the presence of water.

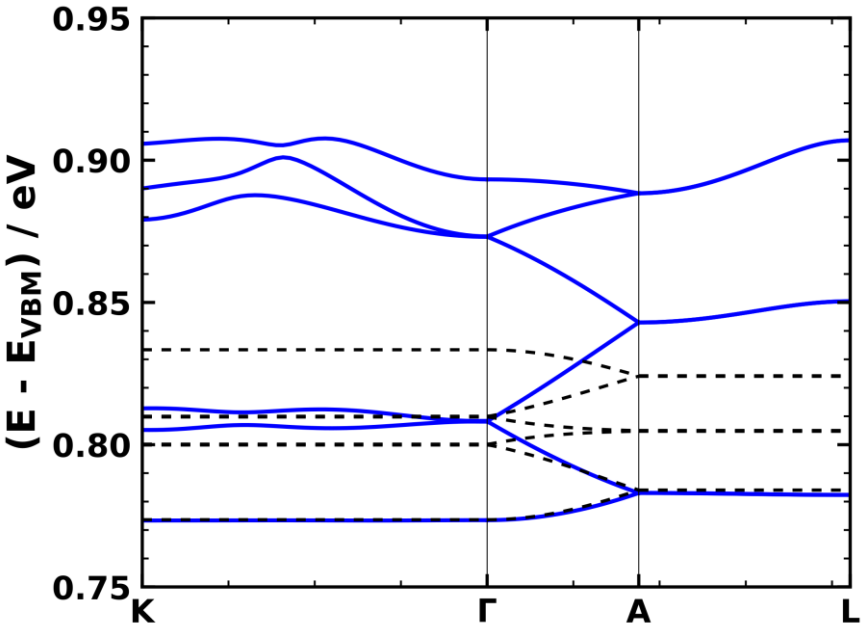

Figure S7. Electronic band structure of the conduction band for Zn_2(TTFTB) in blue and the corresponding TTF model stack as the black dashed line. One can see that bands along reciprocal space directions perpendicular to the TTF stacks show a small dispersion (~20 meV), which means that for the conduction band there is a small coupling between neighboring stacks.

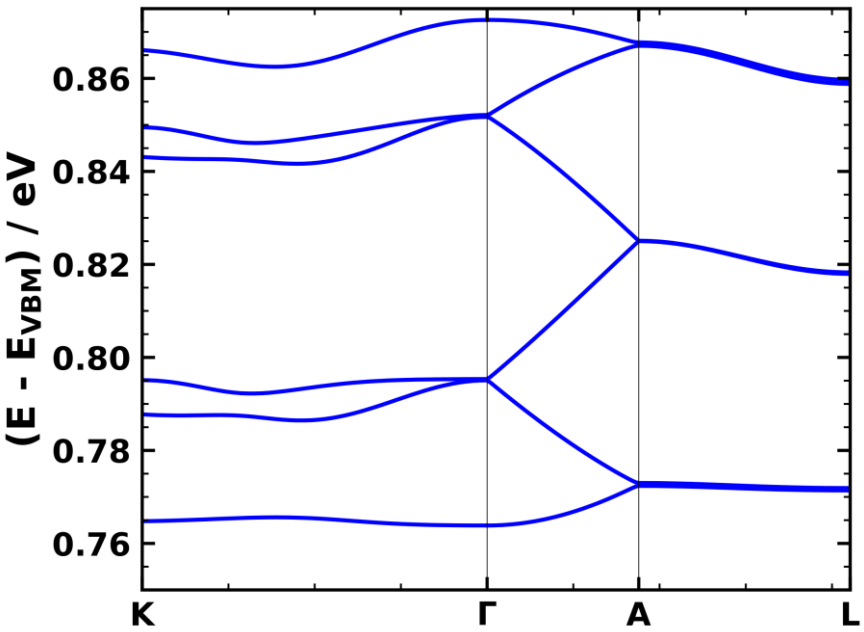

Figure S8. Electronic band structure of the conduction band for Zn_2(TTFTB) with water coordinated to the Zn atoms. One can observe that in comparison to the system without water, the dispersion along directions perependicular to the TTF stacks is reduced significantly.

2.6. Electronic structure of a stack consisting of the central TTF core of the TTFTB linkers plus the phenylene rings

From the projected density of states in the main manuscript one can already conclude that the phenyl rings show a non-negligible contribution to the valence band of Zn_2(TTFTB). To show this in a more explicit way we, extracted a stack of TTFTB molecules from the MOF and replaced the carboxyl groups with H (see structure in Figure S9). After relaxing the atomic positions of these H atoms we calculated the electronic band structure of this model system. Comparing the valence bands of the model system and of the full Zn_2(TTFTB) MOF in Figure S9 reveals an excellent agreement between the band structures of the two systems.

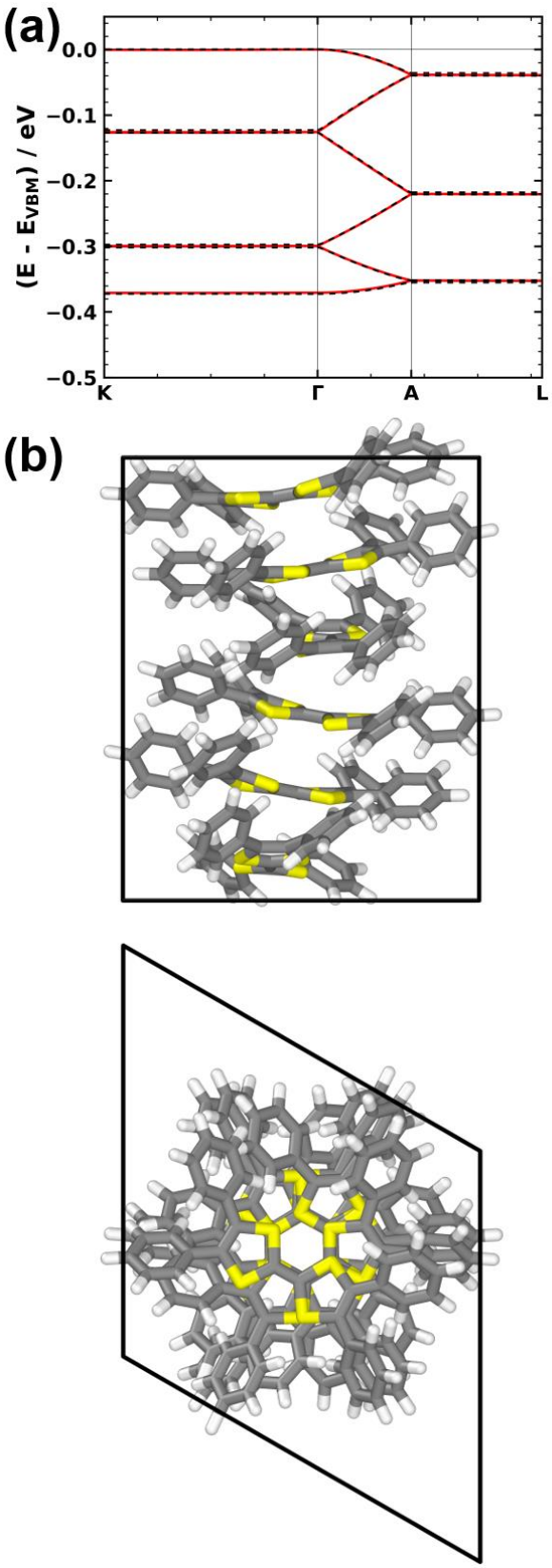

Figure S9. (a) Electronic band structure of Zn_2(TTFTB) in red and of the isolated and saturated TTFTB stack (black). (b) In the lower panel the unit cell of the TTFTB stack is shown.

2.7. Electronic band structures of the considered TTF stacks

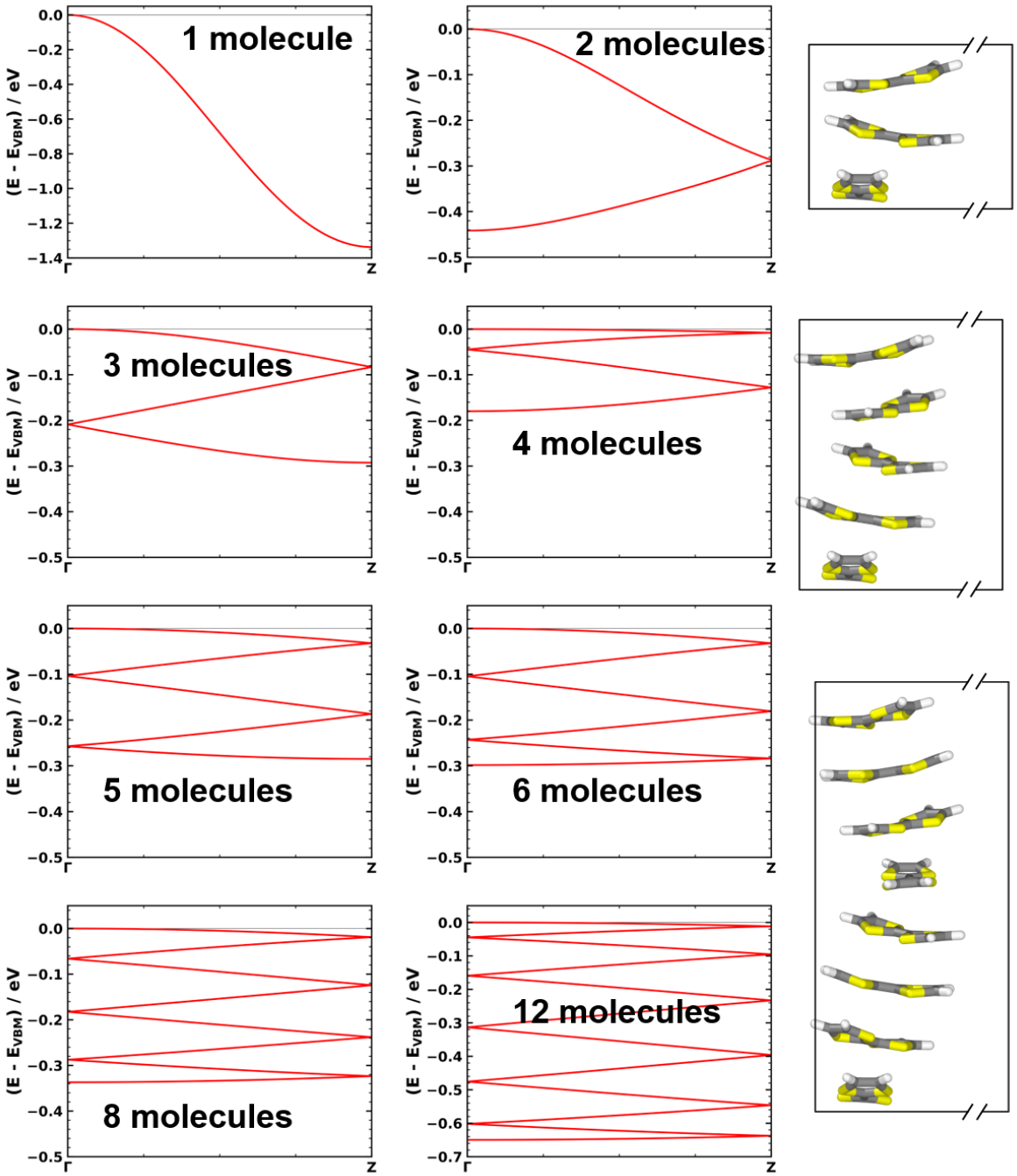

Figure S10. Electronic band structures of the TTF model stacks with 1, 2, 3, 4, 5, 6, 8, 12 repeat units. In the right panel unit cells for systems with 3, 5, and 8 repeat units are shown as examples.

2.8. Electronic band structures deviating from the simple tight-binding picture

For certain systems we found that the electronic band structure of the valence band deviates from the shape one would expect for a simple 1D tight-binding model (see section 1.2 of SM). For relaxed with 4, boat and planar molecular geometries with 5 repeat units we find that the band maximum is slightly off Γ, but with an energy difference significantly smaller than 25 meV (k_BT at room temperature). In these systems the n-fold backfolded valence band splits into two electronic bands. For determining the band width we, thus, consider the entire energy range covered by these

bands. For planar TTF with 3 repeat units we see that the band has picked up a contribution with a higher frequency, meaning that electronic couplings beyond the nearest neighbor become relevant.[2]

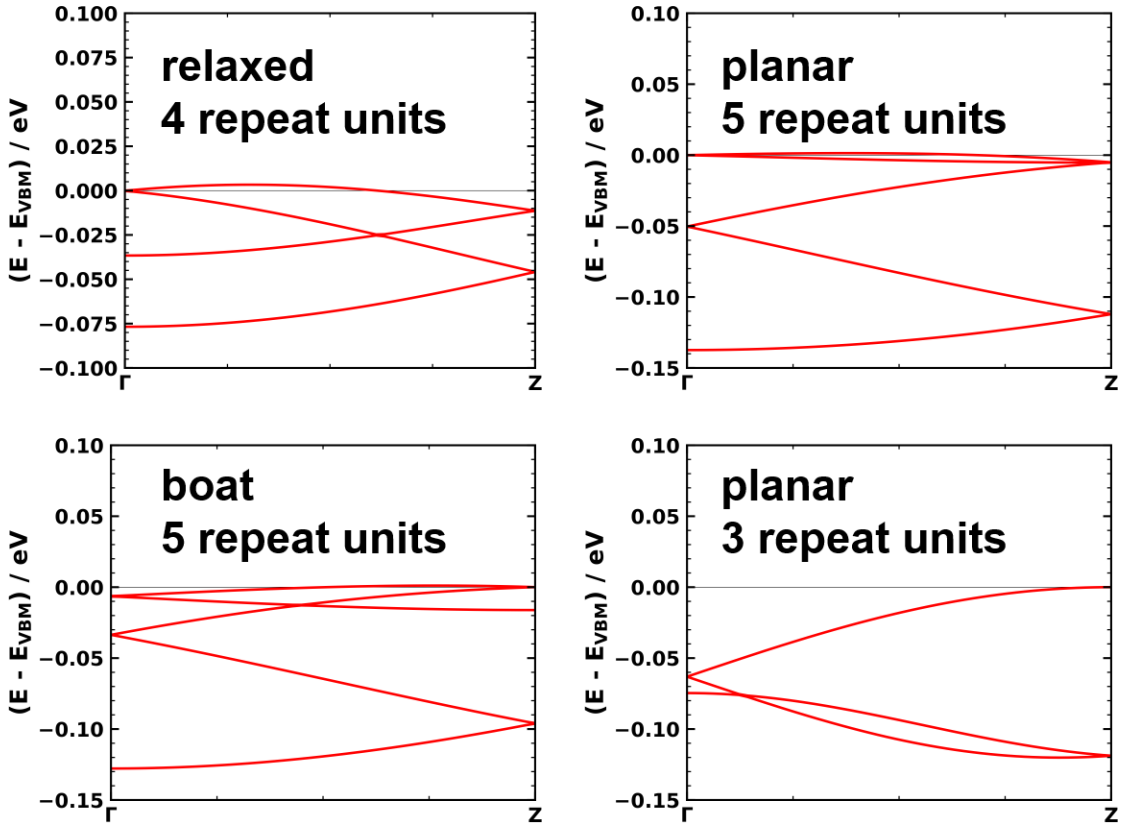

Figure S11. Electronic band structure of the stacks marked by black frames in Figure 3 of the main manuscript. For these systems we find that the electronic band structures deviate from the shape one would expect from a simple 1D tight-binding model with a single TTF molecule as "electronic" repeat unit.

2.9. Total energies of the optimized TTF stacks

Considering the total energies per TTF repeat unit of the relaxed TTF model stacks (see Figure S12a) we find that except for the cofacial system (1 repeat unit) and the the 2 repeat unit system all stacks exhibit energies within less than 35 meV. Considering the planar TTF model system shown in Figure S12b one can find a correlation between the total energy and the transfer integral (band width), especially for large rotation angles. Such a behavior is, in fact, not unexpected considering the role of exchange interactions as described in [4]. One can, however, also observe that the vdW interactions between the TTF molecules play an important role in determining the energetic stability of certain arrangements (TTF stacks). For the fully optimized structures, such a correlation is less pronounced, which is a consequence of different distortions of the molecules at different rotation angles significantly changing the distances between atoms in neighboring molecules.

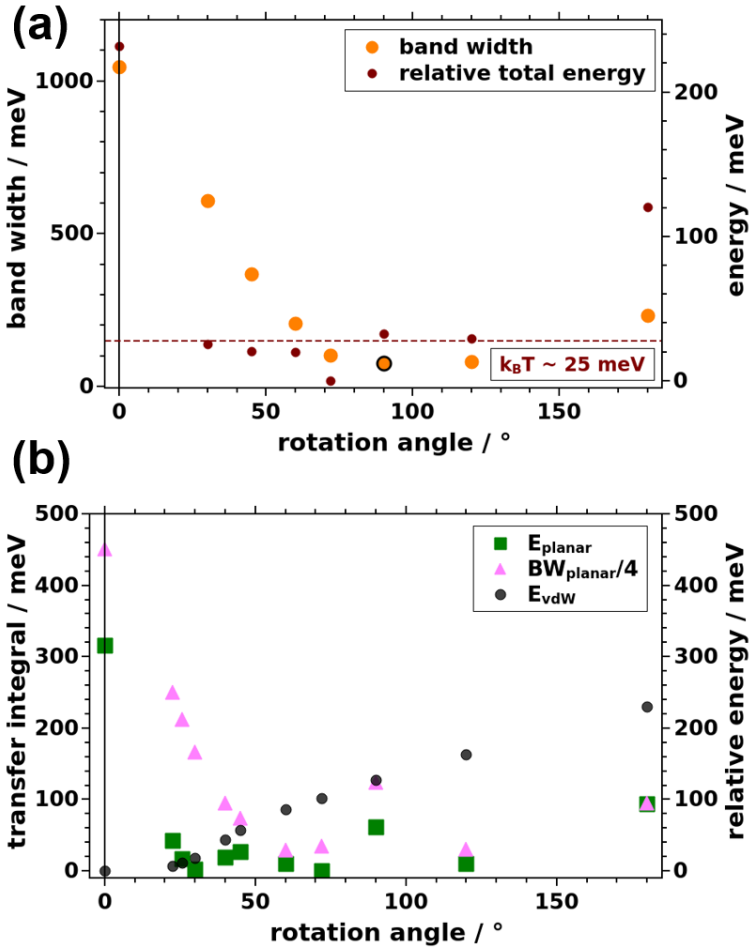

Figure S12. Evolution of the band width (transfer integral) and the total energy per TTF molecule for theTTF model stacks. (a) Band width and relative total energy for the relaxed TTF model stack. (b) Transfer integral as (1/4)* valence band width, relative total energy, and vdW energy for the planar TTF model stack. For the planar model stack additional data points for 9, 14, and 16 repeat units were added. This was done to clarify the evolution of the relative total energy for angles between 20° and 50°. The energies are aligned to the global minimum, this means that positive energies result in less stable arrangements.

2.10. Transfer integral for a planar TTF dimer with a centered rotation axis

To investigate the influence of the position of the rotation axis on the evolution of the transfer integrals we considered a planar TTF dimer with the screw axis connecting the centers of the planar molecules. Varying the relative rotation angles of the two monomers with respect to this rotation axis results in the evolution shown in Figure S13a. The data points for a rotation angle of 0° are the same as for the planar geometry in Figure 3b of the main manuscript and one again observes a decrease of the coupling with increasing rotation angle. The absolute magnitude of the coupling is minimized for an intermediate rotation (~50°). In contrast to the situation for the off-center screw axis in Figure 3b, for a centered screw axis one never observes a change in the signs of the band widths and transfer integrals. This can be traced back to the fact that the orbitals never change their order, consequently also the transfer integral always exhibits the same sign. The respective orbitals for the extrema of the transfer integral are shown in Figure S13b.

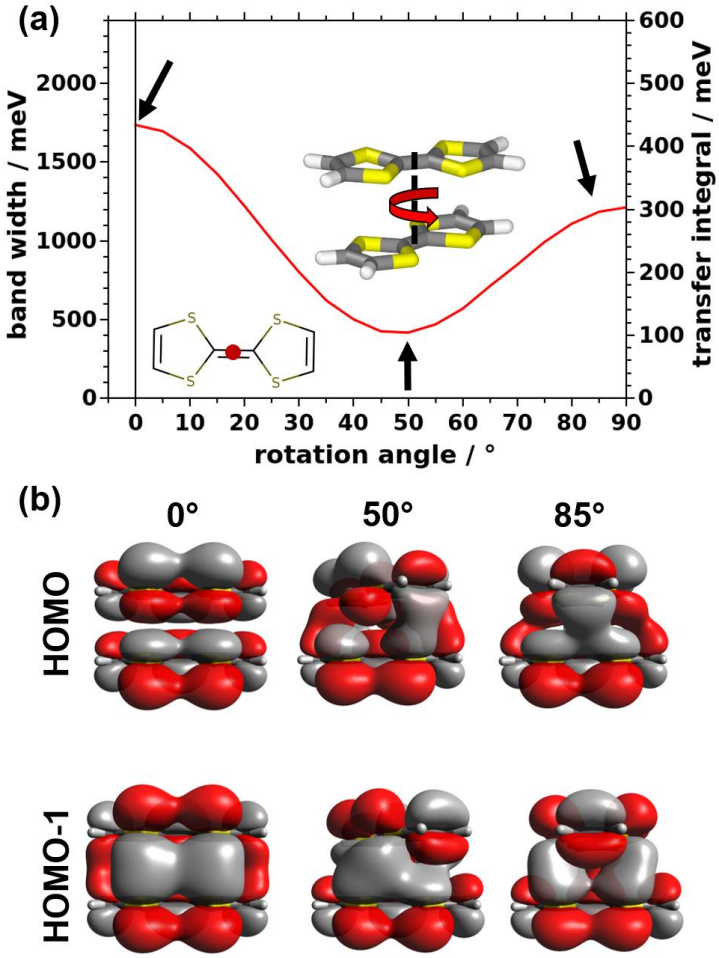

Figure S13. Electronic structure of Planar planar TTF dimers with the rotation axis placed in the center of the TTF molecules. Panel (a) shows the evolution of the band-width and the transfer integral as a function of rotation angle. Panel (b) shows the molecular orbitals (HOMO and HOMO-1) for rotation angles corresponding to local the extrema of the band-width (marked with black arrows).

3. Data for additional systems considered in the current manuscript: Cd_2(TTFTB), Zn_2(TSFTB)

3.1. Electronic structure of Cd_2(TTFTB)

As an additional MOF system considered here is Cd_2(TTFTB) (structure from ref [3]), which is isostructural to Zn_2(TTFTB). For this system we relaxed the atomic positions within the reported unit cell[3] and then calculated the electronic band structure for this relaxed geometry. The resulting species projected density of states and the valence band structure are shown in Figure S13.

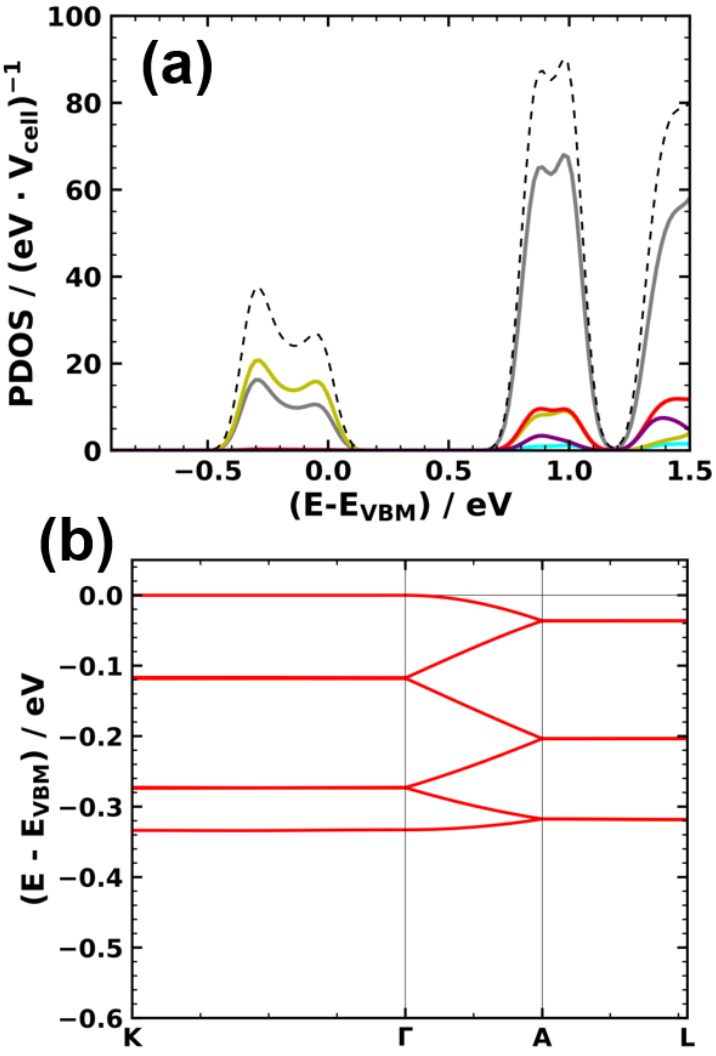

Figure S14. Electronic structure of the Cd_2(TTFTB) MOF. (a) species projected density of states (C—grey, H—cyan, O—red, Se—yellow, Cd—purple) and (b) valence band aligned to its maximum.

3.2. Electronic structure of Zn_2(TSFTB)

Also the electronic structure (PDOS and electronic band structure) of a MOF with Tetraselenafulvalene ($C_6H_4Se_4$) replacing TTF has been calculated. The structure of this system was obtained by taking the structure of Zn_2(TTFTB) and replacing S with Se, i.e. replacing TTF with TSF. As no experimental cell for this system exists and as we expect the larger p-orbitals of Se to cause an increase of the stacking distance, we relaxed the atomic positions of the starting geometry as well as the cell vectors. For comparison we also calculated the electronic for the system when relaxing the atomic positions while keeping the unit cell fixed. The obtained species projected density of states and the structure of the valence band for the system with the relaxed unit cell are shown in Figure S15. The data for the system with relaxed atomic positions but within the unit cell of Zn_2(TTFTB) are

shown in Figure S16. For the fully relaxed system we obtain 678 meV for the valence band width and an effective mass of 0.98 m_e. For the system in the Zn_2(TTFTB) unit cell we get 641 meV and 1.06 m_e, so there is hardly any difference between the relevant quantities of these systems.

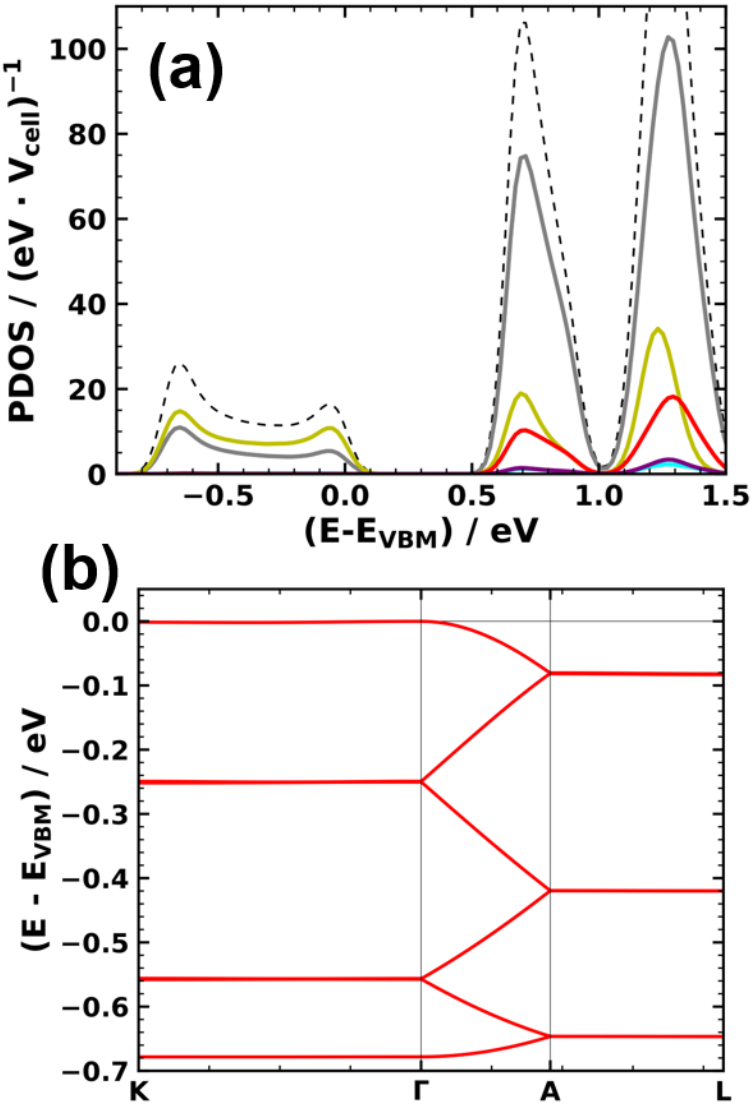

Figure S15. Electronic structure of the Zn_2(TSFTB) MOF for the relaxed unit cell. (a) Projected density of states (C—grey, H—cyan, O—red, Se—yellow, Zn—purple, total—black dashed) and (b) electronic band structure of the valence band aligned to its maximum.

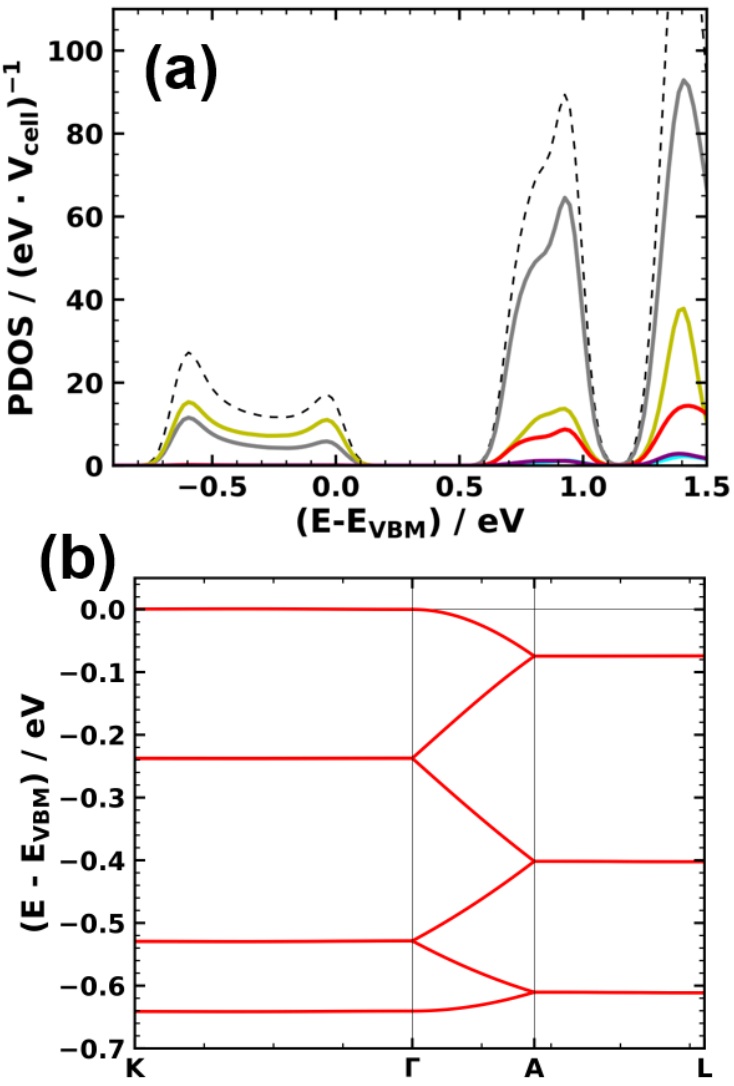

Figure S16. Electronic structure of Zn_2(TSFTB) MOF in the unit cell of Zn_2(TTFTB). (a) Projected density of states (C—grey, H—cyan, O—red, Se—yellow, Zn—purple, total—black dashed) and (b) electronic band structure of the valence band aligned to its maximum.

4. Additional data for defects within the MOF and the model systems

4.1. Electronic structure of a TTF model systems with a displaced rotation axis

To show the influence of other potential defects we considered also shifts of the center of rotation for one of the TTF molecules. The resulting band structures are shown in Figure S17. Again one can see that upon introducing of such defects a gaps open at the BZ boundary and at the G point. These gaps and the resulting changes of the band dispersion y lead to an increase of the effective mass (Table S2), i.e a decrease of the transfer integral – similar to the data presented in the main manuscript.

Table 2. Effective mass depending on the offset of the rotation center of one of the TTF molecules in the model stack.

Shifts (Δx, Δy)/Å	Effective mass m*/me
(0.0, 0.0)	2.48
(0.0, 0.1)	2.55
(-0.1, 0.1)	2.57
(-0.25, 0.25)	3.28
(-0.5, 0.5)	4.70
(-1.25, 1.40)	12.62

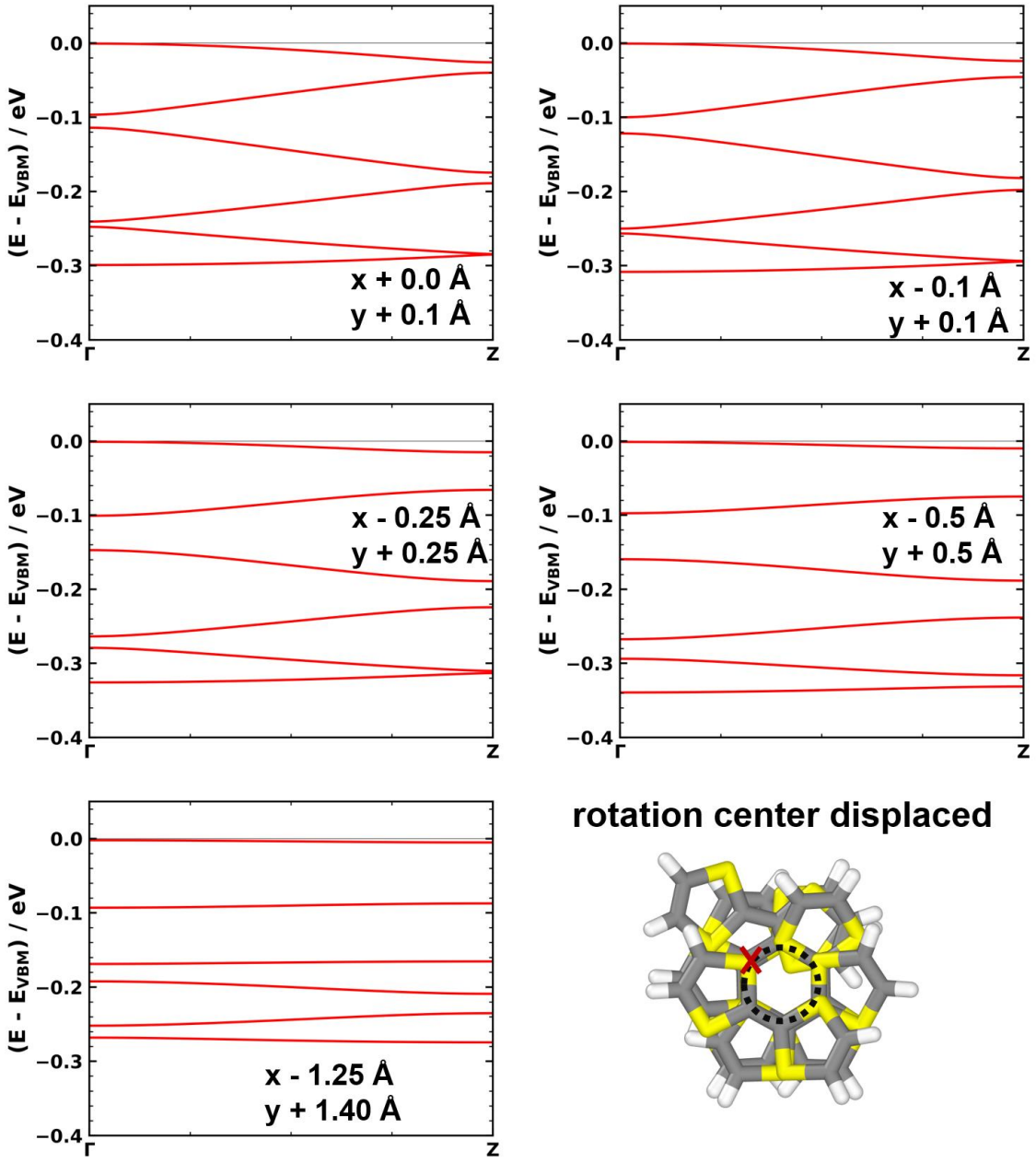

Figure S17. Electronic band structures for TTF model stacks where the rotation axis for one of the molecules is displaced from the equilibrium position.

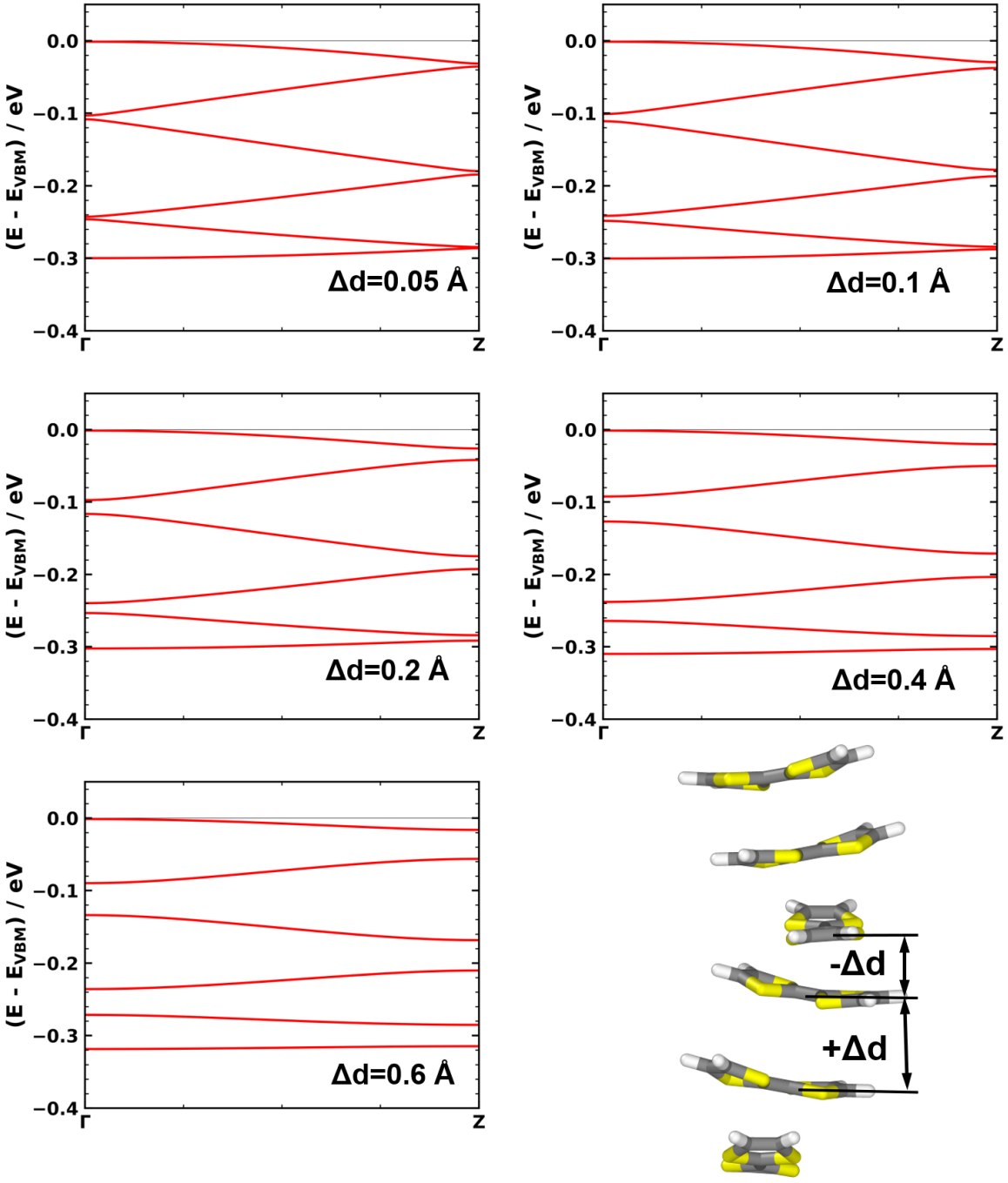

Figure S18. Electronic band structure of the valence band for the 6 repeat units TTF model stack with dimerization defects Δd.

4.3. Electronic band structures for the "displaced molecule" defect data

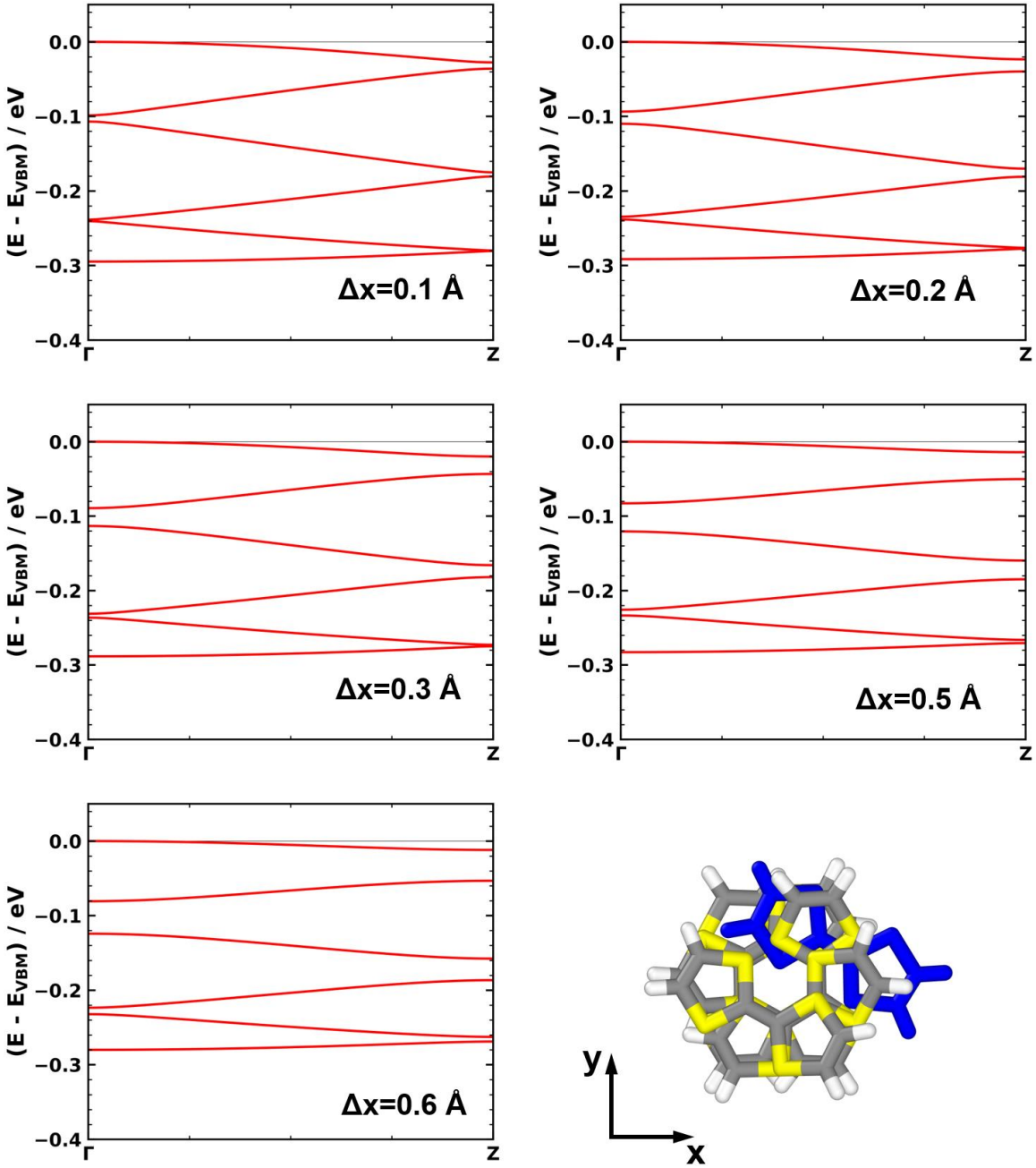

Figure S19. Electronic band structure of the valence band for the 6 repeat units TTF model stack with "displaced molecule" defects Δx.

References

1. Blum, V.; Gehrke, R.; Hanke, F.; Havu, P.; Havu, V.; Ren, X.; Reuter, K.; Scheffler, M. Ab initio molecular simulations with numeric atom-centered orbitals. *Comput. Phys. Commun.* **2009**, *180*, 2175–2196.
2. Winkler, C.; Mayer, F.; Zojer, E. Analyzing the Electronic Coupling in Molecular Crystals—The Instructive Case of α-Quinacridone. *Adv. Theory Simulations* **2019**, *2*, 1800204, doi:10.1002/adts.201800204.
3. Park, S.S.; Hontz, E.R.; Sun, L.; Hendon, C.H.; Walsh, A.; Van Voorhis, T.; Dincə, M. Cation-dependent intrinsic electrical conductivity in isostructural tetrathiafulvalene-based microporous metal-organic frameworks. *J. Am. Chem. Soc.* **2015**, *137*, 1774–1777, doi:10.1021/ja512437u.

4. Winkler, C.; Jeindl, A.; Mayer, F.; Hofmann, O.T.; Tonner, R.; Zojer, E. Understanding the Correlation between Electronic Coupling and Energetic Stability of Molecular Crystal Polymorphs: The Instructive Case of Quinacridone. *Chem. Mater.* **2019**, *31*, 7054–7069, doi:10.1021/acs.chemmater.9b01807.

5. Role of electrostatic and dispersion interactions for the stacking motif of covalent organic frameworks

5.1. Author contributions

E. Zojer and C. Winkler conceived the idea to investigate the stacking arrangement of COFs and which interactions determine certain prefered arrangements. C. Winkler performed all calculations together with a primary analysis of the data. C. Winkler also wrote the first version of the manuscript and prepared all figures. The project was supervised by E. Zojer.

The following paper has been prepared for submission and is inserted here as original publication together with the Supporting Information. "Winkler C., and Zojer E., Determining the role of electrostatic and dispersion interactions for the stacking motif of covalent organic frameworks".

5.2. Main paper

Determining the role of electrostatic and dispersion interactions for the stacking motif of covalent organic frameworks

Christian Winkler[1] *and Egbert Zojer*[1,]*

[1] Institute of Solid State Physics, NAWI Graz, Graz University of Technology, Petersgasse 16, 8010 Graz, Austria

Covalent organic frameworks (COFs) are porous crystalline materials that have attracted significant attention for various applications owing to their tunable structures. Particular attention has been paid to two-dimensional COFs where the organic building units are linked by covalent bonds within a plane. The bulk systems of these COFs then consist of stacks of the two-dimensional layers which are held together by attractive van der Waals interactions. Many properties of such layered systems are then dominated by the actual interlayer arrangement. In the present contribution, for the representative test system of COF-1, we investigate the different types of interactions between the layers, comprising van der Waals interactions, Coulomb interactions, and Pauli repulsion plus orbital rehybridization, as a function of interlayer arrangement. It is found that for constant interlayer stacking distance Pauli repulsion plus orbital rehybridization enforce shifted layer arrangements to be energetically favorable. On the contrary, for systems with optimized stacking distances, the individual interactions show quite different behavior. Interestingly, Pauli repulsion favors a cofacial arrangement, while Coulomb and van der Waals interactions favor shifted structures. The latter two dominate, thus, enforce shifted layer arrangements to be energetically favorable. Similarly, for several additional COFs with differently sized π-systems and topologies it is observed that Coulomb and van der Waals interactions push the structures towards shifted layer arrangements.

1. INTRODUCTION

Covalent organic frameworks (COFs) are porous crystalline materials consisting of organic building blocks linked together through covalent bonds.[1–7] Because of their tunable structures, COFs have demonstrated great potential in various applications like gas storage,[8–10] gas separation,[11–14] catalysis,[15–17] energy storage,[18–20] and optoelectronics.[21–27] Among the different topologies of COFs, two-dimensional (2D) systems have received particular attention. Special about such 2D systems is that the individual organic building units are linked via covalent bonds within a plane, forming highly regular 2D layers. These layers then stack on top of each other and the resulting stacks are held together by comparably weak van der Waals interactions. Important for the properties (electronic, optical, and catalytic) of the resulting three-dimensional (3D) stacks is the packing motif of consecutive 2D layers.[7,26,28–32] This packing motif defines the shape of the pores and the overlap of the π-systems between neighboring sheets. The latter is essential for the electronic structure of the system, as depending on that overlap (in particular the symmetry and nodal structure of the involved orbitals/wavefunctions) systems can be insulating, semiconducting, or even metallic.[33,34] Depending on the desired functionality of the COF, both, pore shape and electronic structure can be equally important.

Apart from a few exceptions almost all reported 2D COFs exhibit either eclipsed (cofacial) or serrated (shifted) AA stacking.[28,30,35,36] More specifically, Zhou et al.[35] found, based on the examples of COF-1 and COF-5 (structures first reported in ref 2), that the total energy is lower for shifted layer arrangements with displacements of around 1 Å. They hypothesized that the alignment of neighboring π-orbitals plays an essential role for these shifts being energetically favorable. Furthermore, the similarity in the stacking motif of the aromatic rings present in the observed COFs compared to graphite has been mentioned, but the individual interactions enforcing this stacking motif have not been investigated.[35] Lukose et al.[36] also performed a computational study on the alignment of layered COFs, again considering COF-1 and COF-5. Similarly, shifts of consecutive layers (~1.4 Å) were identified as the energetically favorable layer arrangements. In this work, as well as in Ref. 37, the authors argued that repulsive Coulomb interactions between B and O linking units of neighboring layers cause the cofacial arrangement (eclipsed AA stacking) to be energetically unfavorable and to enforce the shifted (serrated) layer arrangement. Certainly, all interactions between the π-orbitals of consecutive layers, electrostatic interactions, and van der Waals interactions will play a role for the energetic stability of the shifted interlayer arrangement. A quantitative assessment of the different types of interactions as a function of the alignment of consecutive layers is, however,

still lacking, which prevents a fundamental understanding of the factors determining the packing motif in 2D COFs. The situation is further complicated by the fact that slightly shifted AA stacking arrangements are hard to determine in experiments due to the large peak broadening in the typically investigated powder samples.[26,35] This calls for an in-depth investigation of the driving forces determining interlayer stacking arrangements of 2D COFs.

A detailed understanding of such driving forces would allow to develop strategies for tuning the COF structures and, consequently, also their electrical, optical, and catalytic properties.[28,29,31] To achieve that, in the present study we employ dispersion corrected density functional theory (DFT) calculations decomposing the interlayer interactions in the prototypical model system COF-1 (see Figure 1 and ref 2 or the structure of this COF) into physically well-defined contributions arising from dispersion forces, electrostatic interactions, and exchange repulsion with orbital rehybridization. To demonstrate the general applicability of the findings we also study COF-5 as well as COFs consisting of porphyrin (Por-COF)[38] and hexabenzocoronene molecules (HBC-COF).[39] The structures of these COFs can be found in Section 3.4 and the corresponding references 38 and 39.

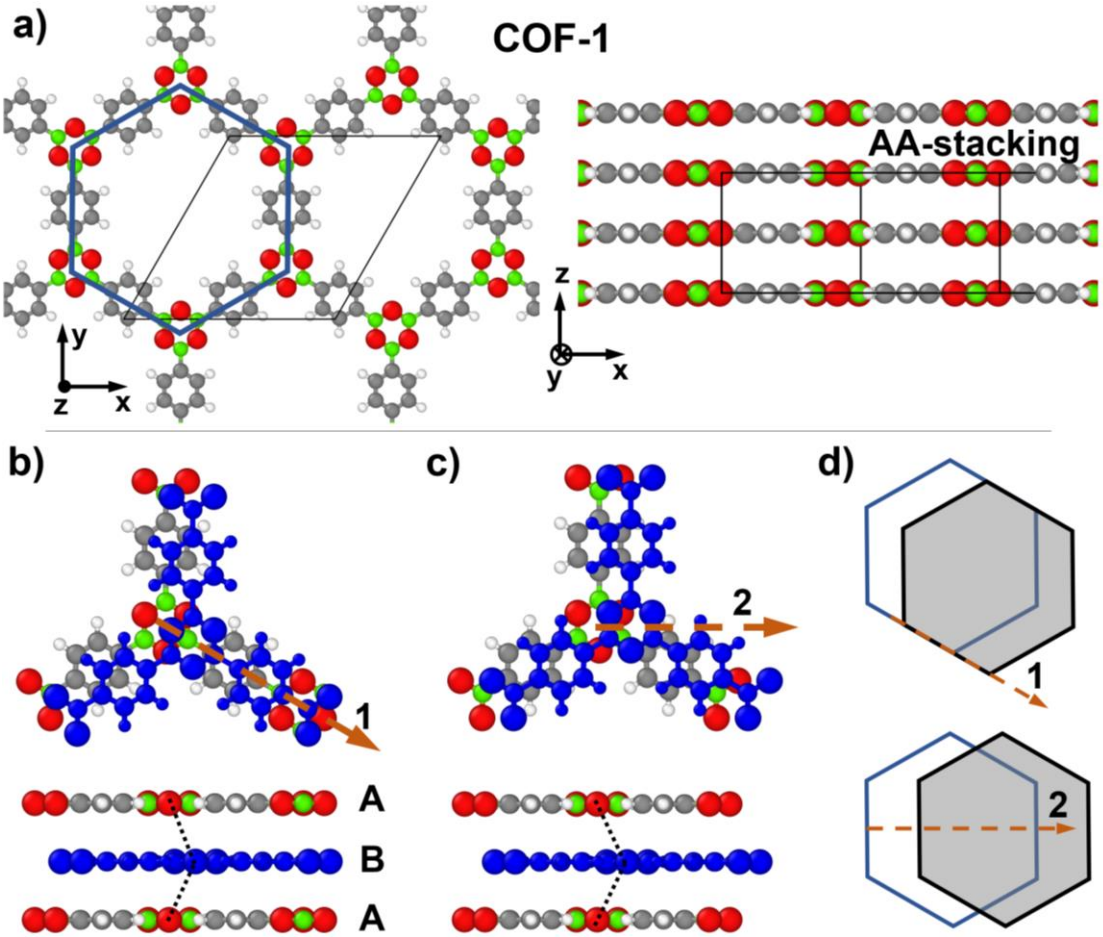

Figure 1. *Structure of COF-1 plus the considered shift directions. Panel (a) shows the top and front view of the structure of COF-1 for cofacial AA-stacking. The unit cell is shown by the*

*black solid lines. In panel (b) a shifted (serrated) arrangement with a displacement of 1.75 Å along a direction parallel to one of the edges of the pore (direction **1**) is shown. How the layers arrange for displacements along a direction perpendicular to the pore edges (direction **2**) is shown in panel (c). The shift directions are shown as orange arrows and the shifted layers are marked in blue. In panel (d) symbolic representations of the shift directions are shown. These symbols will be used in the following to label the data. Color code of the atoms: C … grey, H … white, B … green, O … red*

2. METHODS

For the investigation of the layered COFs considered in this study we employed dispersion corrected density functional theory, DFT, as implemented in the FHI-aims code.[40,41] During these calculations the PBE functional[42,43] was used and van der Waals interactions were considered by using the Tkatchenko-Scheffler[44] scheme. The electronic band structure of COF-1 has also been calculated using the HSE06[45,46] hybrid functional. The corresponding data are shown in the Supporting Information (SI). We used the conventional "tight" basis functions with details for each atomic species described in the Supporting Information. For all bulk systems of the COFs a grid consisting of 3x3x6 k-points was employed for sampling reciprocal space, unless stated otherwise. The total energy for this grid appeared to be well converged to within less than 1 meV.

The calculations for COF-1 shifted along directions **1** and **2** were performed by using the in-plane lattice constants reported in literature (a=b=15.420 Å).[2] Employing the literature unit cell, the bulk of COF-1 was constructed by relaxing the atomic positions of a monolayer in the respective unit cell until the largest remaining force component on any of the atoms was smaller than 0.01 eV/Å and then stacking these layers along the direction perpendicular to the plane to form the bulk. The interlayer distance between these layers is set to the literature value of 3.328 Å.[2] The unit cell of COF-1 is constructed such that it contains two layers in stacking direction (layers A and B), which enables displacing these layers along directions **1** and **2**, as shown in Figure 1.

As for some of the additional COFs considered in this work, no experimentally determined lattice parameters exist, we chose to perform an optimization of the unit cell parameters for these systems, as described in the following. The optimal in plane lattice parameters for the individual COFs were evaluated by considering a COF monolayer (4x4x1 k-point grid, total energy converged within less than 1 meV) and gradually shrinking the unit cell size while keeping the symmetry. For each unit cell size the atomic positions were relaxed and the total energy was calculated. These data were fitted with a Birch-Murnaghan equation of state[47] to

obtain the equilibrium in-plane lattice parameters. These unit cell parameters and the atomic positions of the relaxed monolayer are then used for constructing the bulk structure of each COF. For the resulting bulk systems we performed additional geometry relaxations. During these relaxations all atomic positions and the unit cell vector in stacking direction were relaxed until the largest remaining force component on any of the atoms was smaller than 0.01 eV/Å. In the Supporting Information we show that for COF-1 optimizing the in-plane lattice parameters results in smaller lattice constants of a=b=15.126 Å but does not change the trends and the relative ratios of the effects studied.

When the layers of COF-1 and COF-5 are shifted along directions **1** and **2** the energies have been calculated for constant interlayer stacking distances as well as for optimized stacking distances. The employed strategy for finding the optimal stacking distances for each shifted layer arrangement of COF-1 and COF-5 is described below. The initial arrangements were achieved by displacing consecutive layers along the desired shift direction (either **1** or **2**) and keeping this shifted arrangement constant. Subsequently, the stacking distance was varied within a range of ±0.75 Å in steps of 0.25 Å and single point calculations were performed to get the total energy of the system for each interlayer spacing. Based on these data we identified the minimum and calculated additional data points around this minimum with ±0.125 Å variation. All data points are then fitted with a Birch-Murnaghan equation of state and the minimum of that fit determines the optimal stacking distance for each layer arrangement.

To get the interaction energy and its individual contributions we started by decomposing the system into fragments. These fragments comprise the two layers in the unit cell (layers A and B), which are shifted relative to each other (see Figure 1). To get these sub-systems, the other layer is removed from the combined system while the unit cell is not altered. Then the total energies of the COF containing layers of types A and B and of the sub-system comprising either layers of type A or of type B were calculated for the respective unit cell of the combined system. The interaction energy is then given by

$$\Delta E_{int} = E_{total}^{AB} - (E_{total}^{A} + E_{total}^{B}) \qquad (1).$$

This interaction energy is then decomposed into the “electronic” interaction energy resulting from the PBE-based DFT calculations and the contribution due to the a posteriori correction for (long range) van der Waals interactions

$$\Delta E_{int} = \Delta E_{int,elec} + \Delta E_{vdW} \qquad (2)$$

Where the individual contributions can be readily obtained from the FHI-Aims output for the full system and the two sub-systems as

$$\Delta E_{int,elec} = E_{PBE}^{AB} - (E_{PBE}^{A} + E_{PBE}^{B}) \quad (3a)$$

And

$$\Delta E_{vdW} = E_{vdW}^{AB} - (E_{vdW}^{A} + E_{vdW}^{B}) \quad (3b)$$

A more difficult step is then to decompose the electronic interaction energy, $\Delta E_{int,elec}$, into the electrostatic contribution due to the Coulombic interactions between the nuclei and electron clouds of the subsystems and contributions due to exchange interactions and orbital rehybridizations. Various decomposition schemes that serve this purpose are available for finite-size systems, but for extended solids described by periodic boundary conditions they are, unfortunately, rare. Therefore, a custom decomposition scheme was developed and implemented. This scheme is largely based on the periodic energy decomposition analysis (pEDA) scheme developed by Raupach and Tonner.[48,49] Within this scheme the authors basically extended the energy decomposition analysis (EDA) method developed by Ziegler/Rauk[50,51] and Morokuma[52] to periodic boundary conditions. The key idea in this method is to partition the interaction energy $\Delta E_{int,elec}$ into well defined terms as shown in equation 4.

$$\Delta E_{int,elec} = \Delta E_{elstat} + (\Delta E_{Pauli} + \Delta E_{orb}) \quad (4)$$

As a first step one can evaluate ΔE_{elstat} by considering the charge densities of the individual fragments A and B and use them to construct a combined system {A,B}. This combined system contains the charge densities of the non-interacting fragments A and B at the positions these fragments exhibit in the combined system. Consequently, the sum of the non-distorted charge densities n_A and n_B is used to describe the combined system. The energy of system {A,B} can then be calculated by performing a single shot DFT calculation without a self-consistency cycle. This calculation yields the electrostatic energy $E_{elstat}^{\{A,B\}}$ of the system as constructed from the fragments. The difference of this energy and the electrostatic energy of the individual fragments then yields the quasiclassical electrostatic interaction between the layers, ΔE_{elstat}, as:

$$\Delta E_{elstat} = E_{elstat}^{\{A,B\}} - E_{elstat}^{A} - E_{elstat}^{B}. \quad (5)$$

Knowing ΔE_{elstat} it is then possible to assess to what extent electrostatic repulsion between consecutive layers is actually responsible for the common appearance of shifted (serrated) structures of 2D COFs. Finally, the wavefunction overlap between the interacting systems triggers orbital rehybridization (which is always attractive) and Pauli repulsion (which is

strongly repulsive). The corresponding contribution to the interaction energy, $\Delta E_{orb,Pauli}$ can be calculated from the overall energy decomposition as:

$$\Delta E_{int} = \Delta E_{elstat} + \Delta E_{orb,Pauli} + \Delta E_{vdW}$$

3. RESULTS AND DISCUSSION

For such layered materials consisting of 2D extended structures, the relative arrangement of the layers can be described by two main factors: (i) the interlayer stacking distance and (ii) the direction and magnitude of shifts of consecutive layers parallel to the plane of these layers. Both factors play a significant role in determining the actual properties of a COF. An advantage of computer simulations is that they allow varying both factors independently. In particular, one can first address the question, how shifts between consecutive layers impact the energetic stability and the properties of 2D COFs for a fixed interlayer distance. In a second step one can then address the question to what extent the situation is altered when the interlayer distance is optimized for each shift. This will be done in the following, where the focus will be on analyzing the impact of the stacking geometry on the interaction energy split into contributions from van der Waals attraction, Coulomb interactions and the impact of orbital rehybridization and Pauli repulsion. As far as the COF properties are concerned, we will restrict the analysis to the electronic structure of the COF manifested in its electronic band structure.

3.1 Constant Interlayer Stacking Distance

In a first step, consecutive layers of COF-1 are shifted relative to each other along the direction parallel to the pore edge (direction **1** in Figure 1), while keeping the interlayer stacking distance constant at the literature value. Figure 2a shows the resulting evolution of the interaction energy, ΔE_{int}, plotted relative to the energy of the cofacial aligned layers. In passing we note that the evolution of ΔE_{int} follows that of the total energy, which is, in fact, apparent from Equ. (1), considering that the energies of the individual segments A and B are independent of the shift. Notably, the value of ΔE_{int} is highest (least negative) for the cofacial arrangement, which indicates that amongst the structures considered here, this is the least stable one. At a displacement of around 1.75 Å the interaction energy displays a pronounced minimum and rises again for larger displacements. This behavior is consistent with the observations reported in literature,[35,36] although the minimum occurs at slightly larger displacements in our investigation. To understand the origin of that trend, the interaction energy is next decomposed into contributions from van der Waals interactions, ΔE_{vdW}, electrostatic interactions, ΔE_{elstat},

and interactions due to Pauli repulsion and orbital rehybridization, $\Delta E_{orb,Pauli}$. ΔE_{vdW} is most attractive for the cofacial arrangement, and then increases (i.e., becomes less negative) upon displacing the layers. This behavior is not unexpected, as by displacing the layers along direction **1**, parts of these layers are moved over pore space, increasing the average interatomic distances causing a drop in vdW attraction. This effect becomes particularly pronounced for displacements above ~1.5 Å.

Interestingly, a similar trend is observed for the electrostatic energy shown by the blue open triangles in Figure 1a. Also for ΔE_{elstat} one observes negative terms (i.e., attraction) for all considered geometries with the cofacial arrangement and small displacements being most stable, in contrast to the speculations in refs 36,37 that electrostatic interactions would be responsible for the shifted geometries of 2D layered COFs.

In fact, for displacements up to around 2 Å, ΔE_{elstat} remains essentially constant, while these electrostatic interactions become less attractive for larger displacements. The overall attractive nature of electrostatic interactions is a consequence of so-called charge penetration effects, which are commonly observed for interacting organic molecules [53–55] and will be discussed in more detail in a separate section below. In contrast to the van der Waals and electrostatic energies, the energy contribution due to Pauli repulsion and orbital rehybridization is always repulsive with a maximum for the cofacial arrangement, significantly destabilizing that structure. In fact, $\Delta E_{orb,Pauli}$ is the factor that is responsible for the energy minimum corresponding to a shifted rather than the cofacial arrangement of successive layers. Another fundamental difference between $\Delta E_{orb,Pauli}$ and the other energy contributions is that $\Delta E_{orb,Pauli}$ changes significantly already for small displacements and then levels off for larger displacements. This is the primary reason, why the sum of ΔE_{vdW}, ΔE_{elstat}, and $\Delta E_{orb,Pauli}$, first drops with the displacement, then forms a minimum at 1.75 Å, and finally rises for larger displacements.

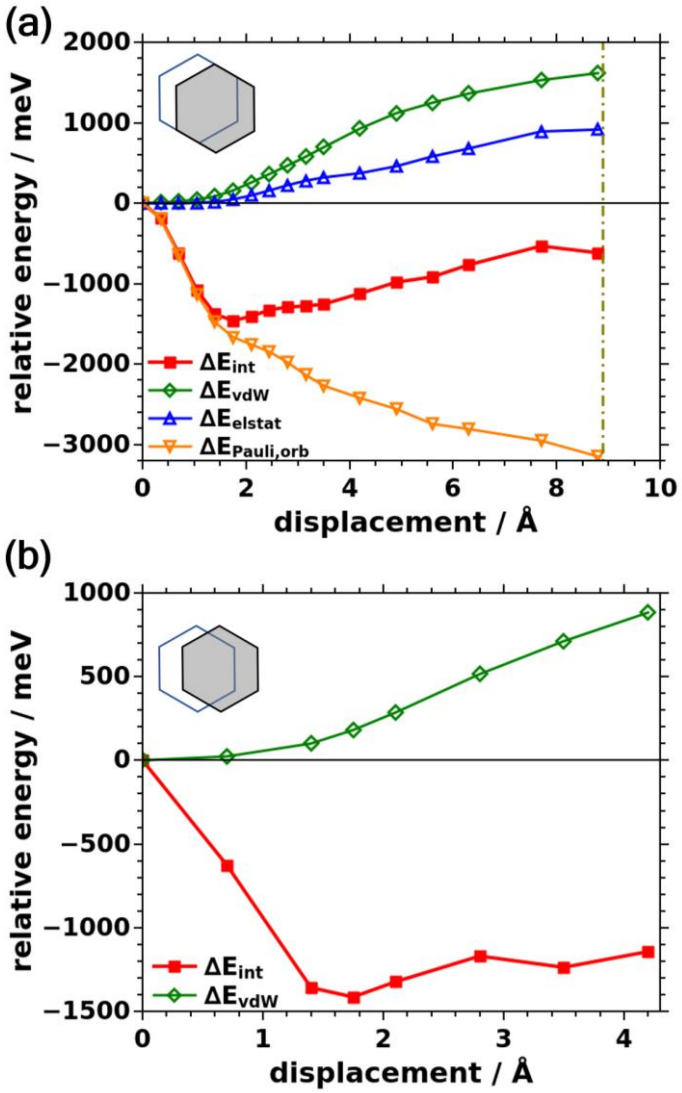

Figure 2. *Relative energies of COF-1 displaced along directions **1** and **2** at a constant interlayer distance. (a) Comparison of interaction energy, vdW energy, electrostatic energy, and Pauli plus orbital rehybridization energy for displacements along shift direction **1**. (b) Comparison of interaction energy and vdW energy for displacements along shift direction **2**. Energy values at 0.0 Å displacement. ΔE_{int}=-1290 meV, $\Delta E_{int,elec}$=2257 meV, ΔE_{vdW}=-3547 meV, $\Delta E_{electrostatic}$=-1344 meV, $\Delta E_{Pauli,orb}$=3601 meV, E_{total}=-70442.671 eV;*

The overall trend of the interaction energy from Figure 2a is also recovered for other shift directions (like a shift perpendicular to the pore edge (direction **2** from Figure 1), as is shown in Figure 2b. Again the interaction energy ΔE_{int} has its highest value for the cofacial arrangement and exhibits a pronounced minimum at displacements around 1.75 Å. Comparing the total energies for the minima found along shift directions **1** and **2**, it is found that the minimum for shifts perpendicular to the pore edges, i.e. direction **2**, is ~40 meV higher in energy.

The crucial role of $\Delta E_{orb,Pauli}$ raises the question, why Pauli repulsion is so large for a cofacial structure. To understand that, one has to keep in mind that when occupied orbitals of two molecules overlap, bonding and antibonding linear combinations are formed, where the bonding one is stabilized less than the antibonding one is destabilized. Now, the energies of the occupied bands (orbitals) contribute to the total energy. Therefore, wavefunction overlap involving fully occupied orbitals results in a repulsive contribution to the total energy. This effect is particularly pronounced for large energetic splittings and, correspondingly, strong electronic couplings.[56] Typically the orbital overlap is largest for a cofacial arrangement, which then should result also in maximized band widths. This is, indeed, observed also here, as shown for the valence band (-width) in Table 1 and Figure S7-1 in the Supporting Information. A consequence of the shift of the layers is a decrease of the bandwidth such that for a certain displacement it even vanishes, then increases again, and so on, an effect that has been intensively investigated for organic semiconductors.[57–63] The shift at which the bandwidth vanishes depends on the symmetry and nodal structure of the lattice periodic functions which are part the Bloch states constituting the different bands. Thus, the shift at which Pauli repulsion due to the specific overlapping occupied bands vanishes depends on the nature of those bands such that one cannot expect a direct correlation between $\Delta E_{orb,Pauli}$ in Figure 2a and the width of the valence band in Figure S7-1. One thing that all bands should, however, have in common is that their widths (and, thus, the associated electronic couplings and effective masses) decrease for small shifts, which is then responsible for the initial sharp drop of $\Delta E_{orb,Pauli}$. In Table 1 one can see the valence bandwidth and associated effective mass along a direction corresponding to the stacking direction of the COF-1 layers for the cofacial and the minimum arrangement observed for the constant interlayer stacking distance. It can be seen that the bandwidth is significantly smaller, i.e. it is reduced by a factor of ~1.8, for the optimum layer arrangement. This change of the bandwidth translates into an even more pronounced change in the associated effective mass, which increases by a factor of more than 2.

Table 1. *Valence bandwidth (VBW) for the electronic band along ΓA, a k-space direction corresponding to the stacking direction of the COF-1 layers, and associated effective mass of COF-1 for the cofacial and the minimum arrangements (1.75 Å shift along direction **1**). The data are given for the shifted COF-1 layers with constant interlayer stacking distance as well as for optimized stacking distances. Transfer integrals can be estimated based on the bandwidth (BW) as BW/4.*

shift / Å	valence bandwidth / meV	effective mass / m_e	stacking distance / Å
literature stacking distance			
0.0	1847	0.61	3.328
1.75	1027	1.29	
optimized stacking distance			
0.0	1154	0.85	3.636
1.75	997	1.31	3.350

3.2 Optimized Interlayer Stacking Distance

The situation is fundamentally modified, when the stacking distance between consecutive COF layers is optimized for each shift. As this optimization procedure requires several calculations for each displacement, we here focus on shifts close to the energetic minimum found for constant interlayer distance, which is most relevant for the present discussion. Again, the interaction energy exhibits a minimum at a layer displacement of around 1.75 Å in full correspondence with the situation for constant interlayer stacking distance. In passing we note that now the evolution of the total energy no longer overlaps with that of the interaction energy, as now the distance between the layers in the sub-systems A and B changes with the shift. Still, the two evolutions evolve essentially in parallel.

A more significant difference compared to the situation discussed in section 3.1 are the evolutions of the different energy contributions: Now the vdW energy becomes more negative up to a displacement of 1.75 Å and rises only afterwards. One can rationalize this behavior by a pronounced decrease of the interlayer stacking distance for small displacements (see SI, Figure S10). For small displacements, this overcompensates the consequences of the decreased spatial overlap of the layers (see above; weighted distance histograms are contained in the SI). This overcompensation vanishes for layer displacements beyond 1.75 Å, where the changes in stacking distance become smaller and where also larger sections of the COF layers come to lie above the (empty) pores of neighboring layers. The decrease in interlayer distance with layer shift also essentially inverts the situation for Pauli repulsion: Now, the above-discussed decrease in the wavefunction overlap for shifted systems due to orbital symmetry and nodal

structure is overcompensated by an increase of the coupling caused by a shrinking interlayer distance. Only for larger displacements the overlap diminishes because of an increasing fraction of the COF-linkers coming to lie above the pores of neighboring layers. This is also manifested in the evolution of the valence bandwidth (see Figure S5b), where a distinct decrease of ~640 meV occurs only for shifts beyond that of the actual minimum structure. As a consequence, the cofacial arrangement also looses is "advantage" over the actual energetic minimum structure as far as transfer integrals estimated as VBW/4 are concerned (see Table 1).

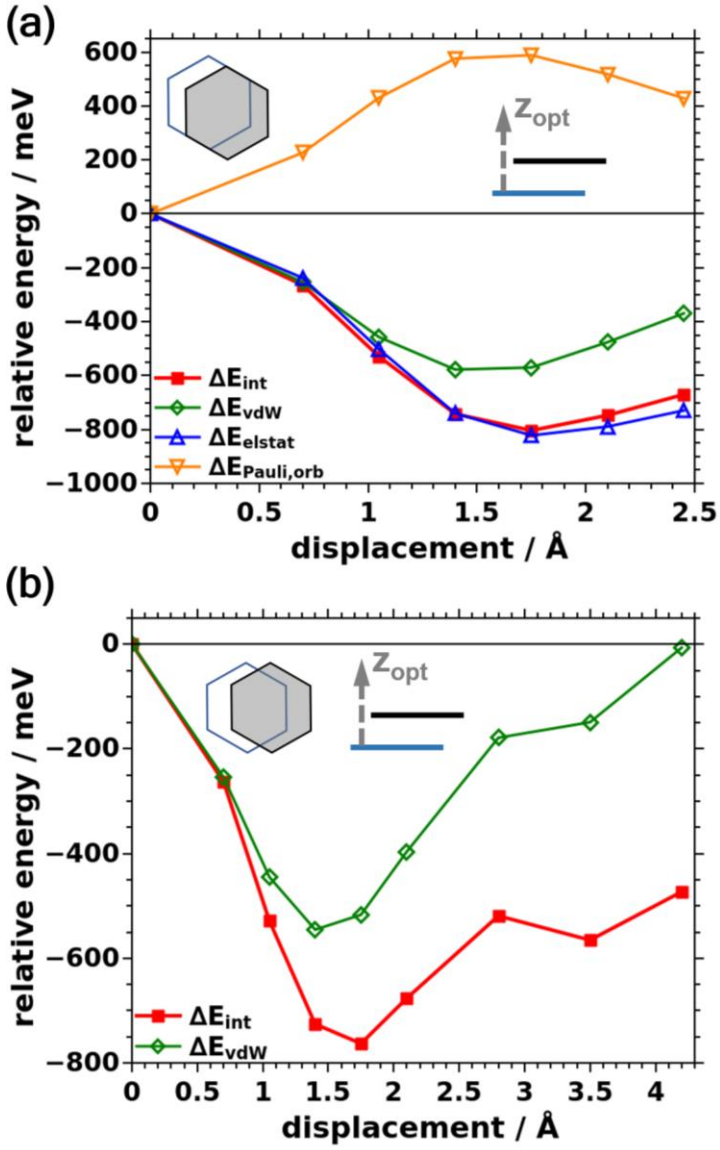

Figure 3. *Relative energies of COF-1 displaced along directions **1** and **2**. The stacking distance has been optimized for each displacement. (a) Comparison of interaction energy, vdW energy, electrostatic energy, and Pauli repulsion plus orbital rehybridization energy for displacements along shift direction **1**. (b) Comparison of interaction energy and vdW energy for displacements along shift direction **2**. Energy values at 0.0 Å displacement.* ΔE_{int}*=-1957 meV,* $\Delta E_{int,elec}$*=812 meV,* ΔE_{vdW}*=-2769 meV,* ΔE_{elstat}*=-385 meV,* $\Delta E_{Pauli,orb}$*=1197 meV,* E_{total}*=-70443.275 eV;*

Interestingly, also the evolution of the (attractive) electrostatic interaction is largely inverted compared to the situation for fixed interlayer distances and the magnitude of the changes is significantly increased. This is again attributed to the decreasing interlayer distance, which amplifies the attractive charge-penetration effects.

An overall interesting observation for optimized interlayer distances is that the shapes of the evolutions of ΔE_{int}, ΔE_{vdW}, ΔE_{elstat}, and $\Delta E_{orb,Pauli}$ in Figure 3a are essentially the same and also the absolute magnitudes of the maximum changes are similar (~600 meV for $\Delta E_{Pauli,orb}$ and ΔE_{vdW} and around 800 meV for ΔE_{elstat}) and occur close to the optimum displacement. The only difference is that now Pauli repulsion favors a cofacial arrangement, while the electrostatic and van der Waals interactions favor shifted structures. Even more surprising is, however, that the displacement that minimizes the energy of the system is the same for both discussed situations despite the observation that the changes in the individual energy contributions with displacement are massively different and this not only in their values, but even in their signs.

A consequence of the evolutions of the individual energy terms is that in systems where both degrees of freedom (layer displacement and stacking distance) are allowed to adapt electrostatic and vdW interactions will be almost equally important and the interplay of those interactions with the Pauli repulsion and orbital rehybridization will determine the preferred layer arrangement.

3.3 Attractive Electrostatic Energy and Charge Penetration Effect

Like demonstrated above, the electrostatic interactions between consecutive layers of COF-1 are always attractive. Nevertheless, under certain circumstances these interactions can indeed promote shifted layer arrangements, as can be seen in Figure 3a. The origin of this promotion, however, cannot be traced back to repulsive interactions between the boroxine linkage groups of the COF, rather it is caused by the decrease in the interlayer stacking distance. In the following, we will have a closer look at the electrostatic interactions ΔE_{elstat} starting by investigating why this interaction is actually attractive.

As mentioned already above, the reason for this attractive interaction is so called charge penetration, an effect that has been discussed extensively for interacting organic materials and organic semiconductor crystals.[53–55] Conceptually, this effect describes that due to the interpenetration of charge/electron clouds the shielding of the positively charged nuclei is

reduced and the attractive electron-nuclei terms become dominant such that the electrostatic interaction becomes attractive. For systems comprising overlapping π-electron clouds, like molecular crystals or layered COFs this effect can become sizable.

For systems like COF-1 one would, however, expect that the significantly different electronegativities of the B and O atoms in the central boroxine (B_3O_3) rings would result in sizable octupole moments resulting in a repulsion of cofacial B_3O_3 rings. To assess the magnitude of the two effects (charge penetration vs. polarization) we split the individual COF-1 layers into two model systems consisting either of benzene or $B_3O_3H_3$ rings (i.e., the only weakly polar molecular building unit and the significantly more polar linkage groups of COF-1) saturated by H atoms. The rings were then arranged in exactly the same positions they adopt in COF-1 with optimized interlayer distances. Then, ΔE_{elstat} was calculated separately for each model system as a function of the shift of consecutive layers. The resulting energy evolution is shown in Figure 4. When considering only the benzene molecules, ΔE_{elstat} is indeed primarily determined by charge penetration effects and is clearly attractive for all considered situations in analogy to the situation observed above for the full COF. Interestingly, when considering only the $B_3O_3H_3$ units, for small displacements, and, thus, large intermolecular distances the electrostatic interactions for the first time are repulsive, in line with the sizable octupole moments of the molecules. It remains like that for displacements of up to ~1 Å; then ΔE_{elstat} becomes negative (i.e., attractive), which we attribute to a superposition of two effects: (i) a smaller distance between the molecular planes resulting in an increased charge penetration (which crucially depends on wavefunction overlap, which is particularly distance-sensitive) and (ii) a decreased repulsion between the octupoles in the shifted configuration. Importantly, as the attractive electrostatic interaction of the benzene rings is always larger than the sometimes repulsive interaction between the $B_3O_3H_3$ units, the sum of the contributions of the two sub-systems is always attractive with the overall evolution with layer displacement very similar to that observed for the full COF-1 system. This explains, why in the actual COF attractive electrostatic interactions prevail despite polarization effects that might suggest otherwise.

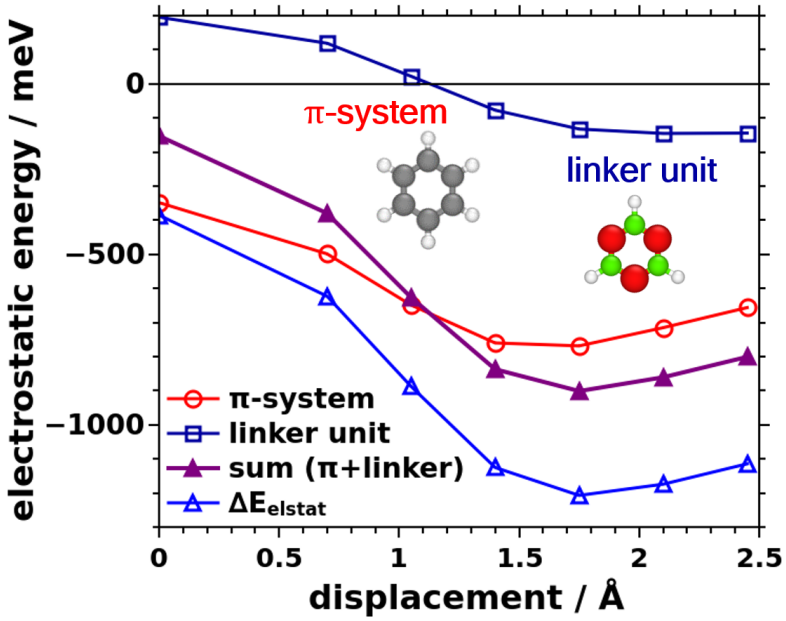

Figure 4. *Electrostatic energy contributions of the COF-1 sub-systems extracted from COF-1 with optimized interlayer stacking distances. The COF was decomposed into two sub-systems (linker unit and π-system) which were used to study the individual contributions to the total electrostatic part of the electronic interaction energy, ΔE_{elstat}. Energy values at 0.0 Å displacement: $E_{elstat,linker\ unit}$=196 meV, $E_{elstat,\pi\text{-}system}$=-348 meV, ΔE_{elstat}=-385 meV*

3.4 Additional Layered COFs

All the above observations suggest that the driving forces (vdW interactions, electrostatic interactions, and Pauli repulsion) causing a stacking arrangement with slightly displaced COF-1 layers to be energetically favorable are of general nature. This finding is further supported by COF-5 showing analogous behavior to COF-1 (as demonstrated in the Supporting Information). Also in literature it has already been speculated that apart from a few exceptions such shifted AA-stacking might be the preferred stacking motif.[35] Considering additional 2D COFs with different sizes of their π-systems and also different pore topologies it is investigated whether these systems also tend to exhibit shifted (serrated) AA-stacking. The additional COFs used for these investigation are COF-5, porphyrin based COFs (Por-COF),[38] and also a hexabenzocoronene based COF (HBC-COF).[39] The structures of these COFs are shown in Figure 5. For the Por-COF we consider two versions of that system, one consisting of Zn-metallated porphyrin (Zn) and one without a metal incorporated in the center of the molecule (NH). Comparing the structures of the above COFs one can see that they exhibit different pore topologies, differently sized π-systems, and different linking units. This renders them ideal

candidates to see whether the individual interactions, Coulomb, van der Waals and Pauli repulsion with orbital rehybridization, show consistent behavior in all COFs.

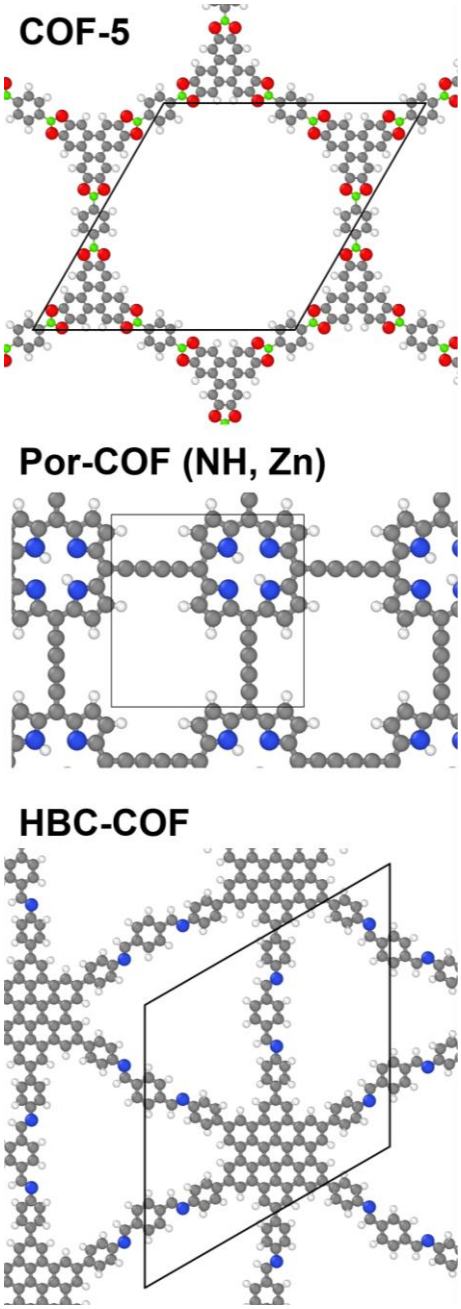

Figure 5. *Structures of the additional COFs considered. C ... grey, H ... white, B ... green, O ... red, N ... blue*

In order to study whether a shifted AA-arrangement is actually the preferred stacking motif, the change of the total energies and the interaction energies for the cofacial arrangement of the COFs are compared to the energies of the optimal layer arrangement obtained by performing a full geometry relaxation including all atomic positions together with the stacking distance. Furthermore also changes in the individual contributions stemming from Coulomb and van der Waals interactions as well as from Pauli repulsion plus orbital rehybridization are evaluated.

The obtained results are summarized in Figure 6 and Table 2. For all the considered systems we find that the energetically favorable arrangement is one with slightly shifted consecutive layers, where for all these arrangements vdW and electrostatic energy are significantly more attractive than for the cofacial arrangement. This suggests that indeed the preferred stacking motif for 2D COFs is a shifted (serrated) AA layer arrangement and that van der Waals and Coulomb interactions enforce these layer arrangements.

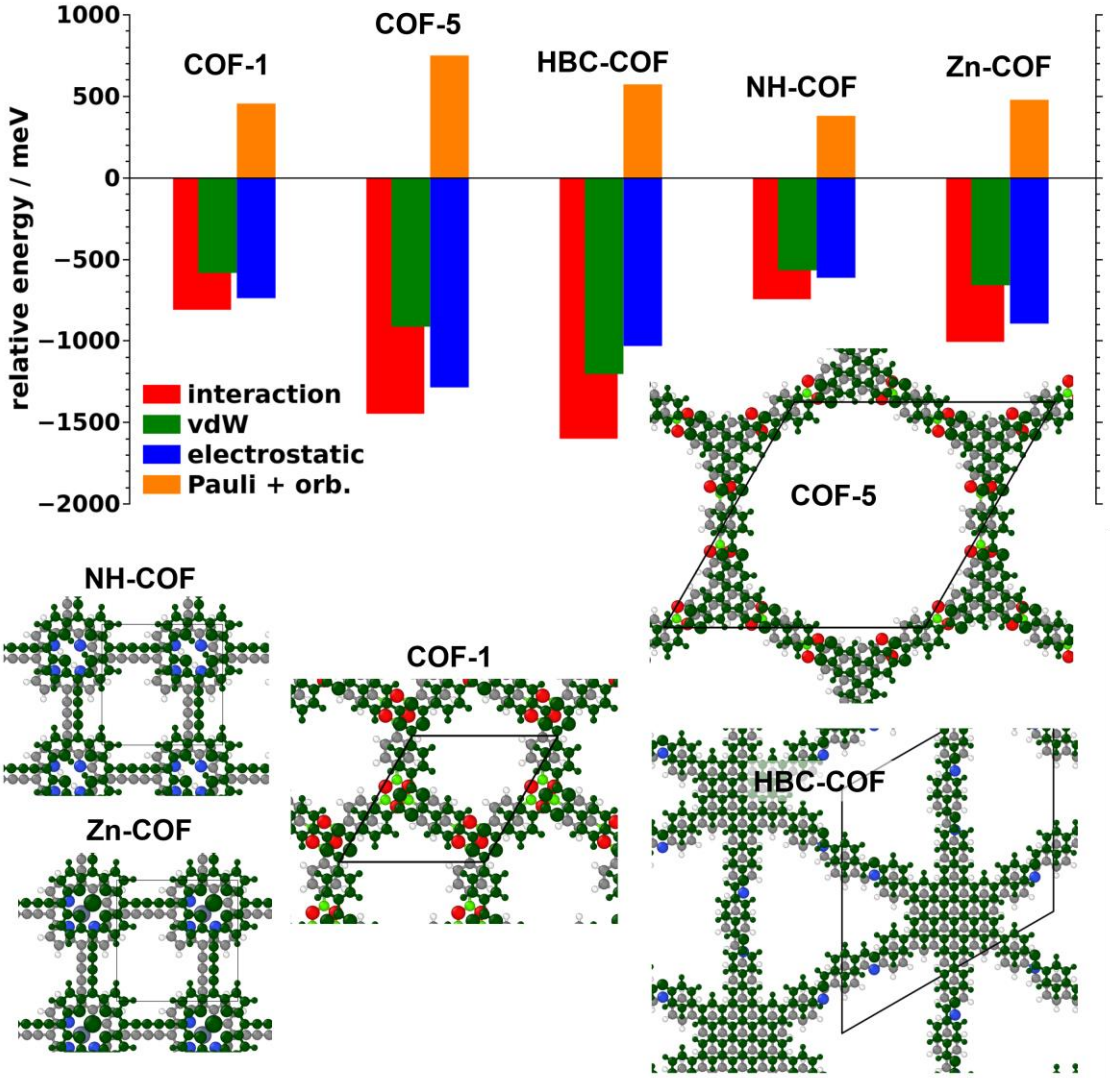

Figure 6. *Energy differences of the interaction energy and the contributions, van der Waals, electrostatic, and Pauli repulsion plus orbital rehybridization, between the cofacial and the optimized structures of the considered COFs (COF-1, COF-5, HBC-COF, NH-Por, Zn-Por, from left to right). The resulting structures of the optimization procedure are shown as insets, where the shifted optimal layer is shown in dark green.*

Such changes in the interlayer arrangement can lead to quite significant changes in the electronic structure. For the example of COF-5 it has been found in literature that band

dispersion as well as the size of the band gap change depending on the interlayer arrangement.[32] Interestingly, from the insets in Figure 6 which show the layer arrangement after optimization and the displacement vectors $\Delta\mathbf{v}_{xy}$ in Table 2 we find that COF-1, COF-5, and HBC-COF exhibit layer displacements along directions parallel to connections between linker unit and π-system. Moreover, the resulting packing motif of the aromatic systems of these COFs indeed show a packing motif similar to graphite.[35] For the Por-COFs we find that their energetic minimum arrangement lies on a mirror axis of the porphyrin molecule (45° diagonal).

Table 2. *Energy differences and structural parameters (displacement vectors, stacking distances) of the considered COFs. The differences are always calculated between the coplanar arrangement and the optimized structure. $\Delta\mathbf{v}_{xy}$ … displacement vector between coplanar and optimized structure, Δz … change of stacking distance upon optimization, z … stacking distance for the optimized layer arrangement, ΔE_{total} … energy difference of total energies of coplanar and optimal stacking, $\Delta(\Delta E_{int})$ … change of interaction energy between coplanar and optimized stacking, $\Delta(\Delta E_{vdW})$ … change of vdW energy between coplanar and optimized stacking, $\Delta(\Delta E_{elstat})$ … change of electrostatic energy contribution between coplanar and optimized stacking, $\Delta(\Delta E_{Pauli,orb})$ … change of Pauli repulsion with orbital rehybridization between coplanar and optimized stacking*

	COF-1	COF-5	HBC-COF	NH-Por	Zn-Por
$\Delta\mathbf{v}_{xy}$/ Å	(1.50,-0.86)	(1.49, -0.46)	(0.00,1.60)	(1.18, 1.18)	(1.24, 1.24)
Δz / Å	-0.26	-0.20	-0.19	-0.22	-0.24
z / Å	3.36	3.39	3.43	3.33	3.32
ΔE_{total} / meV	-861	-1541	-1026	-775	-1033
$\Delta(\Delta E_{int})$ / meV	-809	-1447	-1600	-744	-1006
$\Delta(\Delta E_{vdW})$ / meV	-583	-913	-1203	-567	-659
$\Delta(\Delta E_{elstat})$ / meV	-738	-1285	-1031	-613	-894
$\Delta(\Delta E_{Pauli,orb})$ / meV	456	751	574	381	479

4. CONCLUSIONS

Based on the example of COF-1 we identified the driving forces that enforce shifted (serrated) AA-stacking arrangements to be energetically favorable. A quantitative assessment of the individual interactions (dispersion, electrostatic, Pauli repulsion plus orbital rehybridization) determining the evolution of the total energy has been provided. For constant interlayer stacking distance it was found that $\Delta E_{orb,Pauli}$ is the factor that is responsible for the energy minimum corresponding to a shifted rather than the cofacial arrangement of successive layers.

For systems with optimized stacking distances it turned out that the individual interactions change quite differently compared to systems with constant stacking distances. Interestingly, Pauli repulsion favors a cofacial arrangement, while the electrostatic and van der Waals interactions favor shifted structures for the systems with optimized stacking distances. Although the individual energy contributions show quite different behavior, the minimum layer arrangement is essentially the same for both situations, comprising a shift of 1.75 Å along direction **1**. Considering additional COFs with differently sized π-systems and differently shaped pores, it was found that also these systems prefer shifted layer arrangements. Furthermore, for all the considered systems with optimized stacking distances, it has been found that Coulomb and van der Waals interactions are responsible for these shifted arrangements to be energetically favorable. This suggests that for obtaining layered COFs with cofacial stacking arrangements one cannot rely on the self-assembly of the individual layers, but has to introduce additional terms that enforce the desired arrangements.

Additionally, we showed that the electrostatic part of the interaction between consecutive COF layers is attractive. This nature was explained by the charge penetration effects playing an important role for such close arrangements of π-systems as in these layered COFs.

AUTHOR INFORMATION

ORCID

Christian Winkler 0000-0002-7463-6840

Egbert Zojer 0000-0002-6502-1721

Corresponding Author

egbert.zojer@tugraz.at

Funding Sources

TU Graz Lead Project “Porous Materials at Work” (LP-03).

ACKNOWLEDGMENT

The work has been financially supported by the TU Graz Lead Project “Porous Materials at Work” (LP-03). The computational results have been in part achieved using the Vienna Scientific Cluster (VSC3).

REFERENCES

(1) Kuhn, P.; Antonietti, M.; Thomas, A. Porous, Covalent Triazine-Based Frameworks Prepared by Ionothermal Synthesis. *Angew. Chemie - Int. Ed.* **2008**, *47*, 3450–3453.

(2) Côté, A. P.; Benin, A. I.; Ockwig, N. W.; O’Keeffe, M.; Matzger, A. J.; Yaghi, O. M. Porous, Crystalline, Covalent Organic Frameworks. *Science* **2005**, *310*, 1166–1170.

(3) El-Kaderi, H. M.; Hunt, J. R.; Mendoza-Cortés, J. L.; Côté, A. P.; Taylor, R. E.; O’Keeffe, M.; Yaghi, O. M. Designed Synthesis of 3D Covalent Organic Frameworks. *Science* **2007**, *316*, 268–272.

(4) Tilford, R. W.; Gemmill, W. R.; Zur Loye, H. C.; Lavigne, J. J. Facile Synthesis of a Highly Crystalline, Covalently Linked Porous Boronate Network. *Chem. Mater.* **2006**, *18*, 5296–5301.

(5) Uribe-Romo, F. J.; Hunt, J. R.; Furukawa, H.; Klöck, C.; O’Keeffe, M.; Yaghi, O. M. A Crystalline Imine-Linked 3-D Porous Covalent Organic Framework. *J. Am. Chem. Soc.* **2009**, *131*, 4570–4571.

(6) Côté, A. P.; El-Kaderi, H. M.; Furukawa, H.; Hunt, J. R.; Yaghi, O. M. Reticular Synthesis of Microporous and Mesoporous 2D Covalent Organic Frameworks. *J. Am. Chem. Soc.* **2007**, *129*, 12914–12915.

(7) Chen, X.; Geng, K.; Liu, R.; Tan, K. T.; Gong, Y.; Li, Z.; Tao, S.; Jiang, Q.; Jiang, D. Covalent Organic Frameworks: Chemical Approaches to Designer Structures and Built-In Functions. *Angew. Chemie - Int. Ed.* **2020**, *59*, 5050–5091.

(8) Furukawa, H.; Yaghi, O. M. Storage of Hydrogen, Methane, and Carbon Dioxide in Highly Porous Covalent Organic Frameworks for Clean Energy Applications. *J. Am. Chem. Soc.* **2009**, *131*, 8875–8883.

(9) Tilford, R. W.; Mugavero, S. J.; Pellechia, P. J.; Lavigne, J. J. Tailoring Microporosity in Covalent Organic Frameworks. *Adv. Mater.* **2008**, *20*, 2741–2746.

(10) Yang, Y.; Faheem, M.; Wang, L.; Meng, Q.; Sha, H.; Yang, N.; Yuan, Y.; Zhu, G. Surface Pore Engineering of Covalent Organic Frameworks for Ammonia Capture through Synergistic Multivariate and Open Metal Site Approaches. *ACS Cent. Sci.* **2018**, *4*, 748–754.

(11) Kang, Z.; Peng, Y.; Qian, Y.; Yuan, D.; Addicoat, M. A.; Heine, T.; Hu, Z.; Tee, L.;

Guo, Z.; Zhao, D. Mixed Matrix Membranes (MMMs) Comprising Exfoliated 2D Covalent Organic Frameworks (COFs) for Efficient CO2 Separation. *Chem. Mater.* **2016**, *28*, 1277–1285.

(12) Qian, H. L.; Yang, C. X.; Yan, X. P. Bottom-up Synthesis of Chiral Covalent Organic Frameworks and Their Bound Capillaries for Chiral Separation. *Nat. Commun.* **2016**, *7*, 1–7.

(13) Baldwin, L. A.; Crowe, J. W.; Pyles, D. A.; McGrier, P. L. Metalation of a Mesoporous Three-Dimensional Covalent Organic Framework. *J. Am. Chem. Soc.* **2016**, *138*, 15134–15137.

(14) Dey, K.; Pal, M.; Rout, K. C.; Kunjattu, S. S.; Das, A.; Mukherjee, R.; Kharul, U. K.; Banerjee, R. Selective Molecular Separation by Interfacially Crystallized Covalent Organic Framework Thin Films. *J. Am. Chem. Soc.* **2017**, *139*, 13083–13091.

(15) Li, H.; Pan, Q.; Ma, Y.; Guan, X.; Xue, M.; Fang, Q.; Yan, Y.; Valtchev, V.; Qiu, S. Three-Dimensional Covalent Organic Frameworks with Dual Linkages for Bifunctional Cascade Catalysis. *J. Am. Chem. Soc.* **2016**, *138*, 14783–14788.

(16) Lin, S.; Diercks, C. S.; Zhang, Y. B.; Kornienko, N.; Nichols, E. M.; Zhao, Y.; Paris, A. R.; Kim, D.; Yang, P.; Yaghi, O. M.; *et al.* Covalent Organic Frameworks Comprising Cobalt Porphyrins for Catalytic CO2 Reduction in Water. *Science* **2015**, *349*, 1208–1213.

(17) Sun, Q.; Aguila, B.; Perman, J.; Nguyen, N.; Ma, S. Flexibility Matters: Cooperative Active Sites in Covalent Organic Framework and Threaded Ionic Polymer. *J. Am. Chem. Soc.* **2016**, *138*, 15790–15796.

(18) Wang, S.; Wang, Q.; Shao, P.; Han, Y.; Gao, X.; Ma, L.; Yuan, S.; Ma, X.; Zhou, J.; Feng, X.; *et al.* Exfoliation of Covalent Organic Frameworks into Few-Layer Redox-Active Nanosheets as Cathode Materials for Lithium-Ion Batteries. *J. Am. Chem. Soc.* **2017**, *139*, 4258–4261.

(19) Deblase, C. R.; Silberstein, K. E.; Truong, T. T.; Abruña, H. D.; Dichtel, W. R. β-Ketoenamine-Linked Covalent Organic Frameworks Capable of Pseudocapacitive Energy Storage. *J. Am. Chem. Soc.* **2013**, *135*, 16821–16824.

(20) Bisbey, R. P.; Dichtel, W. R. Covalent Organic Frameworks as a Platform for Multidimensional Polymerization. *ACS Cent. Sci.* **2017**, *3*, 533–543.

(21) Mandal, A. K.; Mahmood, J.; Baek, J. B. Two-Dimensional Covalent Organic Frameworks for Optoelectronics and Energy Storage. *ChemNanoMat* **2017**, *3*, 373–391.

(22) Yadav, V. K.; Mir, S. H.; Mishra, V.; Gopakumar, T. G.; Singh, J. K. A Simple Molecular Design for Tunable Two-Dimensional Imine Covalent Organic Frameworks for Optoelectronic Applications. *Phys. Chem. Chem. Phys.* **2020**, *22*, 21360–21368.

(23) Babu, H. V.; Bai, M. G. M.; Rajeswara Rao, M. Functional π-Conjugated Two-Dimensional Covalent Organic Frameworks. *ACS Appl. Mater. Interfaces* **2019**, *11*, 11029–11060.

(24) Ding, S. Y.; Wang, W. Covalent Organic Frameworks (COFs): From Design to Applications. *Chem. Soc. Rev.* **2013**, *42*, 548–568.

(25) Wan, S.; Guo, J.; Kim, J.; Ihee, H.; Jiang, D. A Belt-Shaped, Blue Luminescent, and Semiconducting Covalent Organic Framework. *Angew. Chemie - Int. Ed.* **2008**, *47*, 8826–8830.

(26) Song, Y.; Sun, Q.; Aguila, B.; Ma, S. Opportunities of Covalent Organic Frameworks for Advanced Applications. *Adv. Sci.* **2019**, *6*.

(27) Ding, X.; Feng, X.; Saeki, A.; Seki, S.; Nagai, A.; Jiang, D. Conducting Metallophthalocyanine 2D Covalent Organic Frameworks: The Role of Central Metals in Controlling π-Electronic Functions. *Chem. Commun.* **2012**, *48*, 8952–8954.

(28) Wu, X.; Han, X.; Liu, Y.; Liu, Y.; Cui, Y. Control Interlayer Stacking and Chemical Stability of Two-Dimensional Covalent Organic Frameworks via Steric Tuning. *J. Am. Chem. Soc.* **2018**, *140*, 16124–16133.

(29) Haase, F.; Gottschling, K.; Stegbauer, L.; Germann, L. S.; Gutzler, R.; Duppel, V.; Vyas, V. S.; Kern, K.; Dinnebier, R. E.; Lotsch, B. V. Tuning the Stacking Behaviour of a 2D Covalent Organic Framework through Non-Covalent Interactions. *Mater. Chem. Front.* **2017**, *1*, 1354–1361.

(30) Geng, K.; He, T.; Liu, R.; Dalapati, S.; Tan, K. T.; Li, Z.; Tao, S.; Gong, Y.; Jiang, Q.; Jiang, D. Covalent Organic Frameworks: Design, Synthesis, and Functions. *Chem. Rev.* **2020**, *120*, 8814–8933.

(31) Keller, N.; Bein, T. Optoelectronic Processes in Covalent Organic Frameworks. **2020**.

(32) Kuc, A.; Springer, M. A.; Batra, K.; Juarez-Mosqueda, R.; Wöll, C.; Heine, T. Proximity Effect in Crystalline Framework Materials: Stacking-Induced Functionality in MOFs and COFs. *Adv. Funct. Mater.* **2020**, *30*, 1908004.

(33) Meng, Z.; Stolz, R. M.; Mirica, K. A. Two-Dimensional Chemiresistive Covalent Organic Framework with High Intrinsic Conductivity. *J. Am. Chem. Soc.* **2019**, *141*, 11929–11937.

(34) Wan, S.; Gándara, F.; Asano, A.; Furukawa, H.; Saeki, A.; Dey, S. K.; Liao, L.; Ambrogio, M. W.; Botros, Y. Y.; Duan, X.; *et al.* Covalent Organic Frameworks with High Charge Carrier Mobility. *Chem. Mater.* **2011**, *23*, 4094–4097.

(35) Zhou, W.; Wu, H.; Yildirim, T. Structural Stability and Elastic Properties of Prototypical Covalent Organic Frameworks. *Chem. Phys. Lett.* **2010**, *499*, 103–107.

(36) Lukose, B.; Kuc, A.; Heine, T. The Structure of Layered Covalent-Organic Frameworks. *Chem. - A Eur. J.* **2011**, *17*, 2388–2392.

(37) Lukose, B.; Kuc, A.; Frenzel, J.; Heine, T. On the Reticular Construction Concept of Covalent Organic Frameworks. *Beilstein J. Nanotechnol.* **2010**, *1*, 60–70.

(38) Thomas, S.; Li, H.; Dasari, R. R.; Evans, A. M.; Castano, I.; Allen, T. G.; Reid, O. G.; Rumbles, G.; Dichtel, W. R.; Gianneschi, N. C.; *et al.* Design and Synthesis of Two-

Dimensional Covalent Organic Frameworks with Four-Arm Cores: Prediction of Remarkable Ambipolar Charge-Transport Properties. *Mater. Horizons* **2019**, *6*, 1868–1876.

(39) Dalapati, S.; Addicoat, M.; Jin, S.; Sakurai, T.; Gao, J.; Xu, H.; Irle, S.; Seki, S.; Jiang, D. Rational Design of Crystalline Supermicroporous Covalent Organic Frameworks with Triangular Topologies. *Nat. Commun.* **2015**, *6*.

(40) Havu, V.; Blum, V.; Havu, P.; Scheffler, M. Efficient O (N) Integration for All-Electron Electronic Structure Calculation Using Numeric Basis Functions. *J. Comput. Phys.* **2009**, *228*, 8367–8379.

(41) Blum, V.; Gehrke, R.; Hanke, F.; Havu, P.; Havu, V.; Ren, X.; Reuter, K.; Scheffler, M. Ab Initio Molecular Simulations with Numeric Atom-Centered Orbitals. *Comput. Phys. Commun.* **2009**, *180*, 2175–2196.

(42) Perdew, J. P.; Burke, K.; Ernzerhof, M. Generalized Gradient Approximation Made Simple. *Phys. Rev. Lett.* **1996**, *77*, 3865–3868.

(43) Perdew, J. P.; Burke, K.; Ernzerhof, M. Erratum: Generalized Gradient Approximation Made Simple (Physical Review Letters (1996) 77 (3865)). *Physical Review Letters*, 1997, *78*, 1396.

(44) Tkatchenko, A.; Scheffler, M. Accurate Molecular van Der Waals Interactions from Ground-State Electron Density and Free-Atom Reference Data. *Phys. Rev. Lett.* **2009**, *102*, 073005.

(45) Heyd, J.; Scuseria, G. E.; Ernzerhof, M. Hybrid Functionals Based on a Screened Coulomb Potential. *J. Chem. Phys.* **2003**, *118*, 8207–8215.

(46) Heyd, J.; Scuseria, G. E.; Ernzerhof, M. Erratum: Hybrid Functionals Based on a Screened Coulomb Potential (Journal of Chemical Physics (2003) 118 (8207)). *J. Chem. Phys.* **2006**, *124*, 219906.

(47) Birch, F. *Finite Elastic Strain of Cubic Crystals*; 1947; Vol. 71.

(48) Raupach, M.; Tonner, R. A Periodic Energy Decomposition Analysis Method for the Investigation of Chemical Bonding in Extended Systems. *J. Chem. Phys.* **2015**, *142*, 194105.

(49) Pecher, L.; Tonner, R. Deriving Bonding Concepts for Molecules, Surfaces, and Solids with Energy Decomposition Analysis for Extended Systems. *Wiley Interdiscip. Rev. Comput. Mol. Sci.* **2019**, *9*, e1401.

(50) Ziegler, T.; Rauk, A. A Theoretical Study of the Ethylene-Metal Bond in Complexes between Cu^{+}, Ag^{+}, Au^{+}, Pt^{0}, or Pt^{2+}, and Ethylene, Based on the Hartree-Fock-Slater Transition-State Method. *Inorg. Chem.* **1979**, *18*, 664.

(51) Ziegler, T.; Rauk, A. On the Calculation of Bonding Energies by the Hartree Fock Slater Method - I. The Transition State Method. *Theor. Chim. Acta* **1977**, *46*, 1–10.

(52) Kitaura, K.; Morokuma, K. A New Energy Decomposition Scheme for Molecular

Interactions within the Hartree-Fock Approximation. *Int. J. Quantum Chem.* **1976**, *10*, 325–340.

(53) Ryno, S. M.; Risko, C.; Brédas, J. L. Noncovalent Interactions and Impact of Charge Penetration Effects in Linear Oligoacene Dimers and Single Crystals. *Chem. Mater.* **2016**, *28*, 3990–4000.

(54) Gryn'ova, G.; Corminboeuf, C. Implications of Charge Penetration for Heteroatom-Containing Organic Semiconductors. *J. Phys. Chem. Lett.* **2016**, *7*, 5198–5204.

(55) Sherrill, C. D. Energy Component Analysis of π Interactions. *Acc. Chem. Res.* **2013**, *46*, 1020–1028.

(56) Winkler, C.; Jeindl, A.; Mayer, F.; Hofmann, O. T.; Tonner, R.; Zojer, E. Understanding the Correlation between Electronic Coupling and Energetic Stability of Molecular Crystal Polymorphs: The Instructive Case of Quinacridone. *Chem. Mater.* **2019**, *31*, 7054–7069.

(57) Winkler, C.; Jeindl, A.; Mayer, F.; Hofmann, O. T.; Tonner, R.; Zojer, E. Understanding the Correlation between Electronic Coupling and Energetic Stability of Molecular Crystal Polymorphs: The Instructive Case of Quinacridone. *Chem. Mater.* **2019**, *31*.

(58) Kwon, O.; Coropceanu, V.; Gruhn, N. E.; Durivage, J. C.; Laquindanum, J. G.; Katz, H. E.; Cornil, J.; Brédas, J. L. Characterization of the Molecular Parameters Determining Charge Transport in Anthradithiophene. *J. Chem. Phys.* **2004**, *120*, 8186–8194.

(59) Lemaur, V.; Da Silva Filho, D. A.; Coropceanu, V.; Lehmann, M.; Geerts, Y.; Piris, J.; Debije, M. G.; Van De Craats, A. M.; Senthilkumar, K.; Siebbeles, L. D. A.; *et al.* Charge Transport Properties in Discotic Liquid Crystals: A Quantum-Chemical Insight into Structure-Property Relationships. *J. Am. Chem. Soc.* **2004**, *126*, 3271–3279.

(60) Coropceanu, V.; Cornil, J.; da Silva Filho, D. A.; Olivier, Y.; Silbey, R.; Brédas, J. L. Charge Transport in Organic Semiconductors. *Chem. Rev.* **2007**, *107*, 926–952.

(61) Zhu, L.; Yi, Y.; Li, Y.; Kim, E. G.; Coropceanu, V.; Brédas, J. L. Prediction of Remarkable Ambipolar Charge-Transport Characteristics in Organic Mixed-Stack Charge-Transfer Crystals. *J. Am. Chem. Soc.* **2012**, *134*, 2340–2347.

(62) Bredas, J. L.; Calbert, J. P.; da Silva Filho, D. A.; Cornil, J. Organic Semiconductors: A Theoretical Characterization of the Basic Parameters Governing Charge Transport. *Proc. Natl. Acad. Sci.* **2002**, *99*, 5804–5809.

(63) da Silva Filho, D. A.; Kim, E.-G.; Brédas, J.-L. Transport Properties in the Rubrene Crystal: Electronic Coupling and Vibrational Reorganization Energy. *Adv. Mater.* **2005**, *17*, 1072–1076.

5.3. Supporting Information

SUPPORTING INFORMATION for

Determining the role of electrostatic and dispersion interactions for the stacking motif of covalent organic frameworks

Christian Winkler[1] *and Egbert Zojer*[1,]*

[1] Institute of Solid State Physics, NAWI Graz, Graz University of Technology, Petersgasse 16, 8010 Graz, Austria

1. Overview of basis functions used in FHI-Aims

Table S1. *Basis functions that have been used for all calculations performed with FHI-AIMS. The abbreviations read as follows: H(nl,z), where H describes the type of the basis function where H stands for hydrogen-like type function, n is the main quantum number, l denotes the angular momentum quantum number, and z denotes an effective nuclear charge which scales the radial function in the defining Coulomb potential.*[1]

	H	C	B	O	N	Zn	
Minimal	1s	[He]+2s2p	[He]+2s2p	[He]+2s2p	[He]+2s2p	[Ar]+4s3p3d	
Tier 1	H(2s,2.1) H(2p,3.5)	H(2p,1.7) H(3d,6) H(2s,4.9)	H(2p,1.4) H(3d,4.8) H(2s,4)	H(2p,1.8) H(3d,7.6) H(3s,6.4)	H(2p,1.8) H(3d,6.8) H(3s,5.8)	H(2p,1.7) H(3s,2.9) H(4p,5.4) H(4f,7.8) H(3d,4.5)	
Tier 2	H(1s,0.85) H(2p,3.7) H(2s,1.2) H(3d,7)	H(3p,5.2) H(3s,4.3) H(3d,6.2) H(4f,9.8) H(5g,14.4)	H(4f,7.8) H(3p,4.2) H(3s,3.3) H(5g,11.2) H(3d,5.4)	H(3p,6.2) H(3d,5.6) H(1s,0.75) H(4f,11.6) H(5g,17.6)	H(3p,5.8) H(1s,0.8) H(3d,4.9)		

2. Additional data

2.1. Relative energies of COF-1 in a fully optimized unit cell

Figure S1 shows the evolution of the relative energies as a function of the displacement along shift direction **1** for COF-1 with a fully optimized unit cell. Here, fully optimized means that the length of all lattice vectors has been relaxed, while the angles between them were held constant. For each displacement the optimal stacking distance was determined using the procedure described in the main manuscript. Now, considering the evolution of the energies in Figure S1 and comparing them to Figure 3 of the main manuscript one observes that the data agree. Only minor numerical differences can be observed. Thus, one can conclude that optimizing in the in-plane lattice parameters does not impact the qualitative behavior of the relative energies of the system.

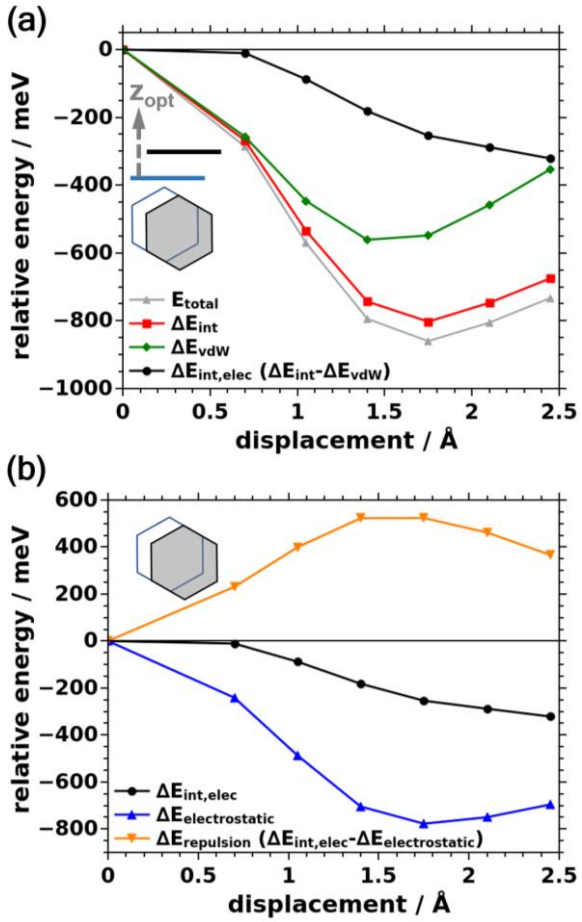

*Figure S1. Relative energies of COF-1 with optimized in-plane lattice parameters. Consecutive layers are shifted along direction **1** and the stacking distance is relaxed at each displacement. (a) Comparison of total energy to the (electronic) interaction energy and the vdW energy (b) Decomposed terms of the electronic interaction energy. Energy values at 0.0 Å displacement. ΔE_{int}=-2029 meV, $\Delta E_{int,elec}$=834 meV, ΔE_{vdW}=-2863 meV, ΔE_{elstat}=-413 meV, $\Delta E_{Pauli,orb}$=1247 meV, E_{total}=-70443.8427 eV;*

2.2. Relative energies of COF-5

In Figure S2 one can see the relative evolution of the energies of COF-5 as a function of displacements along a shift direction parallel to the edges of the pore, analogous to direction **1** of COF-1. For each displacement the stacking distance of consecutive COF-5 layers was optimized. Considering the evolution of the interaction energy we find that it exhibits a minimum at a displacement of around 1.5 Å, which is similar to COF-1. For both COFs, cofacial arrangements are energetically unfavorable and driving forces exist pushing these systems towards shifted layer arrangements. Decomposing the interaction energy into individual contributions comprising vdW interactions, electrostatic interactions and Pauli repulsion plus orbital rehybridization we find that their evolution shown in Figure S2b shows again very similar behavior compared to COF-1. Electrostatic and vdW interactions become more attractive upon layer displacements up to 1.5 Å and then, for larger displacements they become weaker. The repulsion term (Pauli repulsion plus orbital rehybridization), on the contrary, gets more repulsive in the range of displacements where vdW and electrostatic contributions got more attractive. Changes in the vdW and the electrostatic interactions are larger than those of the repulsion, thus, they determine the formation of the minimum at the shifted layer arrangement of 1.5 Å.

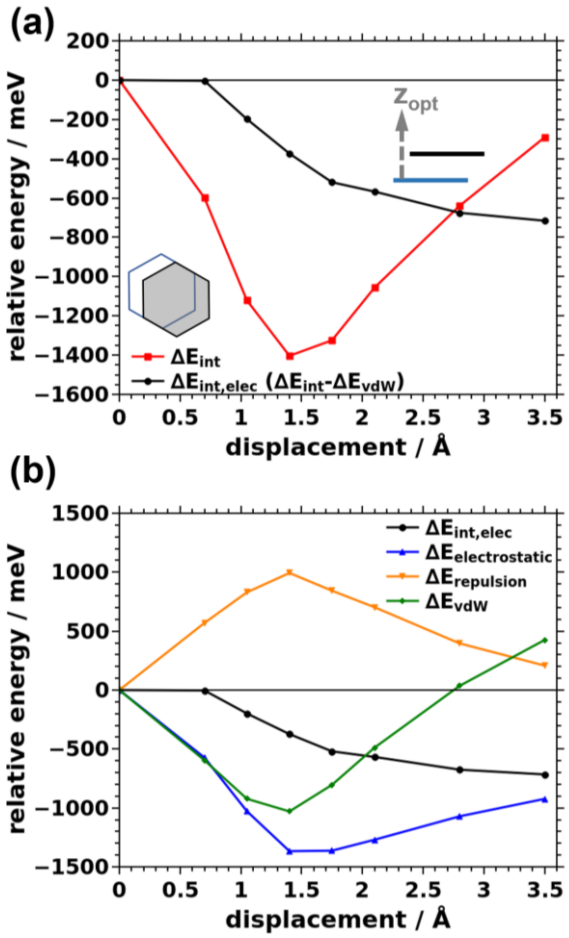

Figure S2. (a) Relative energies of COF-5 as a function of the shift direction. The interlayer stacking distance was optimized at each displacement. (b) Decomposed electronic interaction energy. Absolute energy values at 0.0 Å displacement: $\Delta E_{int,elec}$=1779 meV, ΔE_{vdW}=-8483 meV, ΔE_{elstat}=-1446 meV, $\Delta E_{Pauli,orb}$=3225 meV, ΔE_{int}=-5238 meV

2.3. Relative energies of COF-1 for an inclined unit cell

To see whether the shifted stacking motif where one of the layers in the unit cell is shifted with respect to the other is different from a displaced layer arrangement achieved by tilting the unit cell vector as shown by the inset in Figure S3, such an inclined unit cell has been constructed and investigated for COF-1. Two molecules are placed in the unit cell, to allow the decomposition of the interaction energy if needed. The interlayer distance was kept constant during these calculations. Now, inspecting the evolution of the total interaction energy, red curve in Figure S3, one can see that also for such realizations of layer displacements, the coplanar arrangement is energetically unfavorable. Note that the powder x-ray diffraction patterns of such an inclined system would exhibit peaks at different scattering angles compared to the system with the original unit cell – see Figure S3-1.

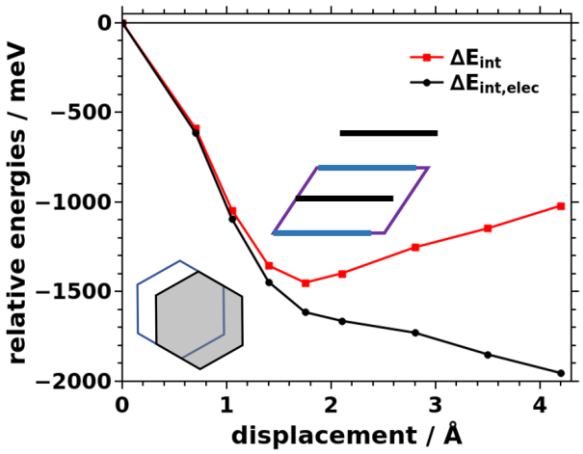

Figure S3. Interaction energy of COF-1 for an inclined unit cell (see inset). The stacking distance is kept constant during the evaluation and the shift direction is the one considered throughout the main manuscript. Absolute energy values at 0.0 Å displacement: ΔE_{int}=-1290 meV, $\Delta E_{int,elec}$=2257 meV

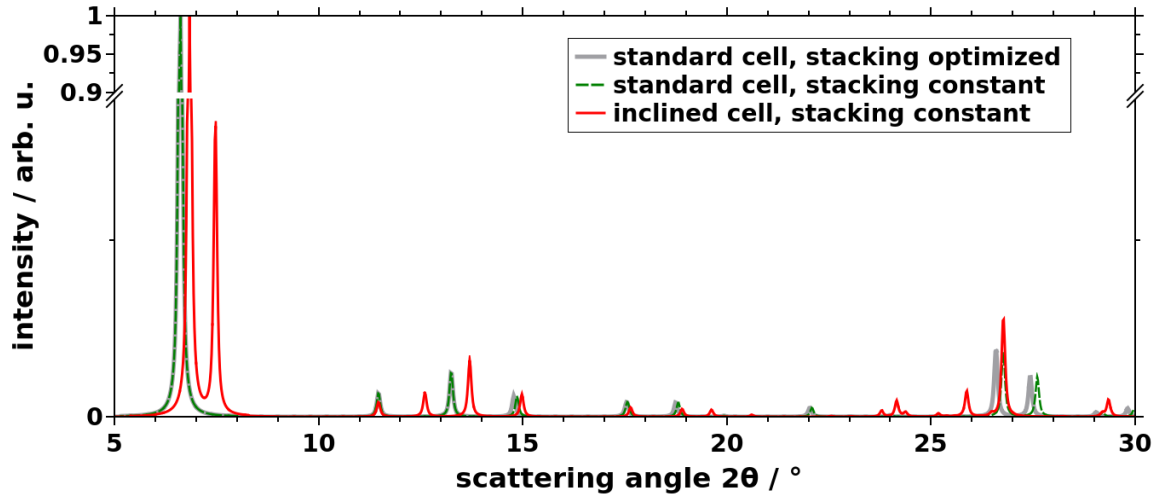

*Figure S3-1. Calculated powder x-ray diffraction patterns for COF-1 in the unit cell with all lattice vectors taken from literature (grey), or with the in-plane vectors from literature and optimized stacking distance (dashed green) and the inclined unit cell (red). All patterns have been calculated for the minimum arrangement found for shifts along direction **1** with a shift of 1.75 Å. A wavelength of 1.54 Å, which corresponds to Cu K-α radiation, has been employed during the calculations. These patterns have been calculated employing the Mercury software package.*[2–6]

2.4. Relative energies of COF-1 for shift direction perpendicular to pore edge

The relative total energy of COF-1 has been determined as a function of displacements along a direction perpendicular to the pore (schematically shown by inset in Figure S4a). These data were determined for constant interlayer stacking distance, see Figure S4a, and optimized stacking distance in Figure S4b. Again, cofacial, AA-stacking arrangements are energetically unfavorable. This is true, no matter whether the stacking distance is optimized or not. Interestingly, for both systems, we find that there appears a local minimum at arrangements with displacements of around 3.5 Å. However, this minimum is almost 200 meV higher in energy than the one found at 1.75 Å for the system with the optimized stacking distance.

For a constant stacking distance between the layers the energetic difference between cofacial arrangement and the shifted arrangement is significantly higher (~700 meV) than for the systems with optimized stacking distances.

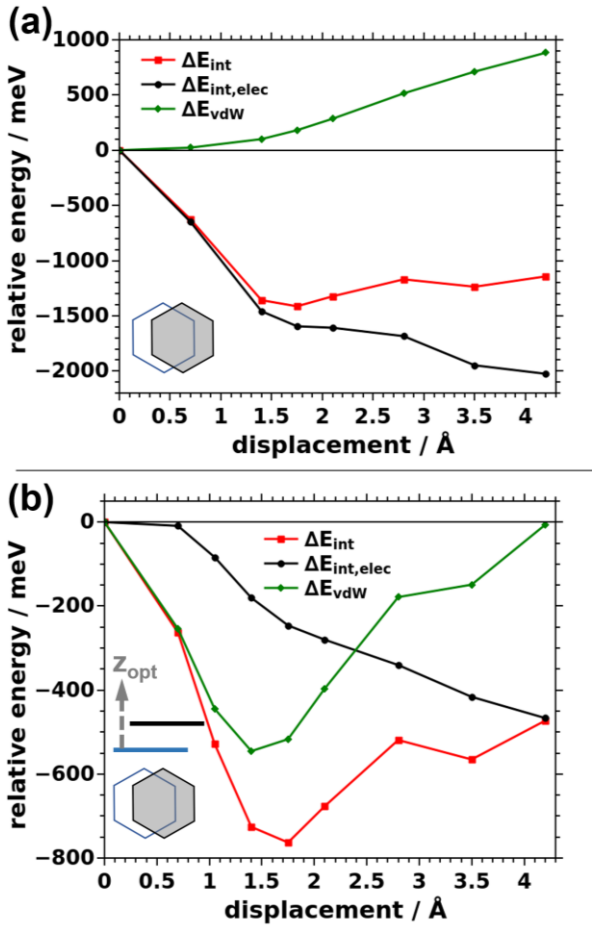

Figure S4. Relative energies of COF-1 shifted along a direction perpendicular to a pore edge (a) for a constant interlayer stacking distance and (b) for the optimized stacking stacking distance at each displacement. Energy values at 0.0 Å displacement: ΔE_{int}=-1290 meV, $\Delta E_{int,elec}$=2257 meV, ΔE_{vdW}=-3547 meV (constant z); ΔE_{int}=-2220 meV, $\Delta E_{int,elec}$=803 meV, ΔE_{vdW}=-2769 meV (z optimized);

2.5. Evolution of the valence bandwidth for COF-1

The width of the valence band along a k-space direction parallel to the stacking direction of the COF-1 layers has been extracted from electronic structure calculations. The resulting values for displacements between 0 and 3.5 Å are shown in Figure S5. First, in Figure S5a one can see the evolution of the valence bandwidth when the interlayer stacking distance is held constant. One can see that it decreases for displacements up to 2.4 Å from 1847 meV at cofacial arrangement to around 300 meV for 2.4 Å displacement. For the data point at 3.5 Å displacement we observe an increased bandwidth of slightly less than 600 meV. When optimizing the stacking distance, see corresponding data in Figure S5b, first of all, one can see that the overall value of the VBW has decreased to less than 1200 meV at cofacial arrangement. For displacements up to 1.4 Å the VBW varies only slightly around this value. Then, for larger displacements the VBW decreases to slightly below 400 meV for 2.4 and 3.5 Å displacement.

Comparing these evolutions to that of the repulsion energy in Figures 2 and 3 of the main manuscript no one to one correlation can be observed between the VBW and this energy. Considering the observations for OSCs in Ref [7], it was found that Pauli repulsion and orbital

rehybridization cause molecular arrangements with large intermolecular electronic couplings (approximated by bandwidths) to be energetically unfavorable. Therefore, one could expect to observe a similar correlation for the layered COFs considered in this work. Several reasons might help to rationalize why a one to one correlation could not be identified here: All occupied bands enter the expression for the energy and, thus, considering solely the valence band might be an incomplete representation of the system. Furthermore, considering the structure of COF-1 – see Figure S6 - one can see that benzene rings 2 and 3 (named dimer 2 and 3 in Figure S6) are shifted towards pore space while dimer 1 is shifted along the edge of the pore. This means that the orbital overlap with neighboring molecules/atoms of consecutive COF layers decreases for dimer 2 and 3. Dimer 1 on the other hand experiences orbital overlap with different parts of the COF, depending on the displacement. At cofacial arrangement, all benzene rings are stacked perfectly on top of each other. Upon displacement parts of dimer 1 start to show significant spatial overlap with parts of the boroxine (B_3O_3) linkage groups. As a result, also corresponding orbitals will show significant overlap. Consequently, the bandwidths of the bands corresponding to the individual dimers will evolve differently. Additionally, we report the sum of Pauli repulsion and orbital rehybridization, further complicating the identification of a correlation between Pauli repulsion and bandwidth.

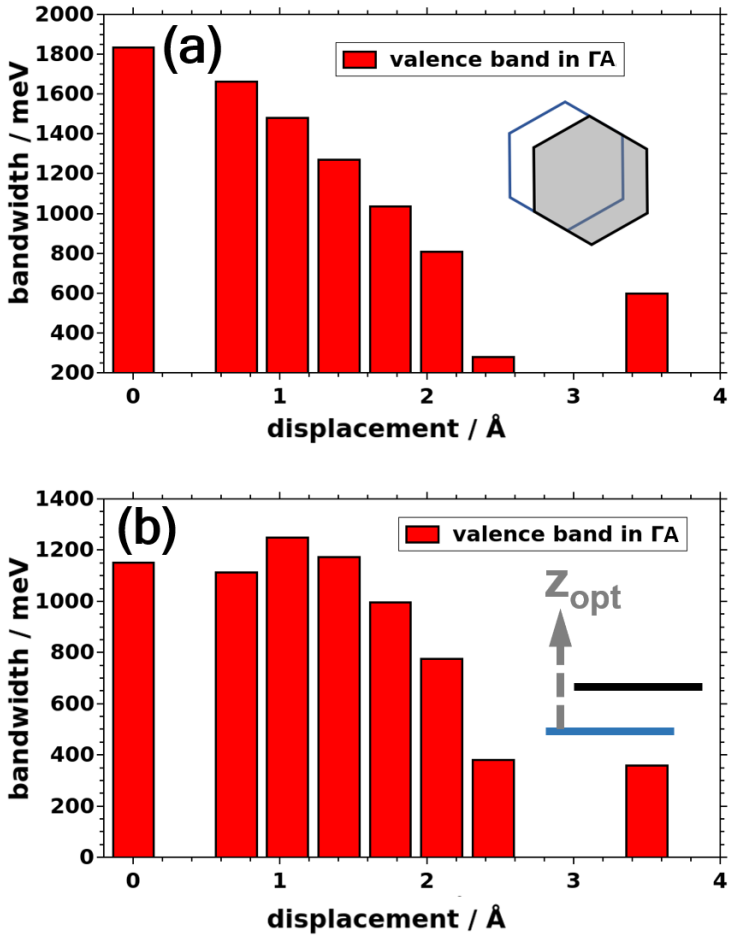

*Figure S5. Width of the valence band in ΓA direction for COF-1 shifted along direction **1** with a constant interlayer spacing (a) and the optimized interlayer spacing (b).*

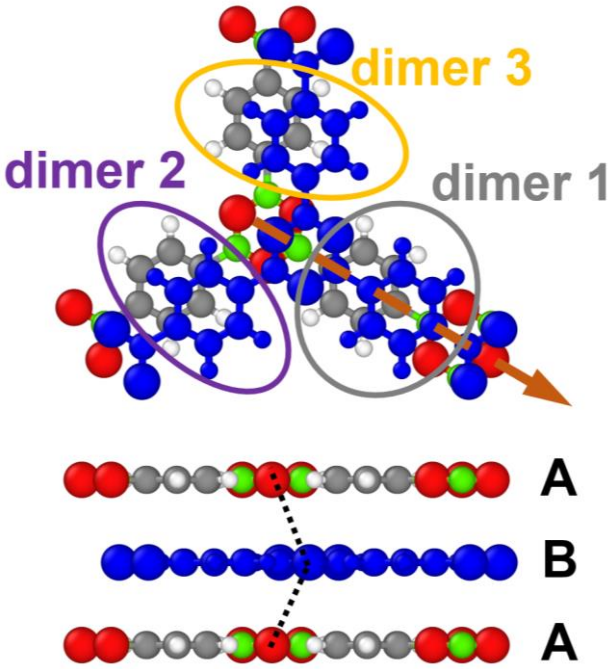

Figure S6. Cutout of the structure of COF-1. The shift between consecutive layers is shown by the original layer and the shifted one in blue. The benzene stacks that are formed are marked by colored ellipses and denoted as dimers 1, 2, and 3. Note that while we call them dimers, in the periodic systems these parts of the COF comprise infinitely extended stacks. The lattice vectors are omitted for clarity.

Additional details regarding the electronic band structure of COF-1

Due to the different benzene units comprising the individual COF-1 layers, the electronic band structure becomes quite complex. Therefore, we briefly discuss this band structure in the following while focusing on the valence band region. In Figure S7-1 one can see data for the electronic structure of COF-1 for the cofacial arrangement as well as for the shifted arrangement (1.75 Å) and for constant interlayer stacking distance. For the electronic band structure for the cofacial arrangement in Figure S7-1a we find a valence band with a width of ~1.8 eV along ΓA, while for the in-plane directions the bands remain relatively flat. Actually, one observes 3 valence bands which are almost degenerate. These bands stem from the 3 benzene dimers, as can be seen from the projected density of states in Figure S7-1b. In ΓA direction the bands are backfolded, as there are two layers in the unit cell. For the shifted arrangement shown in Figures S7-1c,d we find that the degeneracy is lost and a single valence band with a width of ~1 eV can be found. This band now comprises contributions solely from dimer 1, as can be seen from the projected density of states and the eigenstate densities in Figures S7-1e,f.

In Figure S7-2 similar observations can be made for the system where the interlayer stacking distance has been optimized. Again, for the shifted layer arrangement the valence band consists of contributions from what we termed dimer 1 in Figure S6. The changes in the bandwidth, however, are not as large as they are when keeping the interlayer stacking distance constant.

For the constant interlayer stacking distance we also calculated the electronic bands employing the hybrid functional HSE06.[8,9] There, we find that the evolutions of the valence band show good agreement comparing PBE and HSE06 results (see Figure S7-3). Nevertheless, the bandwidths obtained with HSE06 are larger (VBW=2045 meV for cofacial and VBW=1165 meV for the shifted arrangement) and the effective mass is smaller (m^*=0.55 m_e for cofacial and m^*=1.13 m_e for the shifted arrangement).

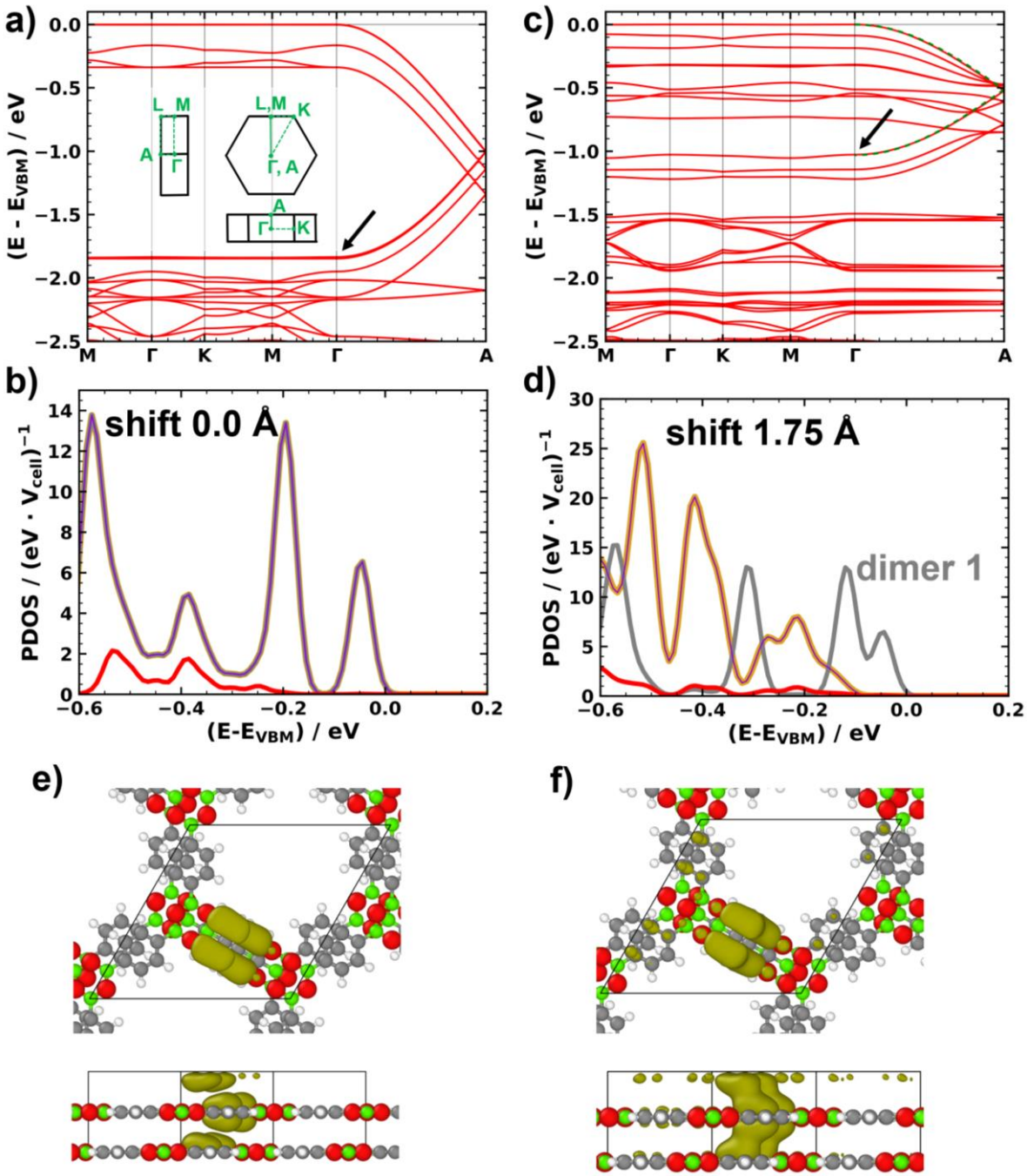

*Figure S7-1. Electronic band structure, projected density of states, and eigenstate density of COF-1 for cofacial and minimum arrangement (shift of 1.75 Å) found for shifts along direction **1** while keeping the interlayer stacking distance constant. (a) Electronic band structure for COF-1 at cofacial arrangement zoomed into the region of the valence band. The first Brillouin zone is shown as an inset. (b) Density of states projected onto sub-parts of the COF-layers for*

cofacial stacking. These sub-parts are dimers 1, 2, and 3 (grey, purple, dark yellow) denoted in Figure S6 and the boroxine linkage groups (red). The energy range close to the valence band is shown. (c) Electronic band structure for the shifted arrangement of COF-1 zoomed into the region of the valence band. The valence band has been fitted by a simple 1D tight-binding model and the result is shown as the dashed green line. (d) Density of states projected onto sub-parts of the COF-layers for the shifted arrangement. (e) and (f) isodensity plots of the electron density of occupied eigenstates at the Γ point for the shifted layer arrangement. The electron density for the highest occupied state (band) is shown in (e) and the electron density of the lower eigenstate corresponding to this band is shown in (f). C ... grey, H ... white, B ... green, O ... red; The black arrows denote the backfolded contribution of the valence band. For the shifted arrangement the eigenstate density was calculated for the corresponding state at the Γ-point.

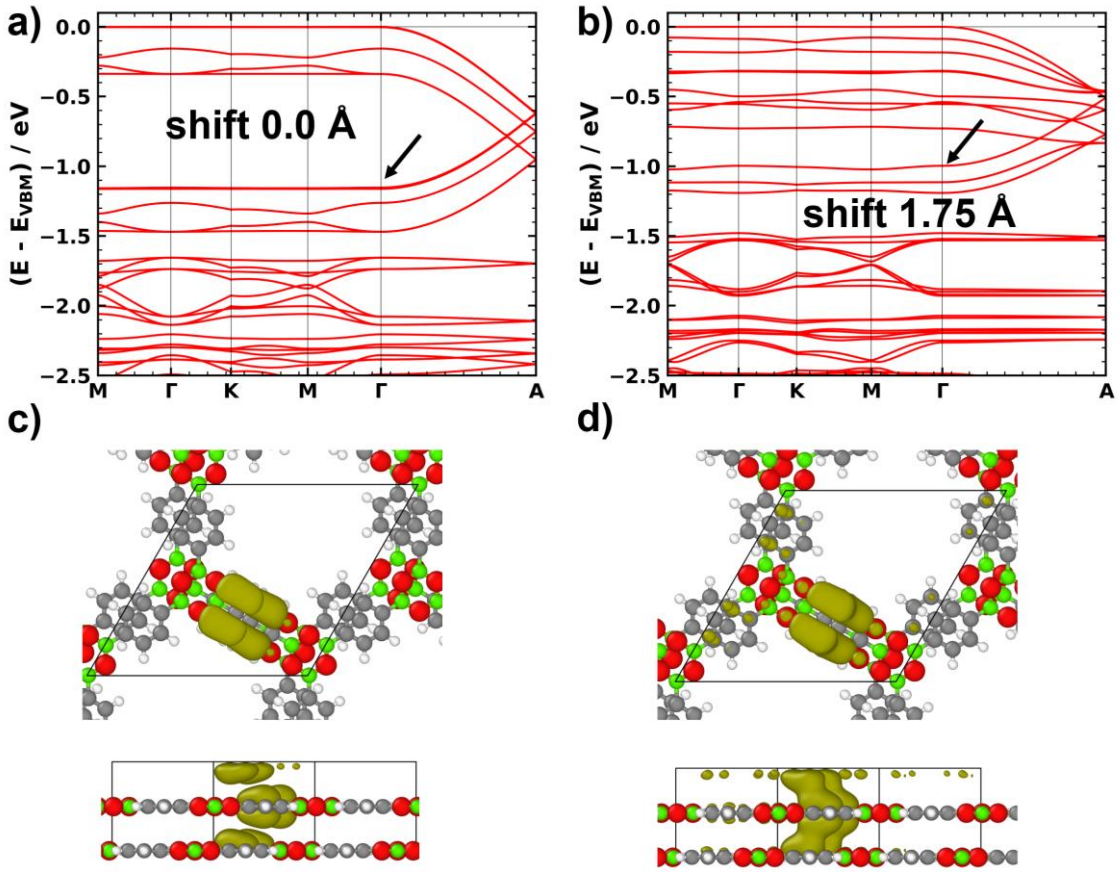

*Figure S7-2. Electronic band structure and eigenstate density of COF-1 for cofacial and minimum arrangement (shift of 1.75 Å) found for shifts along direction **1** when optimizing the interlayer stacking distance. (a) Electronic band structure for COF-1 at cofacial arrangement zoomed into the region of the valence band. (c) and (d) isodensity plots of the electron density of occupied eigenstates at the Γ point and for the shifted layer arrangement. The electron density for the highest occupied state (band) is shown in (c) and the electron density of the lower eigenstate corresponding to this band is shown in (d). C ... grey, H ... white, B ... green, O ... red;*

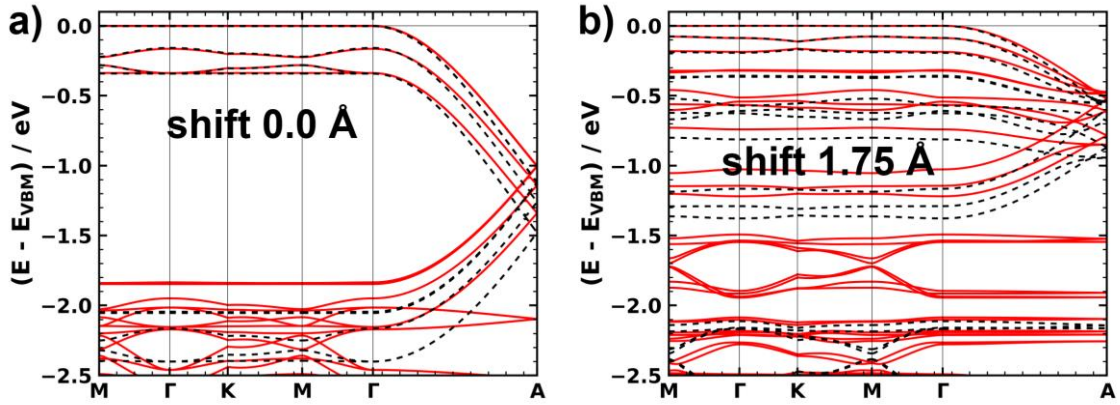

*Figure S7-3. Electronic band structure of COF-1 for cofacial (a) and minimum arrangement (a), equal to a shift of 1.75 Å, found for shifts along direction **1** for constant interlayer stacking distance. The band structures have been calculated using the PBE (solid red lines) functional and the hybrid HSE06 (dashed black lines) functional.*

2.6. Distance weighted histograms for COF-1

For rationalizing the evolution of the vdW interactions reported in the main manuscript we calculated histograms that show the number of atoms within a certain distance interval, i.e. that are within a sphere of a particular radius. This number of atoms was then weighted with the individual distance to the power of -6. This $1/R^6$ weight is inspired by terms that are included in typical pairwise vdW corrections. In Figure S8 the data for COF-1 shifted along the edge of the pores and relaxed interlayer stacking distances is shown. Figure S9 shows the data for the system without relaxed stacking distance. Lastly, the evolution of the optimized stacking distance is shown in Figure S10.

Now, considering Figure S8, one finds that the low distance contributions to the weighted number of atoms actually increase for displacements up to 1.75 Å. This trend is perfectly in line with the vdW interactions becoming more attractive in this range of displacements. For constant stacking distance, one observes that for layer displacements up to 1.75 Å only little changes in the histogram appear, which correlates with the almost constant vdW interaction for that range. For larger displacements significant changes are observed, which is again consistent with the vdW interactions showing larges changes for such layer arrangements.

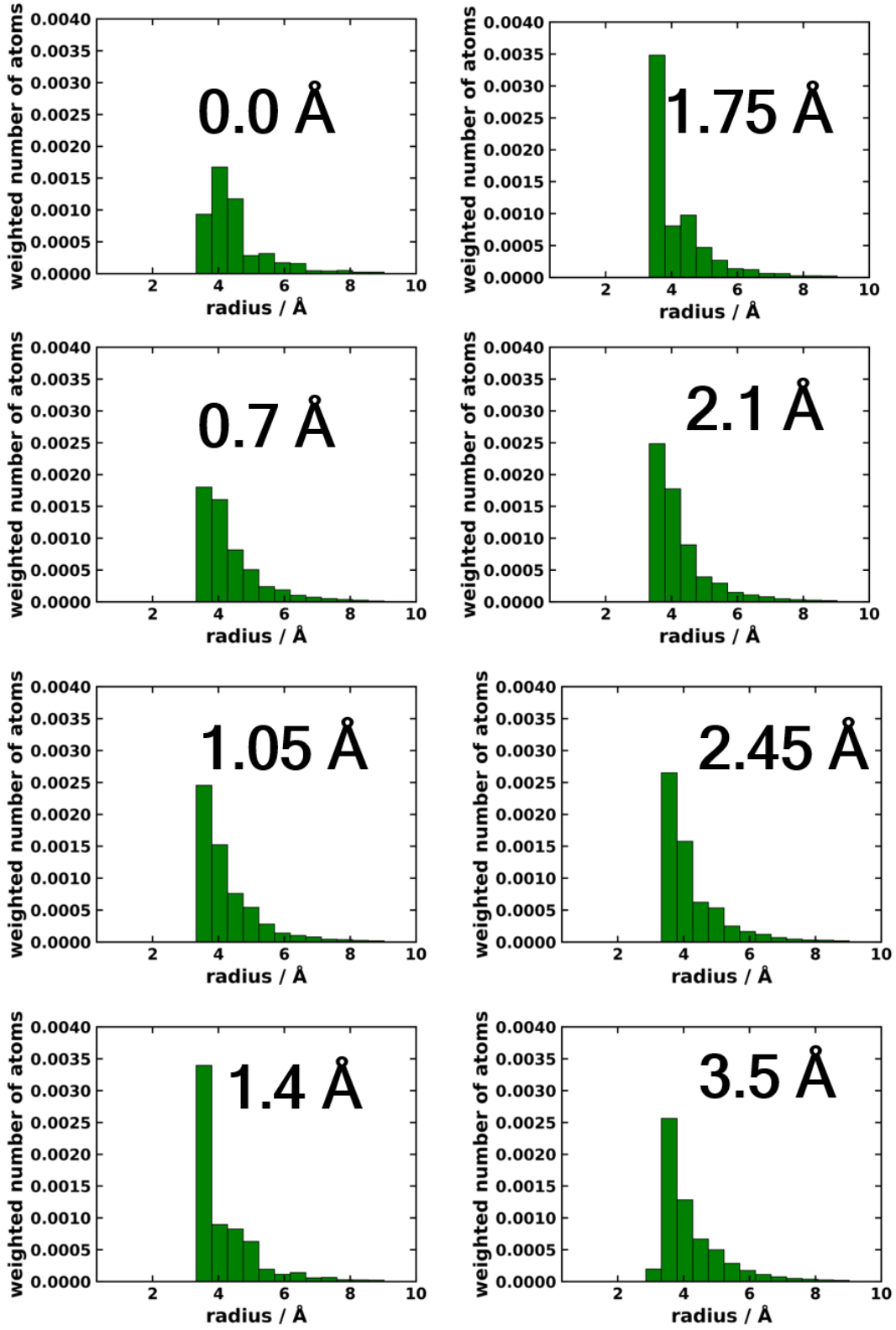

Figure S8. Histogram showing the number of atoms found within a certain interlayer distance interval and weighted by this distance to the power of -6 (#atoms/(r^6)) for COF-1 with optimized stacking distance. At each layer displacement such a histogram is created. One can see that the low distance contributions to this weighted number of atoms actually increase for displacements up to 1.75 Å. Which is perfectly in line with the vdW interactions becoming more attractive in this region.

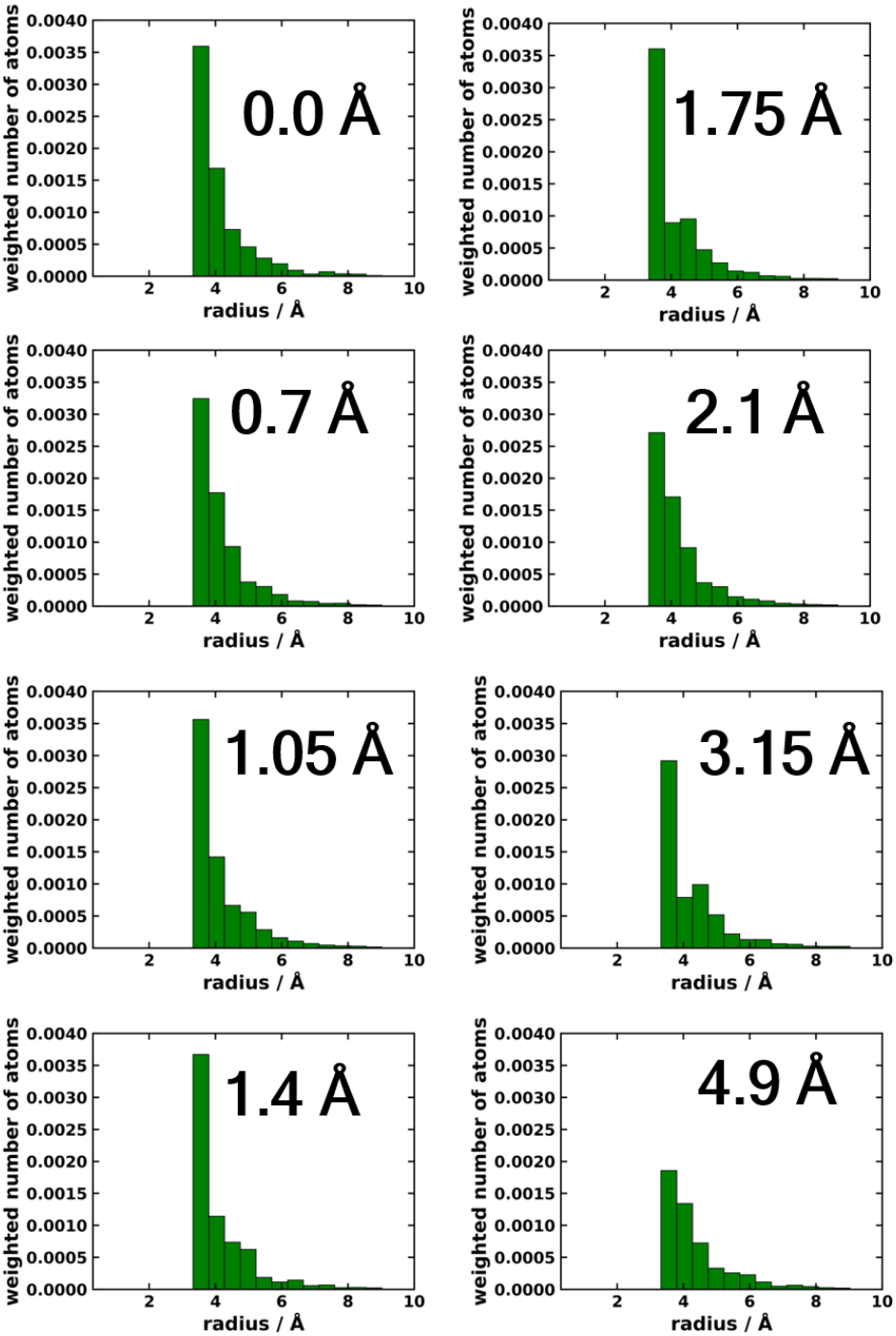

Figure S9. Histogram showing the number of atoms found within a certain interlayer distance interval and weighted by this distance to the power of -6 (#atoms/(r^6)) for COF-1 with constant stacking distance. At each layer displacement such a histogram is created. For layer displacements up to 1.75 Å one can see only little changes in the histogram, which correlated with the almost constant vdW interaction for that range. For larger displacements significant changes are observed, again perfectly consistent with the vdW showing larges changes for such layer arrangements.

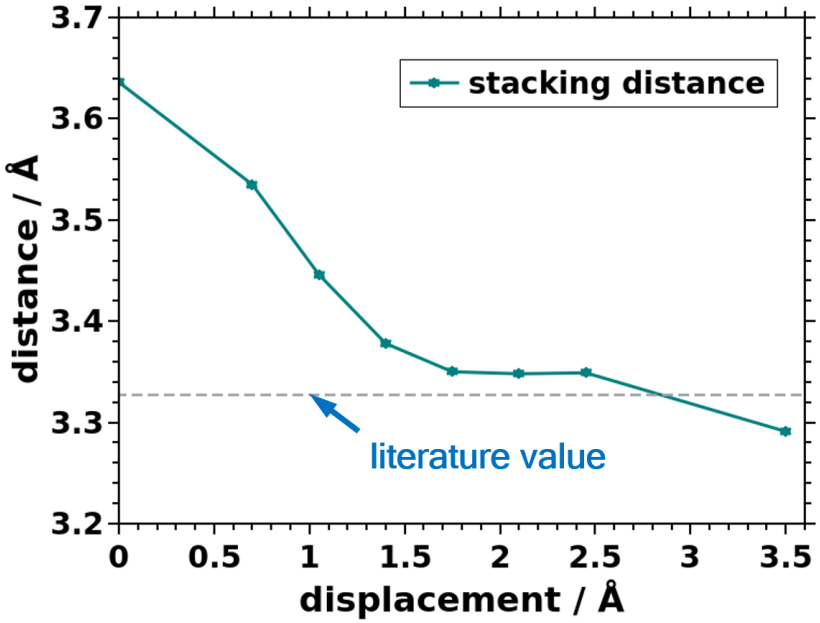

Figure S10. Evolution of the stacking distance for COF-1 as a function of the layer displacement. The literature value shown as a grey dashed line is taken from Ref [10].

2.7 Additional considerations regarding the decomposition scheme

Writing out equation 5 of the main manuscript in explicit terms the following expression describing the interlayer electrostatic interaction energy as a function of nuclear charges Z, electron densities n, nuclear, and electronic coordinates R and r is obtained:

$$\Delta E_{elstat} = \sum_{\nu \epsilon A} \sum_{\mu \epsilon B} \frac{Z_\mu Z_\nu}{|\vec{R}_\mu - \vec{R}_\nu|} - \sum_{\nu \epsilon A} \int \frac{Z_\nu n_B(\vec{r}_i)}{|\vec{R}_\nu - \vec{r}_i|} d\vec{r}_i - \sum_{\mu \epsilon B} \int \frac{Z_\mu n_A(\vec{r}_i)}{|\vec{R}_\mu - \vec{r}_i|} d\vec{r}_i$$

$$+2 \iint \frac{n_A(\vec{r}_i) n_B(\vec{r}_i)}{|\vec{r}_i - \vec{r}_j|} d\vec{r}_i d\vec{r}_j$$

2.8. Comparison of total energy and interaction energy for COF-1

In Figure S11 one can see the evolution of the total energy and that of the interaction energy for COF-1 shifted along direction **1** and with optimized stacking distances for each displacement. Both energies are aligned to their respective values at cofacial arrangement. One can see that these energies essentially evolve in parallel and that only minor numerical differences occur. The reason why these energies do not coincide is that for each displacement the stacking distance, thus the unit cell vector along that direction, changes and so also the energy between fragments A and B, entering the determination of ΔE_{int} is different for each displacement. Nevertheless, two energy curves show a excellent qualitative agreement.

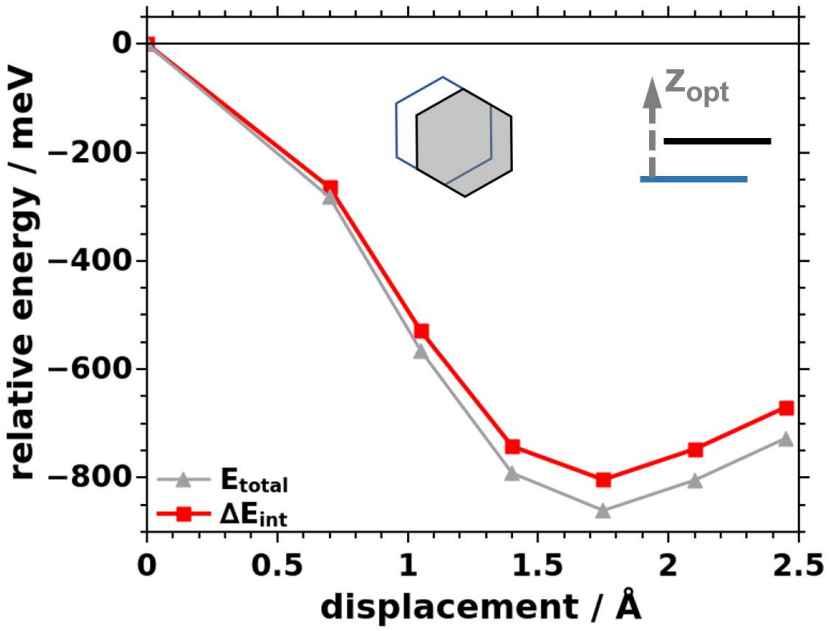

*Figure S11. Comparison of the evolution of the total energy (grey triangles and line) and the interaction energy (red squares and line) for COF-1 shifted along direction **1** and with optimized stacking distances. Energies at cofacial arrangement: ΔE_{int}=-1957 meV, E_{total}=-70443.275 eV;*

REFERENCES

(1) Blum, V.; Gehrke, R.; Hanke, F.; Havu, P.; Havu, V.; Ren, X.; Reuter, K.; Scheffler, M. Ab Initio Molecular Simulations with Numeric Atom-Centered Orbitals. *Comput. Phys. Commun.* **2009**, *180*, 2175–2196.

(2) Macrae, C. F.; Bruno, I. J.; Chisholm, J. A.; Edgington, P. R.; McCabe, P.; Pidcock, E.; Rodriguez-Monge, L.; Taylor, R.; Van De Streek, J.; Wood, P. A. Mercury CSD 2.0 - New Features for the Visualization and Investigation of Crystal Structures. *Journal of Applied Crystallography*, 2008, *41*, 466–470.

(3) Taylor, R.; Macrae, C. F. Rules Governing the Crystal Packing of Mono-and Dialcohols. *Acta Crystallogr. Sect. B Struct. Sci.* **2001**, *57*, 815–827.

(4) Bruno, I. J.; Cole, J. C.; Edgington, P. R.; Kessler, M.; Macrae, C. F.; McCabe, P.; Pearson, J.; Taylor, R. New Software for Searching the Cambridge Structural Database and Visualizing Crystal Structures. *Acta Crystallogr. Sect. B Struct. Sci.* **2002**, *58*, 389–

397.

(5) Macrae, C. F.; Edgington, P. R.; McCabe, P.; Pidcock, E.; Shields, G. P.; Taylor, R.; Towler, M.; Van De Streek, J. Mercury: Visualization and Analysis of Crystal Structures. *Journal of Applied Crystallography*, 2006, *39*, 453–457.

(6) MacRae, C. F.; Sovago, I.; Cottrell, S. J.; Galek, P. T. A.; McCabe, P.; Pidcock, E.; Platings, M.; Shields, G. P.; Stevens, J. S.; Towler, M.; *et al.* Mercury 4.0: From Visualization to Analysis, Design and Prediction. *J. Appl. Crystallogr.* **2020**, *53*, 226–235.

(7) Winkler, C.; Jeindl, A.; Mayer, F.; Hofmann, O. T.; Tonner, R.; Zojer, E. Understanding the Correlation between Electronic Coupling and Energetic Stability of Molecular Crystal Polymorphs: The Instructive Case of Quinacridone. *Chem. Mater.* **2019**, *31*, 7054–7069.

(8) Heyd, J.; Scuseria, G. E.; Ernzerhof, M. Hybrid Functionals Based on a Screened Coulomb Potential. *J. Chem. Phys.* **2003**, *118*, 8207–8215.

(9) Heyd, J.; Scuseria, G. E.; Ernzerhof, M. Erratum: Hybrid Functionals Based on a Screened Coulomb Potential (Journal of Chemical Physics (2003) 118 (8207)). *J. Chem. Phys.* **2006**, *124*, 219906.

(10) Côté, A. P.; Benin, A. I.; Ockwig, N. W.; O'Keeffe, M.; Matzger, A. J.; Yaghi, O. M. Porous, Crystalline, Covalent Organic Frameworks. *Science* **2005**, *310*, 1166–1170.

6. Summary

In this thesis the electronic structure of various molecule-based materials has been modelled using state-of-the-art computational methods. Of particular interest were crystalline organic semiconductors (OSCs), metal-organic frameworks (MOFs), and covalent organic frameworks (COFs). From the electronic structure of these systems, parameters relevant for charge transport were derived and their dependence on the actual intermolecular arrangement was investigated. In the following, we briefly recapitulate the findings of the individual sections of this thesis and connect them to each other.

Let us start by comparing the structures of the investigated systems, shown in Figure 6.1. An important similarity with respect to charge transport within these systems is that in the bulk structures of OSCs, in the studied MOFs, and COFs continous stacks of (relatively) large π-systems are formed. These π-systems either belong to an organic molecule in the case of OSCs, are parts of organic linkers in MOFs, or belong to the conjugated organic building blocks of COFs. Based on the structural similarities, i.e. continuous stacks of π-systems, and assuming that charge transport occurs along these π-stacking pathways one can already suggest that similar transport mechanisms will be important for all the considered materials. Therefore, one can start by revisiting the transport theories of the already quite advanced field of OSCs.

Essential for charge transport is the orbital overlap of neighboring π-systems, as an increased orbital overlap typically results in enlarged intermolecular electronic couplings, i.e. in larger transfer integrals t. These transfer integrals are insofar relevant, as a review of the currently applied transport models for OSCs shows that their amplitude is directly coupled to the charge carrier mobility μ. More precisely, $\mu \propto t^2$ is found for hopping transport while $\mu \propto t$ applies for band transport. These two models represent the edge cases for fully localized states, described by hopping transport, and entirely delocalized states, resulting in band transport. For intermediate cases, where charges are neither fully localized nor entirely delocalized, there is no such clear proportionality between t and the mobility μ. What counts in these situations is the anisotropy of a systems' transfer integrals together with the ratio of thermally induced variations of these transfer integrals and the absolute value of the corresponding t. More details on the individual charge

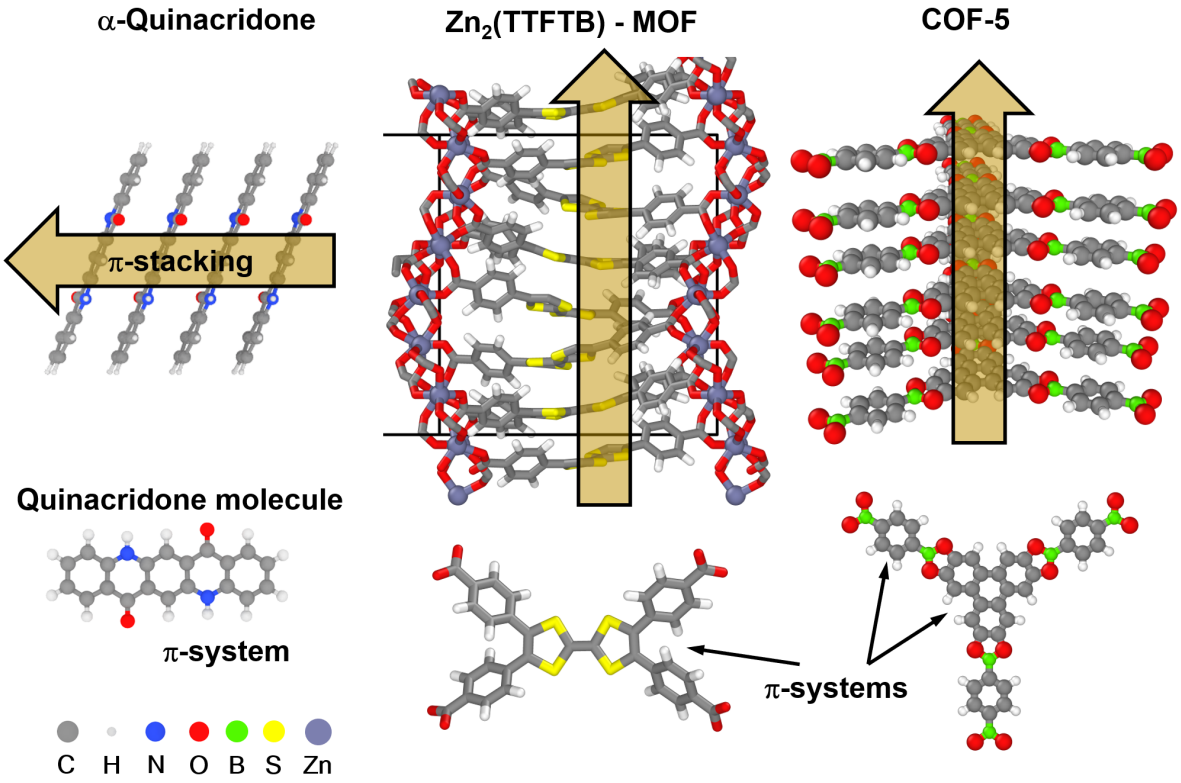

Figure 6.1.: Structure of the considered systems: α-quinacridone (adapted from Ref [2], i.e. Publication I), Zn_2(TTFTB) MOF (adapted from Ref [4], i.e. Publication III), and COF-5 (taken from Publication IV). The arrows indicate the π-stacking direction within the individual materials.

transport mechanisms can be found in the introductory part of this thesis, especially in Section 1.1 and in the cited references. However, these transport models are not restricted to OSCs. Especially band and hopping transport are general concepts which can be directly employed to MOFs and COFs.

As a starting point, the findings that have been obtained for OSCs are reviewed. In these materials, the relative arrangement of neighboring molecules determines the transfer integral and consequently the mobility μ. More precisely speaking, the orbital overlap, which is determined by the symmetry and nodal structure of the involved molecular orbitals, determines the transfer integral. Knowing that transfer integrals are essential quantities for analyzing charge transport one has to consider how one can get a reliable description of these parameters for periodic systems. Therefore, in ***Publication I***, the electronic band structure of a representative organic semiconductor, α-quinacridone, was analyzed. In essence, three approaches were compared to each other: The first one relies solely on bandwidths along certain directions extracted from the electronic band structure. The second one is based on the extraction of molecular dimers from the periodic systems

and calculating the electronic coupling for these dimers using the energy splitting in dimer (ESD) method.[21] The use of this method is justified by the molecules constituting the considered molecular dimers being symmetry equivalent. For dimers where the molecules are actually symmetry inequivalent more advanced methods have to be employed as the ESD method would not account for differences in site-energies that arise from the molecules polarizing each other differently.[173] Finally, the third approach is based on fitting a tight-binding model to the electronic band structure. This tight-binding model is based on the expression for the energy which has been derived for one molecule per cell (Section 1.4.2) and contributions from all nearest neighbors have been included.

Employing these three approaches to the chosen test system, one observes that each approach has its problems and thus, can be quite misleading. Merely relying on extracted bandwidths would be a reliable approach for very simple electronic band structures only. Simple, means that only transfer integrals between neighboring molecules along a direction parallel to the $\boldsymbol{k}$-path of the respective electronic band determine the evolution, i.e. the width, of this band. One example where the electronic band is too complex for the bandwidth approach is shown in Figure 6.2a. There, one can see the conduction band along a $\boldsymbol{k}$-path parallel to the H-bonding direction. After succesfully fitting a tight-binding function, which includes contributions from all nearest neighbors, to the conduction band, one can decompose the band into individual contributions. Based on these contributions one finds that actually the transfer integral along direction $\boldsymbol{a}_2$ dominates the conduction band along the direction parallel to $\boldsymbol{a}_1 + \boldsymbol{a}_2$. As a result, if one estimated the transfer integral between neighboring molecules along $\boldsymbol{a}_1 + \boldsymbol{a}_2$ by employing a one-dimensional tight-binding model to the band along $\boldsymbol{a}_1 + \boldsymbol{a}_2$, one would severly overestimate this transfer integral. This simple bandwidth approach would yield 25 meV for the transfer integral, while from the elaborate tight binding approach we find a transfer integral of -5 meV. Furthermore, also situations where couplings between next-nearest neighbors become important are neither covered by the dimer nor the bandwidth approach - see Figure 6.2b. Importantly, it turned out that, at least for systems with one molecule per unit cell, fitting elaborate tight-binding model functions to the electronic band structure is a viable strategy. Another nice aspect of this approach is that the fitted tight-binding band structure provides an analytic expression for the electronic bands. Based on this expression quantities like the effective mass tensor can be calculated in a straightforward and computationally (almost) effortless manner. Based on this tensor the effective mass along any spatial direction can be evaluated and the anisotropy of the material can be studied.

The findings of ***Publication I*** provide a set of tools which can then be employed to study transfer integrals within molecule-based materials in a reliable manner. Moreover,

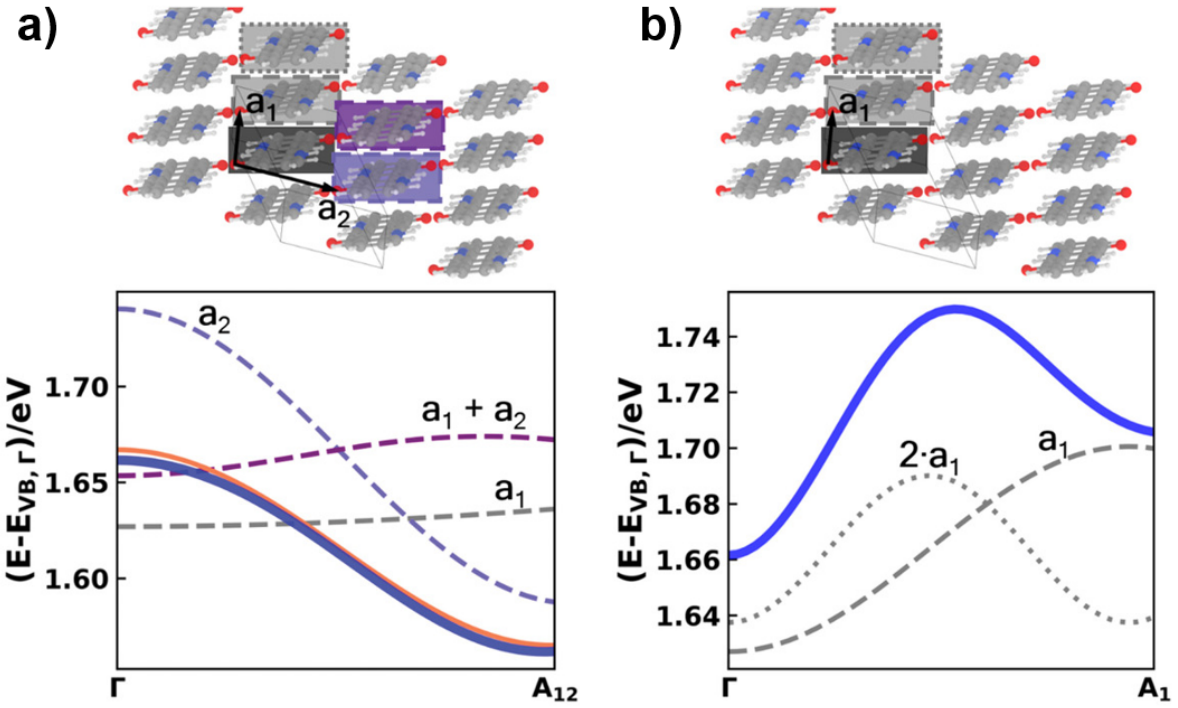

Figure 6.2.: Conduction band and main components of the tight-binding model for two $\boldsymbol{k}$-paths parallel to a) the H-bonding direction and b) the π-stacking direction. The DFT bands are shown as solid blue lines, the contributions from individual tight-binding components as dashed lines and the sum of these components is shown as an orange line in a). Adapted from Publication I, i.e. Ref [2].

Publication I provides the limitations of the considered approaches. Based on these limitations and upon a first inspection of the electronic band structure of the materials of interest one can decide which approach might be employed. Furthermore, one has to consider that for systems with two or more inequivalent molecules per unit cell also the tight-binding approach shall be used with caution, as mentioned briefly in the introduction section. Although it is appealing to get the transfer integrals directly from the electronic band structure by using elaborate tight-binding models, sometimes the simpler approaches might already be sufficient. Potentially, a combination of the various approaches, based on the electronic band structure or based on molecular dimers, might be the best solution to gain a decent understanding of the electronic couplings / transfer integrals in organic semiconductor crystals.

With this set of methods at hand one can go ahead and study the interplay between the energetic stability of certain structural (molecular) arrangements and charge transport properties for organic semiconductor crystals. This is done in ***Publication II***. For this investigation we relied on the three established polymorphs of quinacridone together with

an orthorhombic model crystal inspired by the packing motif of α-quinacridone. Upon displacing the two quinacridone molecules present in the unit cell relative each other, calculating transport relevant parameters as well as total and interaction energies, and decomposing the interaction energies into physically well-defined contributions, several important aspects were found: First of all, the evolution of the bandwidth and that of the transfer integral relevant for charge transport in π-stacking direction coincide. Therefore, we could rely on the bandwidth as a qualitative descriptor for the transport properties. Secondly, evaluating two-dimensional maps of the total energy and the valence-bandwidth, as shown in Figure 6.3, revealed that molecular arrangements with large bandwidths are energetically unfavorable. This suggested the existence of a general driving force which pushes the molecular crystals towards arrangements with smaller bandwidths, i.e. lower transfer integrals. The physical origin of this driving force was studied by decomposing the interaction energy between consecutive quinacridone layers. This decomposition revealed that Pauli repulsion and orbital rehybridization destabilize molecular arrangements with large transfer integrals. As a consequence, for realizing high-mobility materials one cannot simply rely on the intrinsic interactions that govern the self-assembly of π-conjugated backbones. Rather, one should attempt to introduce additional energy terms, e.g. steric effects, which can help to overcome the driving force towards low transfer integral arrangements. At this point, MOFs become interesting, as they offer a fine control over their structural arrangement which is hard to achieve in OSCs. This higher level of control allows to exploit combining linkers and nodes with known geometry and coordination environments as a strategy for designing MOFs with specific structures, i.e. structural arrangements.[45,50,51] Enforcing a certain arrangement of the organic linkers π-systems could, therefore, be employed to engineer the charge transport properties of MOFs.

Thus, in ***Publication III***, the interplay between structural arrangement and charge transport properties was investigated for a prototypical MOF, Zn_2(TTFTB= tetrathiafulvalene tetrabenzoate). This system exhibits a comparably large bandwidth of around 370 meV which is dominated by contributions from the π-system of the organic linker (see Figure 6.1). As a starting point, it was demonstrated that the valence band structure can be safely described by a stack of the central tetrathiafulvalene (TTF) part of the linker, see Figure 6.4a. This is a quite important observation, as it allows the transfer of all the insights from Publications I and II directly to this MOF system. Based on the TTF model stack, several degress of freedom were explored in order to study the effect of structural arrangements on the valence bandwidth and, consequently, the transfer integral. It turned out that reducing the rotation angle between neighboring TTF units increases the valence bandwidth significantly, as shown in Figure 6.4c. Additionally, it

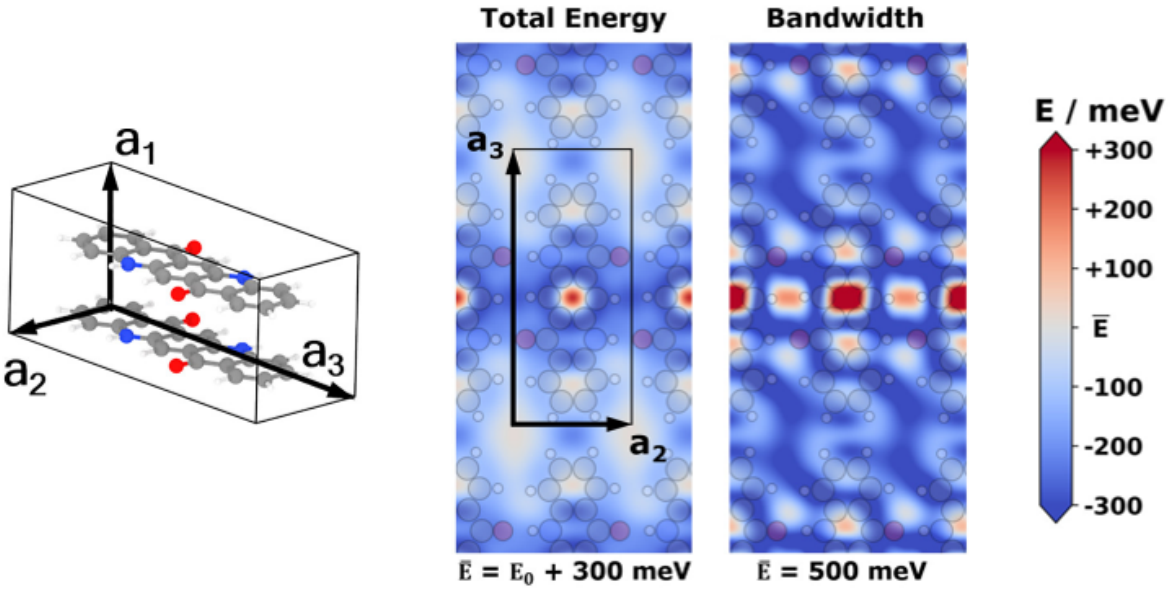

Figure 6.3.: Structure of the orthorhombic quinacridone model crystal as well as two-dimensional maps showing the total energy and the valence bandwidth as a function of interlayer displacements. Adapted with permission from Ref [3]. Copyright 2019 American Chemical Society.

was found that the impact of changes in the relative rotation and molecular conformation of the TTF molecules on the observed bandwidth is more pronounced than the impact of moderate modifications in the stacking distance[4] - see Figure 6.4d. Experimentally, such modifications to the stacking distance have been investigated by replacing the Zn atoms in the metal nodes of the MOFs with Cd atoms.[100] As the associated structural changes only show moderate effects, we hypothesize in ***Publication III*** that the increase of the electrical conductivity by two-orders of magnitude for Cd_2(TTFTB) compared to Zn_2(TTFTB)[100] must either be caused by significantly modified concentrations of mobile carriers or must be a consequence of different defect densities in the two systems. For unraveling such discrepancies it would be essential to know the charge carrier mobilities of Cd_2(TTFTB) and Zn_2(TTFTB). Therefore, we highly encourage experimentalists to measure and report the charge carrier mobilities of their samples, as is commonly done in the field of OSCs. In combination with theory this will allow us to gain a deeper and more fundamental understanding of charge transport in MOFs.

Furthermore, also the influence of defects on charge-transport relevant quantities was investigated in ***Publication III***. The impact of most static defects that were considered (displaced molecules, molecular pairing along the stack, or misrotations of specific molecules) turned out to be rather moderate. This changes, for the case of a missing linker defect (electronic band structure in Figure 6.4b). Because of the 1D nature of

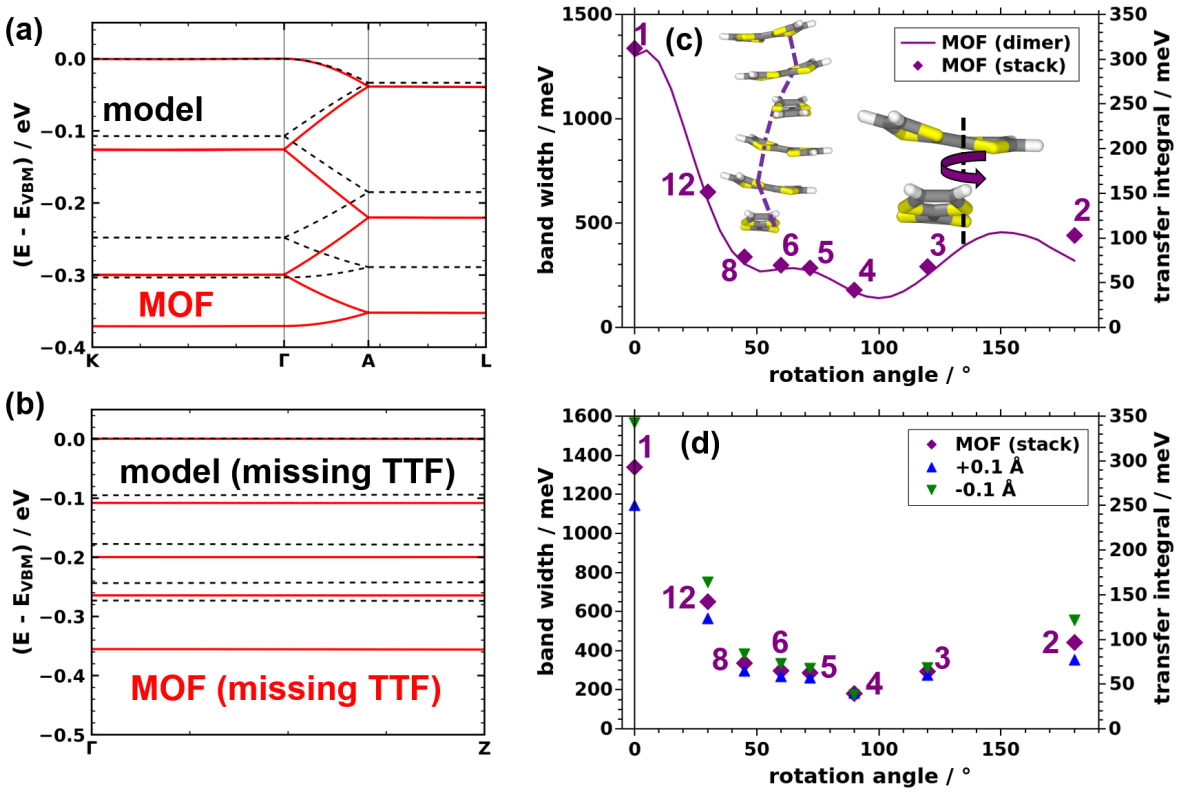

Figure 6.4.: Electronic structure of Zn_2(TTFTB) MOF and corresponding model stacks. (a) Valence band structure of the MOF (in red) and the TTF model stack (black dashed). (b) Valence band of MOF and model stack, each with a missing linker defect. (c) Valence bandwidth and transfer integral as a function of the rotation angle between consecutive TTF molecules. (d) Valence bandwidth and transfer integral depending on the rotation angle and on the intermolecular displacement. Adapted from Ref [4].

the transport pathways of the investigated systems, such a missing linker constitutes a massive obstacle for charge transport, which is manifested, for example, by a factor of 10 increase of the effective mass. Summarizing these findings, it was observed that engineering the arrangement of organic linkers in MOFs can yield improved charge-transport properties. Furthermore, it was found that these properties are highly sensitive to structural imperfections in MOFs, i.e. defects. As a result, experimentally observed trends might be severly impacted by variations of the defect densities present in the investigated MOFs.

For the above MOFs with fairly complex structural arrangements (see Figure 6.1) several handles for tuning their charge-transport properties have been identified. However, it might not be straightforward to exploit these handles experimentally. Especially decreasing the rotation angle between the TTF molecules (i.e. increasing the number of

TTF molecules in the unit cell), which appeared to be the most effective tuning handle seems challenging. Thus, it would be helpful to have systems which possess only a few degrees of freedom, that need to be controlled. Furthermore, these degrees of freedom should be more easily accessible. Layered MOFs and especially COFs represent such systems with few degrees of freedom. Lateral and vertical displacements of individual layers are the (most important) degrees of freedom that can be exploited to tune the bandwidths. Relative rotations of certain segments around their respective short and long molecular axes as well as changes in their conformation are essentially blocked. This, together with the large π-conjugated parts usually present in COFs, renders these systems interesting for producing porous, electrically conductive materials. Again one can build on knowledge that has been obtained for OSCs and apply it to COFs: lateral and vertical displacements of stacked molecules have been shown to severly impact the corresponding transfer integrals. In fact, changes by orders of magnitude for displacements of around 1 Å are not rare in typical OSCs.[3,32–35] Therefore, it is of utter importance to understand the interactions that determine the interlayer arrangement of COFs. This understanding is an essential prerequisite for the design of structures exhibiting the desired interlayer arrangement. In ***Publication IV*** the interaction energy of layered COFs was investigated as a function of the interlayer arrangement. Furthermore, this energy was decomposed into van der Waals, electrostatic, and Pauli repulsion plus orbital rehybridization contributions, by a newly implemented energy decomposition scheme.

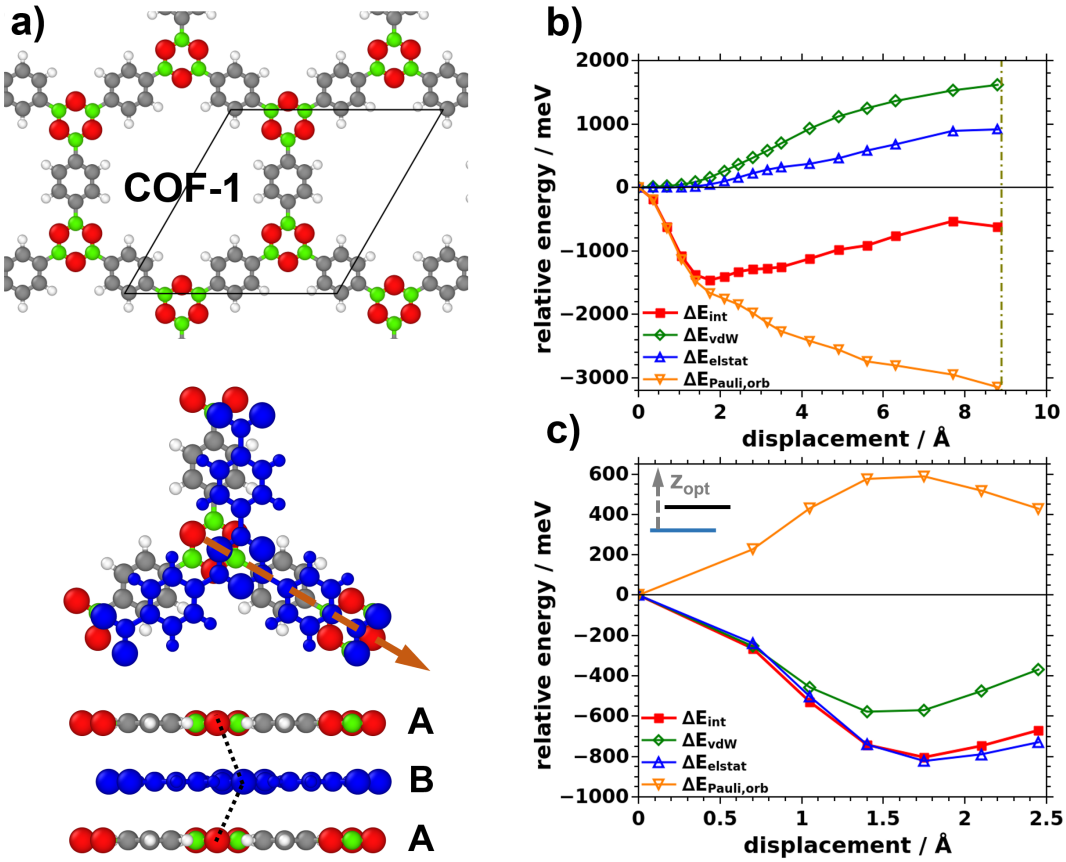

Figure 6.5.: Structure and relative energies of COF-1. a) Structure of a single COF-1 layer is shown in the top panel. The bottom panel shows a cutout of the periodic (bulk) structure of COF-1. Two layers are present in the unit cell in stacking direction and the layer marked in blue is displaced along the direction indicated by the arrow. As a result one obtains an $(AB)_n$ sequence of layers as indicated. Atoms are shown in: C ... grey, H ... white, B ... green, O ... red. b) The relative energies, interaction energy ΔE_{int}, vdW ΔE_{vdW}, electrostatic ΔE_{elstat}, and Pauli repulsion with orbital rehybridization energy $\Delta E_{Pauli,orb}$ are shown as a function of the interlayer displacement and aligned to their respective values at cofacial arrangement. The stacking distance was held constant for all displacemets. c) The relative energies as a function of the interlayer displacement where for each displacement the stacking distance has been optimized are shown.

Several important findings were obtained by performing such an investigation on exemplary test systems. First of all, the preferred layer arrangement is a shifted AA-stacking. In all the investigated COFs, it turned out that a displacement of consecutive COF layers by around 1.5 Å, along a vector parallel to the plane of the COF layers, resulted in a layer arrangement which is significantly more stable than cofacial AA-stacking. Furthermore, considering the example of COF-1 (shown in Figure 6.5), a rather deep local minimum in the total energy was found for moderate displacements of around 1.5 Å, i.e. the total energy of the displaced arrangement is around 0.8 eV lower. Important to note is that

such moderate displacements are typically not resolved in experiment due to the large peak broadening observed in the x-ray pattern.[137,174]

Nevertheless, already these moderate displacements change the electronic properties quite dramatically, as demostrated by a reduction of the valence bandwidth and an increase of the corresponding effective mass for COF-1 studied in ***Publication IV***. This further highlights the necessity of being able to control the interlayer arrangement effectively in order to tune the properties of layered COFs. Studying the individual contributions to the interaction energy (shown in Figure 6.5b) it was found that for constant interlayer stacking distances the repulsive contributions from the term comprising Pauli repulsion with orbital rehybridization lead to the formation of the energetic minimum for the shifted layer arrangement. On the contrary, when optimizing the interlayer stacking distance it was found that attractive van der Waals and electrostatic interactions favor shifted arrangements, while Pauli repulsion with orbital rehybridization would be favorable for cofacial arrangements. As van der Waals and electrostatic interactions dominate, shifted layer arrangements are again energetically favorable. Actually, this is in contrast to the findings for OSCs in ***Publication II***. This might be partially due to the stacking distance kept constant in the investigations in ***Publication II***, while it was optimized for the COFs in ***Publication IV***. How optimizing the stacking distance influences the interplay of the individual energy components in OSCs is certainly an aspect that has to be investigated in future studies, as it can be seen that, at least for the examples of COF-1 and COF-5, optimizing the stacking distance significantly alters the relative energy contributions. As a little side note, the importance of charge penetration effects, well-known for OSCs, is also highlighted in ***Publication IV***. This implies that simple electrostatic arguments, which have been used for rationalizing the interlayer arrangement in the past, are not applicable for layered COFs and that a more detailed analysis of the different contributions is crucial for achieving a thorough understanding of the driving forces that determine the structures of layered COFs.

In summary, in the course of this PhD thesis, quantum mechanical computer simulations were used to study organic and hybrid nanomaterials. Several approaches for obtaining a reliable description of transfer integrals in crystalline systems were tested, while also the srengths and weaknesses of each approach have been assessed. Further, combining electronic structure calculations with energy decomposition schemes for periodic systems, the existence of a driving force pushing organic semiconductor crystals towards molecular arrangements with low intermolecular electronic couplings was demonstrated. For metal organic frameworks the influence of the structural changes of the π-systems on the electronic band structure were investigated. In this context several tuning strategies for enhancing bandwidths and transfer integrals were identified. Additionally, the importance

of understanding the influence of defects on the electronic band structure of MOFs has been highlighted. Finally, an energy decomposition scheme was developed and used to understand the details of the formation of shifted layer arrangements in covalent organic frameworks.

Appendix

Appendix A.

Energy Decomposition Scheme for Periodic Systems

A.1. Validation of the Energy Decomposition Scheme

An energy decomposition scheme based on the pEDA scheme[140,168,172] has been implemented to work with FHI-Aims and in order to test its validity, we re-calculated the model system of ***Publication II*** and compared the results obtained with the original pEDA scheme and my own scheme.

The results for FHI-aims have been obtained employing a 4x2x4 $\boldsymbol{k}$-point grid together with a *tight* full tier2 basis set for all atomic species. Furthermore, a radial multiplier of 2 was used.

Comparing the interaction energies for the reference data to the FHI-aims calculations one can see in Figure A.1 that both data sets show good agreement. When calculating the average deviation of the FHI-aims calculatios from the reference data one finds that the interaction energy ΔE_{int} is overestimated by 19 meV in our calculations. When we exclude the outlier at a displacement of 6.72 Å we find that the interaction energy is still overestimated by an average value of 13 meV. To check whether the data for a displacement of 6.72 Å can really be classified as an outlier, an additional data point for a slightly smaller displacemet of 6.68 Å has been calculated. We find that ΔE_{int} for this point agrees very well with the reference data at the slightly larger displacement. Thus, the FHI-aims data for 6.72 Å can be classified as an outlier. The reason for the apparent deviation is not entirely clear at the moment, but is likely of numerical origin.

As a next step, the values of the electrostatic part of the interaction energy (ΔE_{elstat}) are compared to the reference data (Figure A.2). In terms of absolute values we find that

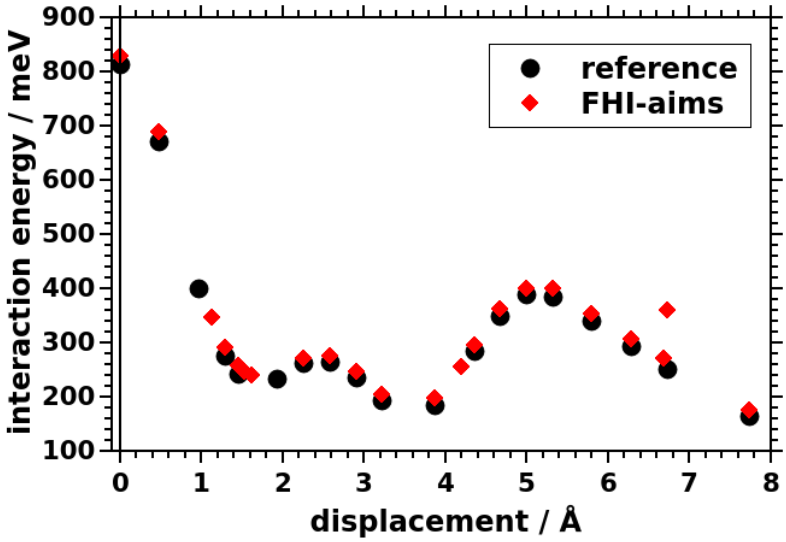

Figure A.1.: Comparison of the total interaction energy evaluated by performing DFT calculations on 4x2x4 k-grid with a full tier2 basis set (red) and the data from Publication II (black).

ΔE_{elstat} is overestimated with respect to the reference by 21 meV (23 meV) including (excluding) the outlier of the interaction energy at 6.72 Å. Note that the deviation is larger when excluding the outlier, as the sign of that deviation is different - meaning for this point, unlike fo all other points, ΔE_{elstat} is actually underestimated in my decomposition scheme. Again when considering the calculated data for a slightly smaller displacement we find that it follows a trend consistent with all other data points, further supporting the notion that the data at 6.72 Å is an outlier. Now, plotting the calculated data as a function of the reference data one can again have a look at the correlation of the two data sets - shown in Figure A.3. There, one can nicely see that only one point, as already mentioned, does not follow the trend and underestimates the electrostatic part of the interaction energy. When fitting a straight line to the presented data (inlcuding the outlier) one finds that this line (shown as a red dash dotted line in Figure A.3) has a slope of 0.92 and an intercept of -79.2 meV. Upon classifying the data point at 6.72 Å as an outlier, exlcuding it from the data set, and fitting a straight line to these data one gets a slope of 1.01 and an intercept of -13.2 meV.

Regarding a correlation one can say that whenever reference data and test data show perfect agreement, all data points must lie on the 45-degree diagonal. Now, when the relative evolutions of the data points agree, but with a (almost) constant offset, as is the case for the electrostatic energy, the data lies on a straight line parallel to the 45-degree diagonal. Or in other words, a straight line fitted to data must exhibit a slope of 1.

Excluding the outlier for the electrostatic data now leads to a slope that is very close to 1, which means that our implemented approach is able to reproduce the relative evolution of the reference data with only very minor deviations. These deviations could be due to the different treatment of the core electrons, in the reference the frozen core approximation was employed while in FHI-aims the core electrons were treated explicitly.

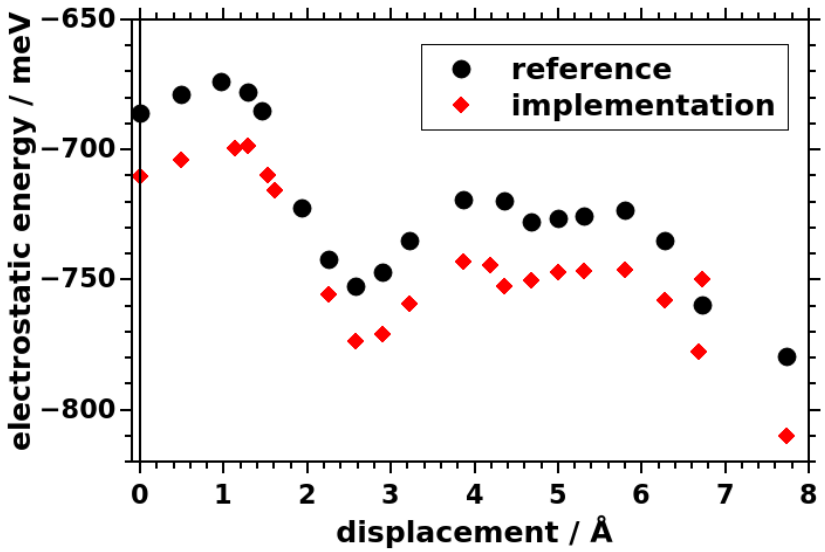

Figure A.2.: Comparison of the electrostatic energy evaluated by performing DFT calculations on 4x2x4 k-grid with a full tier2 basis set and the data from Ref [3].

As a next step, we consider the electrostatic part of the interaction energy ΔE_{elstat} aligned to its value at 0.0 Å displacement and the reference data also aligned to its value at 0.0 Å displacement and compare these data. In Figure A.4 one can see that the evolution of ΔE_{elstat} for the implementation and the reference agree well. For most points the deviations of these data are well below 10 meV.

Considering the aligned data in a correlation plot, as shown in figure A.5 one can see that most data points scatter around a straight line with a slope equal to 1 and that their deviation from this line is usually less than 10 meV. When fitting a straight line to the data, excluding the outlier, we get a slope of 1.01 and an intercept of 1.2 meV. Including the outlier, the slope drops to 0.92 and the intercept also changes to -0.6 meV. Similar to the data which has not been aligned to the zero displacement values we find that the calculated electrostatic part (ΔE_{elstat}) of the total interaction energy agrees well with the reference data, which can be concluded from the various comparisons provided before and also the slope of the linear fit curve being almost equal to 1. Therefore,

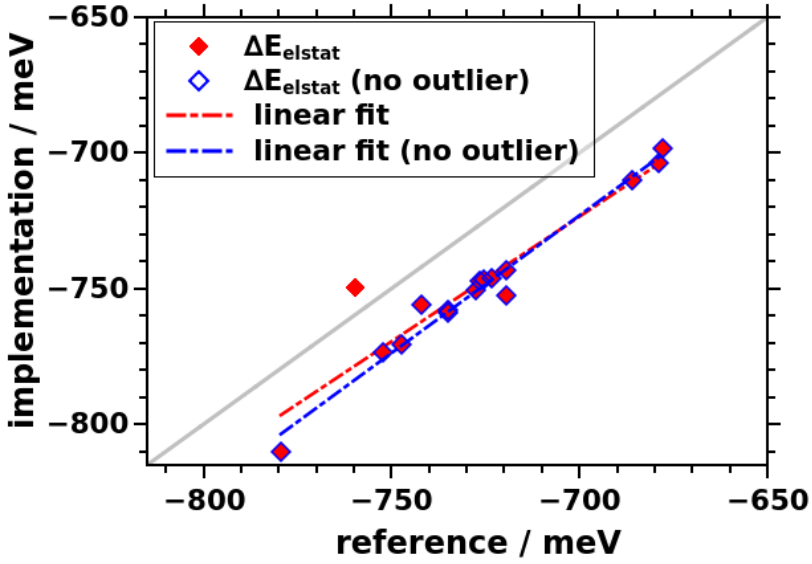

Figure A.3.: Correlation plot between the interaction energy obtained from the FHI-aims calculations with a full tier2 basis set and the reference data from Ref [3]. The data has been fitted by a straight line as $y = A + B * x$ with A=-13.2 (-79.2) meV and B=1.01 (0.92) excluding (inlcuding) the outlier at 6.72 Å.

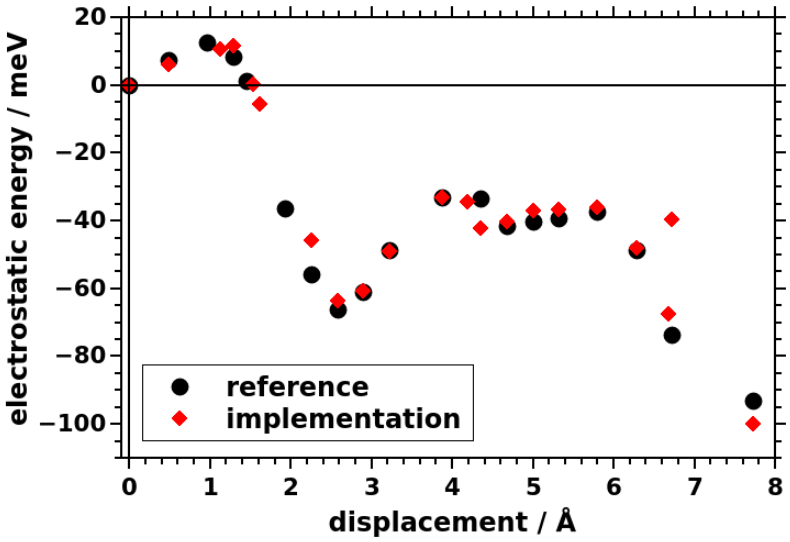

Figure A.4.: Comparison of the electrostatic energy evaluated by performing DFT calculations on 4x2x4 k-grid with a full tier2 basis set and the data from Ref [3]. Both data sets are aligned to their respective values at 0.0 Å displacement

we conclude that the relative evolution of ΔE_{elstat} is evaluated correctly and that our approach works. Minor quantitative deviations of around 3% of the reference energy might be due to the variations in the basis sets that have been used. In our approach all electrons, inlcuding the core electrons, are considered explicitly. For the reference data the frozen core approximation has been employed.

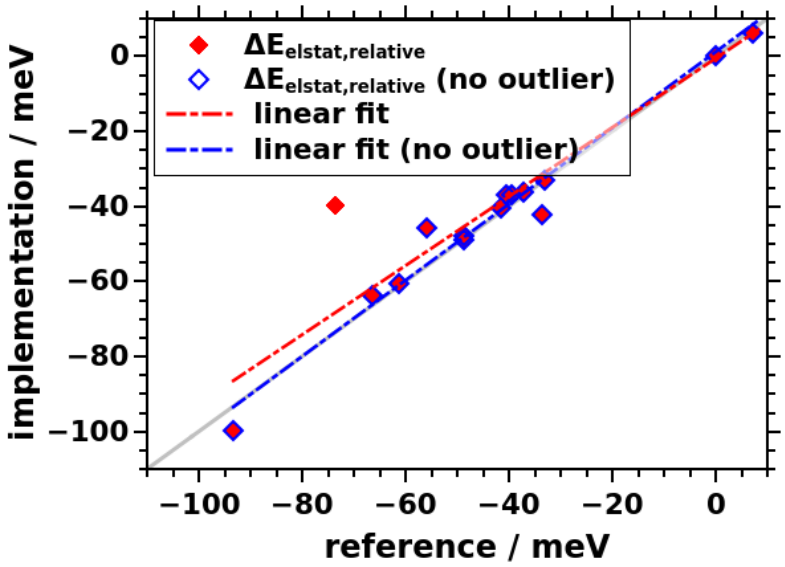

Figure A.5.: Correlation plot between the interaction energy obtained from the FHI-aims calculations with a full tier2 basis set and the reference data from Ref [3]. Both data sets are aligned to their respective values at 0.0 Ådisplacement. The data have been fitted by a straight line as $y = A + B * x$ with A=1.2 (-0.6) meV and B=1.01 (0.92) excluding (inlcuding) the outlier at 6.72 Å.

A.2. Further Methodological and Technical Details

In this section we would like to elaborate a bit more on some details of the decomposition and the determination of the individual terms.
Let us start from the coefficient matrix $\mathbb{C}_{\{AB\}}(\boldsymbol{k})$ that has been constructed based on the eigenvectors of the isolated fragments. Technically, this matrix is constructed by grouping the eigenvectors of the fragments as shown in equation A.1.

$$\mathbb{C}_{\{AB\}}(\boldsymbol{k}) = \begin{bmatrix} \mathbb{C}_{A,occ}(\boldsymbol{k}) & 0 \\ 0 & \mathbb{C}_{B,occ}(\boldsymbol{k}) \\ \mathbb{C}_{A,virt}(\boldsymbol{k}) & 0 \\ 0 & \mathbb{C}_{B,virt}(\boldsymbol{k}) \end{bmatrix} \tag{A.1}$$

Each row of this matrix corresponds to a specific state l and the columns correspond to the individual basis functions. The constructed coefficient matrix $\mathbb{C}_{\{AB\}}(\boldsymbol{k})$ is then written to restart files for FHI-aims together with the occupation vector (see 1.62). From these restart files a single shot DFT calculation without performing an scf cycle is started. To trigger the calculation of the electrostatic energy for the electron density corresponding to the eigenvectors that are supplied in the restart, one has to specify a few keywords:

```
mixer linear
charge_mix_param 0
preconditioner kerker off
```

The preconditioner is turned off and the charge densiting mixing procedure is set to a linear mixer with a mixing parameter of 0. The detailed meaning and consequences associated with these keywords are discussed in a subsequent section and can also be found in Ref [141]. Here we will continue to show that the constructed coefficient matrix $\mathbb{C}_{\{AB\}}(\boldsymbol{k})$ indeed yields the electrostatic energy between the fragments A and B.

From the restarted DFT calculation one obtains the total energy as well as the electrostatic energy $E_{elstat}^{\{AB\}}$ of system $\mathbb{C}_{\{AB\}}(\boldsymbol{k})$. Following the decomposition scheme, the electrostatic contribution to the interaction energy of the system AB can then be obtained according to equation A.2. All energy terms needed for this evaluation can be taken from the output of the respective DFT calculations.

$$\Delta E_{elstat} = E_{elstat}^{\{AB\}} - (E_{elstat}^{A} + E_{elstat}^{B}) \tag{A.2}$$

In the following we demonstrate that the relation shown in equation A.2 is valid, i.e. that restarting from coefficient matrix $\mathbb{C}_{\{AB\}}$ and then subtracting the electrostatic energies of the fragments from the one corresponding to $\mathbb{C}_{\{AB\}}$ actually yields the electrostatic energy term shown in equation 1.63. To do so, we consider the electrostatic energy terms for the individual fragments and the combined system $\mathbb{C}_{\{AB\}}$.

Let us start by considering fragment A:

$$E^A_{elstat} = \frac{1}{2}\sum_{\nu\epsilon A}\sum_{\mu\epsilon A}\frac{Z_\mu Z_\nu}{|\boldsymbol{R}_\mu - \boldsymbol{R}_\nu|} - \sum_{\nu\epsilon A}\int\frac{Z_\nu n_A(\boldsymbol{r}_i)}{|\boldsymbol{R}_\nu - \boldsymbol{r}_i|}d\boldsymbol{r}_i + \frac{1}{2}\int\int\frac{n_A(\boldsymbol{r}_i)n_A(\boldsymbol{r}_j)}{|\boldsymbol{r}_i - \boldsymbol{r}_j|}d\boldsymbol{r}_i d\boldsymbol{r}_j \quad \text{(A.3)}$$

An analogous expression for fragment B reads as follows:

$$E^B_{elstat} = \frac{1}{2}\sum_{\nu\epsilon B}\sum_{\mu\epsilon B}\frac{Z_\mu Z_\nu}{|\boldsymbol{R}_\mu - \boldsymbol{R}_\nu|} - \sum_{\nu\epsilon B}\int\frac{Z_\nu n_B(\boldsymbol{r}_i)}{|\boldsymbol{R}_\nu - \boldsymbol{r}_i|}d\boldsymbol{r}_i + \frac{1}{2}\int\int\frac{n_B(\boldsymbol{r}_i)n_B(\boldsymbol{r}_j)}{|\boldsymbol{r}_i - \boldsymbol{r}_j|}d\boldsymbol{r}_i d\boldsymbol{r}_j \quad \text{(A.4)}$$

From equation A.5 it becomes apparent that the electron density n_{AB} corresponding to the combined system $\mathbb{C}_{\{AB\}}$ can simply be written as the sum $n_A + n_B$ of the charge densities of the fragments.

$$n(\boldsymbol{r}) = \sum_l\sum_{\boldsymbol{k}} f_{l,\boldsymbol{k}}\left|\Psi_{l,\boldsymbol{k}}(\boldsymbol{r})\right|^2 = \sum_l\sum_{\boldsymbol{k}} f_{l,\boldsymbol{k}}\left(\sum_i\sum_j c^*_{li}(\boldsymbol{k})c_{lj}(\boldsymbol{k})\ \chi^*_{i,\boldsymbol{k}}(\boldsymbol{r})\chi_{j,\boldsymbol{k}}(\boldsymbol{r})\right) \quad \text{(A.5)}$$

Here $\chi_{i,\boldsymbol{k}}(\boldsymbol{r})$ are defined in terms of the atom-centered basis functions $\phi_i(\boldsymbol{r})$ as:

$$\chi_{i,\boldsymbol{k}}(\boldsymbol{r}) = \sum_m e^{i\boldsymbol{k}\boldsymbol{T}_m}\phi^{at}_i(\boldsymbol{r} - \boldsymbol{T}_m). \quad \text{(A.6)}$$

Based on the finding that the electron density of $\mathbb{C}_{\{AB\}}$ can be written as the sum $n_A + n_B$, the electrostatic energy for the combined system $\mathbb{C}_{\{AB\}}$ can be written in explicit form as:

$$E_{elstat}^{\{AB\}} = \frac{1}{2}\sum_{\nu\epsilon A\cup B}\sum_{\mu\epsilon A\cup B}\frac{Z_\mu Z_\nu}{|\boldsymbol{R}_\mu - \boldsymbol{R}_\nu|} - \sum_{\nu\epsilon A\cup B}\int\frac{Z_\nu(n_A(\boldsymbol{r}_i)+n_B(\boldsymbol{r}_i))}{|\boldsymbol{R}_\nu - \boldsymbol{r}_i|}d\boldsymbol{r}_i + \frac{1}{2}\int\int\frac{(n_A(\boldsymbol{r}_i)+n_B(\boldsymbol{r}_i))(n_A(\boldsymbol{r}_j)+n_B(\boldsymbol{r}_j))}{|\boldsymbol{r}_i - \boldsymbol{r}_j|}d\boldsymbol{r}_i d\boldsymbol{r}_j. \tag{A.7}$$

Using the expressions for the electrostatic energies of the fragments and the combined system, one can evaluate equation A.2:

$$\begin{aligned}\Delta E_{elstat} &= E_{elstat}^{\{AB\}} - (E_{elstat}^{A} + E_{elstat}^{B}) \\ &= \cancel{\frac{1}{2}\sum_{\nu\epsilon A}\sum_{\mu\epsilon A}\frac{Z_\mu Z_\nu}{|\boldsymbol{R}_\mu - \boldsymbol{R}_\nu|}} + \cancel{\frac{1}{2}\sum_{\nu\epsilon B}\sum_{\mu\epsilon B}\frac{Z_\mu Z_\nu}{|\boldsymbol{R}_\mu - \boldsymbol{R}_\nu|}} \\ &\quad + \sum_{\nu\epsilon A}\sum_{\mu\epsilon B}\frac{Z_\mu Z_\nu}{|\boldsymbol{R}_\mu - \boldsymbol{R}_\nu|} \\ &\quad - \sum_{\nu\epsilon A}\int\frac{Z_\nu(\cancel{n_A(\boldsymbol{r}_i)} + n_B(\boldsymbol{r}_i))}{|\boldsymbol{R}_\nu - \boldsymbol{r}_i|}d\boldsymbol{r}_i - \sum_{\nu\epsilon B}\int\frac{Z_\nu(n_A(\boldsymbol{r}_i) + \cancel{n_B(\boldsymbol{r}_i)})}{|\boldsymbol{R}_\nu - \boldsymbol{r}_i|}d\boldsymbol{r}_i \\ &\quad + \int\int\frac{\cancel{n_A(\boldsymbol{r}_i)n_A(\boldsymbol{r}_j)} + n_A(\boldsymbol{r}_i)n_B(\boldsymbol{r}_j) + n_B(\boldsymbol{r}_i)n_A(\boldsymbol{r}_j) + \cancel{n_B(\boldsymbol{r}_i)n_B(\boldsymbol{r}_j)}}{|\boldsymbol{r}_i - \boldsymbol{r}_j|}d\boldsymbol{r}_i d\boldsymbol{r}_j\end{aligned}$$

This finally yields the expression for the electrostatic contribution to the total interaction energy presented in equation 1.63 in Section 1.4.3 as:

$$\Delta E_{elstat} = \sum_{\nu\epsilon A}\sum_{\mu\epsilon B}\frac{Z_\mu Z_\nu}{|\boldsymbol{R}_\mu - \boldsymbol{R}_\nu|} - \sum_{\nu\epsilon A}\int\frac{Z_\nu n_B(\boldsymbol{r}_i)}{|\boldsymbol{R}_\nu - \boldsymbol{r}_i|}d\boldsymbol{r}_i - \sum_{\nu\epsilon B}\int\frac{Z_\nu n_A(\boldsymbol{r}_i)}{|\boldsymbol{R}_\nu - \boldsymbol{r}_i|}d\boldsymbol{r}_i + 2\int\int\frac{n_A(\boldsymbol{r}_i)n_B(\boldsymbol{r}_j)}{|\boldsymbol{r}_i - \boldsymbol{r}_j|}d\boldsymbol{r}_i d\boldsymbol{r}_j \tag{A.8}$$

Problems Associated with the Kinetic Energy

In this section the complications that we are facing for implementing the second stage of the decomposition scheme are outlined. That second stage would be the determination of the Pauli repulsion and the orbital rehybridization terms. As a starting, it is reviewed how the total energy is determined within FHI-Aims.[141]

Let us start by considering the Kohn-Sham functional, which defines the total energy in DFT as

$$E_{KS}[n] = T_S[n] + \int d\boldsymbol{r} V_{ext}(\boldsymbol{r}) n(\boldsymbol{r}) + E_{Hartree}[n] + E_{xc}[n] + E_{II}. \tag{A.9}$$

with $T_s[n]$ the Kohn-Sham kinetic energy, the external potential energy $V_{ext}(\boldsymbol{r})$, the classical electrostatic energy of the electron density $E_{Hartree}[n]$, the exchange-correlation functional $E_{xc}[n]$, and the internuclear repulsion energy E_{II}.

The energy expression that is evaluated in FHI-Aims is not the KS-functional from equation A.9 but rather the so-called Harris functional - see equation A.10.[141] Within the Harris functional terms which are available from a previous $\mu - 1$ and the current scf iteration step μ are combined as shown below in equation A.10. Important is that when self-consistency is reached, the KS total energy functional and the Harris functional are equal.

$$\begin{aligned} E^{\mu}_{Harris} = \sum_{l=1}^{N_{states}} f_l^{(\mu)} \epsilon_l^{(\mu)} - \int d^3r [n^{(\mu-1)}(\mathbf{r}) V_{xc}[n^{(\mu-1)}](\mathbf{r})] + E_{xc}^{\mu-1} - \\ \frac{1}{2} \int d^3r [n^{(\mu-1)}(\mathbf{r}) V_{Hartree}^{(\mu-1)}(\mathbf{r})] + E_{II} \end{aligned} \tag{A.10}$$

As we need the energy or specific energy terms corresponding to exactly the eigenvectors, i.e. the resulting electron density, which we re-enter to the DFT code we cannot perform a self-consistency cycle (scf) for the restarted calculation. Consequently, not all terms that are determined when evaluating the Harris functional correspond to this input density. Especially the eigenvalues $\epsilon_l^{(\mu)}$ are evaluated for an updated version of the density, i.e. they correspond to the eigenvectors (density) that are obtained when solving KS-equations.

As this has immediate consequences for the current version of the decomposition scheme we elaborate a bit more on the indidvidual steps and corresponding terms during the scf cycle. At the beginning, the calculation is started with a certain initial electron density $n^{(0)}$ that can either be created (guessed) from a superposition of spherical free atom densities or that is read in from restart files. The latter is the case for dealing with the combined system $\mathbb{C}_{\{AB\}}$ relevant for the decomposition scheme. As a next step, the density change between consecutive scf iterations $(\mu - 1)$ and μ is damped by mixing the new KS electron density n^{μ}_{KS} with a certain amount of the density of the previous iteration μ. The most simple way is to use a linear mixing scheme with a mixing operator that is equal to a constant G which can take values between 0 and 1. The corresponding equation reads as follows:

$$n^{\mu}_{mix} = n^{\mu-1} + G(n^{\mu}_{KS} - n^{\mu-1}). \tag{A.11}$$

By setting G to 0 or 1 one can choose between the electron densities n^{μ}_{KS} and $n^{\mu-1}$ for the further evaluation. Here, one has to note a very important ambiguity when evaluating equation A.10 before self-convergency is reached: The evaluation of the single-particle kinetic energy $T_s[n]$ requires a set of Kohn-Sham eigenstates that are consistent with the electron density n.[141] This means that (at the current state) in FHI-aims one can only evaluate $T_s[n]$ for the ouptut density of a given iteration n^{μ}_{KS}, but not for the input density $n^{(\mu-1)}$. However, the electrostatic potential $V_{Hartree}$ is computed for the input density $n^{\mu-1}$, but not for the output density. For efficiency reasons the electrostatic energy is thus evaluated for the input density $n^{\mu-1}$.[141]

For the implemented decomposition scheme this means that we can get the electrostatic energy corresponding to system $\{AB\}$ by restarting a DFT calculation from the corresponding eigenvectors and occupations specifying a linear mixer of 0. In a first step, the electrostatic energy is then calculated for the electron density corresponding to the input. The single particle eigenvalues, are only obtained after solving the KS-equations. Therefore, they no longer correspond to the input density but rather to the obtained solution of the KS-equations. This is especially important, as the density corresponding to $\mathbb{C}_{\{AB\}}$ is certainly not converged. As a consequence, we cannot obtain the kinetic energy corresponding to the input and thus we cannot obtain Pauli repulsion and orbital rehybridization contributions, at least at the current state of the codes.

Below I will briefly mention the term that would have to be determined for getting the correct kinetic energy. The expression that one needs to determine for the input electron density $n^{(\mu-1)}$ looks like the following:

$$\begin{aligned} E_{kin}\left[n^{(\mu-1)}\right] = \langle \Psi\left[n^{(\mu-1)}\right] | \hat{T}_s | \Psi\left[n^{(\mu-1)}\right] \rangle &= \langle \Psi\left[n^{(\mu-1)}\right] | -\frac{1}{2}\sum_{j=1}^{N_{el}/2} \boldsymbol{\nabla}_j^2 | \Psi\left[n^{(\mu-1)}\right] \rangle \\ &= -\frac{1}{2}\sum_{l=1}^{N_{el}/2} \langle \Psi_l\left[n^{(\mu-1)}\right] | \boldsymbol{\nabla}^2 | \Psi_l\left[n^{(\mu-1)}\right] \rangle. \end{aligned} \tag{A.12}$$

Inspecting the expression above and considering the atom centered basis functions which are used, one finds that the integrals that have to be evaluated can be written as:

$$c_{il}^{*} c_{jl} \int \phi_i^{at}(\boldsymbol{r} - \boldsymbol{R}_{at}) \ \boldsymbol{\nabla}^2 \ \phi_j^{at}(\boldsymbol{r} - \boldsymbol{R}_{at}) d\boldsymbol{r} \tag{A.13}$$

Summing all these terms up, one can then obtain the kinetic energy. It turns out that while these quantities are well defined their actual determination poses a challenge. Close to the position of the nuclei $\boldsymbol{R}_{at}$ these integrals diverge for periodic systems. Now, getting a converging expression for the kinetic energy is the remaining challenge for bringing the decomposition towards its second stage. Then the repulsion term $\Delta E_{Pauli,orb}$ can be further decomposed into orbital rehybridization and Pauli exchange repulsion, as outlined in Section 1.4.3 and Refs [140, 168, 172].

Appendix B.

Tutorial for Performing Tight-Binding Fits

The following tutorial has been designed to familiarize new students in our group with the tight-binding fit (TB-fit) package written by Florian Mayer and myself. The underlying theory has already been introduced in Section 1.4.2. Therefore, only the parts of the tutorial which focus on the usage of the TB-fit package are included here. The actual implementation of the basic parts of the code is documented in the Master Thesis of Florian Mayer [165]. These basic parts include the construction of the model function, the actual fitting routine, and the evaluation of the fit. Parts of this tutorial, especially for the one-dimensional model systems, are based on test calculations that have been carried out during the Bachelor thesis of Maximilian Kendler. Furthermore, my experiences gathered when teaching him how to use the TB-fit package are incorporated in this tutorial.

B.1. One Dimensional Systems

In this section of the tutorial we are going to look at one dimensional systems with either one or two molecules per unit cell. For each of the resulting 1D chains the distance between neighboring molecules is set to 4.5 Å. The electronic band structure for each of the systems is calculated by using density functional theory (DFT) as implemented in FHI-Aims[141] and then the intermolecular electronic couplings are determined by, first defining a proper tight-binding model function, and then fitting this model function to the DFT data.

B.1.1. 1D Ethen, single atom per cell

As a first step, we start by considering a one-dimensional chain of ethen atoms with a stacking distance of 4.5 Å and one molecule per cell. Thus, a very simple model function with one molecule per unit cell can be used to describe the system. The *geometry.in* file for the FHI-aims calculations is given below and the structure of ethen as well as the resulting 1D crystal structure are shown in Figures B.1 and B.2. Now the first task is to calculate the electronic band structure of this system.

```
lattice_vector 0.0 0.0 4.5
lattice_vector 15.0 0.0 0.0
lattice_vector 0.0 15.0 0.0
atom        0.00000000      0.66608038      0.00000000 C
atom        0.00000000     -0.66608038      0.00000000 C
atom        0.92758972      1.23990807      0.00000000 H
atom       -0.92758972      1.23990807      0.00000000 H
atom        0.92758972     -1.23990807      0.00000000 H
atom       -0.92758972     -1.23990807      0.00000000 H
```

For this very simple and highly symmetric example we only want to include electronic couplings (transfer integrals) between nearest neighbors. These couplings are denoted as t_{R_1} and t_{-R_1} in Figure B.2. Now, considering only these two couplings and taking into account that they are symmetry equivalent one ends up with equation B.1 for the energy.

$$E(\mathbf{k}) = t^{AA}_{R_0} + 2t^{AA}_{R_1}\cos(\mathbf{kR}_1) \tag{B.1}$$

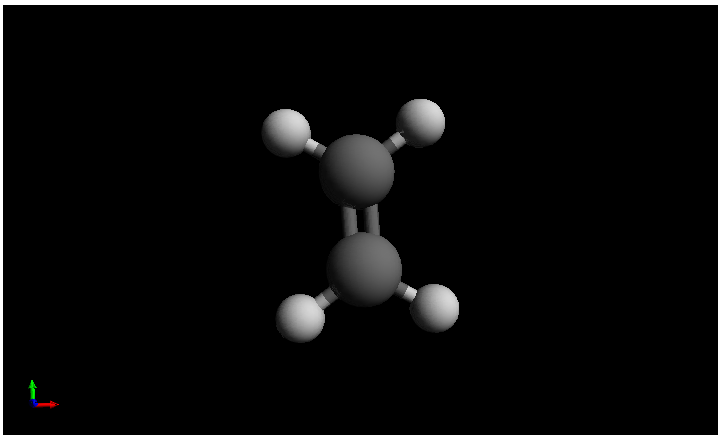

Figure B.1.: Structure of a single ethen molecule. C atoms are shown in grey and H atoms in white.

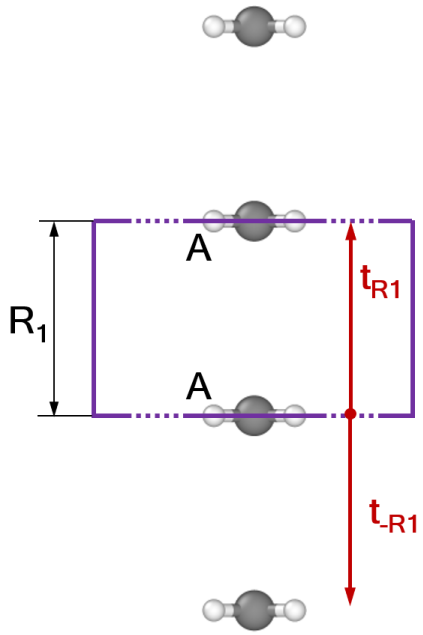

Figure B.2.: Structure of a 1D chain of ethen atoms.

This model is the one to be fitted to the calculated electronic bands. The remaining task now is to set up this model within the TB-fit package. To achieve this, several lines of the input section of the main function of the code have to be changed. As a first step, one has to enter the path to the DFT calculation:

```
path='/path/to/my/DFT/calculation/'
```

Then, one has to define the model, meaning that first one has to enter the lattice vectors which enter and second one has to specify their symmetries:

```
R_ab=np.array([R0, -R1])
R_ba=np.array([R0, R1])
R_aa=np.array([R0, R1, -R1])
```

As a next step, one also has to specify the symmetries of the system, meaning that one has to enter which transfer integrals are symmetry equivalent, therefore equal. Please note that the number N in the labels tN_AA stands for the position of the corresponding distance vector in the array R_aa. So in this case the transfer integrals belonging to R1 and -R1 are equal.

```
t_symmetries = ['t2_AA=t1_AA']
```

Now, as the tight-binding function for one molecule per cell always describes a single energy band one has to specify which energetic band should be fitted. This number

can be taken from the FHI-aims output file. In our case it is the number of the highest occupied band, see below:

```
n_val=7
```

The following variables also have to be specified for each calculation:

```
k_tick_labels = ['$\mathbf{\Gamma}$', 'Z'] # labels for plot
n_bands = len(k_tick_labels)-1 # number of bands
# save Figure and Transfer integrals
save = 'yes' # yes/no
N_molecule = 1 # 1,2 or N molecules per cell
TODO = 'Fit'
```

After entering these variables one can run the code and perform the first tight-binding fit! Whether everything worked one can find out by checking the output of the code. First of all, one can check what is written out to the terminal:

```
Symmetry-eqivalent couplings have been stated!
Indizes of equivalent couplings
[[2], [1]]
[[Fit Statistics]]
# fitting method   = leastsq
# function evals   = 25
# data points      = 80
[[Variables]]
t0_AA: -6.64929333 (init = 0)
t1_AA:  0.09895860 (init = 0)
t2_AA:  0.00000000 (init = 0)
t0_AB:  0.00000000 (init = 0)
t1_AB:  0.00000000 (init = 0)
Symmetry-eqivalent couplings have been stated!
Indizes of equivalent couplings
[[2], [1]]
5.2 meV
```

The code outputs some information on which evaluation mode has been chosen and, more importantly, the obtained transfer integrals are written out in eV. Please be aware that you set t1_AA=t2_AA, so t2_AA is equal to 0.09896 eV and not to 0.0 eV as specified in the output. Furthermore, AB was not used during the fit, therefore these lines can be ignored. The obtained transfer integrals are also written to a file named 'Transer_Integrals_Fit.dat'. In this file also the symmetries that were used during the calculation are reported. The last output of the code is a plot where the DFT data (along user specified $\boldsymbol{k}$-paths) is compared to the data generated by the model using the

obtained transfer integrals - see Figure B.3. This way one can actually nicely see whether the fit worked well. To quantify the differences between the actual DFT data for the electronic band and the band obtained from the tight model, the RMSE between model and DFT data is calculated as:

$$RMSE = \sqrt{\frac{\sum_{i=1}^{N} |E_{i,DFT} - E_{i,TB}|^2}{N}}. \tag{B.2}$$

Here, $E_{i,DFT}$ denotes the energy calculated using DFT and $E_{i,TB}$ denotes the energy obtained from the tight-binding model.

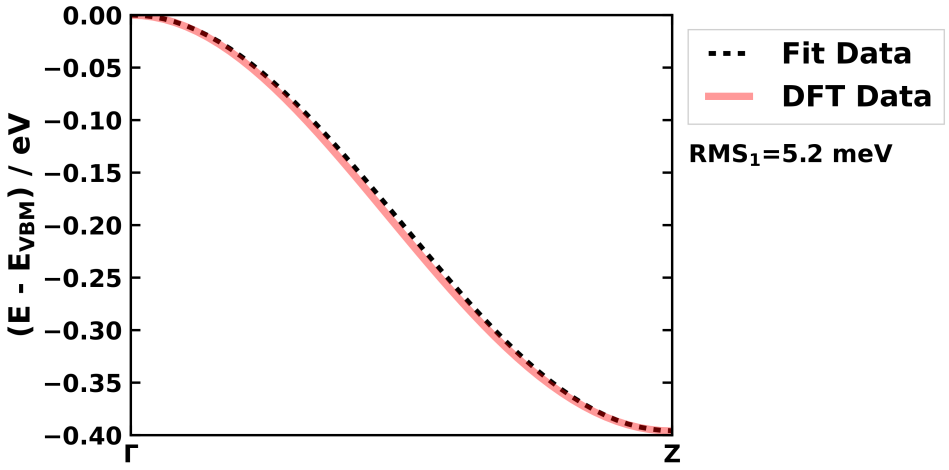

Figure B.3.: Electronic band structure obtained by performing a DFT calculation compared to the results generated by using the applied tight-binding model with the fitted transfer integrals.

From the comparison between the DFT data and the tight-binding model one can see that the fit worked well, although only one parameter was used for describing the energy dispersion relation. Now, as the next challenge we are going to have a look at a system with two ethen molecules per cell.

B.1.2. 1D Ethen, two atoms per cell

The unit cell size is now doubled in the stacking direction and a second ethen molecule is placed in the unit cell at a distance of 4.5 Å from the original molecule. The second molecule is then rotated around its long molecular axis by a certain angle. The task is now to come up with a suitable tight-binding model and then fit to the DFT calculated

band structure. The first step is again to identify the symmetries of the present system. The relevant transfer integrals for setting up a model are shown in Figure B.4

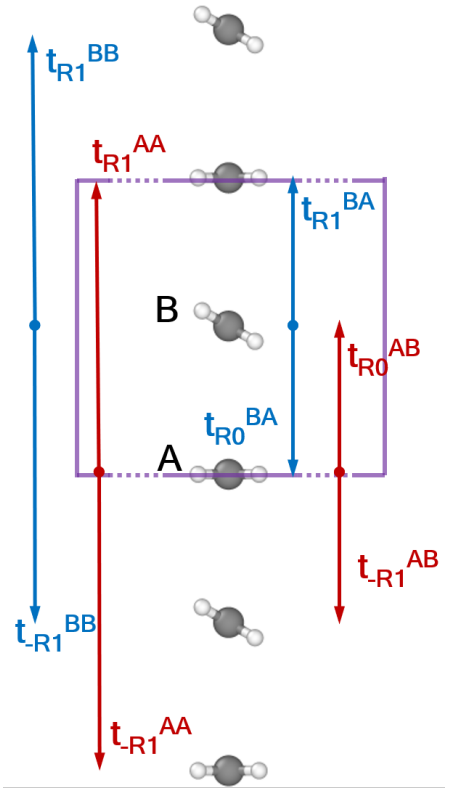

Figure B.4.: Structure of a 1D chain of ethen molecules where two molecules are in the unit cell and rotated relative to each other.

The following symmetries can be identified:

$$
\begin{aligned}
t^{AA}_{-R_1} &= t^{AA}_{R_1} \\
t^{BB}_{-R_1} &= t^{BB}_{R_1} \\
t^{AB}_{-R_1} &= t^{AB}_{R_0} \\
t^{BA}_{R_0} &= t^{AB}_{R_0} \\
t^{BA}_{R_1} &= t^{AB}_{R_0}
\end{aligned}
$$

With these symmetries one can reduce the fit function to the following form shown in equation B.3.

$$E_{1,2} = \frac{t_{R_0}^{AA} + t_{R_0}^{BB} + 2(t_{R_1}^{AA} + t_{R_1}^{BB})\cos(\mathbf{kR}_1)}{2} \pm \sqrt{\frac{[t_{R_0}^{AA} - t_{R_0}^{BB} + 2(t_{R_1}^{AA} - t_{R_1}^{BB})\cos(\mathbf{kR}_1)]^2}{4} + 2(t_{R_0}^{AB})^2(1+\cos(\mathbf{kR}_1))} \tag{B.3}$$

Now, similar to the one molecule per unit cell example simply enter the model function and fit it to the DFT data. Be careful that you enter the correct distance vectors R and the corresponding symmetries:

```
R_ab=np.array([R0, -R1])
R_ba=np.array([R0, R1])
R_aa=np.array([R0, R1, -R1])
R_bb=R_aa

t_symmetries = ['t2_AA=t1_AA', 't2_BB=t1_BB',\
't1_AB=t0_AB','t0_BA=t0_AB','t1_BA=t0_AB']

n_val=15
```

And also change N_molecule to 2. As a first step perform a fit for the system with no rotation between the two molecules in the unit cell. The physics of this system did not change, which means you should get the same transfer integral describing the interaction between nearest neighbor molecules as for the one molecule per unit cell example. Indeed, comparing the results for the two systems, one finds that they agree. Both yield a transfer integral equal to 99 meV. Note that for the system with one molecule per cell $t_{R_1}^{AA}$ denoted the transfer integral between nearest neighbors, whereas for the two molecules per cell system $t_{R_0}^{AB}$ denotes the transfer integrals between nearest neighbors. One difference is, however that for the two molecule per unit cell case only the square of the transfer integral is obtained, which means that the information regarding the sign cannot be determined.

At this point we are going to stop the considerations on one-dimensional systems and go on with two-dimensional models.

B.2. Two Dimensional Systems

In this part of the Tutorial we are going to have a look at two dimensional systems of ethen molecules, as shown in Figure B.5. Only the molecular arrangement where the A

and B molecules within the unit cell are displaced relative to each other by 1.0 Å (see figure B.5) is considered as an example.

The first task now is to construct the geometry for this study and to calculate the electronic band structure using DFT. The molecule itself can be taken from the 1D systems and used for this construction. All relevant distances for constructing the model crystal can be found in figure B.5 . Before starting the DFT calculation Please check whether you adopted the k-grid to the now 2D nature of the system (e.g. 1x20x20 k-points). It is important to fit the model function to a dense grid covering all $\boldsymbol{k}$-space and not just along a $\boldsymbol{k}$-path connecting the high-symmetry points.

As a next step one can set up a proper tight-binding model, considering all symmetries which can be identified. Please include the transfer integrals to the following lattice vector (combinations):

$$\begin{aligned} &\pm R_1^{AB,BA} \\ &\pm R_2^{AB,BA} \\ \pm(R_1^{AB,BA} &+ R_2^{AB,BA}) \\ &\pm R_1^{AA,BB} \\ &\pm R_2^{AA,BB} \end{aligned}$$

Considering these distances and the system shown in Figure B.5 define all relevant symmetries and set up the tight-binding model. Then fit this model to the DFT data and rationalize the results.

Assuming that the DFT calculation worked properly and that the you used a correct model for fitting the data you should end up with plots similar to Figure B.6. Here, the results are shown for an ethen model crystal with a shift of 1 Å along direction R_2 between A and B layers. For comparison, the electronic couplings have been calculated using the fragment orbital method and entered into the tight-binding model. The resulting electronic band structure is shown in Figure B.7.

One very interesting aspect that can be observed when inspecting the obtained transfer integrals is that t_{R0}^{AB} and t_{-R2}^{AB}, equalling t0_AB and t2_AB in the listing below, appear to be switched. Based on the values obtained for the situation with 0 Å displacement and considering the small displacement of 1 Å one would assume that t_{R0}^{AB} should be the larger transfer integral. This guess is supported by the transfer integrals calculated for the extracted dimers and employing the fragment orbital method as: $t_{R0}^{AB} = 81\ meV$ and $t_{-R2}^{AB} = 12\ meV$. Indeed the opposite is found based on the output of the tight-binding fit. What happened? Did the fit go wrong, or is the chosen model wrong?

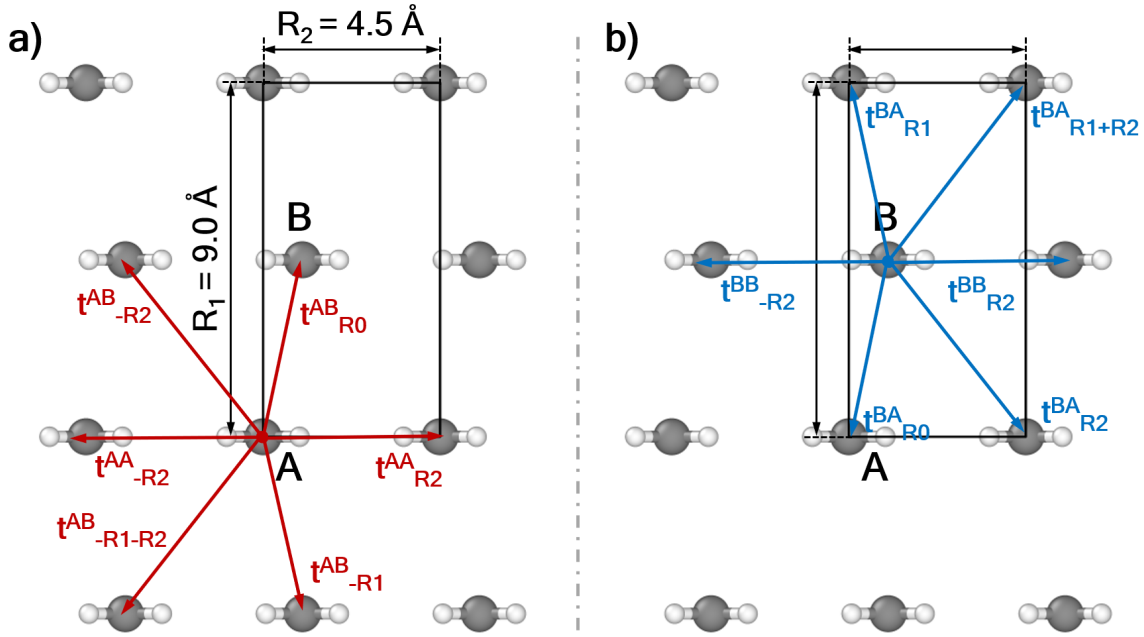

Figure B.5.: Structure of a 2D arrangement of ethen molecules A and B. The two molecules are shifted by 1.0 Å relative to each other along the short molecular axis.

The answer is no, the model is correct and also the fit did not go wrong! Rather it is a property of the specific model function that the individual values of these two transfer integrals cannot be uniquely determined. Deriving the analytical expression for the tight-binding function considering all symmetry equivalent transfer integrals, one ends up with expression B.4.

$$E_{1,2} = t_{R_0}^{AA} + 2t_{R_2}^{AA} cos(\boldsymbol{kR}_2) \pm 2 \left| cos\left(\frac{\boldsymbol{kR}_1}{2}\right) \right| \sqrt{(t_{R_0}^{AB})^2 + (t_{R_2}^{AB})^2 + 2t_{R_0}^{AB} t_{R_2}^{AB} cos(\boldsymbol{kR}_2)} \tag{B.4}$$

Considering the transfer integrals between molecules A and B within this system one finds that after a succesfull fit, these transfer integrals are determined by a nonlinear set of equations as follows:

$$\begin{aligned} c_1 &= (t_{R_0}^{AB})^2 + (t_{R_1}^{AB})^2 \\ c_2 &= 2t_{R_0}^{AB} t_{R_1}^{AB} \end{aligned} \tag{B.5}$$

For calculating the individual transfer integrals, one has to solve this nonlinear system of

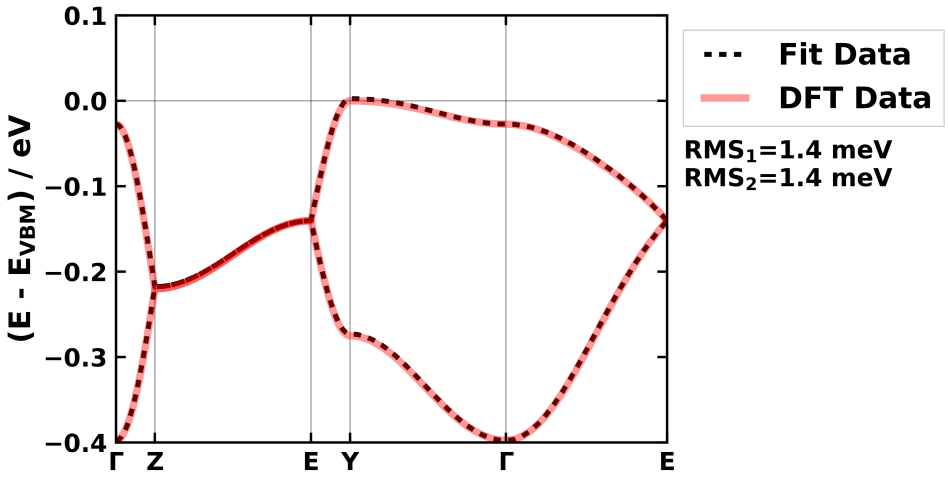

Figure B.6.: Electronic band structure of the two-dimensional model system. The fitted band structure is shown as a dashed line. The RMSE for each band is shown below the legend and denoted as RMS_1 respectively RMS_2.

equations. For this system shown here, one would end up with 4 solutions for the transfer integrals.

$$\begin{aligned} t_{R_0}^{AB} &= \pm\sqrt{\frac{1}{2}\left(c_1 \pm \sqrt{c_1^2 - c_2^2}\right)} \\ t_{R_1}^{AB} &= \frac{c_2}{2t_{R_0}^{AB}} \end{aligned} \tag{B.6}$$

So what you have found is one of the possible solutions, which might not be the physically "correct" one. Including prior knowledge on the size of the individual transfer integrals as start values for the fit might help to mitigate this dilemma. However, for systems with fewer symmetries, thus more complex analytical expressions, one obtains a set of nonlinear equations of higher order and therefore retrieving the physically correct solution can become challenging.

```
#Transfer Integrals and RMS
Name,   Transfer Integral / meV,   Remark
t0_AA,   -6931.19,
t1_AA,   -1.01,
t2_AA,   0.0,       at initial value
t3_AA,   0.0,       at initial value
t4_AA,   0.0,       at initial value
t0_BB,   -6921.97,
t1_BB,   3.61,
```

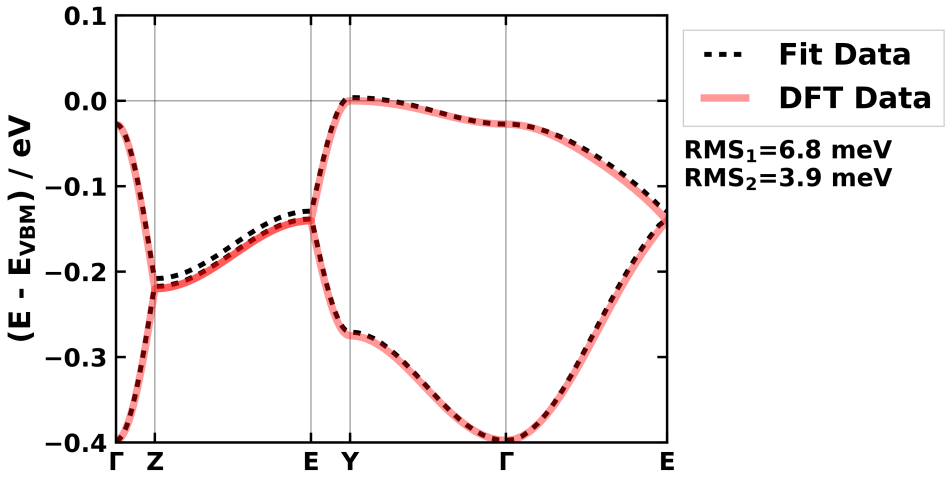

Figure B.7.: Electronic band structure of the two-dimensional model system. The band structure derived from the FO couplings is shown as a dashed line.

```
t2_BB,    0.0,       at initial value
t3_BB,    -19.34,
t4_BB,    0.0,       at initial value
t0_AB,    11.91,
t1_AB,    0.0,       at initial value
t2_AB,    80.59,
t3_AB,    0.0,       at initial value
t0_BA,    0.0,       at initial value
t1_BA,    0.0,       at initial value
t2_BA,    0.0,       at initial value
t3_BA,    0.0,       at initial value

RMS$_{1}$ (DFT, Fit): [1.413 1.353] meV
['t2_AA=t1_AA', 't4_AA=t3_BB', 't3_AA=t3_BB', 't2_BB=t1_BB', 't4_BB=
   t3_BB', 't1_AB=t0_AB', 't3_AB=t2_AB', 't0_BA=t0_AB', 't1_BA=t0_AB',
    't2_BA=t2_AB', 't3_BA=t2_AB']
```

Note that the model system considered above is similar to the system discussed in Ref [3]. Similar observations were made for that system and the problem was addressed briefly in the Supporting Information of that paper.

One aspect that I would like to mention briefly is that so far all the systems that we considered had well seperated frontier electronic bands without any band crossings. When this is not the case, i.e. the electronic bands cross, it is not straightforward to assign the DFT calculated eigenvalues to the correct band. Therefore, for such situations one has to think of a different ansatz. If you would like to learn more about the ideas that exist

for dealing with such situations then contact me.

After performing the above tasks, one should be able to use the TB-fit package.

Bibliography

(1) Winkler, C.; Harivyasi, S. S.; Zojer, E. Controlling the electronic properties of van der Waals heterostructures by applying electrostatic design. *2D Materials* **2018**, *5*, 035019 (cit. on p. xi).

(2) Winkler, C.; Mayer, F.; Zojer, E. Analyzing the Electronic Coupling in Molecular Crystals—The Instructive Case of α-Quinacridone. *Advanced Theory and Simulations* **2019**, *2*, 1800204 (cit. on pp. xiii, 7, 8, 14, 34, 212, 214).

(3) Winkler, C.; Jeindl, A.; Mayer, F.; Hofmann, O. T.; Tonner, R.; Zojer, E. Understanding the Correlation between Electronic Coupling and Energetic Stability of Molecular Crystal Polymorphs: The Instructive Case of Quinacridone. *Chemistry of Materials* **2019**, *31*, 7054–7069 (cit. on pp. xiii, 216, 218, 227–229, 247).

(4) Winkler, C.; Zojer, E. Strategies for controlling through-space charge transport in metal-organic frameworks via structural modifications. *Nanomaterials* **2020**, *10*, 1–21 (cit. on pp. xiii, 212, 216, 217).

(5) Pope, M.; Kallmann, H. P.; Magnante, P. Electroluminescence in organic crystals. *The Journal of Chemical Physics* **1963**, *38*, 2042–2043 (cit. on p. 3).

(6) Morel, D. L.; Ghosh, A. K.; Feng, T.; Stogryn, E. L.; Purwin, P. E.; Shaw, R. F.; Fishman, C. High-efficiency organic solar cells. *Applied Physics Letters* **1978**, *32*, 495–497 (cit. on p. 3).

(7) Barlow, S.; Brédas, J. L.; Getmanenko, Y. A.; Gieseking, R. L.; Hales, J. M.; Kim, H.; Marder, S. R.; Perry, J. W.; Risko, C.; Zhang, Y. Polymethine materials with solid-state third-order optical susceptibilities suitable for all-optical signal-processing applications. *Materials Horizons* **2014**, *1*, 577–581 (cit. on p. 3).

(8) Tang, C. W. Two-layer organic photovoltaic cell. *Applied Physics Letters* **1986**, *48*, 183–185 (cit. on p. 3).

(9) Koezuka, H.; Tsumura, A.; Ando, T. Field-effect transistor with polythiophene thin film. *Synthetic Metals* **1987**, *18*, 699–704 (cit. on p. 3).

(10) Burroughes, J. H.; Bradley, D. D.; Brown, A. R.; Marks, R. N.; Mackay, K.; Friend, R. H.; Burns, P. L.; Holmes, A. B. Light-emitting diodes based on conjugated polymers. *Nature* **1990**, *347*, 539–541 (cit. on p. 3).

(11) Hiramoto, M.; Fujiwara, H.; Yokoyama, M. Three-layered organic solar cell with a photoactive interlayer of codeposited pigments. *Applied Physics Letters* **1991**, *58*, 1062–1064 (cit. on p. 3).

(12) Garnier, F.; Hajlaoui, R.; Yassar, A.; Srivastava, P. All-polymer field-effect transistor realized by printing techniques. *Science* **1994**, *265*, 1684–1686 (cit. on p. 3).

(13) Horowitz, G. Field-effect transistors based on short organic molecules. *Journal of Materials Chemistry* **1999**, *9*, 2021–2026 (cit. on p. 3).

(14) Hales, J. M.; Matichak, J.; Barlow, S.; Ohira, S.; Yesudas, K.; Brédas, J. L.; Perry, J. W.; Marder, S. R. Design of polymethine dyes with large third-order optical nonlinearities and loss figures of merit. *Science* **2010**, *327*, 1485–1488 (cit. on p. 3).

(15) Gieseking, R. L.; Mukhopadhyay, S.; Shiring, S. B.; Risko, C.; Brédas, J. L. Impact of bulk aggregation on the electronic structure of streptocyanines: Implications for the solid-state nonlinear optical properties and all-optical switching applications. *Journal of Physical Chemistry C* **2014**, *118*, 23575–23585 (cit. on p. 3).

(16) Mishra, A.; Bäuerle, P. Small molecule organic semiconductors on the move: Promises for future solar energy technology. *Angewandte Chemie - International Edition* **2012**, *51*, 2020–2067 (cit. on p. 3).

(17) Root, S. E.; Savagatrup, S.; Printz, A. D.; Rodriquez, D.; Lipomi, D. J. Mechanical Properties of Organic Semiconductors for Stretchable, Highly Flexible, and Mechanically Robust Electronics. *Chemical Reviews* **2017**, *117*, 6467–6499 (cit. on p. 3).

(18) Głowacki, E. D.; Irimia-Vladu, M.; Bauer, S.; Sariciftci, N. S. Hydrogen-bonds in molecular solids-from biological systems to organic electronics. *Journal of Materials Chemistry B* **2013**, *1*, 3742–3753 (cit. on p. 3).

(19) Daniel Głowacki, E.; Leonat, L.; Irimia-Vladu, M.; Schwödiauer, R.; Ullah, M.; Sitter, H.; Bauer, S.; Serdar Sariciftci, N. Intermolecular hydrogen-bonded organic semiconductors-Quinacridone versus pentacene. *Applied Physics Letters* **2012**, *101*, 0233051–0233055 (cit. on p. 3).

(20) Głowacki, E. D.; Irimia-Vladu, M.; Kaltenbrunner, M.; Gsiorowski, J.; White, M. S.; Monkowius, U.; Romanazzi, G.; Suranna, G. P.; Mastrorilli, P.; Sekitani, T.; Bauer, S.; Someya, T.; Torsi, L.; Sariciftci, N. S. Hydrogen-bonded semiconducting pigments for air-stable field-effect transistors. *Advanced Materials* **2013**, *25*, 1563–1569 (cit. on pp. 3, 13).

(21) Coropceanu, V.; Cornil, J.; da Silva Filho, D. A.; Olivier, Y.; Silbey, R.; Brédas, J. L. Charge transport in organic semiconductors. *Chemical Reviews* **2007**, *107*, 926–952 (cit. on pp. 3, 5, 6, 11, 23, 213).

(22) Oberhofer, H.; Reuter, K.; Blumberger, J. Charge Transport in Molecular Materials: An Assessment of Computational Methods. *Chemical Reviews* **2017**, *117*, 10319–10357 (cit. on pp. 3–8).

(23) Fratini, S.; Mayou, D.; Ciuchi, S. The transient localization scenario for charge transport in crystalline organic materials. *Advanced Functional Materials* **2016**, *26*, 2292–2315 (cit. on pp. 3, 5, 10–12, 19).

(24) Einstein, A. Über die von der molekularkinetischen Theorie der Wärme geforderte Bewegung von in ruhenden Flüssigkeiten suspendierten Teilchen. *Annalen der Physik* **1905**, *322*, 549–560 (cit. on p. 4).

(25) Von Smoluchowski, M. Zur kinetischen Theorie der Brownschen Molekularbewegung und der Suspensionen. *Annalen der Physik* **1906**, *326*, 756–780 (cit. on p. 4).

(26) Tessler, N.; Preezant, Y.; Rappaport, N.; Roichman, Y. Charge transport in disordered organic materials and its relevance to thin-film devices: A tutorial review. *Advanced Materials* **2009**, *21*, 2741–2761 (cit. on p. 5).

(27) Fratini, S.; Ciuchi, S.; Mayou, D.; De Laissardière, G. T.; Troisi, A. A map of high-mobility molecular semiconductors. *Nature Materials* **2017**, *16*, 998–1002 (cit. on pp. 5, 11–13).

(28) Fratini, S.; Ciuchi, S. Bandlike motion and mobility saturation in organic molecular semiconductors. *Physical Review Letters* **2009**, *103*, 266601 (cit. on pp. 5, 11).

(29) Troisi, A.; Cheung, D. L. Transition from dynamic to static disorder in one-dimensional organic semiconductors. *Journal of Chemical Physics* **2009**, *131*, 014703 (cit. on p. 5).

(30) Marcus, R. A. On the theory of oxidation-reduction reactions involving electron transfer. *The Journal of Chemical Physics* **1956**, *24*, 966–978 (cit. on p. 6).

(31) Marcus, R. A. Electron transfer reactions in chemistry. Theory and experiment The use of chemically modified. *Reviews of Modern Physics* **1993**, *65* (cit. on p. 6).

(32) Kwon, O.; Coropceanu, V.; Gruhn, N. E.; Durivage, J. C.; Laquindanum, J. G.; Katz, H. E.; Cornil, J.; Brédas, J. L. Characterization of the molecular parameters determining charge transport in anthradithiophene. *Journal of Chemical Physics* **2004**, *120*, 8186–8194 (cit. on pp. 6, 11, 21, 23, 39, 218).

(33) Lemaur, V.; Da Silva Filho, D. A.; Coropceanu, V.; Lehmann, M.; Geerts, Y.; Piris, J.; Debije, M. G.; Van De Craats, A. M.; Senthilkumar, K.; Siebbeles, L. D.; Warman, J. M.; Brédas, J. L.; Cornil, J. Charge Transport Properties in Discotic Liquid Crystals: A Quantum-Chemical Insight into Structure-Property Relationships. *Journal of the American Chemical Society* **2004**, *126*, 3271–3279 (cit. on pp. 6, 11, 21, 23, 39, 218).

(34) Bredas, J. L.; Calbert, J. P.; da Silva Filho, D. A.; Cornil, J. Organic semiconductors: A theoretical characterization of the basic parameters governing charge transport. *Proceedings of the National Academy of Sciences* **2002**, *99*, 5804–5809 (cit. on pp. 6, 11, 21, 23, 39, 218).

(35) da Silva Filho, D. A.; Kim, E.-G.; Brédas, J.-L. Transport Properties in the Rubrene Crystal: Electronic Coupling and Vibrational Reorganization Energy. *Advanced Materials* **2005**, *17*, 1072–1076 (cit. on pp. 6, 11, 21, 23, 39, 218).

(36) Kazmaier, P. M.; Hoffmann, R. A Theoretical Study of Crystallochromy. Quantum Interference Effects in the Spectra of Perylene Pigments. *Journal of the American Chemical Society* **1994**, *116*, 9684–9691 (cit. on pp. 6, 11, 23).

(37) Gross, R.; Marx, A., *Festkörperphysik*; Oldenbourg Wissenschaftsverlag Verlag: München, 2013 (cit. on pp. 7–9).

(38) Eggeman, A. S.; Illig, S.; Troisi, A.; Sirringhaus, H.; Midgley, P. A. Measurement of molecular motion in organic semiconductors by thermal diffuse electron scattering. *Nature Materials* **2013**, *12*, 1045–1049 (cit. on p. 11).

(39) Xie, X.; Santana-Bonilla, A.; Troisi, A. Nonlocal Electron-Phonon Coupling in Prototypical Molecular Semiconductors from First Principles. *Journal of Chemical Theory and Computation* **2018**, *14*, 3752–3762 (cit. on p. 11).

(40) Schweicher, G. et al. Chasing the "Killer" Phonon Mode for the Rational Design of Low-Disorder, High-Mobility Molecular Semiconductors. *Advanced Materials* **2019**, *31*, 1902407 (cit. on p. 11).

(41) Ciuchi, S.; Fratini, S.; Mayou, D. Transient localization in crystalline organic semiconductors. *Physical Review B - Condensed Matter and Materials Physics* **2011**, *83*, 081202 (cit. on p. 11).

(42) Ciuchi, S.; Fratini, S. Electronic transport and quantum localization effects in organic semiconductors. *Physical Review B - Condensed Matter and Materials Physics* **2012**, *86*, 245201 (cit. on p. 11).

(43) Paulus, E. F.; Leusen, F. J. J.; Schmidt, M. U. Crystal structures of quinacridones. *CrystEngComm* **2007**, *9*, 131–143 (cit. on p. 13).

(44) Głowacki, E. D. Hydrogen-bonded pigments for organic electronic applications., Dissertation, Johannes Kepler University Linz, 2013 (cit. on p. 13).

(45) Yaghi, O. M.; Kalmutzki, M. J.; Diercks, C. S., *Introduction to Reticular Chemistry*; Wiley: 2019 (cit. on pp. 15, 19, 215).

(46) Yaghi, O. M.; O'Keeffe, M.; Ockwig, N. W.; Chae, H. K.; Eddaoudi, M.; Kim, J. Reticular synthesis and the design of new materials. *Nature* **2003**, *423*, 705–714 (cit. on p. 15).

(47) Li, M.; Li, D.; O'Keeffe, M.; Yaghi, O. M. Topological Analysis of Metal–Organic Frameworks with Polytopic Linkers and/or Multiple Building Units and the Minimal Transitivity Principle. *Chemical Reviews* **2014**, *114*, 1343–1370 (cit. on p. 15).

(48) James, S. L. Metal-organic frameworks. *Chemical Society Reviews* **2003**, *32*, 276–288 (cit. on p. 15).

(49) Rowsell, J. L.; Yaghi, O. M. Metal-organic frameworks: A new class of porous materials. *Microporous and Mesoporous Materials* **2004**, *73*, 3–14 (cit. on p. 15).

(50) Furukawa, H.; Cordova, K. E.; O'Keeffe, M.; Yaghi, O. M. The chemistry and applications of metal-organic frameworks. *Science* **2013**, *341*, DOI: 10.1126/science.1230444 (cit. on pp. 15, 19, 215).

(51) Stassen, I.; Burtch, N.; Talin, A.; Falcaro, P.; Allendorf, M.; Ameloot, R. An updated roadmap for the integration of metal-organic frameworks with electronic devices and chemical sensors. *Chemical Society Reviews* **2017**, *46*, 3185–3241 (cit. on pp. 15–17, 19, 215).

(52) Meek, S. T.; Greathouse, J. A.; Allendorf, M. D. Metal-Organic Frameworks: A Rapidly Growing Class of Versatile Nanoporous Materials. *Advanced Materials* **2011**, *23*, 249–267 (cit. on p. 15).

(53) Li, H.; Eddaoudi, M.; O'Keeffe, M.; Yaghi, O. M. Design and synthesis of an exceptionally stable and highly porous metal-organic framework. *Nature* **1999**, *402*, 276–279 (cit. on p. 15).

(54) Chui, S. S.; Lo, S. M.; Charmant, J. P.; Orpen, A. G.; Williams, I. D. A chemically functionalizable nanoporous material [Cu3(TMA)2 (H2O)3](n). *Science* **1999**, *283*, 1148–1150 (cit. on p. 15).

(55) Rosi, N. L.; Kim, J.; Eddaoudi, M.; Chen, B.; O'Keeffe, M.; Yaghi, O. M. Rod packings and metal-organic frameworks constructed from rod-shaped secondary building units. *Journal of the American Chemical Society* **2005**, *127*, 1504–1518 (cit. on pp. 15, 16).

(56) Rowsell, J. L.; Yaghi, O. M. Effects of functionalization, catenation, and variation of the metal oxide and organic linking units on the low-pressure hydrogen adsorption properties of metal-organic frameworks. *Journal of the American Chemical Society* **2006**, *128*, 1304–1315 (cit. on p. 15).

(57) Eddaoudi, M.; Kim, J.; Rosi, N.; Vodak, D.; Wachter, J.; O'Keeffe, M.; Yaghi, O. M. Systematic design of pore size and functionality in isoreticular MOFs and their application in methane storage. *Science* **2002**, *295*, 469–472 (cit. on p. 15).

(58) Murray, L. J.; Dinca, M.; Long, J. R. Hydrogen storage in metal-organic frameworks. *Chemical Society Reviews* **2009**, *38*, 1294–1314 (cit. on p. 15).

(59) Pascanu, V.; González Miera, G.; Inge, A. K.; Martín-Matute, B. Metal-Organic Frameworks as Catalysts for Organic Synthesis: A Critical Perspective. *Journal of the American Chemical Society* **2019**, *141*, 7223–7234 (cit. on p. 15).

(60) Zhu, L.; Liu, X. Q.; Jiang, H. L.; Sun, L. B. Metal-Organic Frameworks for Heterogeneous Basic Catalysis. *Chemical Reviews* **2017**, *117*, 8129–8176 (cit. on p. 15).

(61) Liu, J.; Chen, L.; Cui, H.; Zhang, J.; Zhang, L.; Su, C. Y. Applications of metal-organic frameworks in heterogeneous supramolecular catalysis. *Chemical Society Reviews* **2014**, *43*, 6011–6061 (cit. on p. 15).

(62) Bloch, E. D.; Queen, W. L.; Krishna, R.; Zadrozny, J. M.; Brown, C. M.; Long, J. R. Hydrocarbon separations in a metal-organic framework with open iron(II) coordination sites. *Science* **2012**, *335*, 1606–1610 (cit. on p. 15).

(63) Chen, B.; Liang, C.; Yang, J.; Contreras, D. S.; Clancy, Y. L.; Lobkovsky, E. B.; Yaghi, O. M.; Dai, S. A microporous metal-organic framework for gas-chromatographic separation of alkanes. *Angewandte Chemie - International Edition* **2006**, *45*, 1390–1393 (cit. on p. 15).

(64) Xie, L. S.; Skorupskii, G.; Dincă, M. Electrically Conductive Metal-Organic Frameworks. *Chemical Reviews* **2020**, *120*, 8536–8580 (cit. on pp. 16–19).

(65) Sun, L.; Campbell, M. G.; Dinca, M. Electrically Conductive Porous Metal-Organic Frameworks. *Angewandte Chemie International Edition* **2016**, *55*, 3566–3579 (cit. on pp. 16–18).

(66) Medina, D. D.; Mähringer, A.; Bein, T. Electroactive Metalorganic Frameworks. *Israel Journal of Chemistry* **2018**, *58*, 1089–1101 (cit. on pp. 16, 17).

(67) Miner, E. M.; Fukushima, T.; Sheberla, D.; Sun, L.; Surendranath, Y.; Dinca, M. Electrochemical oxygen reduction catalysed by Ni3 (hexaiminotriphenylene)2. *Nature Communications* **2016**, *7*, 10942 (cit. on p. 16).

(68) Miner, E. M.; Wang, L.; Dinca, M. Modular O2 electroreduction activity in triphenylene-based metal-organic frameworks. *Chemical Science* **2018**, *9*, 6286–6291 (cit. on p. 16).

(69) Downes, C. A.; Clough, A. J.; Chen, K.; Yoo, J. W.; Marinescu, S. C. Evaluation of the H2 Evolving Activity of Benzenehexathiolate Coordination Frameworks and the Effect of Film Thickness on H2 Production. *ACS Applied Materials and Interfaces* **2018**, *10*, 1719–1727 (cit. on p. 16).

(70) Dong, R.; Zheng, Z.; Tranca, D. C.; Zhang, J.; Chandrasekhar, N.; Liu, S.; Zhuang, X.; Seifert, G.; Feng, X. Immobilizing Molecular Metal Dithiolene–Diamine Complexes on 2D Metal–Organic Frameworks for Electrocatalytic H2Production. *Chemistry - A European Journal* **2017**, *23*, 2255–2260 (cit. on p. 16).

(71) Clough, A. J.; Yoo, J. W.; Mecklenburg, M. H.; Marinescu, S. C. Two-dimensional metal-organic surfaces for efficient hydrogen evolution from water. *Journal of the American Chemical Society* **2015**, *137*, 118–121 (cit. on p. 16).

(72) Campbell, M. G.; Liu, S. F.; Swager, T. M.; Dinca, M. Chemiresistive Sensor Arrays from Conductive 2D Metal-Organic Frameworks. *Journal of the American Chemical Society* **2015**, *137*, 13780–13783 (cit. on p. 16).

(73) Campbell, M. G.; Sheberla, D.; Liu, S. F.; Swager, T. M.; Dinca, M. Cu3(hexaiminotriphenylene)2: An electrically conductive 2D metal-organic framework for chemiresistive sensing. *Angewandte Chemie - International Edition* **2015**, *54*, 4349–4352 (cit. on pp. 16, 18).

(74) Meng, Z.; Aykanat, A.; Mirica, K. A. Welding Metallophthalocyanines into Bimetallic Molecular Meshes for Ultrasensitive, Low-Power Chemiresistive Detection of Gases. *Journal of the American Chemical Society* **2019**, *141*, 2046–2053 (cit. on p. 16).

(75) Smith, M. K.; Mirica, K. A. Self-Organized Frameworks on Textiles (SOFT): Conductive Fabrics for Simultaneous Sensing, Capture, and Filtration of Gases. *Journal of the American Chemical Society* **2017**, *139*, 16759–16767 (cit. on p. 16).

(76) Rubio-Giménez, V.; Almora-Barrios, N.; Escorcia-Ariza, G.; Galbiati, M.; Sessolo, M.; Tatay, S.; Martí-Gastaldo, C. Origin of the Chemiresistive Response of Ultrathin Films of Conductive Metal–Organic Frameworks. *Angewandte Chemie - International Edition* **2018**, *57*, 15086–15090 (cit. on p. 16).

(77) Aubrey, M. L.; Kapelewski, M. T.; Melville, J. F.; Oktawiec, J.; Presti, D.; Gagliardi, L.; Long, J. R. Chemiresistive Detection of Gaseous Hydrocarbons and Interrogation of Charge Transport in Cu[Ni(2,3-pyrazinedithiolate) 2] by Gas Adsorption. *Journal of the American Chemical Society* **2019**, *141*, 5005–5013 (cit. on p. 16).

(78) Sheberla, D.; Bachman, J. C.; Elias, J. S.; Sun, C. J.; Shao-Horn, Y.; Dinca, M. Conductive MOF electrodes for stable supercapacitors with high areal capacitance. *Nature Materials* **2017**, *16*, 220–224 (cit. on p. 16).

(79) Park, J.; Lee, M.; Feng, D.; Huang, Z.; Hinckley, A. C.; Yakovenko, A.; Zou, X.; Cui, Y.; Bao, Z. Stabilization of Hexaaminobenzene in a 2D Conductive Metal-Organic Framework for High Power Sodium Storage. *Journal of the American Chemical Society* **2018**, *140*, 10315–10323 (cit. on p. 16).

(80) Shinde, S. S.; Lee, C. H.; Jung, J. Y.; Wagh, N. K.; Kim, S. H.; Kim, D. H.; Lin, C.; Lee, S. U.; Lee, J. H. Unveiling dual-linkage 3D hexaiminobenzene metal-organic frameworks towards long-lasting advanced reversible Zn-air batteries. *Energy and Environmental Science* **2019**, *12*, 727–738 (cit. on p. 16).

(81) Stukowski, A. Visualization and analysis of atomistic simulation data with OVITO–the Open Visualization Tool. *Modelling and Simulation in Materials Science and Engineering* **2010**, *18*, 015012 (cit. on p. 16).

(82) Sun, L.; Hendon, C. H.; Minier, M. A.; Walsh, A.; Dinca, M. Million-fold electrical conductivity enhancement in Fe2(DEBDC) versus Mn2(DEBDC) (E = S, O). *Journal of the American Chemical Society* **2015**, *137*, 6164–6167 (cit. on p. 18).

(83) Sun, L.; Miyakai, T.; Seki, S.; Dinca, M. Mn2(2,5-disulfhydrylbenzene-1,4-dicarboxylate): A microporous metal-organic framework with infinite (-Mn-S-) chains and high intrinsic charge mobility. *Journal of the American Chemical Society* **2013**, *135*, 8185–8188 (cit. on p. 18).

(84) Sun, L.; Hendon, C. H.; Park, S. S.; Tulchinsky, Y.; Wan, R.; Wang, F.; Walsh, A.; Dinca, M. Is iron unique in promoting electrical conductivity in MOFs? *Chemical Science* **2017**, *8*, 4450–4457 (cit. on p. 18).

(85) Sheberla, D.; Sun, L.; Blood-Forsythe, M. A.; Er, S.; Wade, C. R.; Brozek, C. K.; Aspuru-Guzik, A.; Dinca, M. High electrical conductivity in Ni3(2,3,6,7,10,11-hexaiminotriphenylene)2, a semiconducting metal-organic graphene analogue. *Journal of the American Chemical Society* **2014**, *136*, 8859–8862 (cit. on p. 18).

(86) Meng, Z.; Mirica, K. A. Two-dimensional d-π conjugated metal-organic framework based on hexahydroxytrinaphthylene. *Nano Research* **2020**, *14*, 369–375 (cit. on p. 18).

(87) Hmadeh, M. et al. New Porous Crystals of Extended Metal-Catecholates. *Chemistry of Materials* **2012**, *24*, 3511–3513 (cit. on p. 18).

(88) Kambe, T.; Sakamoto, R.; Kusamoto, T.; Pal, T.; Fukui, N.; Hoshiko, K.; Shimojima, T.; Wang, Z.; Hirahara, T.; Ishizaka, K.; Hasegawa, S.; Liu, F.; Nishihara, H. Redox control and high conductivity of nickel bis(dithiolene) complex π-nanosheet: A potential organic two-dimensional topological insulator. *Journal of the American Chemical Society* **2014**, *136*, 14357–14360 (cit. on p. 18).

(89) Huang, X.; Sheng, P.; Tu, Z.; Zhang, F.; Wang, J.; Geng, H.; Zou, Y.; Di, C. A.; Yi, Y.; Sun, Y.; Xu, W.; Zhu, D. A two-dimensional π-d conjugated coordination polymer with extremely high electrical conductivity and ambipolar transport behaviour. *Nature Communications* **2015**, *6*, 1–8 (cit. on p. 18).

(90) Foster, M. E.; Sohlberg, K.; Spataru, C. D.; Allendorf, M. D. Proposed Modification of the Graphene Analogue Ni3(HITP)2 To Yield a Semiconducting Material. *The Journal of Physical Chemistry C* **2016**, *120*, 15001–15008 (cit. on pp. 18, 21, 22).

(91) Talin, A. A.; Centrone, A.; Ford, A. C.; Foster, M. E.; Stavila, V.; Haney, P.; Kinney, R. A.; Szalai, V.; El Gabaly, F.; Yoon, H. P.; Léonard, F.; Allendorf, M. D. Tunable Electrical Conductivity in Metal-Organic Framework Thin-Film Devices. *Science* **2014**, *343*, 66 LP –69 (cit. on p. 19).

(92) Goswami, S.; Ray, D.; Otake, K.-i.; Kung, C.-W.; Garibay, S. J.; Islamoglu, T.; Atilgan, A.; Cui, Y.; Cramer, C. J.; Farha, O. K.; Hupp, J. T. A porous, electrically conductive hexa-zirconium(iv) metal–organic framework. *Chemical Science* **2018**, *9*, 4477–4482 (cit. on p. 19).

(93) Kung, C.-W.; Otake, K.; Buru, C. T.; Goswami, S.; Cui, Y.; Hupp, J. T.; Spokoyny, A. M.; Farha, O. K. Increased Electrical Conductivity in a Mesoporous Metal–Organic Framework Featuring Metallacarboranes Guests. *Journal of the American Chemical Society* **2018**, *140*, 3871–3875 (cit. on p. 19).

(94) Souto, M.; Calbo, J.; Mañas-Valero, S.; Walsh, A.; Espallargas, G. M. Charge-transfer interactions between fullerenes and a mesoporous tetrathiafulvalene-based metal-organic framework. *Beilstein Journal of Nanotechnology* **2019**, *10*, 1883–1893 (cit. on p. 19).

(95) Le Ouay, B.; Boudot, M.; Kitao, T.; Yanagida, T.; Kitagawa, S.; Uemura, T. Nanostructuration of PEDOT in Porous Coordination Polymers for Tunable Porosity and Conductivity. *Journal of the American Chemical Society* **2016**, *138*, 10088–10091 (cit. on p. 19).

(96) Kung, C.-W.; Platero-Prats, A. E.; Drout, R. J.; Kang, J.; Wang, T. C.; Audu, C. O.; Hersam, M. C.; Chapman, K. W.; Farha, O. K.; Hupp, J. T. Inorganic "Conductive Glass" Approach to Rendering Mesoporous Metal–Organic Frameworks Electronically Conductive and Chemically Responsive. *ACS Applied Materials & Interfaces* **2018**, *10*, 30532–30540 (cit. on p. 19).

(97) Gershenson, M. E.; Podzorov, V.; Morpurgo, A. F. Colloquium: Electronic transport in single-crystal organic transistors. *Reviews of Modern Physics* **2006**, *78*, 973–989 (cit. on p. 19).

(98) Narayan, T. C.; Miyakai, T.; Seki, S.; Dinca, M. High charge mobility in a tetrathiafulvalene-based microporous metal-organic framework. *Journal of the American Chemical Society* **2012**, *134*, 12932–12935 (cit. on p. 20).

(99) Xie, L. S.; Dinca, M. Novel Topology in Semiconducting Tetrathiafulvalene Lanthanide Metal-Organic Frameworks. *Israel Journal of Chemistry* **2018**, *58*, 1119–1122 (cit. on p. 20).

(100) Park, S. S.; Hontz, E. R.; Sun, L.; Hendon, C. H.; Walsh, A.; Van Voorhis, T.; Dinca, M. Cation-dependent intrinsic electrical conductivity in isostructural tetrathiafulvalene-based microporous metal-organic frameworks. *Journal of the American Chemical Society* **2015**, *137*, 1774–1777 (cit. on pp. 20, 216).

(101) Sun, L.; Park, S. S.; Sheberla, D.; Dincă, M. Measuring and Reporting Electrical Conductivity in Metal-Organic Frameworks: Cd2(TTFTB) as a Case Study. *Journal of the American Chemical Society* **2016**, *138*, 14772–14782 (cit. on p. 20).

(102) Xie, L. S.; Alexandrov, E. V.; Skorupskii, G.; Proserpio, D. M.; Dinca, M. Diverse π-π Stacking motifs modulate electrical conductivity in tetrathiafulvalene-based metal-organic frameworks. *Chemical Science* **2019**, *10*, 8558–8565 (cit. on p. 20).

(103) Scheurle, P. I.; Mähringer, A.; Jakowetz, A. C.; Hosseini, P.; Richter, A. F.; Wittstock, G.; Medina, D. D.; Bein, T. A highly crystalline anthracene-based MOF-74 series featuring electrical conductivity and luminescence. *Nanoscale* **2019**, *11*, 20949–20955 (cit. on p. 21).

(104) Kuc, A.; Springer, M. A.; Batra, K.; Juarez-Mosqueda, R.; Wöll, C.; Heine, T. Proximity Effect in Crystalline Framework Materials: Stacking-Induced Functionality in MOFs and COFs. *Advanced Functional Materials* **2020**, *30*, 1908004 (cit. on pp. 21, 23).

(105) Foster, M. E.; Sohlberg, K.; Allendorf, M. D.; Talin, A. A. Unraveling the Semiconducting/Metallic Discrepancy in Ni3(HITP)2. *Journal of Physical Chemistry Letters* **2018**, *9*, 481–486 (cit. on pp. 21, 22).

(106) Clough, A. J.; Skelton, J. M.; Downes, C. A.; De La Rosa, A. A.; Yoo, J. W.; Walsh, A.; Melot, B. C.; Marinescu, S. C. Metallic Conductivity in a Two-Dimensional Cobalt Dithiolene Metal-Organic Framework. *Journal of the American Chemical Society* **2017**, *139*, 10863–10867 (cit. on p. 21).

(107) Shimoni, R.; He, W.; Liberman, I.; Hod, I. Tuning of Redox Conductivity and Electrocatalytic Activity in Metal-Organic Framework Films Via Control of Defect Site Density. *Journal of Physical Chemistry C* **2019**, *123*, 5531–5539 (cit. on p. 22).

(108) Svane, K. L.; Bristow, J. K.; Gale, J. D.; Walsh, A. Vacancy defect configurations in the metal–organic framework UiO-66: energetics and electronic structure. *J. Mater. Chem. A* **2018**, *6*, 8507–8513 (cit. on p. 22).

(109) De Vos, A.; Hendrickx, K.; Van Der Voort, P.; Van Speybroeck, V.; Lejaeghere, K. Missing Linkers: An Alternative Pathway to UiO-66 Electronic Structure Engineering. *Chemistry of Materials* **2017**, *29*, 3006–3019 (cit. on p. 22).

(110) Xiang, W.; Zhang, Y.; Chen, Y.; Liu, C. J.; Tu, X. Synthesis, characterization and application of defective metal-organic frameworks: Current status and perspectives. *Journal of Materials Chemistry A* **2020**, *8*, 21526–21546 (cit. on p. 22).

(111) Taddei, M.; Schukraft, G. M.; Warwick, M. E.; Tiana, D.; McPherson, M. J.; Jones, D. R.; Petit, C. Band gap modulation in zirconium-based metal-organic frameworks by defect engineering. *Journal of Materials Chemistry A* **2019**, *7*, 23781–23786 (cit. on p. 22).

(112) Jiang, J.; Zhao, Y.; Yaghi, O. M. Covalent Chemistry beyond Molecules. *Journal of the American Chemical Society* **2016**, *138*, 3255–3265 (cit. on p. 22).

(113) Côté, A. P.; Benin, A. I.; Ockwig, N. W.; O'Keeffe, M.; Matzger, A. J.; Yaghi, O. M. Porous, crystalline, covalent organic frameworks. *Science* **2005**, *310*, 1166–1170 (cit. on p. 22).

(114) Côté, A. P.; El-Kaderi, H. M.; Furukawa, H.; Hunt, J. R.; Yaghi, O. M. Reticular synthesis of microporous and mesoporous 2D covalent organic frameworks. *Journal of the American Chemical Society* **2007**, *129*, 12914–12915 (cit. on p. 22).

(115) El-Kaderi, H. M.; Hunt, J. R.; Mendoza-Cortés, J. L.; Côté, A. P.; Taylor, R. E.; O'Keeffe, M.; Yaghi, O. M. Designed synthesis of 3D covalent organic frameworks. *Science* **2007**, *316*, 268–272 (cit. on p. 22).

(116) Uribe-Romo, F. J.; Hunt, J. R.; Furukawa, H.; Klöck, C.; O'Keeffe, M.; Yaghi, O. M. A crystalline imine-linked 3-D porous covalent organic framework. *Journal of the American Chemical Society* **2009**, *131*, 4570–4571 (cit. on p. 22).

(117) Chen, X.; Geng, K.; Liu, R.; Tan, K. T.; Gong, Y.; Li, Z.; Tao, S.; Jiang, Q.; Jiang, D. Covalent Organic Frameworks: Chemical Approaches to Designer Structures and Built-In Functions. *Angewandte Chemie - International Edition* **2020**, *59*, 5050–5091 (cit. on pp. 22, 23).

(118) Kuhn, P.; Antonietti, M.; Thomas, A. Porous, covalent triazine-based frameworks prepared by ionothermal synthesis. *Angewandte Chemie - International Edition* **2008**, *47*, 3450–3453 (cit. on p. 22).

(119) Tilford, R. W.; Gemmill, W. R.; Zur Loye, H. C.; Lavigne, J. J. Facile synthesis of a highly crystalline, covalently linked porous boronate network. *Chemistry of Materials* **2006**, *18*, 5296–5301 (cit. on p. 22).

(120) Furukawa, H.; Yaghi, O. M. Storage of hydrogen, methane, and carbon dioxide in highly porous covalent organic frameworks for clean energy applications. *Journal of the American Chemical Society* **2009**, *131*, 8875–8883 (cit. on p. 22).

(121) Yang, Y.; Faheem, M.; Wang, L.; Meng, Q.; Sha, H.; Yang, N.; Yuan, Y.; Zhu, G. Surface Pore Engineering of Covalent Organic Frameworks for Ammonia Capture through Synergistic Multivariate and Open Metal Site Approaches. *ACS Central Science* **2018**, *4*, 748–754 (cit. on p. 22).

(122) Kang, Z.; Peng, Y.; Qian, Y.; Yuan, D.; Addicoat, M. A.; Heine, T.; Hu, Z.; Tee, L.; Guo, Z.; Zhao, D. Mixed Matrix Membranes (MMMs) Comprising Exfoliated 2D Covalent Organic Frameworks (COFs) for Efficient CO2 Separation. *Chemistry of Materials* **2016**, *28*, 1277–1285 (cit. on p. 22).

(123) Qian, H. L.; Yang, C. X.; Yan, X. P. Bottom-up synthesis of chiral covalent organic frameworks and their bound capillaries for chiral separation. *Nature Communications* **2016**, *7*, 1–7 (cit. on p. 22).

(124) Dey, K.; Pal, M.; Rout, K. C.; Kunjattu, S. S.; Das, A.; Mukherjee, R.; Kharul, U. K.; Banerjee, R. Selective Molecular Separation by Interfacially Crystallized Covalent Organic Framework Thin Films. *Journal of the American Chemical Society* **2017**, *139*, 13083–13091 (cit. on p. 22).

(125) Baldwin, L. A.; Crowe, J. W.; Pyles, D. A.; McGrier, P. L. Metalation of a Mesoporous Three-Dimensional Covalent Organic Framework. *Journal of the American Chemical Society* **2016**, *138*, 15134–15137 (cit. on p. 22).

(126) Li, H.; Pan, Q.; Ma, Y.; Guan, X.; Xue, M.; Fang, Q.; Yan, Y.; Valtchev, V.; Qiu, S. Three-Dimensional Covalent Organic Frameworks with Dual Linkages for Bifunctional Cascade Catalysis. *Journal of the American Chemical Society* **2016**, *138*, 14783–14788 (cit. on p. 22).

(127) Lin, S.; Diercks, C. S.; Zhang, Y. B.; Kornienko, N.; Nichols, E. M.; Zhao, Y.; Paris, A. R.; Kim, D.; Yang, P.; Yaghi, O. M.; Chang, C. J. Covalent organic frameworks comprising cobalt porphyrins for catalytic CO2 reduction in water. *Science* **2015**, *349*, 1208–1213 (cit. on p. 22).

(128) Sun, Q.; Aguila, B.; Perman, J.; Nguyen, N.; Ma, S. Flexibility Matters: Cooperative Active Sites in Covalent Organic Framework and Threaded Ionic Polymer. *Journal of the American Chemical Society* **2016**, *138*, 15790–15796 (cit. on p. 22).

(129) Wang, S.; Wang, Q.; Shao, P.; Han, Y.; Gao, X.; Ma, L.; Yuan, S.; Ma, X.; Zhou, J.; Feng, X.; Wang, B. Exfoliation of Covalent Organic Frameworks into Few-Layer Redox-Active Nanosheets as Cathode Materials for Lithium-Ion Batteries. *Journal of the American Chemical Society* **2017**, *139*, 4258–4261 (cit. on p. 22).

(130) Deblase, C. R.; Silberstein, K. E.; Truong, T. T.; Abruña, H. D.; Dichtel, W. R. β-ketoenamine-linked covalent organic frameworks capable of pseudocapacitive energy storage. *Journal of the American Chemical Society* **2013**, *135*, 16821–16824 (cit. on p. 22).

(131) Bisbey, R. P.; Dichtel, W. R. Covalent Organic Frameworks as a Platform for Multidimensional Polymerization. *ACS Central Science* **2017**, *3*, 533–543 (cit. on p. 22).

(132) Mandal, A. K.; Mahmood, J.; Baek, J. B. Two-dimensional covalent organic frameworks for optoelectronics and energy storage. *ChemNanoMat* **2017**, *3*, 373–391 (cit. on p. 22).

(133) Yadav, V. K.; Mir, S. H.; Mishra, V.; Gopakumar, T. G.; Singh, J. K. A simple molecular design for tunable two-dimensional imine covalent organic frameworks for optoelectronic applications. *Physical Chemistry Chemical Physics* **2020**, *22*, 21360–21368 (cit. on p. 22).

(134) Babu, H. V.; Bai, M. G.; Rajeswara Rao, M. Functional π-Conjugated Two-Dimensional Covalent Organic Frameworks. *ACS Applied Materials and Interfaces* **2019**, *11*, 11029–11060 (cit. on p. 22).

(135) Ding, S. Y.; Wang, W. Covalent organic frameworks (COFs): From design to applications. *Chemical Society Reviews* **2013**, *42*, 548–568 (cit. on p. 22).

(136) Wan, S.; Guo, J.; Kim, J.; Ihee, H.; Jiang, D. A belt-shaped, blue luminescent, and semiconducting covalent organic framework. *Angewandte Chemie - International Edition* **2008**, *47*, 8826–8830 (cit. on p. 22).

(137) Song, Y.; Sun, Q.; Aguila, B.; Ma, S. Opportunities of Covalent Organic Frameworks for Advanced Applications. *Advanced Science* **2019**, *6*, DOI: 10.1002/advs.201801410 (cit. on pp. 22, 220).

(138) Ding, X.; Feng, X.; Saeki, A.; Seki, S.; Nagai, A.; Jiang, D. Conducting metallophthalocyanine 2D covalent organic frameworks: The role of central metals in controlling π-electronic functions. *Chemical Communications* **2012**, *48*, 8952–8954 (cit. on p. 22).

(139) Geng, K.; He, T.; Liu, R.; Dalapati, S.; Tan, K. T.; Li, Z.; Tao, S.; Gong, Y.; Jiang, Q.; Jiang, D. Covalent Organic Frameworks: Design, Synthesis, and Functions. *Chemical Reviews* **2020**, *120*, 8814–8933 (cit. on p. 22).

(140) Raupach, M.; Tonner, R. A periodic energy decomposition analysis method for the investigation of chemical bonding in extended systems. *Journal of Chemical Physics* **2015**, *142*, 194105 (cit. on pp. 24, 40, 41, 43, 225, 235).

(141) Blum, V.; Gehrke, R.; Hanke, F.; Havu, P.; Havu, V.; Ren, X.; Reuter, K.; Scheffler, M. Ab initio molecular simulations with numeric atom-centered orbitals. *Computer Physics Communications* **2009**, *180*, 2175–2196 (cit. on pp. 24, 30, 44, 230, 232–234, 237).

(142) Martin, R. M., *Electronic Structure*; Cambridge University Press: 2020 (cit. on pp. 24, 26, 29).

(143) Born, M.; Oppenheimer, R. Zur Quantentheorie der Molekülen. *Annalen der Physik* **1927**, *389*, 457–484 (cit. on p. 25).

(144) Hohenberg, P.; Kohn, W. Inhomogeneous Electron Gas. *Physical Review* **1964**, *136*, B864–B871 (cit. on p. 25).

(145) Kohn, W.; Sham, L. J. Self-Consistent Equations Including Exchange and Correlation Effects. *Physical Review* **1965**, *140*, A1133–A1138 (cit. on p. 26).

(146) Perdew, J. P.; Burke, K.; Ernzerhof, M. Generalized gradient approximation made simple. *Physical Review Letters* **1996**, *77*, 3865–3868 (cit. on pp. 28, 29).

(147) Kümmel, S.; Kronik, L. Orbital-dependent density functionals: Theory and applications. *Reviews of Modern Physics* **2008**, *80*, 3–60 (cit. on p. 29).

(148) Perdew, J. P.; Zunger, A. Self-interaction correction to density-functional approximations for many-electron systems. *Physical Review B* **1981**, *23*, 5048–5079 (cit. on p. 29).

(149) Dori, N.; Menon, M.; Kilian, L.; Sokolowski, M.; Kronik, L.; Umbach, E. Valence electronic structure of gas-phase 3,4,9,10-perylene tetracarboxylic acid dianhydride: Experiment and theory. *Physical Review B* **2006**, *73*, 195208 (cit. on p. 29).

(150) Marom, N.; Hod, O.; Scuseria, G. E.; Kronik, L. Electronic structure of copper phthalocyanine: A comparative density functional theory study. *Journal of Chemical Physics* **2008**, *128*, 164107 (cit. on p. 29).

(151) Körzdörfer, T.; Kümmel, S.; Marom, N.; Kronik, L. When to trust photoelectron spectra from Kohn-Sham eigenvalues: The case of organic semiconductors. *Physical Review B* **2009**, *79*, 201205 (cit. on p. 29).

(152) Körzdörfer, T.; Kümmel, S.; Marom, N.; Kronik, L. Erratum: When to trust photoelectron spectra from Kohn-Sham eigenvalues: The case of organic semiconductors [Phys. Rev. B 79, 201205 (2009)]. *Physical Review B* **2010**, *82*, 201205 (cit. on p. 29).

(153) Jensen, F., *Introduction to computational chemistry*, 2. ed..; Chichester : Wiley: 2007 (cit. on p. 29).

(154) Adamo, C.; Barone, V. Toward reliable density functional methods without adjustable parameters: The PBE0 model. *The Journal of Chemical Physics* **1999**, *110*, 6158–6170 (cit. on p. 29).

(155) Heyd, J.; Scuseria, G. E.; Ernzerhof, M. Hybrid functionals based on a screened Coulomb potential. *Journal of Chemical Physics* **2003**, *118*, 8207–8215 (cit. on p. 29).

(156) Heyd, J.; Scuseria, G. E.; Ernzerhof, M. Erratum: Hybrid functionals based on a screened Coulomb potential (Journal of Chemical Physics (2003) 118 (8207)). *Journal of Chemical Physics* **2006**, *124*, 219906 (cit. on p. 29).

(157) Tkatchenko, A.; Scheffler, M. Accurate molecular van der Waals interactions from ground-state electron density and free-atom reference data. *Physical Review Letters* **2009**, *102*, 073005 (cit. on p. 30).

(158) Ehrlich, S.; Moellmann, J.; Grimme, S. Dispersion-Corrected Density Functional Theory for Aromatic Interactions in Complex Systems. *Accounts of Chemical Research* **2013**, *46*, 916–926 (cit. on p. 30).

(159) Cohen, A. J.; Mori-Sánchez, P.; Yang, W. Challenges for Density Functional Theory. *Chemical Reviews* **2012**, *112*, 289–320 (cit. on p. 30).

(160) Klimeš, J.; Michaelides, A. Perspective: Advances and challenges in treating van der Waals dispersion forces in density functional theory. *The Journal of Chemical Physics* **2012**, *137*, 120901 (cit. on p. 30).

(161) Distasio, R. A.; Gobre, V. V.; Tkatchenko, A. Many-body van der Waals interactions in molecules and condensed matter. *Journal of Physics Condensed Matter* **2014**, *26*, 213202 (cit. on p. 30).

(162) Hermann, J.; DiStasio, R. A.; Tkatchenko, A. First-Principles Models for van der Waals Interactions in Molecules and Materials: Concepts, Theory, and Applications. *Chemical Reviews* **2017**, *117*, 4714–4758 (cit. on p. 30).

(163) Kresse, G.; Furthmüller, J. Efficient iterative schemes for ab initio total-energy calculations using a plane-wave basis set. *Physical Review B - Condensed Matter and Materials Physics* **1996**, *54*, 11169–11186 (cit. on p. 30).

(164) Lejaeghere, K. et al. Reproducibility in density functional theory calculations of solids. *Science* **2016**, *351*, aad3000 (cit. on p. 31).

(165) Mayer, F. Electronic Couplings in Molecular Crystals: Development and Benchmarking of Advanced Strategies., Master Thesis, Graz University of Technology, 2019 (cit. on pp. 31, 237).

(166) Schober, C.; Reuter, K.; Oberhofer, H. Virtual Screening for High Carrier Mobility in Organic Semiconductors. *Journal of Physical Chemistry Letters* **2016**, *7*, 3973–3977 (cit. on p. 39).

(167) Kunkel, C.; Schober, C.; Margraf, J. T.; Reuter, K.; Oberhofer, H. Finding the Right Bricks for Molecular Legos: A Data Mining Approach to Organic Semiconductor Design. *Chemistry of Materials* **2019**, *31*, 969–978 (cit. on p. 39).

(168) Pecher, L.; Tonner, R. Deriving bonding concepts for molecules, surfaces, and solids with energy decomposition analysis for extended systems. *Wiley Interdisciplinary Reviews: Computational Molecular Science* **2019**, *9*, e1401 (cit. on pp. 40, 43, 225, 235).

(169) Ziegler, T.; Rauk, A. On the calculation of bonding energies by the Hartree Fock Slater method - I. The transition state method. *Theoretica Chimica Acta* **1977**, *46*, 1–10 (cit. on p. 40).

(170) Ziegler, T.; Rauk, A. A Theoretical Study of the Ethylene-Metal Bond in Complexes between Cu^{+}, Ag^{+}, Au^{+}, Pt^{0}, or Pt^{2+}, and Ethylene, Based on the Hartree-Fock-Slater Transition-State Method. *Inorganic Chemistry* **1979**, *18*, 664 (cit. on p. 40).

(171) Kitaura, K.; Morokuma, K. A new energy decomposition scheme for molecular interactions within the Hartree-Fock approximation. *International Journal of Quantum Chemistry* **1976**, *10*, 325–340 (cit. on p. 40).

(172) Raupach, M. Quantenchemische Untersuchungen zur chemischen Bindung an Oberflächen., Ph.D. Thesis, Philipps-Universität Marburg, 2015 (cit. on pp. 40, 43, 225, 235).

(173) Valeev, E. F.; Coropceanu, V.; Da Silva Filho, D. A.; Salman, S.; Brédas, J. L. Effect of electronic polarization on charge-transport parameters in molecular organic semiconductors. *Journal of the American Chemical Society* **2006**, *128*, 9882–9886 (cit. on p. 213).

(174) Zhou, W.; Wu, H.; Yildirim, T. Structural stability and elastic properties of prototypical covalent organic frameworks. *Chemical Physics Letters* **2010**, *499*, 103–107 (cit. on p. 220).